THE UNIVERSITY OF READING
Department of Meteorology

Interaction of turbulence with a free surface

Miguel Ângelo Cortez Teixeira

A thesis submitted for the degree of Doctor of Philosophy

April 2000

Esta Tese é dedicada a Meus Pais

Abstract

Different interactions between turbulence and a free surface are investigated, by considering idealised problems where the distortion of the turbulence by external forcings can be regarded as rapid.

The viscous coupling and the nonlinear interactions among the turbulence near a flat free surface are first considered. Calculated profiles of the turbulence dissipation rate show very good agreement with available numerical simulation data. The dissipation has a minimum at the boundary, promoting an increase of the turbulent kinetic energy. Nonlinear interactions limit the growth of the viscous boundary layer, and lead to large net strains at the boundary, associated with zones of impinging and ejecting flow, which further enhance the turbulent kinetic energy. These interactions produce pressure fluctuations correlated with the strain rates of the flow, promoting a return to isotropy of the turbulence everywhere except in zones of impinging flow, near the boundary.

The interaction between turbulence and surface waves is then considered. Wave initiation from a flat free surface by a turbulent shear flow in the water is found to be much more efficient than wave initiation by an equivalent flow in the air, because the decorrelation time scale of the pressure fluctuations is longer in the water. Calculated curvature spectra of these waves show a bimodal angular energy distribution at low wavenumbers, for sufficiently high shears, which is consistent with laboratory data. Finally, the distortion of turbulence in the water by much larger waves is examined. The turbulent velocity fluctuations transverse to the direction of wave propagation are amplified in time, due to vorticity tilting and stretching by the Stokes drift, and originate intense and elongated streamwise vortices akin to Langmuir circulations. The energy transfer to these vortices is associated with wave decay, and estimated wave attenuation rates are shown to be in order-of-magnitude agreement with laboratory data.

Acknowledgements

I would like to express my gratitude to all of those who, in various ways, have contributed to a successful completion of this thesis.

First of all, I thank my supervisor, Dr. Stephen Belcher, for his constant enthusiasm and encouragement, for his useful suggestions of problems to treat and bibliography, and for his comments and constructive criticisms, which have greatly improved this thesis. I am grateful to the members of my Thesis Committee, Dr. George Craig and Dr. David Marshall, for the time spent in monitoring my progress during the last 3 years, and for their suggestions, comments and criticisms. I acknowledge the assistance provided by members of the Boundary Layer research group and by members of staff and colleagues in general at the Department of Meteorology, who have helped me in ways it would be too lengthy to describe here.

It was both pleasant and instructive to talk to Prof. Julian Hunt in a few occasions during the course of this work. His useful suggestions concerning problems to be treated and references are gratefully acknowledged. I am indebted to Dr. Jakob Mann for his assistance with the RDT shear-flow model and also for sending me a copy of his PhD thesis. Thanks are also due to Dr. Blair Perot for sending me a copy of his PhD thesis and to DAMTP library for sending me a copy of Paul Durbin's PhD thesis. This work has been accomplished with the financial support of the Portuguese Fundação para a Ciência e Tecnologia (FCT), under Grant PraxisXXI/BD/9401/96.

On a more personal note, I would like to thank my brother Paulo Teixeira for his company and support during the course of my PhD. Finally, and most importantly, I would like to thank my parents Ivo and Judite Teixeira, to whom this thesis is dedicated, for their love, support and encouragement throughout my life.

Contents

CHAPTER 1

Introduction

The interaction of turbulence with a free surface is a complicated physical process, which has implications for a wide range of fundamental and applied fields of research. These include: turbulence modelling (Hunt, 1988; Johansson & Hallbäck, 1994), surface wave dynamics (Phillips, 1957, 1959) and mass transfer at air-water interfaces (Hunt, 1984*b*; Komori *et al.*, 1989). This thesis addresses a number of simple model problems where turbulence is explicitly simulated, aiming to clarify different aspects of the fundamental physics of turbulent flows near free surfaces.

For turbulence modelling purposes, it is important to understand how turbulence is modified by the presence of a free surface, because numerical models of flows that do not resolve the smallest scales in the turbulence require closures for the turbulent terms which are not represented explicitly (Salvetti *et al.*, 1997). These closures have to behave appropriately near boundaries, namely by reproducing as closely as possible the results of models that resolve the flow entirely. While most turbulence closures have been developed for flows near walls (Durbin, 1993), the development of closures for flows near free surfaces is of interest for numerical simulations of, for example, open-channel flows (Pan & Banerjee, 1995; Komori *et al.*, 1993; Borue *et al.*, 1995) or atmosphere-ocean interaction (Melville, 1996; Kitaigorodskii, 1997). The development of turbulence closures with a sound physical basis is only possible by studying the turbulence itself.

One of the important features characterising air-water interfaces are surface waves. The importance of turbulence in the generation and in the decay of these waves has long been recognised (Phillips, 1957; Kitaigorodskii & Lumley, 1983). Waves at an initially flat free surface are initiated by turbulent pressure fluctuations being advected in the flow either side of the interface (Phillips, 1957), and it is only later that the instability growth mechanisms relying on the existence of, at least, a small perturbation (Miles, 1957; Belcher & Hunt, 1993), and the nonlinear interactions among waves (Hasselmann, 1962) can become active. Furthermore, turbulence contributes to the decay of surface waves, through the energy transfer that takes place from the waves to turbulence, where the turbulence acts like a damping viscosity (Ölmez & Milgram, 1992). The turbulence also scatters (Phillips, 1959) and distorts the wave field (Longuet-Higgins, 1996). Waves are known to organise the oceanic turbulence into vortices aligned with their own propagation direction and with the mean wind (Craik & Leibovich, 1976). These vortices are called *Langmuir circulations*. Finally, breaking waves are an important source of turbulence in the ocean surface layer (Melville, 1996). Clearly then, any treatment of turbulence near free surfaces must also account for surface waves.

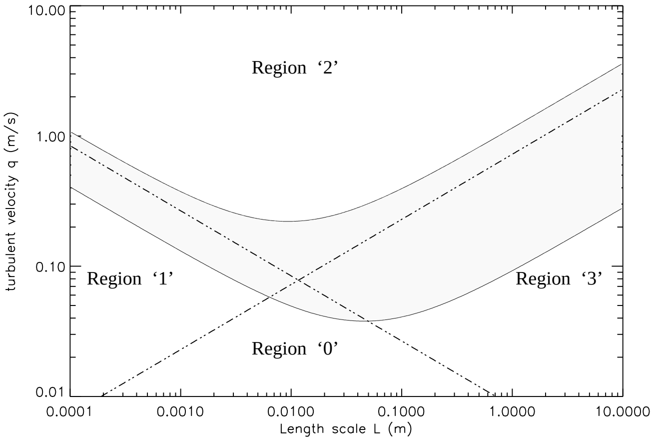

Figure 1.1 Reproduction of figure 3 of Brocchini & Peregrine (2000*a*). The turbulence velocity scale u is here denoted by q and the turbulence length scale l is here denoted by L. The dash-dotted lines correspond to the critical Froude and Weber numbers, Fr_c and We_c. The shaded area represents the region of marginal wave breaking.

Mass transfer at air-water interfaces influences the climate, since it controls the abundance in the atmosphere of gases like carbon dioxide, which have great meteorological importance (Simpson, 1984). The transfer of gases from the air to the water is controlled by the characteristics of the turbulence in the water (Brumley & Jirka, 1987; Theofanous, 1984), and also by the characteristics of the wave field at the air-water interface (Kitaigorodskii & Donelan, 1984). Relating the properties of the gas transfer to the properties of the turbulence and the waves in order to obtain gas-transfer models requires a good fundamental understanding of the underlying physics of these processes, as noted by Brocchini & Peregrine (2000*a*). These applications motivate the developments presented in this thesis.

A free surface bounding a water mass responds to turbulence in the water in a variety of ways. Brocchini & Peregrine (2000*a*) distinguish 4 basic regimes, depending on the length scale l and the velocity scale u of the turbulence, or equivalently on the value of the Froude number $Fr = u/(gl)^{1/2}$ and the Weber number of the turbulence $We = u^2 l/\gamma$ (where g is the acceleration of gravity and γ is the surface tension). If Fr and We are both lower than certain threshold values, Fr_c and We_c, the turbulence can be classified as weak, and the boundary remains approximately flat (region '0' in figure 1.1). The turbulence is then primarily affected by blocking and viscous effects (Perot & Moin, 1995*a*; Walker *et al.*, 1996). Blocking is a purely kinematic constraint similar to that imposed by a rigid wall. Viscous effects are obviously different from those imposed by a rigid wall and determine the value of the viscous stress near the boundary, which influences the shape of the tangential velocity profiles, and the turbulence dissipation rate. These effects are controlled by the Reynolds number of the turbulence, $Re = ul/\nu$ (where ν is the kinematic viscosity). The Kolmogorov microscale, η, at which most of the dissipation occurs, is $\eta \approx l Re^{-\frac{3}{4}}$ (Tennekes & Lumley, 1972). Gas transfer across the free surface is controlled by how thin the viscous boundary layer remains and how fast the fluid beneath the viscous boundary layer is renewed by the turbulent motions (Hunt, 1984*b*). The thickness of the viscous boundary layer is $\delta \approx l Re^{-\frac{1}{2}}$ (Tennekes & Lumley, 1972), while the horizontal divergence of the flow, which is a factor determining surface renewal, receives a dominant contribution from the scales of the turbulence of $O(\eta)$.

When the turbulence is more vigorous (u larger), but the length scale is relatively small ($l \leq$ 17mm), $Fr > Fr_c$ but $We < We_c$, and waves dominated by surface tension are present at the free surface. This corresponds to region '1' in figure 1.1. When the turbulence is more vigorous than in region '0' but the length scale is relatively large ($l \geq$ 17mm), $Fr < Fr_c$ but $We > We_c$, and the surface waves are dominated by gravity. This corresponds to region '3' in figure 1.1. Finally, when the turbulence is more vigorous than in all previous cases, $Fr > Fr_c$ and $We > We_c$. In that situation, which corresponds to region '2' in figure 1.1, the waves existing at the free surface have large slope. For sufficiently high values of Fr and We, the free surface becomes disintegrated, and there is permanent wave breaking, with the presence of bubbles in the water and spray in the air.

Obviously, a treatment of this last situation is not simple, and requires a reformulation of the equations of motion (Brocchini & Peregrine, 2000*b*), in order to make them able to simulate 'two-phase' flows. However, many important interactions between waves and turbulence that do not involve wave breaking can be understood by considering situations corresponding to regions '0', '1' and '3' in figure 1.1 (where $Fr < Fr_c$ or $We < We_c$). In most of the cases, the length scale of the turbulence is $l >$ 17mm (regions '0' and '3'), so the slope of the waves is small, and the waves may be treated using linear theory. Examples of interactions which have been treated successfully using linear theory are wave generation at the initial stage (Phillips, 1957), wave distortion in turbulent zones (Longuet-Higgins, 1996), and wave scattering by turbulence (Phillips, 1959). In all the problems considered in this thesis, the turbulence is taken to be weak, so that wave breaking is excluded and surface waves, when present, can also be treated using linear theory.

Although nonlinear interactions in the turbulence are by definition strong, there are a number of situations of practical relevance where these interactions are relatively unimportant when compared with other external forcings. For example, at the initial stage of the development of the viscous boundary layer in a turbulent flow near a boundary, viscous diffusion dominates the turbulence evolution close to the boundary. Similarly, in the boundary layer of a turbulent shear flow, if the shear rate is much higher than the typical frequency of the turbulent eddies, as tends to occur near the boundary, the shearing of the turbulence by the mean flow is the dominant physical process. Or when a wave coexists with turbulence in the ocean, if the slope and the frequency of the wave are sufficiently high, the straining imposed by the wave on the turbulence dominates over other physical processes affecting the turbulence. In all these examples, the equations of motion may be linearised with respect to the turbulent velocity. This linearisation forms the basis of the mathematical method employed throughout this thesis, which is called *rapid-distortion theory* (for a review, see Hunt & Carruthers, 1990).

Formally, the linearisation used in rapid-distortion theory is entirely analogous to that used in the theory of infinitesimal waves. The difference is that, since the turbulence is never infinitesimal by definition, greater care needs to be taken to ensure that the linearisation is valid. Quantitatively, the theory is applicable to situations where both the turbulence intensity and the strain rate associated with the interaction of the turbulence with itself are much smaller than the mean velocity and the mean strain rate, or alternatively, if the time since the ‘introduction’ of a distortion is shorter than one eddy turn-over time. Because the initial state of the turbulence has finite amplitude, it can not be assumed that a single wavenumber will dominate the response of the turbulence as time progresses. This requires the turbulence before the distortion to be characterised by a given energy spectrum and certain symmetry properties (for example, homogeneity and isotropy). It is then possible to determine statistics of the turbulence after distortion by a boundary or a mean flow, or both (Hunt, 1973).

Rapid-distortion theory was first used by Taylor (1935) to evaluate the changes suffered by turbulence passing through a wind-tunnel contraction. Taylor modelled the mean flow as a uniform straining flow, and considered only one harmonic of the turbulent velocity. This treatment was extended by Batchelor & Proudman (1954) to a full energy spectrum, allowing the calculation of turbulence intensities. The axisymmetric straining flow adopted by Taylor (1935) and Batchelor & Proudman (1954) is also used in chapter 3 of this thesis to model the large scales of shear-free turbulence. Townsend (1970) investigated the distortion of turbulence in a boundary layer, modelling the mean flow as a uniform shear. This approach will also be followed in chapter 4 of this thesis, where the generation of surface waves by turbulence at the initial stage is addressed. Subsequently, Hunt (1973) extended rapid-distortion theory further to situations where the mean distorting flow is not uniform, and the resulting turbulence is inhomogeneous (see also Goldstein, 1978). A non-uniform mean flow is also considered in chapter 5 of this thesis, where the distortion of turbulence by a surface water wave is addressed. Hunt’s (1973) treatment accounted for the effect of solid boundaries, and this aspect was explored in more detail in Hunt & Graham (1978), where the boundary condition at a solid wall is satisfied by adding an irrotational correction to the velocity field. This is also done when addressing the effect of boundaries in chapters 2, 3 and 5 of this thesis. Although the flows used in the model problems to be considered are simplified approximations to real flows, they enable a relatively straightforward interpretation of the physical processes involved. Since these physical processes are also important in real flows, the model problems can be seen as building blocks or tools that aid the understanding of real flows. An overview of the model problems considered in the thesis is presented next.

1.1 Overview of the thesis

In chapter 2, the linear dynamics of shear-free turbulence near a flat boundary are investigated, focussing on the viscous boundary layer. Calculated turbulence dissipation profiles are compared with recent direct numerical simulation data (Perot & Moin, 1993, 1995*b*). Studying the behaviour of turbulence dissipation is important both for developing turbulence closures for numerical models, where dissipation is parameterised, and for gas transfer across air-water interfaces, because the dissipation is related to the surface divergence of the flow. In this chapter, the rapid-distortion model of Hunt & Graham (1978) for the initial distortion of turbulence by a flat boundary is extended to account fully for viscous processes. Two types of boundary are considered: a solid wall and a free surface with $Fr \ll 1$ and $We \ll 1$. The model is used to investigate the differences between the two types of boundary. Profiles of the turbulent Reynolds stresses and dissipation rates are calculated, and shown to be in excellent agreement with data for short times, while remaining in good qualitative agreement for longer times. This is due to the fact that nonlinear processes arrest the growth of the viscous boundary layer at a relatively early stage, preserving the profiles determined by linear processes (blocking and viscous diffusion). The dissipation is found to be enhanced near a solid wall, due to the no-slip boundary condition, but reduced near a free-surface, due to the no-stress boundary condition. This partly explains the large turbulence intensity observed near free surfaces (Perot & Moin, 1995*a*). The model shows that the turbulent pressure fluctuations are associated with nonlinear processes. Since the model is linearised with respect to the turbulent velocity, it does not produce pressure fluctuations, and would be unable to generate surface waves even if the assumptions $Fr \ll 1$ and $We \ll 1$ were relaxed.

Chapter 3 addresses some of the nonlinear processes that occur in shear-free turbulence near a flat boundary outside the viscous boundary layer, which were neglected in chapter 2. Again, the flat boundary can be a solid wall or a free surface with $Fr \ll 1$ and $We \ll 1$. Attention is focussed on the behaviour of turbulence in upwelling and downwelling zones. As noted by Perot & Moin (1995*a*), these zones are salient features of turbulence near boundaries and deserve a careful study. Following Kida & Hunt (1989), an inviscid rapid-distortion model is adopted that treats the large, long-lived eddies in the turbulence as a mean flow and the smaller eddies as the fluctuating flow. Upwelling or downwelling zones in the turbulence are modelled as axisymmetric straining flows. It is found that the turbulence intensity is enhanced near boundaries by the net strain to which upwelling and downwelling zones subject the smaller scale turbulence, which makes the turbulent kinetic energy increase. This interaction between the large and the small scales of the flow produces a turbulent pressure field, which would, in principle, be able to generate waves in the case of a free surface. However, these are excluded by the assumptions $Fr \ll 1$ and $We \ll 1$. On the other hand, the added complexity of the flow (compared with that used in chapter 2) enables the calculation of various inviscid source terms in the turbulent kinetic energy budget, of which the most important are the pressure-strain terms. Studying the behaviour of these terms is important for the development of closures for the pressure-strain correlations in numerical models. It is found that the pressure-strain terms in the turbulent kinetic energy equation contribute to make the small-scale turbulence more isotropic everywhere in downwelling zones and also far from the boundary in upwelling zones, but move the turbulence away from isotropy near the boundary in upwelling zones.

In chapter 4, the assumptions $Fr \ll 1$ and $We \ll 1$ are relaxed, and the initial generation of surface waves by a turbulent shear flow, departing from a flat free surface, is investigated. This interaction is considered for times sufficiently short that the waves remain small and have no effect on the mean flow or on the turbulence. The model is used to assess the relative importance of surface wave generation by a turbulent shear flow in the water (coupled case) and a turbulent shear flow in the air (uncoupled case). This problem is important in the context of surface wave dynamics, since the role of turbulence in the water in wave generation at the initial stage has often been overlooked (Giovanangeli & Memponteil, 1985; Kahma & Donelan, 1988). The original theory of Phillips (1957) is extended by relating the turbulent pressure fluctuations responsible for generating the waves to the velocity fluctuations in the turbulence, using the rapid-distortion approach developed by Durbin (1978). In both the coupled and the uncoupled cases, the mean flow is assumed to have a constant shear rate, and represents the part of the boundary layer profile that gives the dominant contribution to the surface pressure. Various statistics of the surface waves generated by the turbulence are calculated, namely their mean-square slope, curvature spectrum and their angular energy distribution. It is found that, for flows producing pressure fluctuations of a similar magnitude, turbulence in the water is much more efficient in generating surface waves than turbulence in the air, essentially because the decorrelation time for the pressure fluctuations is longer in the water than in the air. In the calculated curvature spectra, a bimodal angular energy distribution is predicted at the lowest wavenumbers for relatively high shear rates of the turbulent flow. This behaviour is consistent with the laboratory measurements of Jähne & Riemer (1990).

Chapter 5 addresses the straining of relatively weak and small-scale turbulence by a fast, progressive, surface wave. This problem can be viewed as complementary to that of chapter 4, because now it is the wave that controls the behaviour of the turbulence. Attention is focussed on the time evolution of the turbulence structure, and the effect of the turbulence on the distorting wave. The first aspect is relevant for pollution dispersion in the ocean, which is controlled by the characteristics of turbulence in the water, and the second is important for surface wave dynamics, since turbulence is known to be one of the factors leading to wave attenuation (Phillips, 1959). In the rapid-distortion model employed, the turbulence is assumed to be shear-free, approximating, for example, turbulence generated by wave breaking (Melville, 1996). It is found that, over a number of wave cycles, the Reynolds stresses transverse to the wave propagation direction are amplified, making the turbulence progressively two-dimensional and dominated by streamwise vortices. The integral length scales of the turbulence show that these vortices become elongated in the streamwise direction. Their structure resembles that of the 'Langmuir turbulence' produced in the large-eddy-simulation study of McWilliams *et al.* (1997). The mechanism for the formation of these streamwise vortices is akin to that proposed by Craik & Leibovich (Leibovich, 1983) for Langmuir circulations. That is the tilting of the vertical vorticity present in the water flow by the Stokes drift of the wave, and its amplification as streamwise vorticity. The turbulent kinetic energy budget is analysed, showing that the energy transfer taking place from the distorting wave to the turbulence leads to an intensification of the streamwise vortices and a slow decay of the wave. The wave attenuation rate associated with this process is estimated, and found to be consistent with existing laboratory data by Ölmez & Milgram (1992).

In chapter 6, the general conclusions of this thesis are presented.

Finally, in an appendix, the problem of surface wave generation by shear-free turbulence is briefly addressed using a simplified rapid-distortion model. The model follows essentially Fernando & Hunt's (1997) treatment of shear-free turbulence and waves near a density interface, but the effect of surface tension has been added. The model parameterises nonlinear effects in the turbulence by relating the frequency and the wavenumber of the turbulent eddies using a kind of 'dispersion relation'. This assumption, which enables the model to produce a turbulent pressure field and therefore to generate waves, is found to be formally inconsistent with the equations of motion. That is the reason why this treatment has not been included in the main body of the thesis. Despite this inconsistency, the model allows a qualitatively correct interpretation of the mechanism for resonant wave growth.

CHAPTER 2

Dissipation of shear-free turbulence near boundaries

2.1 Introduction

Turbulence at finite Reynolds number is always subject to dissipation by viscosity. And when a turbulent flow is unforced, it decays in a time that scales on the decorrelation time for the energy-containing turbulent fluctuations (Batchelor, 1953). Hence the dissipation rate, together with the turbulent kinetic energy, provide a time scale for the evolution of the turbulent flow. Parameterisation of the dissipation rate is therefore at the heart of many Reynolds-averaged models of turbulent flows. Nevertheless, there are at present few calculations of the dissipation rate. In the present chapter an exact calculation of the dissipation rate in the rapid-distortion limit is developed.

The study of the dissipation rate of turbulence presented here was motivated by a general desire to understand better turbulence near a free surface, and has practical importance for transfer of sparingly soluble gases into the liquid that is in turbulent flow (Theofanous, 1984). Now, free surfaces cannot support mean shear, since by definition a ‘free’ surface must support zero surface stress. Hence, attention is focussed here on turbulence near a free surface in the absence of mean shear.

Shear-free turbulence near boundaries has been the subject of extensive study following the pioneering laboratory measurements of Uzkan & Reynolds (1967) and Thomas & Hancock (1977). The definitive theoretical study of Hunt & Graham (1978), based on rapid-distortion theory, shows that the boundary leads to a layer of blocking, where the normal velocity fluctuations are brought to zero, and to a thinner viscous layer, where the tangential velocity fluctuations adjust to the condition at the boundary. More recently, Perot & Moin (1995*a*) and Walker *et al.* (1996) have reported direct numerical simulations of shear-free boundary layers, which provide *inter alia* data for profiles of the rate of dissipation of the turbulence and other correlations. These studies reveal significant differences between shear-free boundary layers near solid walls and free surfaces, such as the higher tangential Reynolds stress and lower dissipation near a free surface. An objective of the present study has been to clarify and quantify the mechanisms responsible for these differences.

In this chapter the rapid-distortion model developed by Hunt & Graham (1978) for the initial response of initially homogeneous turbulence to the sudden imposition of a boundary is further developed to account fully for the viscous effects of free surfaces and solid walls. The dissipation rate of the turbulence is then calculated from the model. There is a significant question over whether or not rapid-distortion theory (hereafter RDT) can be usefully used to calculate dissipation. The reason is that the crucial assumption used in RDT of neglecting nonlinear interactions within the turbulence is usually justified, following the original RDT paper of Batchelor & Proudman (1954), by scaling estimates based on the dynamics of the energy-containing eddies; dissipation, in contrast, is usually associated with the smallest eddies, for which nonlinear processes become important at earlier times. The calculations presented here show how and why RDT can be used to provide useful estimates of dissipation.

The remainder of the chapter is organised as follows. In §2.2 a scaling analysis of the equations of motion is presented, which identifies some conditions for the validity of the RDT model. In §2.3 the response of a single Fourier mode of the turbulence to a solid wall and to a free surface is calculated. These Fourier modes are integrated over a spectrum in §2.4 to obtain statistics of the flow near the boundary. In §2.5 results are presented for the Reynolds stresses and dissipation rate and compared with the DNS data of Perot & Moin (1993, 1995*a*, 1995*b*). Finally, in §2.6, conclusions are presented.

2.2 Scaling the equations of motion

Following Hunt & Graham (1978), the following model problem is studied. For times $t < 0$, there everywhere exists homogeneous and isotropic turbulence, characterised by an integral length scale, l, and a root-mean-square velocity scale, u. At time $t = 0$, a boundary is introduced at $x_3 = 0$ and the initial response and subsequent evolution of the turbulence for $t > 0+$ below the interface $x_3 < 0$ is investigated. Two types of boundary are considered: a solid wall and a free surface. A solid wall imposes the condition that $u_i = u_3 = 0$ at $x_3 = 0$, where u_i ($i = 1$ or 2) are the tangential velocity components and u_3 is the normal velocity component. The distortion of the turbulence by a free surface in the limit of very low Froude number, $Fr \ll 1$, and very low Weber number, $We \ll 1$, is considered, hence the interface remains nearly flat. The free surface then imposes the conditions that the surface is stress free, $\tau_i = \mu \partial u_i / \partial x_3 = 0$ (for $i = 1$ or 2), and vanishing normal velocity, $u_3 = 0$. Far below the boundary, the turbulence returns to the homogeneous form it took before insertion of the boundary.

As shown originally by Hunt & Graham (1978), flow in the vicinity of the boundary has a two-layer structure. Following Hunt & Graham, the thickest layer is here called the *source layer*. This layer is associated with the kinematic blocking effect of the boundary, wherein irrotational motions are induced to bring the normal component of the fluid velocity to zero at the boundary. The source layer responds immediately to the introduction of the boundary and has thickness and velocity scales l and u, the scales of the turbulence far below the boundary. The thinner inner-most layer, called here the *viscous layer*, is associated with the viscous effect of the boundary, and is where rotational motions are induced to adjust the tangential motions to the surface boundary condition: in the case of a solid wall the tangential velocity is brought to zero, or in the case of a free surface the tangential stress is brought to zero. The viscous layer is characterised by velocity and length scales determined by its own internal dynamics, so that immediately after the boundary is introduced the viscous layer has zero thickness; it then grows with time as momentum is diffused by molecular viscosity away from the boundary.

For the purposes of scaling the equations of motion, it is useful to split the turbulent velocity field into three components: the velocity field associated with the homogeneous turbulence in the absence of the boundary, $u_i^{(H)}$; the velocity field induced in the source layer, $u_i^{(S)}$; and the velocity field induced in the viscous layer, $u_i^{(V)}$; namely

$$u_i = u_i^{(H)} + u_i^{(S)} + u_i^{(V)}, \quad i = 1, 2, 3. \tag{2.1}$$

According to the description given above, both $u_i^{(H)}$ and $u_i^{(S)}$ scale as u and vary over the integral length scale l. The depth of the viscous layer scales as $\delta(t)$ and the velocity there varies parallel to the flat interface over the scale l. The tangential components of the velocity in the viscous layer, $u_i^{(V)}$ ($i = 1$ or 2), have magnitudes that are determined from the additional boundary condition at the interface. Hence for a solid wall the no-slip boundary condition yields $u_i^{(V)} = O(u)$ ($i = 1$ or 2), so that by continuity $u_3^{(V)} = O(u\delta/l)$. And for a free surface the no-stress boundary condition, $\partial u_i/\partial x_3 = 0$ ($i = 1$ or 2), yields $u_i^{(V)} = O(u\delta/l)$, so that by continuity $u_3^{(V)} = O(u\delta^2/l^2)$. The free surface evidently leads to a weaker constraint on the turbulence and hence induces smaller velocities in the viscous layer.

In order to scale the dynamical equations controlling these velocity components, it is helpful to define two time scales. The first is the time scale for turbulent velocity fluctuations to decorrelate, $T_L = l/u$, also called lagrangian time scale or eddy turn-over time. The second is the viscous time scale, which is a measure of the time it takes for the viscous layer to grow to a thickness δ, and is defined as $T_\nu = \delta^2/\nu$, where ν is the kinematic viscosity. Here the initial development of the turbulence after insertion of the boundary and hence times such that $T_\nu \ll T_L$ are considered. This limit can be expressed in terms of the Reynolds number of the turbulence, $Re_T = ul/\nu$, and the ratio of the thickness of the viscous layer to the integral length scale of the turbulence, $\delta' = \delta/l$, to yield $Re_T\delta'^2 \ll 1$. When the boundary is introduced instantaneously at time $t = 0$, the viscous layer initially grows as $\delta \sim (\nu t)^{\frac{1}{2}}$ and $T_\nu \sim t$; however, it is useful to retain the designation T_ν in order to emphasise that the scalings of the viscous layer depend on the thickness of that layer and not explicitly on time.

On substituting the decomposition of the velocity into components (2.1), and on using their scalings described above, it is found that, in the limit that $T_\nu \ll T_L$, flow near either a solid boundary or a free surface is described by a simplified form of the vorticity equation, namely,

$$\frac{\partial \omega_i^{(V)}}{\partial t} = \nu \frac{\partial^2 \omega_i^{(V)}}{\partial x_3^2} \tag{2.2}$$

or

$$\frac{\partial}{\partial t}\left(\frac{\partial u_i^{(V)}}{\partial x_3}\right) = \nu \frac{\partial^2}{\partial x_3^2}\left(\frac{\partial u_i^{(V)}}{\partial x_3}\right), \quad i = 1, 2, \tag{2.3}$$

where $\omega^{(V)} = \nabla \times \mathbf{u}^{(V)}$. The tangential vorticity budget is therefore dominated by changes induced by viscous diffusion. Inviscid processes, such as vortex stretching, are negligibly small in this limit. Hence the vorticity changes only in the viscous layer, since this layer is by definition the layer of fluid affected by viscous diffusion. It is also concluded, as did Hunt & Graham (1978), that in the source layer the vorticity is unaffected by insertion of the boundary and hence perturbations to the velocity there, $u_i^{(S)}$, are irrotational and can be described by a velocity potential, such that $u_i^{(S)} = \partial\phi^{(S)}/\partial x_i$. The physical reason for this is that the blocking effect of the boundary is felt instantaneously, whereas vorticity generated by inviscid nonlinear processes takes a time of order T_L to become important. Therefore, when $t \ll T_L$, the velocity perturbation $u_i^{(S)}$ induced by the boundary is essentially irrotational. Since initially $T_\nu \sim t$, the scalings presented here show that both the appearance of an irrotational velocity component in the source layer due to blocking by the boundary and tangential vorticity generation by viscous processes in the viscous layer are more important than vorticity generation by inviscid processes in the limit $T_\nu \ll T_L$. Hence, the criteria for both these approximations turn out to be the same in practice, although the scaling of the viscous layer is based on T_ν, whereas the scaling of the source layer is based explicitly on time.

The tangential momentum equation may be scaled in a similar way and, if $T_\nu \ll T_L$, it is found to take the simplified form

$$\frac{\partial u_i^{(V)}}{\partial t} = \nu \frac{\partial^2 u_i^{(V)}}{\partial x_3^2}, \quad i = 1, 2, \tag{2.4}$$

for a solid wall. So, to this approximation, not only does the inviscid part of the flow, $u_i^{(H)} + u_i^{(S)}$, have constant vorticity but it also has constant velocity. Thus, $u_i^{(H)}$ and $u_i^{(S)}$ are approximately steady compared with the viscous part of the flow, $u_i^{(V)}$.

The tangential velocity components, $u_i^{(V)}$ ($i = 1$ or 2), exist inside the viscous layer so that the boundary condition on tangential velocity is satisfied. These tangential motions vary along the boundary and generate regions of convergence and divergence and hence a normal velocity component, of order $u_i^{(V)}\delta/l$ ($i = 1$ or 2), at the outer edge of the viscous layer. These motions slightly modify the flow in the source layer. The corresponding corrections are treated by expanding the solutions for $u_i^{(S)}$ and $u_i^{(V)}$ in power series of the small parameter $\delta' = \delta/l$, for example

$$u_1^{(S)} = u_1^{(S0)} + u_1^{(S1)} + u_1^{(S2)} + \ldots, \quad u_1^{(V)} = u_1^{(V0)} + u_1^{(V1)} + u_1^{(V2)} + \ldots, \tag{2.5}$$

where the powers of δ' have been incorporated into the terms of the series. In the following, the series for $u_i^{(V)}$ ($i = 1$ or 2) and $u_i^{(S)}$ will be calculated to second order in δ' in the case of a solid wall and to third order in δ' in the case of a free surface. Higher order terms are affected by nonlinear processes and have been neglected. A detailed justification of this procedure is presented in §2.4.2. The series expansion of the normal velocity, $u_3^{(V)}$, is truncated at one order higher than those of the tangential components. This is done so that the series conserve mass exactly, which is important to do if the Reynolds stresses and the dissipation rates are to have the correct behaviour near the boundary. The price paid is that the solutions have small errors far from the boundary, but these are deemed less serious, since it is the near-wall region that is of interest here.

2.3 Distortion of a single Fourier component of velocity fluctuation

The model developed in the previous section, based on the diffusion equations (2.4) and (2.3), is now solved for the cases of a solid wall and a free surface, respectively. Here the modal solutions are calculated for the Fourier amplitudes of the flow variables. These modal solutions will be integrated over the spectrum of the turbulence in §2.4.

2.3.1 Solid wall

First of all, the effects of a solid wall will be considered. If the series (2.5) are substituted into the tangential momentum equation, then, to the 3 lowest orders in δ', the equation for velocity in the viscous layer becomes

$$\frac{\partial u_i^{(Vj)}}{\partial t} = \nu \frac{\partial^2 u_i^{(Vj)}}{\partial x_3^2}, \tag{2.6}$$

where $i = 1$ or 2 and $j = 0, 1$ or 2. Mass conservation then determines the normal component of velocity.

In the source layer, where as argued above $u_i^{(S)} = \partial\phi^{(S)}/\partial x_i$, mass conservation requires that the velocity potential $\phi^{(S)}$ satisfies the Laplace equation, which means that for $j = 0, 1$ or 2

$$\nabla^2 \phi^{(Sj)} = 0. \tag{2.7}$$

The boundary conditions are as follows. The flow tends to the original homogeneous turbulence, $u_i^{(H)}$, far below the boundary. Hence both $\phi^{(Sj)}$ and $u_i^{(Vj)}$ tend to zero far below the boundary. The normal and tangential velocity components vanish at the boundary. Finally, the initial condition states that the initial vorticity equals the vorticity in the homogeneous turbulence. Hence $u_i^{(V)}$ vanishes everywhere at $t = 0+$.

These equations are solved, following Hunt & Graham (1978), by noting firstly that the homogeneous turbulent velocity $u_i^{(H)}$ may be expressed as a superposition of Fourier modes,

$$u_i^{(H)}(\mathbf{x}) = \iiint \hat{u}_i^{(H)}(\mathbf{k})\, \mathrm{e}^{\mathrm{i}\mathbf{k}\cdot\mathbf{x}} \mathrm{d}k_1 \mathrm{d}k_2 \mathrm{d}k_3, \quad i = 1, 2, 3, \tag{2.8}$$

where $\hat{u}_i^{(H)}(\mathbf{k})$ is the Fourier amplitude and $\mathbf{k} = (k_1, k_2, k_3)$ is the wavenumber vector. Note secondly that, due to the geometry of the problem, $u_i^{(V)}$ and $u_i^{(S)}$ (and hence also $\phi^{(S)}$) are homogeneous in the directions tangential to the boundary, and so they can equally be expressed as a superposition of Fourier modes along those directions:

$$\begin{aligned} \phi^{(S)}(\mathbf{x}, t) &= \iint \hat{\phi}^{(S)}(k_1, k_2, x_3, t)\, \mathrm{e}^{\mathrm{i}(k_1 x_1 + k_2 x_2)} \mathrm{d}k_1 \mathrm{d}k_2 \\ u_i^{(V)}(\mathbf{x}, t) &= \iint \hat{u}_i^{(V)}(k_1, k_2, x_3, t)\, \mathrm{e}^{\mathrm{i}(k_1 x_1 + k_2 x_2)} \mathrm{d}k_1 \mathrm{d}k_2. \end{aligned} \tag{2.9}$$

Hence, since the equations are linear, the response of one Fourier mode only needs to be considered.

The solution for the Fourier amplitude of the velocity potential in the source layer obtained by solving (2.7) is found to be

$$\hat{\phi}^{(S)} = -\int \frac{\hat{u}_3^{(H)}}{k_{12}} \left[1 - \frac{\delta}{\pi^{1/2}} (\mathrm{i}k_3 - k_{12}) \left(1 + \frac{\delta k_{12}}{\pi^{1/2}}\right)\right] \mathrm{e}^{k_{12} x_3} \mathrm{d}k_3, \tag{2.10}$$

where $k_{12} = (k_1^2 + k_2^2)^{\frac{1}{2}}$, and which is correct up to second order in δ'. The zeroth-order part of (2.10) is the well-known inviscid solution of Hunt & Graham (1978); the corrections of $O(\delta')$ and $O(\delta'^2)$ are new. The components of $u_i^{(S)}$ are easily calculated from the potential $\phi^{(S)}$.

The viscous solution may be found by solving (2.6) subject to the boundary and initial conditions.

The Fourier amplitude of the tangential velocity is

$$\hat{u}_i^{(V)} = -\int \left\{ \hat{u}_i^{(H)} - \frac{\mathrm{i}k_i}{k_{12}}\hat{u}_3^{(H)} \left[1 - \frac{\delta}{\pi^{1/2}}(\mathrm{i}k_3 - k_{12})\left(1+\frac{\delta k_{12}}{\pi^{1/2}}\right)\right]\right\}\left[\mathrm{erf}\left(\frac{x_3}{\delta}\right)+1\right]\mathrm{d}k_3, \tag{2.11}$$

where $i = 1$ or 2 and $\delta = 2(\nu t)^{\frac{1}{2}}$. The corresponding Fourier amplitude of the normal velocity is

$$\begin{aligned}\hat{u}_3^{(V)} = -\int \delta\hat{u}_3^{(H)}(\mathrm{i}k_3 - k_{12})\Bigg\{&\left(1+\frac{\delta k_{12}}{\pi^{1/2}}+\frac{\delta^2 k_{12}^2}{\pi}\right)\left[\frac{x_3}{\delta}\left(\mathrm{erf}\left(\frac{x_3}{\delta}\right)+1\right)\right.\\ &\left.+\frac{1}{\pi^{1/2}}\mathrm{e}^{-x_3^2/\delta^2}\right] - \frac{\delta^2 k_{12}^2}{\pi^{3/2}}\Bigg\}\,\mathrm{d}k_3.\end{aligned} \tag{2.12}$$

2.3.2 Free surface

The solutions are now calculated for turbulence near a free surface. If in the viscous layer the series (2.5) are substituted into (2.3) then for $j = 0, 1, 2$ or 3 the tangential velocity components satisfy

$$\frac{\partial}{\partial t}\frac{\partial u_i^{(Vj)}}{\partial x_3} = \nu\frac{\partial^2}{\partial x_3^2}\frac{\partial u_i^{(Vj)}}{\partial x_3}, \tag{2.13}$$

where $i = 1$ or 2, and, as for the solid wall, the vertical velocity component is obtained from continuity. In the source layer the velocity potential satisfies the Laplace equation (2.7) as for a solid wall.

The boundary conditions ensure that the turbulent velocity tends to the homogeneous turbulence far below the boundary, and that at the boundary, $x_3 = 0$, the normal velocity component and the normal derivative of the tangential velocity components (and hence also the tangential stress) vanish.

The solution for the Fourier amplitude of the velocity potential in the source layer, correct to third order in δ', is found to be

$$\hat{\phi}^{(S)} = -\int \frac{\hat{u}_3^{(H)}}{k_{12}}\left(1+\frac{\delta^2 k^2}{4}\right)\mathrm{e}^{k_{12}x_3}\mathrm{d}k_3. \tag{2.14}$$

Again, the zeroth-order part of (2.14) is the well-known inviscid solution of Hunt & Graham (1978) and is identical to the solution calculated for a solid wall. The corrections, which arise due to vertical motions induced in the viscous layer, are new and are different from the corrections to $\hat{\phi}^{(S)}$ obtained for a solid wall because the solutions in the viscous layer are different. The velocity in the source layer is easily calculated from the velocity potential $\phi^{(S)}$.

The viscous solution for the amplitude of the tangential velocity is

$$\hat{u}_i^{(V)} = -\int \delta \left[\mathrm{i}k_3 \hat{u}_i^{(H)} - \mathrm{i}k_i \hat{u}_3^{(H)} \left(1 + \frac{\delta^2 k^2}{4}\right)\right] \left[\frac{x_3}{\delta}\left(\mathrm{erf}\left(\frac{x_3}{\delta}\right) + 1\right) + \frac{1}{\pi^{1/2}} \mathrm{e}^{-x_3^2/\delta^2}\right] \mathrm{d}k_3, \qquad (2.15)$$

where $i = 1$ or 2. The corresponding amplitude of the normal velocity is

$$\begin{aligned} \hat{u}_3^{(V)} \quad = \quad & \int \delta^2 k^2 \hat{u}_3^{(H)} \left\{ \left(1 + \frac{\delta^2 k_{12}^2}{4}\right) \left[\frac{x_3^2}{2\delta^2}\left(\mathrm{erf}\left(\frac{x_3}{\delta}\right) + 1\right) + \frac{x_3}{2\pi^{1/2}\delta} \mathrm{e}^{-x_3^2/\delta^2} \right.\right. \\ & \left.\left. + \frac{1}{4}\left(\mathrm{erf}\left(\frac{x_3}{\delta}\right) + 1\right)\right] - \frac{\delta^2 k_{12}^2}{16} \right\} \mathrm{d}k_3. \qquad (2.16) \end{aligned}$$

The differences between the solutions for a solid wall and a free surface will be illustrated later when statistics of the flow have been calculated.

2.4 Integration of Fourier amplitudes to obtain statistics

In §2.3, solutions were found for how the Fourier amplitudes of the flow variables respond to the presence of the boundary. These modal solutions are now integrated over a spectrum of wavenumbers in order to understand the response of turbulence consisting of fluctuations on a wide range of scales. In this way the turbulence near the boundary is related to the spectrum of the undistorted turbulence far from the boundary. Firstly, to validate the RDT method used here, profiles of the Reynolds stresses are calculated and compared with the profiles that Perot & Moin (1993, 1995*a*) obtained by DNS. Then rates of turbulence dissipation are calculated using the model, which have not been calculated hitherto with RDT. Finally, these results are compared with the dissipation rates computed by Perot & Moin (1993, 1995*b*).

Statistics of the distorted turbulence are related to statistics of the undistorted turbulence far from the boundary using the framework developed by Hunt (1973). The solution for a single mode of the velocity fluctuation is given by the distorted Fourier amplitude $\hat{u}_i(k_1, k_2, x_3, t)$, which is related to the complete velocity field $u_i(\mathbf{x}, t)$ by

$$u_i(\mathbf{x}, t) = \iint \hat{u}_i(k_1, k_2, x_3, t)\, \mathrm{e}^{\mathrm{i}(k_1 x_1 + k_2 x_2)} \mathrm{d}k_1 \mathrm{d}k_2. \qquad (2.17)$$

Since the RDT model is linear, the distorted Fourier amplitude is linearly related to the Fourier amplitude of the undistorted turbulence, $\hat{u}_i^{(H)}$, and so can be written

$$\hat{u}_i(k_1, k_2, x_3, t) = \int M_{ik}(\mathbf{k}, x_3, t)\, \hat{u}_k^{(H)}(\mathbf{k}) \mathrm{d}k_3. \qquad (2.18)$$

The matrix M_{ik} is extracted from the solutions calculated in §2.3 and is listed in the appendix (§2.7). Statistics of the flow are then calculated on recalling that the Fourier amplitude of the undistorted turbulence is related to the three-dimensional wavenumber spectrum, $\Phi_{ij}^{(H)}$, by

$$\overline{\hat{u}_i^{(H)}(\mathbf{k})\hat{u}_j^{(H)}(\mathbf{k}')} = \Phi_{ij}^{(H)}(\mathbf{k})\delta(\mathbf{k}-\mathbf{k}'), \tag{2.19}$$

where the overbar denotes ensemble averaging.

Using (2.17), (2.18) and (2.19), the Reynolds stresses can then be written

$$\overline{u_i^2}(x_3,t) = \iiint M_{ik}^* M_{il}\Phi_{kl}^{(H)} \mathrm{d}k_1\mathrm{d}k_2\mathrm{d}k_3, \tag{2.20}$$

where $i = 1, 2$ or 3. The diagonal elements of the Reynolds stress tensor (the velocity variances) are the only non-zero components for the initially isotropic shear-free turbulence treated here. Accordingly, in the dissipation tensor, only the diagonal components are non-zero. They are defined by

$$\varepsilon_{ii}(x_3,t) = 2\nu\left[\overline{\left(\frac{\partial u_i}{\partial x_1}\right)^2} + \overline{\left(\frac{\partial u_i}{\partial x_2}\right)^2} + \overline{\left(\frac{\partial u_i}{\partial x_3}\right)^2}\right], \tag{2.21}$$

where $i = 1, 2$ or 3. The variances of velocity derivatives along the boundary are calculated from the undistorted turbulence by

$$\overline{\left(\frac{\partial u_i}{\partial x_j}\right)^2} = \iiint k_j^2 M_{ik}^* M_{il}\Phi_{kl}^{(H)} \mathrm{d}k_1\mathrm{d}k_2\mathrm{d}k_3, \tag{2.22}$$

where $i = 1, 2$ or 3 and $j = 1$ or 2. The variances of derivatives normal to the boundary are calculated from the undistorted turbulence by

$$\overline{\left(\frac{\partial u_i}{\partial x_3}\right)^2} = \iiint \frac{\partial M_{ik}^*}{\partial x_3}\frac{\partial M_{il}}{\partial x_3}\Phi_{kl}^{(H)} \mathrm{d}k_1\mathrm{d}k_2\mathrm{d}k_3. \tag{2.23}$$

Thus, the Reynolds stresses and the components of the dissipation rate tensor are calculated from the spectrum of the undistorted turbulence.

In order to proceed further, recall that the undistorted turbulence far from the boundary is supposed to be homogeneous and isotropic. The three-dimensional velocity spectrum is then related to the energy spectrum $E(k)$ by

$$\Phi_{ij}^{(H)} = \left(\delta_{ij} - \frac{k_i k_j}{k^2}\right)\frac{E(k)}{4\pi k^2}, \tag{2.24}$$

where the energy spectrum is defined by

$$\frac{1}{2}\left(\overline{u_1^{(H)2}}+\overline{u_2^{(H)2}}+\overline{u_3^{(H)2}}\right)=\int_0^\infty E(k)\mathrm{d}k. \tag{2.25}$$

Once the form of the energy spectrum is specified, (2.20) and (2.21) can be evaluated to give profiles of the Reynolds stresses and the dissipation rates. The model for the energy spectrum is considered next.

2.4.1 The model for the energy spectrum

In their inviscid RDT calculations, Hunt & Graham (1978) used the von Kármán form of the energy spectrum

$$E(k)=u^2 l\frac{g_2(kl)^4}{(g_1+(kl)^2)^{17/6}}, \tag{2.26}$$

where g_1 and g_2 are dimensionless constants. This form has an inertial subrange (where the spectrum decays as $k^{-5/3}$) that extends to $k\to\infty$, corresponding to infinite Reynolds number. This spectrum is appropriate for calculating quantities that receive their greatest contribution from the energy containing part of the spectrum, such as the Reynolds stresses, but it is not appropriate for calculating quantities that receive a significant contribution from the high wavenumbers, such as the dissipation rate. In fact, because the von Kármán spectrum does not have a viscous cut off at high wavenumbers, the integrals that give the dissipation rate, (2.22) and (2.23), diverge. Hence, here it is necessary to use a form for the energy spectrum that accounts for the viscous processes at high wavenumbers.

According to Tennekes & Lumley (1972, p.269), for large Reynolds number the energy spectrum at high wavenumbers takes the form

$$E(k)\sim\alpha_k\varepsilon^{2/3}k^{-5/3}\exp\left[-\frac{3}{2}\alpha_k(k\eta)^{4/3}\right], \tag{2.27}$$

where α_k is a constant approximately equal to 1.5 and the Kolmogorov microscale, η, is given by

$$\eta=\left(\frac{\nu^3}{\varepsilon}\right)^{1/4}, \tag{2.28}$$

where $\varepsilon=1/2(\varepsilon_{11}+\varepsilon_{22}+\varepsilon_{33})$ is the isotropic dissipation rate in the homogeneous turbulence.

Hence, an obvious extension of (2.26) for finite Reynolds numbers is

$$E(k) = u^2 l \frac{g_2 (kl)^4}{(g_1 + (kl)^2)^{17/6}} \exp\left[-\frac{3}{2}\alpha_k (k\eta)^{4/3}\right]. \tag{2.29}$$

This form must be made to satisfy 3 constraints in order to become completely defined. The first constraint results from the definition of root mean square velocity, $u^2 = \overline{u_i^{(H)2}}$, with $i = 1, 2$ or 3. Since the total kinetic energy of the homogeneous turbulence is given by the integral over all wavenumbers of $E(k)$ (see (2.25)), then

$$\int_0^\infty E(k)\mathrm{d}k = \frac{3}{2}u^2. \tag{2.30}$$

The second constraint is that the length scale l in (2.29) is defined as the longitudinal integral length scale, so that

$$l = \frac{\int_0^\infty \overline{u_1^{(H)}(x_1, x_2, x_3) u_1^{(H)}(x_1 + r, x_2, x_3)}\mathrm{d}r}{\overline{u_1^{(H)2}}} = \frac{3\pi}{4}\frac{\int_0^\infty k^{-1}E(k)\mathrm{d}k}{\int_0^\infty E(k)\mathrm{d}k}. \tag{2.31}$$

The third constraint is given by the definition of viscous dissipation in homogeneous isotropic turbulence, namely

$$\varepsilon = 2\nu \int_0^\infty k^2 E(k)\mathrm{d}k. \tag{2.32}$$

If these constraints are cast into dimensionless form they can be used to determine the unknown coefficients in (2.29).

If the dimensionless wavenumber is defined as $k' = kl$ then equation (2.28) shows that η/l is

$$\frac{\eta}{l} = Re_T^{-3/4}\left(\frac{\varepsilon l}{u^3}\right)^{-1/4} = Re_T^{-3/4}\varepsilon'^{-1/4}. \tag{2.33}$$

where ε' is the dimensionless dissipation rate. The dimensionless energy spectrum, defined as $E'(k') = E(k)/(u^2 l)$, is then

$$E'(k') = \frac{g_2 k'^4}{(g_1 + k'^2)^{17/6}} \exp\left[-\frac{3}{2}\alpha_k Re_T^{-1}\varepsilon'^{-1/3}k'^{4/3}\right]. \tag{2.34}$$

The three constraints (2.30), (2.31) and (2.32) then take the dimensionless form

$$\int_0^\infty E'(k')\mathrm{d}k' = \frac{3}{2}, \quad \int_0^\infty k'^{-1}E'(k')\mathrm{d}k' = \frac{2}{\pi}, \quad \int_0^\infty k'^2 E'(k')\mathrm{d}k' = \frac{1}{2}Re_T\,\varepsilon'. \tag{2.35}$$

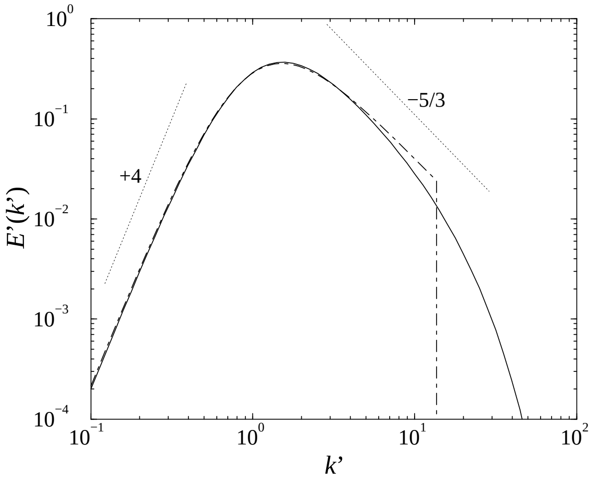

Figure 2.1 Dimensionless energy spectrum as a function of the dimensionless wavenumber, at $Re_T = 70$. Solid line, complete spectrum (2.34); dash-dotted line, truncated von Kármán spectrum (2.36).

Hence, for a given value of α_k and a given Reynolds number, the dimensionless spectrum (2.34) contains 3 unknown parameters: g_1, g_2 and ε', which can be determined uniquely by solving the implicit equation set (2.35).

The numerical evaluation of the integrals that determine the dissipation rate is made simpler if this form of the spectrum (2.34) is approximated by truncating at a finite wavenumber, k_{max}, namely

$$\begin{aligned} E'(k') &= \frac{g_2 k'^4}{(g_1 + k'^2)^{17/6}} \quad \text{if} \quad k' \leq k'_{max} \\ E'(k') &= 0 \quad \text{if} \quad k' > k'_{max}. \end{aligned} \tag{2.36}$$

where $k'_{max} = k_{max} l$ is the dimensionless cutoff wavenumber. Here k'_{max} is determined by requiring that the dimensionless dissipation rate is correct. In the limit of high Re_T the high wavenumbers dominate the dissipation rate, hence the full spectrum (2.34) gives

$$\int_0^\infty k'^2 E'(k')\mathrm{d}k' \approx \int_0^\infty g_2 k'^{1/3} \exp\left[-\frac{3}{2}\alpha_k Re_T^{-1} \varepsilon'^{-1/3} k'^{4/3}\right]\mathrm{d}k' = \frac{g_2}{2\alpha_k} Re_T\, \varepsilon'^{1/3}. \tag{2.37}$$

whereas the truncated spectrum gives

$$\int_0^{k'_{max}} k'^2 E'(k')\mathrm{d}k' \approx \int_0^{k'_{max}} g_2 k'^{1/3}\mathrm{d}k' = \frac{3}{4} g_2 k'^{4/3}_{max}. \tag{2.38}$$

So, in this regime, the cutoff wavenumber is obtained by comparing (2.38) and (2.37):

$$k'_{max} = \left(\frac{2}{3\alpha_k}\right)^{3/4} \varepsilon'^{1/4} Re_T^{3/4}. \tag{2.39}$$

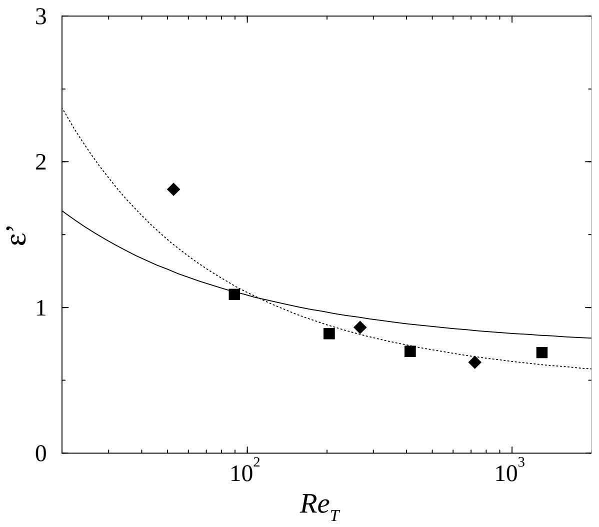

Figure 2.2 Variation of the dimensionless dissipation with the Reynolds number. Solid line, theory using the truncated spectrum (2.36) and $\alpha_k = 1.5$; dotted line, theory using the complete spectrum (2.34) and $\alpha_k = 2$; squares, data of Jiménez *et al.* (1993); diamonds, data of Wang *et al.* (1996).

This procedure yields $k_{max}\eta = [2/(3\alpha_k)]^{3/4} \approx 0.54$, as found by Tennekes and Lumley. Hence k_{max} is of order $1/\eta$.

Figure 2.1 shows plots of the dimensionless profiles of the truncated spectrum (2.36) and full spectrum (2.34) for $Re_T = 70$ and $\alpha_k = 1.5$. Figure 2.2 displays the dependence of dimensionless dissipation on the Reynolds number for the complete spectrum and the truncated spectrum, together with values computed with DNS by Jiménez *et al.* (1993) and Wang *et al.* (1996). In the complete spectrum, $\alpha_k = 2$ (chosen so as to optimise the fit), whereas in the truncated spectrum, $\alpha_k = 1.5$, as suggested by Tennekes and Lumley (1972). While it is clear that the complete spectrum gives an excellent fit to the data, the truncated spectrum also reproduces the general trend quite well for $Re_T > 70$. In what follows, all calculations will be performed using the truncated spectrum (with $\alpha_k = 1.5$), because this considerably shortens the time required for numerical integration.

2.4.2 Validity of the model

There are two conditions that must be satisfied if the current model is to be valid. Firstly, nonlinear processes in the turbulence have to be negligible compared with the diffusive growth of the viscous layer. As shown in §2.2, this condition is met provided $Re_T\,\delta'^2 \ll 1$. Secondly, the small effect of viscosity was included by treating it as a small perturbation to the inviscid processes. Hence the velocity components were expanded as series in (2.5), and these series were truncated after the first three terms. Now, when statistics are calculated from the modal solutions for velocity, the magnitude of the neglected terms depends on the distribution of energy within the spectrum. Hence, the condition required for these truncated expansions to be valid will now be determined.

The solution for M_{ik} given in the appendix (§2.7), which is in the form of a power series in δ, together with the expression for the Reynolds stresses (2.20) show that, for example, the streamwise Reynolds stress is also a series in δ, namely

$$\overline{u_1^2} = \int_0^\infty f_0(k,x_3)E(k)\mathrm{d}k + \delta\int_0^\infty f_1(k,x_3)E(k)\mathrm{d}k + \delta^2\int_0^\infty f_2(k,x_3)E(k)\mathrm{d}k + ..., \tag{2.40}$$

where the functions $f_n(k,x_3) = O(k^n)$. The peak of the spectrum dominates in the first integral of (2.40), which is therefore independent of k_{max}, but the high-wavenumber tail of the spectrum dominates the second and third integrals. Having in mind that $E(k) \propto k^{-5/3}$ at high wavenumbers, these integrals can be estimated to scale as

$$\begin{aligned} &\int_0^{k_{max}} f_0(k,x_3)E(k)\mathrm{d}k = O\left(u^2\right) \\ &\int_0^{k_{max}} f_1(k,x_3)E(k)\mathrm{d}k = O\left(u^2 l^{-2/3}\int_0^{k_{max}} k k^{-5/3}\mathrm{d}k\right) = O\left(u^2 l^{-2/3} k_{max}^{1/3}\right) \\ &\int_0^{k_{max}} f_2(k,x_3)E(k)\mathrm{d}k = O\left(u^2 l^{-2/3}\int_0^{k_{max}} k^2 k^{-5/3}\mathrm{d}k\right) = O\left(u^2 l^{-2/3} k_{max}^{4/3}\right). \end{aligned} \tag{2.41}$$

And the series expansion for the Reynolds stress becomes

$$\overline{u_1^2}/u^2 = b_0 + b_1 k_{max}'^{1/3}\delta' + b_2 k_{max}'^{4/3}\delta'^2 + ..., \tag{2.42}$$

where the coefficients $b_n = O(1)$. This expansion is asymptotic provided

$$k_{max}'\delta' \ll 1. \tag{2.43}$$

This condition arises physically from the treatment of the viscous layer as a thin boundary layer, i.e. the assumption that variations across the viscous layer, normal to the surface, are much more rapid than variations along the boundary layer, parallel to the surface. The smallest-scale variations in the source layer just outside the viscous layer are determined by the smallest scale in the turbulence, namely $\eta \sim k_{max}^{-1}$. Hence this boundary layer approximation is valid only when these smallest scales are much larger than the thickness of the viscous layer.

Since the viscous layer grows initially with time as $\delta = 2(\nu t)^{\frac{1}{2}}$, this condition (2.43) together with the definitions of $\delta' = \delta/l$ and k_{max}' given in (2.39), give a condition on time, namely

$$\frac{ut}{l} \ll C Re_T^{-1/2} \tag{2.44}$$

where $C = 1/4(3\alpha_k/2)^{3/2}\varepsilon'^{-1/2} \approx 1$ for $\alpha_k = 1.5$. Hence for very large Reynolds numbers, when the turbulence has very small scales, the model developed here for the dissipation is valid for only short times. Such a dependence on the Reynolds number in the comparisons between the model and the DNS has indeed been detected.

If the scaling analysis is carried out again for the velocity fluctuations taking into account the dependence of their magnitude on the spectrum, as implied by (2.42), then it is found that the terms retained in the expansions for the velocity fluctuations are larger than the nonlinear terms that were neglected provided $T_\nu \ll T_L$, i.e. that $t \ll l/u$. This is the conventional requirement for the validity of RDT: in the present flow, the particular form of the spectrum apparently does not affect the form of this approximation.

2.4.3 Truncation errors

Finally, before showing results from the model, a practical aspect of implementing the current solutions in calculating statistics of the turbulence near the boundary should be noted.

The Reynolds stresses are the square of velocity. So, if the power-series solutions for the velocity are multiplied together, then the highest order terms in this product series, which correspond to the products of the highest order terms of the velocity series, are of higher order than the truncation error. Hence these higher-order terms might be considered negligible. However, the original expansions for the velocity satisfy the boundary conditions at $x_3 = 0$ exactly. Hence, if the high-order products are neglected, then the resulting statistics become unreliable very close to the boundary. The truncated and the non-truncated expressions both have the same formal accuracy, since they differ from each other only by terms of the order the truncation error. Therefore, the full products are prefered here as they preserve the exact boundary conditions at $x_3 = 0$, and they are adopted everywhere hereafter.

2.5 Results and discussion

In this section, theoretical results obtained with the model developed in the preceding sections will be compared with the DNS data presented in Perot & Moin (1993) (hereafter referred to as PM93) and Perot & Moin (1995*a*, 1995*b*) (hereafter referred to as PM95a and PM95b, respectively). Two important preliminary considerations must be made before carrying out such a task.

Firstly, the turbulence length and velocity scales defined by these authors are different from those used in this chapter until now, and have to be related before any comparison is possible. Perot & Moin normalise their data by defining a velocity scale, u^*, and length scale, l^*, based on the values of the turbulent kinetic energy K and dissipation rate ε far from the boundary, i.e.

$$u^* = K^{1/2}, \quad l^* = \frac{K^{3/2}}{\varepsilon}. \tag{2.45}$$

They then define a Reynolds number in terms of l^* and u^*:

$$Re_T^* = \frac{u^* l^*}{\nu} = \frac{K^2}{\varepsilon \nu}. \tag{2.46}$$

Noting that the kinetic energy is defined in the present chapter as $K = (3/2)u^2$, the two sets of length and velocity scales and Reynolds numbers are found to be related by

$$u^* = \left(\frac{3}{2}\right)^{1/2} u, \quad l^* = \left(\frac{3}{2}\right)^{3/2} \varepsilon'^{-1} l, \quad Re_T^* = \frac{9}{4}\varepsilon'^{-1} Re_T. \tag{2.47}$$

Secondly, the flow computed by Perot & Moin is unforced and so the turbulence decays with time. This decay changes some aspects of the flow, although the main features are the same as if the turbulence were stationary, particularly for short times. In the current model, stationary and homogeneous turbulence away from the boundary is assumed. Comparison with data obtained where the turbulence decays might be thought to introduce a new limitation on the time interval over which the model is valid. This is not so, however. Viscous decay of energy in the bulk of the flow is just a manifestation of viscous diffusion of momentum or vorticity in the turbulence far from the boundary, a physical process which was shown to be negligible at early times in the scalings of §2.2.

PM93 used Reynolds numbers of $Re_T^* = 54$, 134 and 374 in their numerical simulations of a solid wall and 6.2, 54 and 134 in their simulations of a free surface. The value of $Re_T^* = 6.2$ is manifestly too low for the concept of a viscous cutoff to work properly (see §2.4.1), and hence this case is not considered here. In terms of the velocity and length scales defined by (2.45), the condition (2.44) for the validity of the analysis of the viscous layer takes the form

$$\frac{u^* t}{l^*} \ll \frac{1}{4}\left(\frac{3\alpha_k}{2}\right)^{3/2} Re_T^{*-1/2}. \tag{2.48}$$

For Reynolds numbers of 54, 134 and 374 this condition requires that $u^* t/l^*$ is smaller than 0.11, 0.07 and 0.04 respectively. Much of the DNS data presented in PM93, PM95a and PM95b are for times when dissipation and nonlinear processes have become important in the dynamics of the turbulence, and the earliest time that Perot & Moin show results of is $u^* t/l^* = 0.1$. Therefore comparisons with the theory are made at $u^* t/l^* = 0.1$ for the cases when $Re_T^* = 54$ and $Re_T^* = 134$. Some qualitative comparisons will be made for later times in §2.5.3.

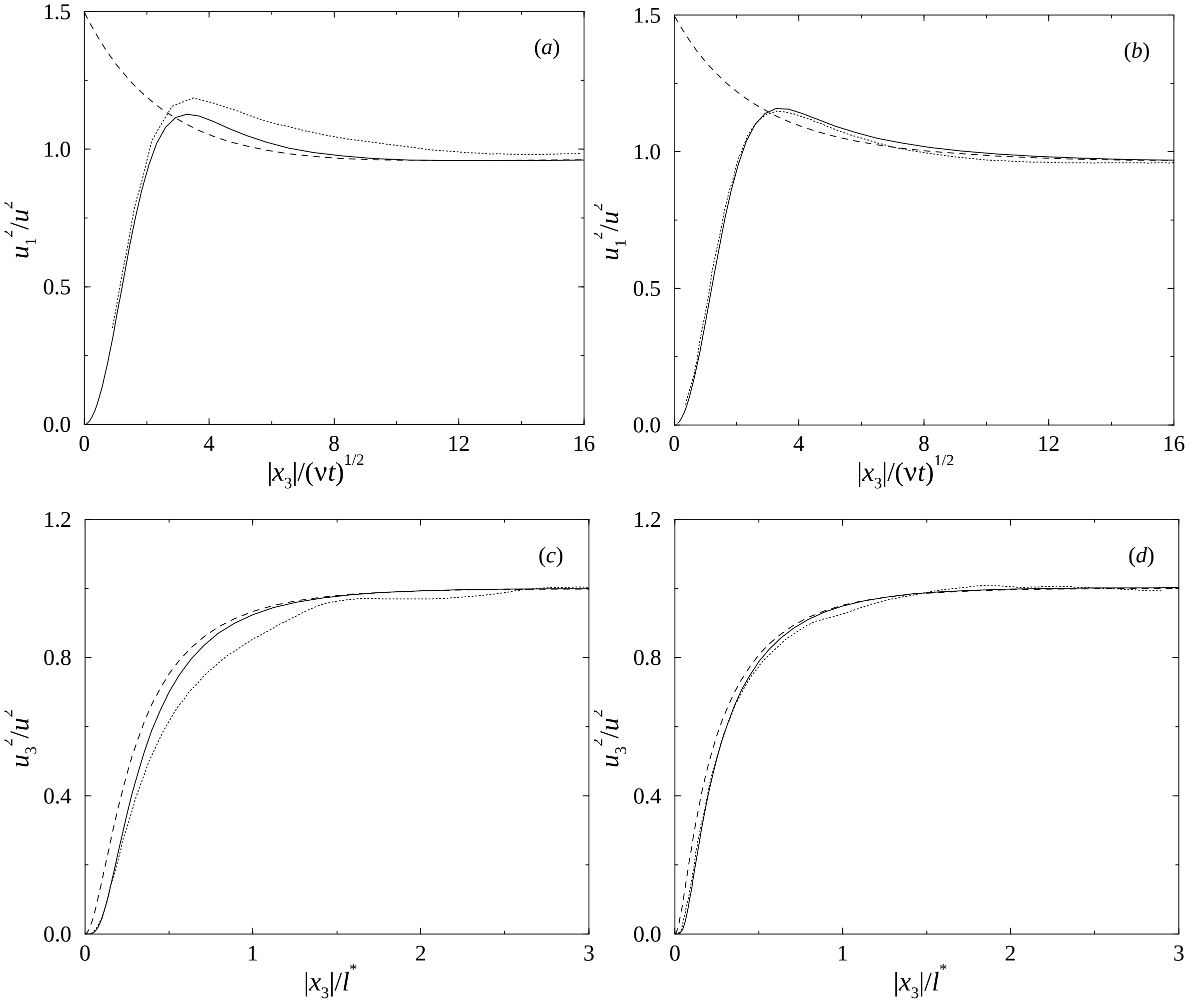

Figure 2.3 Reynolds stress profiles near a solid wall at $u^*t/l^* = 0.1$. Solid line, viscous theory; dashed line, inviscid theory; dotted line, DNS data. (*a*) tangential component, $Re_T^* = 54$; (*b*) tangential component, $Re_T^* = 134$; (*c*) normal component, $Re_T^* = 54$; (*d*) normal component, $Re_T^* = 134$.

2.5.1 Profiles of the Reynolds stresses

Figure 2.3 presents profiles of the Reynolds stress for a solid wall and figure 2.4 profiles for a free surface, at a dimensionless time of $u^*t/l^* = 0.1$ and at Reynolds numbers of 54 and 134. The DNS data presented in figure 2.3 were taken from figures 15(*a*, *b*), 17(*a*, *b*) of PM95a and those presented in figure 2.4 were taken from figures 9(*a*, *b*), 12(*a*, *b*) of PM95a. The results from the DNS are compared with the current model accounting for the viscous layer, called here the *viscous theory*, and with inviscid model results, which are obtained from the present model when the viscous layer is ignored (i.e. $\delta' = 0$), called here the *inviscid theory*.

Figures 2.3(*a*, *b*) show profiles of the tangential Reynolds stress, $\overline{u_i^2}$ ($i = 1$ or 2), near a solid wall for $Re_T^* = 54$, 134. The general shape of the DNS curves, as well as the location of their maxima,

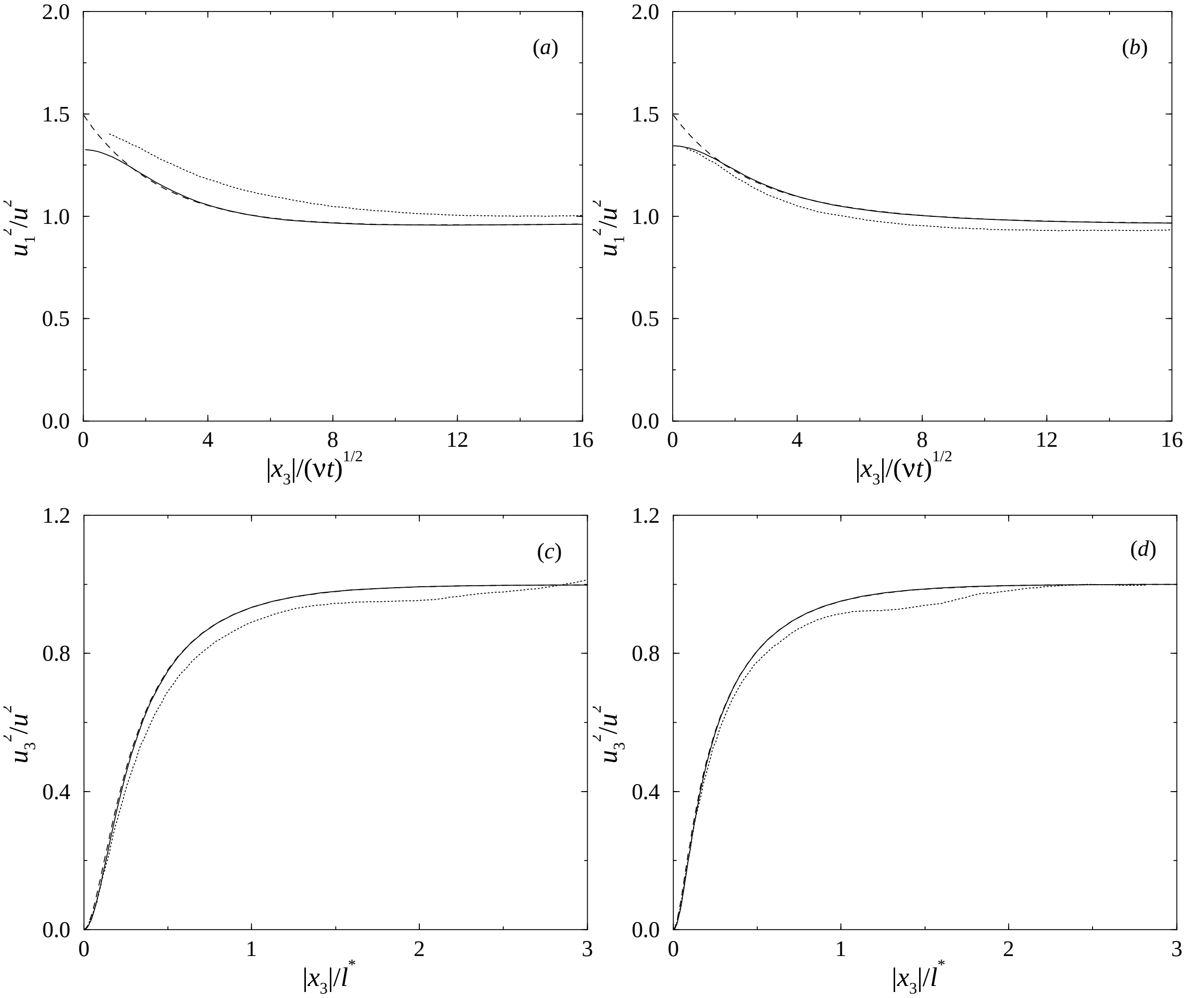

Figure 2.4 Reynolds stress profiles near a free surface at $u^* t/l^* = 0.1$. Solid line, viscous theory; dashed line, inviscid theory; dotted line, DNS data. (*a*) tangential component, $Re_T^* = 54$; (*b*) tangential component, $Re_T^* = 134$; (*c*) normal component, $Re_T^* = 54$; (*d*) normal component, $Re_T^* = 134$.

are well reproduced by the viscous theory. For $Re_T^* = 134$ the profile from the viscous theory is in excellent agreement with data, while for $Re_T^* = 54$ the theory gives slightly lower values, although the general agreement remains good. In the inviscid theory the stresses increase monotonically towards the boundary, however the viscous processes arrest this increase and lead to a reduction of the stresses, varying approximately as an error function, so that they are zero actually at the surface. Hence there is a maximum in the tangential Reynolds stress at the thickness of the viscous layer, namely $|x_3| \approx 3(\nu t)^{\frac{1}{2}}$. The maximum value obtained from the model is slightly larger for the larger Reynolds number because, for a given time, the larger the Reynolds number, the thinner the viscous layer. The DNS profiles shown in figures 15(*a*–*c*) of PM95a show a maximum that increases between $Re_T^* = 134$ to $Re_T^* = 374$, in agreement with this argument. However, in going from $Re_T^* = 54$ to $Re_T^* = 134$ the maximum in the DNS profiles actually decreases. This behaviour might be attributed to an imperfect ensemble average for the case of $Re_T^* = 54$.

Figures 2.3(*c*, *d*) show profiles of the normal Reynolds stress, $\overline{u_3^2}$, near a solid wall. In this case, the magnitude and general behaviour of theory and data agree very well, particularly in figure 2.3(*d*), but it is also true that viscous and inviscid theory differ much less. The small differences between the theory and the DNS data in figure 2.3(*c*) are attributed to an imperfect ensemble averaging, since they are due to a lack of smoothness in the DNS curve. The curve from the viscous theory captures quite well the viscous behaviour in the region immediately adjacent to the boundary, where $\overline{u_3^2} \propto x_3^4$ due to the no-slip boundary condition.

Figures 2.4(*a*, *b*) present profiles of the tangential Reynolds stress near a free surface. For the same reason as in figures 2.3(*a*, *b*), the quantitative agreement between theory and data is considerably better for a Reynolds number of 134 than for a Reynolds number of 54 (although not as good as in figure 2.3(*b*)). As the Reynolds number increases, the viscous model shows a slight increase in the maximum value of the stress, which lies at the free surface. The model shows that this happens because the viscous layer becomes thinner. Surprisingly, the DNS data shows the opposite trend. The enforcement of the boundary condition $\partial\overline{u_i^2}/\partial x_3 = 0$ ($i = 1$ or 2) is evident in the viscous theory profiles, and this is clearly an improvement upon the inviscid theory result.

Figures 2.4(*c*, *d*) show profiles of the normal Reynolds stress near a free surface. Apart from the anomalous behaviour of the DNS data between approximately $|x_3|/l^* = 0.5$ and $|x_3|/l^* = 2$, which again may be attributed to an imperfect ensemble averaging, the theoretical and DNS profiles are in very good agreement. The shape of the viscous theory profile is now even closer to inviscid theory, because the effect of the viscous layer on normal velocity is very weak.

2.5.2 Profiles of the turbulence dissipation rate

Figures 2.5 and 2.6 present profiles of the turbulence dissipation rate for a solid wall and for a free surface, respectively. In both figures, the dimensionless time is $u^*t/l^* = 0.1$ and the Reynolds numbers are 54 and 134. The DNS data presented in figure 2.5 were taken from figures 3.3.9, 3.3.10, 3.3.18 and 3.3.19 of PM93 and those presented in figure 2.6 were taken from figures 3.2.10, 3.2.11, 3.2.21 and 3.2.22 of PM93.

Figures 2.5(*a*, *b*) show profiles of the rate of dissipation of tangential Reynolds stress, normalised by their value far from the boundary. The agreement of the viscous theory profiles with the DNS data is very good. Even in the viscous layer adjacent to the boundary, where the profiles display large variations because the velocity gradients are large there, the theoretical values show good agreement with the DNS. The inviscid theory, of course, completely fails to model dissipation correctly in this region, giving values which are much lower than observed.

Figures 2.5(*c*, *d*) present profiles of dissipation of normal Reynolds stress near a solid wall. The

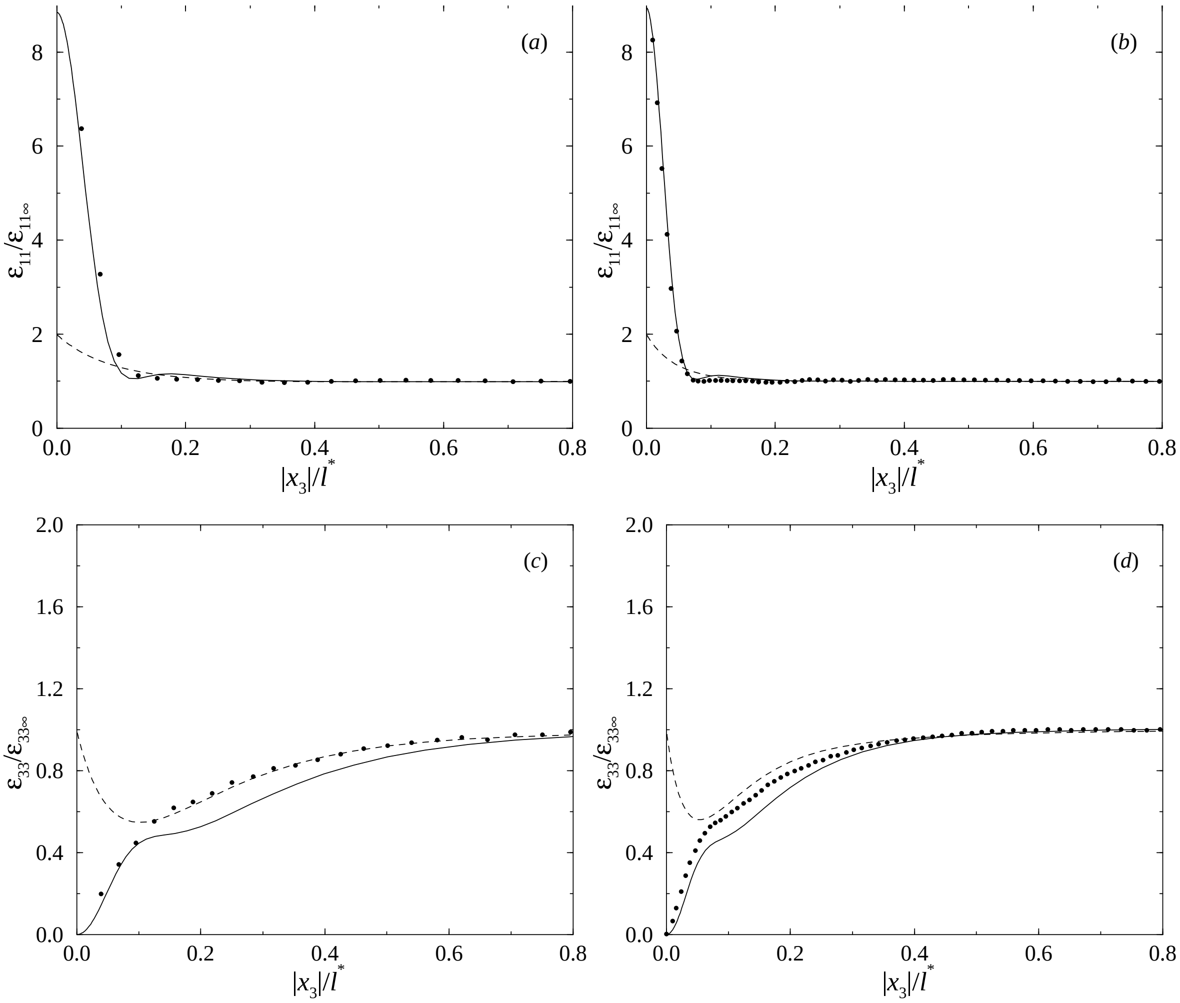

Figure 2.5 Dissipation rate profiles near a solid wall at $u^*t/l^* = 0.1$. Solid line, viscous theory; dashed line, inviscid theory; circles, DNS data. (*a*) tangential component, $Re_T^* = 54$; (*b*) tangential component, $Re_T^* = 134$; (*c*) normal component, $Re_T^* = 54$; (*d*) normal component, $Re_T^* = 134$.

agreement of the viscous theory with the DNS data is good, although dissipation given by the model is slightly smaller in an intermediate region between the boundary and the far-field. Curiously, in this region, the inviscid theory gives a better approximation to the data, particularly in figure 2.5(*c*) but, as would be expected, the inviscid theory behaves much worse than the viscous theory inside the viscous layer, where the dissipation decreases to zero towards the boundary.

Figures 2.6(*a, b*) show profiles of the tangential dissipation rate near a free surface. The agreement of the viscous theory and DNS data is good, although there is an overestimation of the maximum in dissipation for $Re_T^* = 54$ and a slight overestimation of the viscous layer thickness for $Re_T^* = 134$. Nevertheless, it is clear that the profiles of the viscous theory are much better than those of the inviscid theory and there are also signs that the ensemble averaging of the DNS data may not have been perfectly stable. The important finding here, which has implications for the evolution of

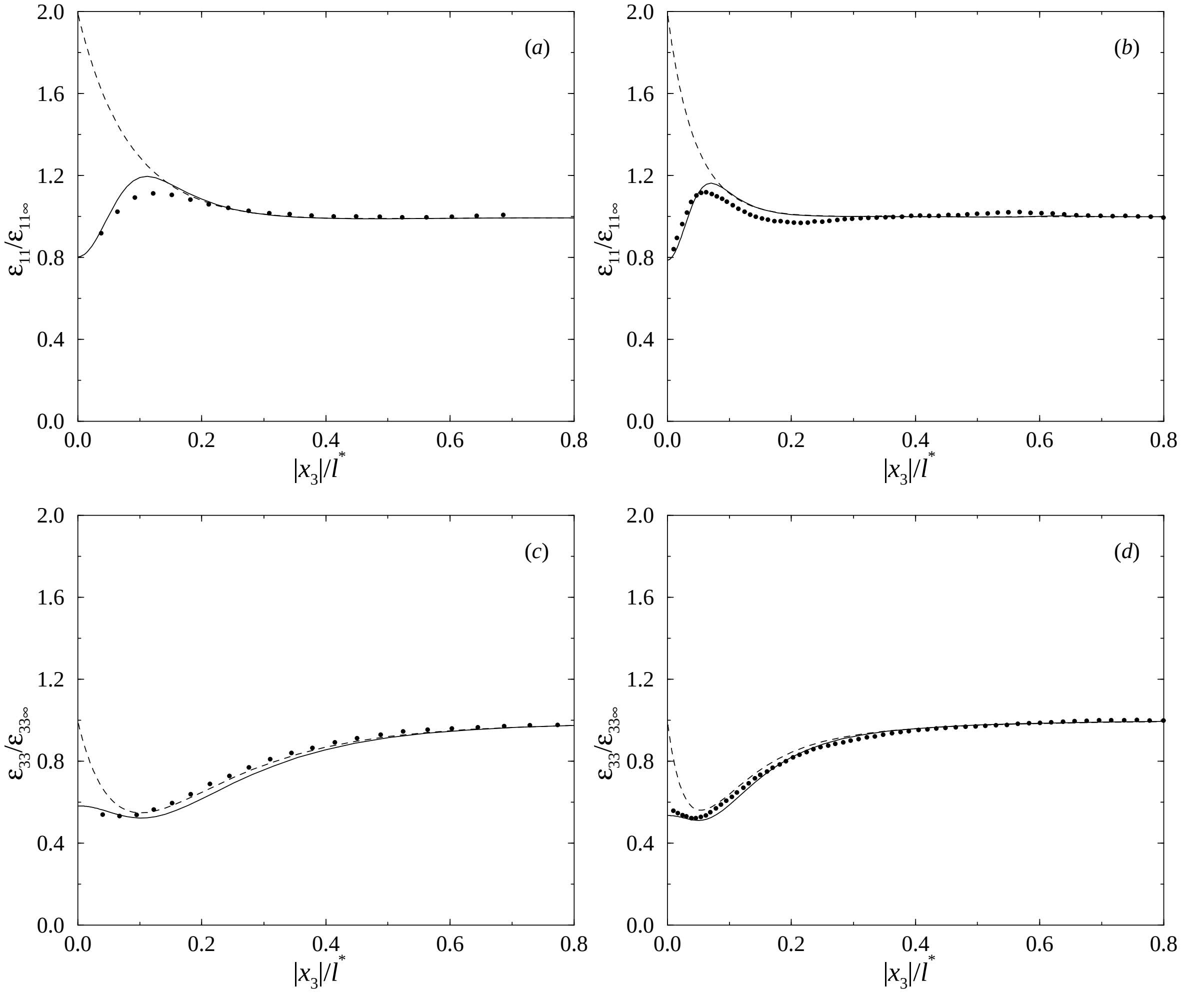

Figure 2.6 Dissipation rate profiles near a free surface at $u^*t/l^* = 0.1$. Solid line, viscous theory; dashed line, inviscid theory; circles, DNS data. (*a*) tangential component, $Re_T^* = 54$; (*b*) tangential component, $Re_T^* = 134$; (*c*) normal component, $Re_T^* = 54$; (*d*) normal component, $Re_T^* = 134$.

the tangential Reynolds stress, is that dissipation attains an absolute minimum exactly at the boundary. This contributes towards an intensification of the turbulence at the free surface, a phenomenon noted by Hunt (1984*a*), PM95a and Walker *et al.* (1996). Using an inviscid model, Hunt (1984*a*) attributed this phenomenon to the distortion of vorticity by the upwelling zones that exist near the boundary. PM95a subsequently suggested that this effect is linked with the pressure-strain terms in the turbulent kinetic energy budget near the boundary. While this physical process surely exists, the present model supports the idea (put forward by PM95a) that the main factor enhancing the tangential Reynolds stresses at short times is the minimum in tangential dissipation at the boundary: the pressure is intrinsically nonlinear and so scaling arguments of §2.2 show that it is negligible at short times.

Figures 2.6(*c*, *d*) present profiles of the normal dissipation rate near a free surface. The agreement of viscous theory with DNS data is very good, particularly for $Re_T^* = 134$. Again, a very substantial improvement in the results is achieved inside the viscous layer by the viscous theory, as compared with inviscid theory. In this layer, dissipation is considerably reduced, but not as much as near a solid wall, and attains a finite value at the free surface.

In all the cases analysed above, the behaviour of the turbulence dissipation profiles can be related to the behaviour of the corresponding Reynolds stresses. Basically, dissipation is high in the regions where the velocity gradients are also high. For example, in the viscous layer of a solid wall, the high tangential dissipation results from the steep gradients in the tangential Reynolds stress which are required to satisfy the no-slip boundary condition. The fact that normal dissipation is zero at the boundary can be explained using mass conservation and the no-slip boundary condition: since the tangential velocity u_i ($i = 1$ or 2) is zero at the boundary, its tangential derivatives are zero, hence by continuity, the normal gradient of the normal velocity is zero. Since the tangential gradients of the normal velocity are also zero, because the boundary is flat, the normal dissipation has to be zero according to (2.21) with $i = 3$.

In the viscous layer of a free surface, the reduced tangential dissipation is attributed to the no-stress boundary condition, which imposes a zero normal gradient of the tangential Reynolds stress at the boundary. The dissipation is not zero at the boundary because there are still tangential gradients of the tangential velocity. The normal component of dissipation, on the other hand, is finite and non-zero at the boundary because the no-stress boundary condition permits the existence of normal gradients of the normal velocity component.

A striking aspect of these comparisons is the success of the RDT model in predicting turbulence dissipation – a process usually associated with the smallest scales of the turbulence. RDT is justified by a time-scale analysis based on the energy-containing eddies, and so is expected to fail for small-scale eddies which evolve on a shorter time scale (Batchelor & Proudman, 1954). However, in the bounded flows studied here, dissipation near the boundary is dominated by the large gradients of the velocities associated with the energy-containing eddies in the viscous layer. The small-scale eddies are of secondary importance in determining the dissipation rate inside the viscous layer. This may explain in part why the normal dissipation rate profiles in figures 2.5(*c*, *d*) agree less well with the DNS data in an intermediate region between the viscous layer and the far-field. In that region, dissipation has not yet reached its far-field value, but the large-scale velocity has already much weaker gradients, so the velocity gradients of the smaller scales have an increased importance and, as a consequence, RDT is less accurate. In the viscous layer, the role of the smallest scales in the turbulence is primarily that of limiting the magnitude of dissipation through the viscous cutoff wavenumber k_{max}, but these small scales are relatively unimportant for determining the actual shape of the dissipation profiles.

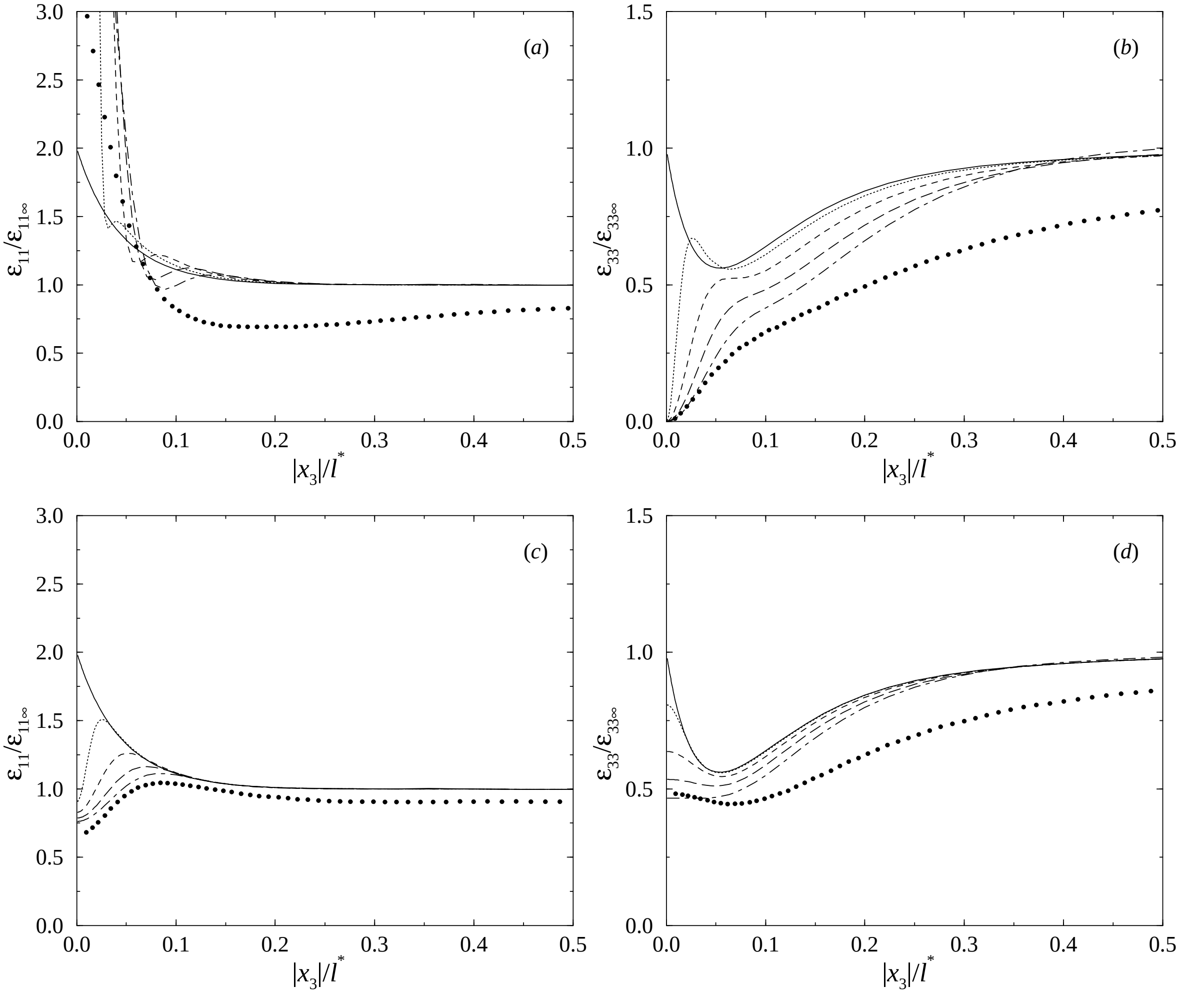

Figure 2.7 Dissipation rate profiles for $Re_T^* = 134$ at various times. Viscous theory at: solid line, $u^*t/l^* = 0$; dotted line, $u^*t/l^* = 0.01$; dashed line, $u^*t/l^* = 0.05$; long-dashed line, $u^*t/l^* = 0.1$; dash-dotted line, $u^*t/l^* = 0.15$; circles, DNS data at $u^*t/l^* = 2$. (*a*) solid wall, tangential component; (*b*) solid wall, normal component; (*c*) free surface, tangential component; (*d*) free surface, normal component.

2.5.3 Time evolution of dissipation

Figure 2.7 shows profiles of the tangential and normal dissipation rates near a solid wall and a free surface, for a Reynolds number of 134, at the times $u^*t/l^* = 0$, 0.01, 0.05, 0.1 and 0.15, as calculated from viscous theory. The DNS data presented in the same figure were taken from figures 2 and 3 of PM95b, and refer to the much later time $u^*t/l^* = 2$.

The evolution of the theoretical solutions with time can be seen. At $t = 0$, the dissipation rates begin by being equal to the dissipation rates calculated from inviscid theory. At the boundary, the tangential dissipation component is twice its value in the far-field, and the dissipation smoothly decays to its far-field value as one moves away from the boundary. The normal dissipation has the same value at the boundary and in the far-field, with a minimum in between located at about $|x_3|/l^* = 0.05$.

As time progresses, the influence of the viscous layer spreads over increasingly larger distances, and the theoretical profiles come to resemble the DNS profiles much closer, in particular regarding the location of maxima and minima. The match is not perfect, however, because while the model gives a reasonable prediction of the thickness of the viscous layer at a model time of $u^*t/l^* = 0.1$ or $u^*t/l^* = 0.15$ (in particular in figures 2.7(*b*–*d*)), the DNS curves tend to decay much slower towards their asymptotic value far from the boundary than the theoretical curves. This behaviour is attributed here to the additional diffusive effect of the turbulent transport (neglected in the model), which can be felt far outside the viscous layer.

Near a solid wall, tangential dissipation (figure 2.7(*a*)) is enhanced inside the viscous layer. As the viscous layer thickens, the maximum in the dissipation, which occurs at the boundary, is reduced as the velocity gradients in the viscous layer reduce. A region where dissipation is lower than in the inviscid profile exists at the edge of the viscous layer. Qualitatively, the DNS profile at the late time, $u^*t/l^* = 2$, displays similar features, as follows. The maximum at the boundary is higher than would be expected from inviscid theory, consistently with the existence of a viscous boundary layer. However, the value at the maximum is considerably lower than at early times, and the region of lowered dissipation noted in the theoretical profiles is more pronounced and spread over a much wider distance.

The time evolution of the normal dissipation shown in figure 2.7(*b*) begins with a local maximum very near the boundary. This maximum is progressively eroded because of the growth of the viscous layer and the constraint that normal dissipation is zero exactly at the boundary. Nevertheless, a residual maximum in curvature persists in the theoretical profiles up to the latest time considered, and this maximum may also be observed in the DNS data. At $u^*t/l^* = 0.15$, the theoretical profile departs slightly from its correct value far from the boundary, because the truncation error has become too large due to the power series of the solution becoming nearly non-asymptotic (see §2.4.2).

For a free surface, the tangential dissipation (figure 2.7(*c*)) begins by having a maximum near the boundary, and a sharp reduction exactly at the boundary, associated with the no-stress condition. As time progresses, these features become smoothed. The maximum decreases and moves away from the boundary and the minimum also decreases slightly, becoming distinctly lower than the dissipation value far from the boundary. The thickness of the viscous layer, as identified by the dissipation maximum, is in good agreement with DNS data for a model time of $u^*t/l^* = 0.15$.

The normal dissipation (figure 2.7(*d*)) initially has a local maximum at the boundary, followed by a minimum before tending to the far-field value. The maximum is soon eroded as the viscous layer grows, so that at the latest time considered in the model, dissipation has become approximately constant in the viscous layer. Again, there is a certain deal of qualitative agreement of the theoretical profiles at $u^*t/l^* = 0.1$ or 0.15 with the DNS profile.

Except for a considerably higher maximum in tangential dissipation at the boundary in the case of a solid wall, and a generally faster decay of the curves towards their far-field values as one moves away from the boundary, which it is argued is due to the absence of turbulent transport, the dissipation profiles presented in figure 2.7 for the viscous theory at $u^*t/l^* = 0.1$ or $u^*t/l^* = 0.15$ resemble the profiles obtained from the DNS at the late time $u^*t/l^* = 2$. This happens partly because the boundary conditions at $x_3 = 0$ are independent of time and also because the viscous layer does not grow indefinitely, but rather its growth is halted by nonlinear effects when $\delta/l \approx Re_T^{-1/2}$ (Hunt & Graham, 1978). The same nonlinear effects are also responsible for the main differences between the theoretical and DNS profiles, namely the diffusion of relatively sharp features like the minimum in tangential dissipation in figure 2.7(*a*).

Nevertheless, the similarities between the RDT and the DNS at late times remain striking, which suggests the concept of a *total diffusion* of the viscous boundary layer, akin to the *total shear* introduced by Townsend (1976), and used more recently by Mann (1994), for matching the results of RDT and measurements of equilibrium shear-flow turbulence. Qualitatively, equilibrium shear-flow turbulence and initially isotropic turbulence suddenly distorted by a constant shear are quite different. In equilibrium turbulence, vorticity tilting and stretching by shear is balanced by turbulent transport and viscous diffusion. In rapid distortion by shear, the turbulence is non-stationary, and dominated by vorticity tilting and stretching. Townsend noted that the first kind of turbulence resembled the second if, in his rapid-distortion model, the total shear since the beginning of the distortion was chosen appropriately.

The current model shows that homogeneous decaying turbulence near a solid or free boundary at relatively long times qualitatively resembles turbulence distorted by the same boundary at a given total diffusion of the viscous boundary layer. This total diffusion corresponds to a time T_ν when the model breaks down due to the growing relevance of neglected physical processes, such as turbulent transport. The main effect of these processes seems to be to arrest the fast evolution of the turbulence at an early distortion stage, changing it only slowly at subsequent times.

2.6 Conclusions

The rapid-distortion model of Hunt & Graham (1978) has been extended to treat the early development of shear-free turbulence near a suddenly introduced solid wall or free surface, taking full account of viscous processes, including the dynamics of the viscous boundary layer. The model is linear and assumes the turbulence to be initially homogeneous and isotropic everywhere, and to remain so far from the boundary. The turbulent velocity field is expressed as a superposition of Fourier modes and then statistics of the velocity field are obtained, given the energy spectrum of the turbulence far from the boundary. The velocity components induced by the boundary are expanded in power series of a small parameter, and terms in the series are considered up to the point where they become comparable with the neglected nonlinear effects. The model is formally valid at short times when (i) the nonlinear terms in the equations of motion are negligible and (ii) the power series of the solution for the turbulent velocity are asymptotic. Condition (i), which is well known from other rapid distortion studies, ensures in this particular case that viscous diffusion dominates over turbulent transport in the dynamics of the viscous layer. Condition (ii), on the other hand, ensures that the viscous layer can be treated as a thin boundary layer, and requires it to be much thinner than the smallest scales in the turbulence. The model makes use of a turbulence spectrum with a viscous cutoff in order to be dynamically consistent. This spectrum was found to lead to a correct dependence of the dimensionless dissipation on the Reynolds number, as compared with recent DNS data.

Reynolds stress and turbulence dissipation profiles were then calculated. The model was able to reproduce the essential observed differences between a solid wall and a free surface. Regarding dissipation, these differences are: dissipation of the tangential Reynolds stress is enhanced near a solid wall, while it is reduced near a free surface; dissipation of the normal Reynolds stress tends to zero near a solid wall, while it is slightly reduced to a non-zero value near a free surface. Results at short times were seen to be in good quantitative agreement with available DNS data, and also to reproduce the qualitative features of DNS data (namely the location of maxima and minima in the profiles) at later times, provided that the time used in the model was appropriately chosen. This suggests that the structure of the turbulence statistics and their differences for each type of boundary are essentially determined by the linear dynamics of the viscous boundary layer.

This study clarifies why the inviscid Hunt & Graham theory can be applied, with relative success, to the prediction of the Reynolds stress profiles near free surfaces at relatively long times (cf. Brumley and Jirka, 1987; Perot & Moin, 1995*a*; Walker *et al.*, 1996). On the one hand, a free surface introduces a relatively weak viscous correction to the essentially inviscid flow associated with the blocking effect of the boundary. That correction reduces only slightly the tangential Reynolds stresses at the boundary so that the boundary condition can be enforced. On the other hand, the tangential dissipation at the free surface is lower than in the bulk of the flow, as referred above, and this leads to a slow enhancement over time of the tangential Reynolds stresses which counteracts the reduction associated with the boundary condition. Because of these two opposing effects, the inviscid solution remains valid for times longer than expected.

Ultimately, the viscous layer stops growing, and the effect of dissipation supersedes that of the boundary condition, leading to the tangential Reynolds stresses at the free surface becoming greater than those predicted from inviscid theory. Alternative explanations for this phenomenon have been suggested, involving energy transfer from the normal to the tangential velocity components by the pressure-strain terms in the turbulent kinetic energy equation. These will be discussed in chapter

3. However, the present model supports the idea, put forward by PM95a, that the minimum in the dissipation profile at the surface plays a crucial role in this phenomenon, at least at the initial stages, because pressure is an intrinsically nonlinear quantity which was seen to be negligible at short times.

Turbulence dissipation also has implications for air-water gas transfer. The speed at which gases are transported across an air-water interface where the water is in turbulent motion is determined by: how thin the viscous boundary layer is forced to remain by the turbulence and how fast the turbulent motions replace old fluid near the surface by new fluid (Theofanous, 1984). This surface renewal is determined by the velocity and length scales of the turbulence, and also by the divergence of the flow at the surface, particularly at high Reynolds numbers (Hunt, 1984*b*). Indirectly, the dissipation profile near a free surface promotes surface renewal by increasing the value of the turbulence velocity scale there. At the same time, the dissipation rate of the normal Reynolds stress, ε_{33}, is linked with the surface divergence, through definition (2.21) with $i = 3$, because at $x_3 = 0$ the tangential derivatives of the normal velocity are zero and the normal derivative of the vertical velocity can be related, using continuity, to the horizontal divergence. The normal dissipation rate is thus proportional to the mean-square surface divergence, and so its behaviour influences surface renewal.

Some more general conclusions are now presented. One of the main findings of this study is that dissipation near a shear-free boundary is primarily determined by the velocity gradients corresponding to the rapid variation across the viscous boundary layer of the energy containing eddies. The small scales in the turbulence were seen to be important mainly for limiting the magnitude of dissipation, but not for determining the shape of the dissipation profiles. Therefore, the reason why rapid-distortion theory is in this case appropriate for calculating dissipation is because the boundary introduces a strong inhomogeneity in the flow.

Another key conclusion is that the shape of the dissipation profiles in turbulence near a solid wall or a free surface is essentially determined by the linear dynamics of the viscous boundary layer, even at late times. The effect of nonlinear processes seems to be primarily to arrest the growth of the viscous boundary layer on the one hand and to slightly diffuse the features in the profiles on the other.

2.7 Appendix. Expressions of the functions M_{ik}

2.7.1 Solid wall

For a solid wall, the functions $M_{ik}(\mathbf{k}, x_3, t)$ are defined as follows:

$$M_{ii} = \mathrm{e}^{\mathrm{i}k_3x_3} - \left[\mathrm{erf}\left(\frac{x_3}{\delta}\right) + 1\right], \quad i = 1, 2$$

$$\begin{aligned}
M_{i3} &= -\frac{\mathrm{i}k_i}{k_{12}}\left[1-\frac{\delta}{\pi^{1/2}}\left(1+\frac{\delta k_{12}}{\pi^{1/2}}\right)(\mathrm{i}k_3-k_{12})\right]\left[\mathrm{e}^{k_{12}x_3}-\left(\mathrm{erf}\left(\frac{x_3}{\delta}\right)+1\right)\right],\\
M_{33} &= \mathrm{e}^{\mathrm{i}k_3x_3}-\mathrm{e}^{k_{12}x_3}+\frac{\delta}{\pi^{1/2}}\left(1+\frac{\delta k_{12}}{\pi^{1/2}}\right)(\mathrm{i}k_3-k_{12})\left(\mathrm{e}^{k_{12}x_3}-1\right)\\
&-(\mathrm{i}k_3-k_{12})\left(1+\frac{\delta k_{12}}{\pi^{1/2}}+\frac{\delta^2k_{12}^2}{\pi}\right)\delta\left[\frac{x_3}{\delta}\left(\mathrm{erf}\left(\frac{x_3}{\delta}\right)+1\right)+\frac{1}{\pi^{1/2}}\left(\mathrm{e}^{-x_3^2/\delta^2}-1\right)\right].
\end{aligned}$$

The remaining elements of the M_{ik} matrix are zero.

Using (2.20), the Reynolds stresses may be expressed in terms of the undistorted turbulence spectrum $\Phi_{ij}^{(H)}$ and using (2.21), (2.22) and (2.23), the dissipation rates may be expressed in terms of the undistorted turbulence spectrum.

The resulting expressions may be further simplified by expressing the integrals involved in spherical polar coordinates and using (2.24). This enables analytical integration in one of the axial variables and the triple integrals become double integrals. That is the simplest form they can take before numerical evaluation, which is carried out using NAG subroutines.

2.7.2 Free surface

For a free surface, the non-zero components of the $M_{ik}(\mathbf{k}, x_3, t)$ tensor can be written as follows:

$$\begin{aligned}
M_{ii} &= \mathrm{e}^{\mathrm{i}k_3x_3}-\mathrm{i}k_3\delta\left[\frac{x_3}{\delta}\left(\mathrm{erf}\left(\frac{x_3}{\delta}\right)+1\right)+\frac{1}{\pi^{1/2}}\mathrm{e}^{-x_3^2/\delta^2}\right], \quad i=1,2\\
M_{i3} &= -\frac{\mathrm{i}k_i}{k_{12}}\left(1+\frac{\delta^2k^2}{4}\right)\left\{\mathrm{e}^{k_{12}x_3}-k_{12}\delta\left[\frac{x_3}{\delta}\left(\mathrm{erf}\left(\frac{x_3}{\delta}\right)+1\right)+\frac{1}{\pi^{1/2}}\mathrm{e}^{-x_3^2/\delta^2}\right]\right\},\\
M_{33} &= \mathrm{e}^{\mathrm{i}k_3x_3}-\mathrm{e}^{k_{12}x_3}+\frac{\delta^2k^2}{4}\left(1-\mathrm{e}^{k_{12}x_3}\right)+\left(1+\frac{\delta^2k_{12}^2}{4}\right)\delta^2k^2\\
&\times\left[\frac{x_3^2}{2\delta^2}\left(\mathrm{erf}\left(\frac{x_3}{\delta}\right)+1\right)+\frac{x_3}{2\pi^{1/2}\delta}\mathrm{e}^{-x_3^2/\delta^2}+\frac{1}{4}\mathrm{erf}\left(\frac{x_3}{\delta}\right)\right].
\end{aligned}$$

Again, using (2.20), (2.21), (2.22) and (2.23), the Reynolds stresses and the dissipation rates may be expressed in terms of the undistorted turbulence spectrum $\Phi_{ij}^{(H)}$.

The integrals contained in those expressions may then be expressed in spherical polar coordinates and integrated analytically over one of the axial variables, becoming double integrals, and then evaluated numerically.

CHAPTER 3

Nonlinear interactions in shear-free turbulence near boundaries

3.1 Introduction

Shear-free turbulence near flat boundaries constitutes a useful first approximation to many naturally occurring flows, such as convection in weak winds in the atmosphere surface layer (Hunt, 1984*a*) or the equivalent situation in the ocean, and turbulence produced by bottom friction that reaches the free surface, in channels or rivers (Borue *et al.*, 1995). Data on shear-free turbulence near flat boundaries are mostly available from numerical (Biringen & Reynolds, 1981; Perot & Moin, 1995*a*, 1995*b*) and experimental wind tunnel studies (Thomas & Hancock, 1977; Aronson *et al.*, 1997), because in these studies it is easier to control the conditions used in the experiments, hence it is possible to isolate more effectively the physical processes specific to this kind of turbulence.

As was seen in chapter 2, shear-free turbulence is affected by a flat boundary through blocking and viscous coupling from very early times. Blocking was treated by introducing an irrotational correction to the velocity that enables the flow to satisfy the boundary condition $u_3 = 0$ at $x_3 = 0$. As shown by Perot & Moin (1995*a*), this irrotational correction is only strictly valid if the boundary is inserted instantaneously at the initial time. In numerical simulations, the condition of instantaneous boundary insertion is easily implemented numerically, and in wind tunnel experiments, the boundary is generally a moving belt with an upstream edge not far away from the points where measurements are taken. So, in either case, the turbulence is distorted by the boundary very rapidly, and the initial changes to the free-stream turbulence must be approximately irrotational. This explains the very good agreement observed between theory and data at early times (Hunt & Graham, 1978). On the time scale of an eddy turn-over time or more, the turbulence also evolves due to the nonlinear interactions among eddies of different sizes and due to dissipation outside the viscous boundary layer. Although the model adopted in chapter 2 allowed to calculate profiles of the viscous dissipation, and thus to predict the likely future evolution of the Reynolds stresses, the model dynamics were totally linear, and nothing could be said about intrinsically nonlinear processes such as those involving pressure.

It was found that the dissipation profile near a free surface displays a minimum at the boundary, promoting a (relative) enhancement of the tangential Reynolds stresses over time in that region, which brings the value of the turbulent kinetic energy (TKE) to levels above those predicted by the theory of Hunt & Graham (1978). This enhancement has been observed both in laboratory experiments (Brumley & Jirka, 1987) and direct numerical simulations (Perot & Moin, 1995*a*; Walker *et al.*, 1996). However, a similar increase in the tangential Reynolds stresses has also been found near solid walls, despite the fact that the dissipation profile has no minimum there. This phenomenon has been attributed to residual shear or frictional heating in the early measurements of Thomas & Hancock (1977), but in a recent paper, Aronson *et al.* (1997) have taken particular care to eliminate any such effect, and they still obtain an enhancement of the tangential Reynolds stresses in the region immediately outside the viscous boundary layer (see their figure 9). For flows of a relatively large scale, such as those associated with atmospheric convection (Hunt, 1984*a*) or large-eddy simulations (Biringen & Reynolds, 1981), the viscous boundary layer is in fact extremely thin compared with the integral length scale of the turbulence, and it is evident that the shape of the dissipation profiles or any other viscous process cannot be responsible for the observed enhancement of the turbulent velocity fluctuations near the boundary.

Hunt (1984*a*) has attributed this enhancement to nonlinear processes, namely the vorticity stretching that occurs in zones where the flow impinges upon the boundary. But he estimated this effect by adapting the result of a model by Durbin (1981) for the flow at the stagnation point of a sphere. While this flow resembles to a certain extent the downwelling zones of turbulence in the atmosphere surface layer, or the upwelling zones of turbulence in the ocean surface layer, the distortion suffered by the turbulence at the stagnation point is infinite (which is certainly not the case in shear free-turbulence), and this makes the tangential Reynolds stress diverge at the boundary (see equation (2.20*b*) of Hunt, 1984*a*). On the other hand, Hunt's solution only applies to impinging flow, whereas turbulence near a boundary contains both upwelling and downwelling zones. Although Hunt argues that zones of impinging flow are more important for turbulence intensification, this has not been shown in practice. To clarify this issue, an inviscid rapid-distortion (RDT) model is used in this chapter to study the dynamics of upwelling and downwelling zones in shear-free turbulence near a flat boundary.

Besides helping to understand how turbulence intensifies near the boundary by nonlinear processes, the study of upwelling and downwelling zones is also interesting from a fundamental fluid dynamical point of view, since these zones (called 'splats' and 'anti-splats' in Perot & Moin, 1995*a*) are salient features in turbulent flows near boundaries. While in most experiments or numerical simulations (e.g. Perot & Moin, 1995*a*), the profiles of the turbulent statistics are averaged over whole planes parallel to the boundary and therefore do not distinguish between upwelling and downwelling zones existing across those planes, it will be seen later that the way in which the turbulent velocity and pressure fluctuations are affected by these two types of flow is far from symmetrical. This has important implications for the parameterisation of subgrid-scale terms in models that, for example, resolve the upwelling/downwelling zones but not the smaller-scale turbulence.

The remainder of this chapter is organised as follows. In §3.2, a simple theoretical model of turbulence in an upwelling or downwelling zone is developed. In §3.3, model results are presented for the time evolution of the Reynolds stresses, and the terms in the TKE budget are evaluated. The structure of the strain field near the boundary is analysed. In §3.4, the model is modified to account for the variation of the strain field with distance from the boundary and comparisons with data are carried out. Finally, in §3.5, the main conclusions are presented.

3.2 Theoretical model

Consider shear-free turbulence beneath a horizontal solid wall at $x_3 = 0$ or a flat free surface (where the Froude number *Fr* and the Weber number *We* are sufficiently low that there is not appreciable surface wave generation). The turbulence consists of large eddies and small eddies. The large eddies are distorted by the boundary (so as to satisfy the boundary condition) over a distance of the order of their own size (Hunt & Graham, 1978) and they are longer lived than the small eddies. From the viewpoint of the small eddies in the turbulence, the large eddies appear near the boundary as flattened structures often resembling upwelling and downwelling zones, which are roughly axisymmetric (Perot & Moin, 1995*a*) and slowly evolving in time.

In this chapter, the situation described above is approximated as follows. The shear-free turbulence is taken as a superposition of a deterministic large-scale flow, which represents the upwelling or downwelling zones, and a random small-scale flow representing the smaller eddies in the turbulence. The large-scale flow takes the form of a steady, axisymmetric, irrotational straining flow aligned with the boundary (cf. Kida & Hunt, 1989). The large-scale velocity U_i is defined as

$$U_i = \alpha_i x_i, \quad i = 1, 2, 3, \tag{3.1}$$

where α_i are the strain rates. For an axisymmetric straining flow, $\alpha_1 = \alpha_2 = -(1/2)\alpha_3 = \alpha$. This is the simplest possible flow possessing the basic characteristics described above for the upwelling or downwelling zones.

The small-scale flow takes the form of a random and time-evolving velocity field, which is assumed to be statistically homogeneous and isotropic far from the boundary at the initial time $t = 0$. Since the large-scale flow (3.1) has a constant strain rate, the small-scale flow remains homogeneous throughout its distortion.

Assume now that the large-scale flow is characterised by a length scale L and velocity scale $U = \alpha L$, and that the small-scale flow is characterised by a length scale l and a velocity scale u. If the velocity scale and the strain rate of the large-scale flow are much larger than those corresponding to the small-scale flow, that is, if

$$\alpha \gg \frac{u}{l}, \quad U \gg u, \tag{3.2}$$

the equations of motion may be linearised with respect to the small-scale flow, and the rapid-distortion approximation is valid.

Assuming additionally that the Reynolds number of the flow $Re = UL/\nu$ (where ν is the kinematic viscosity) is high enough, the vorticity equation takes the linearised and inviscid form

$$\frac{\partial \omega_i}{\partial t} + U_j \frac{\partial \omega_i}{\partial x_j} = \omega_j \frac{\partial U_i}{\partial x_j}, \tag{3.3}$$

where $\omega = \nabla \times \mathbf{u}$ is the vorticity of the small-scale flow. In the derivation of (3.3), the irrotationality of the large-scale flow (3.1) was taken into account.

An additional condition is necessary for the rapid-distortion approximation to remain valid. This results from the fact that nonlinear effects become more important when the degree of anisotropy of the small-scale flow due to distortion by the large-scale flow is very large. Assuming initially isotropic small-scale turbulence, this condition places an upper limit on the parameter αt, which ensures that the turbulence does not become unrealistically anisotropic.

The model is then solved for the small-scale turbulent velocity u_i and used to estimate the nonlinear interactions in the turbulence, regarded here as the distortion of the small-scales by the straining flow representing the upwelling or downwelling zone. This is done in the same way as in Kida & Hunt (1989) and Kevlahan & Hunt (1997), but the blocking effect of the boundary on the small-scale turbulence is also taken into account.

For the conditions (3.2) to be satisfied, a large separation has to exist between the velocity and the length scales of the assumed two components of the flow. In real turbulence, there is no clean-cut separation between the scales of the large and small eddies, since the turbulence spectrum is continuous. It may be argued, however, that the greatest contributions to the distortion of the small eddies come from the large eddies satisfying the conditions (3.2). Furthermore, the studies of Kida & Hunt (1989) and Kevlahan & Hunt (1997) have shown that models using the rapid-distortion approximation yield results that are useful for a fundamental understanding of the nonlinear interactions in the turbulence.

Obviously, since the upwelling and downwelling zones are treated as uniform straining flows, this model is only valid near the boundary but not at distances $|x_3| \approx L$ of the order of the size of the large eddies or greater, because over those distances the strain rate of the flow can no longer be realistically considered uniform. The aim of the model is to see what features of shear-free turbulence near boundaries can be attributed simply to the distortion by a large-scale uniform straining flow and the blocking effect.

3.2.1 Mathematical formulation

Subject to the conditions specified in the preceding subsection, the RDT model consists of the linearised vorticity equation (3.3), together with the large-scale straining flow (3.1). At sufficiently large distances from the boundary, the small-scale turbulence is homogeneous in the 3 spatial directions, although it becomes anisotropic due to distortion by the straining flow (Batchelor & Proudman, 1954). In that region, it is therefore possible to express both the velocity and the vorticity of the small-scale turbulence, $u_i^{(H)}$ and $\omega_i^{(H)}$, as three-dimensional Fourier integrals,

$$\begin{aligned} u_i^{(H)}(\mathbf{x},t) &= \iiint \hat{u}_i^{(H)}(\mathbf{k},t)\mathrm{e}^{\mathrm{i}\mathbf{k}\cdot\mathbf{x}}\mathrm{d}k_1\mathrm{d}k_2\mathrm{d}k_3, \\ \omega_i^{(H)}(\mathbf{x},t) &= \iiint \hat{\omega}_i^{(H)}(\mathbf{k},t)\mathrm{e}^{\mathrm{i}\mathbf{k}\cdot\mathbf{x}}\mathrm{d}k_1\mathrm{d}k_2\mathrm{d}k_3, \end{aligned} \tag{3.4}$$

where $\mathbf{k}(t) = (k_1, k_2, k_3)$ is a time-dependent wavenumber vector which takes into account the distortion by the straining flow. Using (3.4), the definition of vorticity yields algebraic equations that relate the Fourier amplitudes of the small-scale turbulent velocity and vorticity, namely

$$\hat{\omega}_i^{(H)} = \varepsilon_{ijk}\mathrm{i}k_j\hat{u}_k^{(H)} \quad \Rightarrow \quad \hat{u}_i^{(H)} = \varepsilon_{ijk}\mathrm{i}\frac{k_j}{k^2}\hat{\omega}_k^{(H)}, \tag{3.5}$$

where $k = (k_1^2 + k_2^2 + k_3^2)^{\frac{1}{2}}$ is the wavenumber magnitude. Making use of (3.4), the vorticity equation (3.3) can be expressed in the spectral domain, and is found to be equivalent to a system of two equations that give the time evolution of the Fourier amplitude of the vorticity, and of the corresponding wavenumber. When, U_i is defined as in (3.1), these equations take the particularly simple form

$$\frac{\mathrm{d}\hat{\omega}_i^{(H)}}{\mathrm{d}t} = \alpha_i\hat{\omega}_i^{(H)}, \quad \frac{\mathrm{d}k_i}{\mathrm{d}t} = -\alpha_i k_i, \tag{3.6}$$

and have the solutions (cf. Kevlahan & Hunt, 1997)

$$\hat{\omega}_i^{(H)}(\mathbf{k},t) = \hat{\omega}_i^{(H)}(\mathbf{k}_0,0)\mathrm{e}^{\alpha_i t}, \quad k_i(t) = k_{0i}\mathrm{e}^{-\alpha_i t}, \tag{3.7}$$

where the initial wavenumber vector has been defined as $k_{0i} = k_i(t=0)$. The first equation of (3.7) can be reformulated in terms of the Fourier amplitudes of the velocity by using (3.5) at the initial and final times, yielding

$$\hat{u}_i^{(H)}(\mathbf{k},t) = -\varepsilon_{ijk}\varepsilon_{klm}\frac{k_j k_{0l}}{k^2}\mathrm{e}^{\alpha_k t}\hat{u}_m^{(H)}(\mathbf{k}_0,0). \tag{3.8}$$

This expression relates the small-scale turbulent velocity at the final time to the small-scale turbulent velocity at the initial time for turbulence distorted by a homogeneous straining flow, exactly as in Batchelor & Proudman (1954) or Kida & Hunt (1989).

3.2.2 Blocking by the boundary

At distances from the boundary of $O(l)$ or smaller, the small-scale turbulence is affected not only by the large-scale upwelling/downwelling flow but also by the boundary itself. Outside the viscous boundary layer, where the present inviscid model is applicable, the effect of the boundary is primarily blocking. This is valid for a solid wall (exactly) or for a free surface with very low Froude and Weber numbers (approximately). In either case, the normal velocity component is forced to decay to zero towards the boundary. As discussed before, if the boundary insertion can be approximated as instantaneous, the correction to the velocity field due to blocking is initially irrotational (Hunt & Graham, 1978). This correction remains approximately irrotational at later times, according to (3.3), because the time variation of the vorticity of the small-scale turbulence only depends, in that equation, on the large-scale flow and on the rotational part of the turbulence.

Therefore, in order to account for the boundary, the velocity field corresponding to the small-scale turbulence is expressed as

$$u_i = u_i^{(H)} + \frac{\partial \phi^{(S)}}{\partial x_i}, \tag{3.9}$$

where $\phi^{(S)}$ is the potential of the velocity correction due to blocking, which satisfies

$$\nabla^2 \phi^{(S)} = 0 \tag{3.10}$$

by continuity. Since the boundary is assumed to be at $x_3 = 0$ and the turbulent fluid exists in the semi-infinite region below ($x_3 < 0$), the velocity potential has to satisfy the boundary conditions

$$\frac{\partial \phi^{(S)}}{\partial x_3}(x_3 = 0) = -u_3^{(H)}(x_3 = 0), \quad \phi^{(S)}(x_3 \to -\infty) \to 0, \tag{3.11}$$

which ensure that no fluid passes through the plane $x_3 = 0$ and that the blocking effect is not felt far from the boundary.

The small-scale turbulence is inhomogeneous in the vertical direction due to blocking by the boundary, but remains homogeneous along the other two directions. The velocity potential $\phi^{(S)}$ and the total small-scale turbulent velocity u_i may thus be expressed as two-dimensional Fourier integrals,

$$\begin{aligned}
\phi^{(S)}(\mathbf{x},t) &= \iint \hat{\phi}^{(S)}(k_1,k_2,x_3,t)\mathrm{e}^{\mathrm{i}(k_1x_1+k_2x_2)}\mathrm{d}k_1\mathrm{d}k_2,\\
u_i(\mathbf{x},t) &= \iint \hat{u}_i(k_1,k_2,x_3,t)\mathrm{e}^{\mathrm{i}(k_1x_1+k_2x_2)}\mathrm{d}k_1\mathrm{d}k_2. \qquad (3.12)
\end{aligned}$$

The first expression may be introduced in (3.10), which then becomes an ordinary differential equation and is easily solved, using the boundary conditions (3.11). The solution for the Fourier amplitude of $\phi^{(S)}$ is

$$\hat{\phi}^{(S)}(k_1,k_2,x_3,t) = -\int \frac{\hat{u}_3^{(H)}(\mathbf{k},t)}{k_{12}}\mathrm{e}^{k_{12}x_3}\mathrm{d}k_3, \qquad (3.13)$$

where $k_{12} = (k_1^2+k_2^2)^{\frac{1}{2}}$. This expression is formally identical to that obtained by Hunt & Graham (1978), with the difference that $\hat{u}_3^{(H)}$ and $\mathbf{k}$ now depend on time. This happens because the input to Hunt & Graham's inviscid model is totally undistorted turbulence, whereas in the present case, the input is turbulence already distorted by the large-scale straining flow corresponding to the upwelling or downwelling zone.

Inserting (3.13) into (3.9) and taking into account (3.12), it is found that the Fourier amplitude of the total small-scale turbulent velocity distorted by the boundary is

$$\begin{aligned}
\hat{u}_i(k_1,k_2,x_3,t) &= \int \left(\hat{u}_i^{(H)}(\mathbf{k},t)\mathrm{e}^{\mathrm{i}k_3x_3} - \hat{u}_3^{(H)}(\mathbf{k},t)\mathrm{i}\frac{k_i}{k_{12}}\mathrm{e}^{k_{12}x_3}\right)\mathrm{d}k_3, \quad i=1,2,\\
\hat{u}_3(k_1,k_2,x_3,t) &= \int \hat{u}_3^{(H)}(\mathbf{k},t)\left(\mathrm{e}^{\mathrm{i}k_3x_3} - \mathrm{e}^{k_{12}x_3}\right)\mathrm{d}k_3. \qquad (3.14)
\end{aligned}$$

Equation (3.14) shows that the Fourier amplitude of the turbulent velocity in the presence of the boundary is related to the Fourier amplitude of the turbulent velocity in the absence of (or far from) the boundary through an expression of the form

$$\hat{u}_i(k_1,k_2,x_3,t) = \int B_{ij}(\mathbf{k},x_3,t)\hat{u}_j^{(H)}(\mathbf{k},t)\mathrm{d}k_3, \qquad (3.15)$$

where

$$\begin{aligned}
B_{ii} &= \mathrm{e}^{\mathrm{i}k_3x_3}, \quad B_{i3} = -\mathrm{i}\frac{k_i}{k_{12}}\mathrm{e}^{k_{12}x_3}, \quad i=1,2,\\
B_{33} &= \mathrm{e}^{\mathrm{i}k_3x_3} - \mathrm{e}^{k_{12}x_3}. \qquad (3.16)
\end{aligned}$$

and the remaining elements of the B_{ij} matrix are zero. On the other hand, (3.8) can also be expressed more compactly as

$$\hat{u}_i^{(H)}(\mathbf{k},t) = W_{ij}(\mathbf{k},t)\hat{u}_j^{(H)}(\mathbf{k}_0,0), \tag{3.17}$$

where

$$W_{im} = -\varepsilon_{ijk}\varepsilon_{klm}\frac{k_j k_{0l}}{k^2}e_k, \tag{3.18}$$

and $e_k = \mathrm{e}^{\alpha_k t}$ is the flow extension along the x_k direction. Together, (3.15) and (3.17) imply that the Fourier amplitude of the distorted small-scale turbulent velocity is related to the Fourier amplitude of the undistorted turbulence through the product of the matrices B_{ij} and W_{ij}, the first accounting for the blocking effect of the boundary and the second accounting for the distortion by the large-scale flow, namely

$$\hat{u}_i(k_1,k_2,t) = \int M_{ik}(\mathbf{k},x_3,t)\hat{u}_k^{(H)}(\mathbf{k},0)\mathrm{d}k_3, \tag{3.19}$$

where $M_{ik} = B_{ij}W_{jk}$. This totally defines the solution to the problem, in a form analogous to that used by Townsend (1980) for unbounded turbulence.

3.2.3 The turbulent pressure fluctuations

The pressure field associated with the turbulent flow already defined can now be derived. In order to do that, it should be noted that the momentum equation consistent with the linearised vorticity equation (3.3) is

$$\frac{\partial u_i}{\partial t} + U_j\frac{\partial u_i}{\partial x_j} + u_j\frac{\partial U_i}{\partial x_j} = -\frac{1}{\rho}\frac{\partial p}{\partial x_i}, \tag{3.20}$$

where ρ is the density of the turbulent fluid and p is the pressure. Taking the divergence of (3.20) yields

$$\nabla^2 p = -2\rho\frac{\partial U_i}{\partial x_j}\frac{\partial u_j}{\partial x_i}, \tag{3.21}$$

which shows that, in the linear approximation, the turbulent pressure is determined by the interaction between the large-scale straining flow and the small-scale turbulence. For the particular flow described by (3.1), this equation simplifies further to

$$\nabla^2 p = -2\rho\alpha_i\frac{\partial u_i}{\partial x_i}. \tag{3.22}$$

The boundary conditions that are necessary to solve (3.22) state that the vertical pressure gradient at the boundary is zero (this results from (3.20) with $i = 3$, applied at $x_3 = 0$ and the boundary condition $u_3 = 0$ at $x_3 = 0$), and that the pressure infinitely far from the boundary is that induced by the velocity field at infinity, namely

$$\frac{\partial p}{\partial x_3}(x_3 = 0) = 0, \quad p(x_3 \to -\infty) \to p^{(H)}, \tag{3.23}$$

where $p^{(H)}$ is defined implicitly as the solution of

$$\nabla^2 p^{(H)} = -2\rho\alpha_i \frac{\partial u_i^{(H)}}{\partial x_i}. \tag{3.24}$$

Being statistically homogeneous in all directions, $p^{(H)}$ can be expressed as a three-dimensional Fourier integral, and (3.24) becomes an easily solvable algebraic equation for its Fourier amplitude. On the other hand, p, because it is affected by the boundary, can only be expressed as a two-dimensional Fourier integral in the form

$$p(\mathbf{x},t) = \iint \hat{p}(k_1,k_2,x_3,t)\mathrm{e}^{\mathrm{i}(k_1x_1+k_2x_2)}\mathrm{d}k_1\mathrm{d}k_2. \tag{3.25}$$

Substituting (3.25) into (3.22) yields an ordinary differential equation for the Fourier amplitude of the turbulent pressure $\hat{p}$. After some lengthy algebraic manipulations, it is found that this amplitude, which is affected by both the distortion of the small-scale turbulence by the large-scale flow and by the blocking effect of the boundary, can be related to the Fourier amplitude of the undistorted turbulent velocity through

$$\hat{p}(k_1,k_2,x_3,t) = \int Q_i(\mathbf{k},x_3,t)\hat{u}_i^{(H)}(\mathbf{k},0)\mathrm{d}k_3, \tag{3.26}$$

where expressions for the Q_i components are given in the appendix (§3.6).

3.2.4 Turbulence statistics

The simplest statistics that characterise the turbulent velocity fluctuations are the Reynolds stresses. In shear-free turbulence, only the diagonal components of the Reynolds stress tensor (the velocity variances, $\overline{u_i^2}$) are appreciable (Thomas & Hancock, 1977). In fact, in the present model, due to the assumption of initial isotropy and due to the type of large-scale distorting flow, the off-diagonal components of the Reynolds stress tensor associated with the small-scale turbulence are zero. For that reason, all future references to 'Reynolds stresses' will be synonymous with 'velocity variances', as in chapter 2. An equation giving the time evolution of the Reynolds stresses can be obtained by multiplying the momentum equation (3.20) by u_i, then taking the ensemble average and rearranging. If the large-scale velocity is also substituted according to (3.1), the following equation results,

$$\frac{\partial}{\partial t}\left(\overline{u_i^2}\right) = -U_3\frac{\partial}{\partial x_3}\left(\overline{u_i^2}\right) - 2\alpha_i\overline{u_i^2} + \frac{2}{\rho}\overline{p\frac{\partial u_i}{\partial x_i}} - \delta_{i3}\frac{2}{\rho}\frac{\partial}{\partial x_i}\left(\overline{pu_i}\right), \tag{3.27}$$

where the overbar denotes ensemble averaging. The term on the left-hand side is the tendency of the Reynolds stress. The terms on the right-hand side are, respectively, the advection, production, pressure-strain and pressure-flux terms. The advection and production terms appear as separated in (3.27) because the flow was artificially split into a large-scale and a small-scale part. In the case where the turbulence is taken as a whole, both of these terms are incorporated in the so-called turbulent transport term (Perot & Moin, 1993). Since the flow is statistically homogeneous in the directions parallel to the boundary, all the spatial derivatives of correlations along those directions are zero. That is why only the vertical components of the advection and the pressure-flux terms appear in (3.27). The various terms of (3.27) will be evaluated in §3.3 in order to determine the physical mechanisms responsible for the time evolution of the Reynolds stresses, following the procedure developed by Maxey (1982) for an unbounded shear flow.

These terms may be related to the statistics of the undistorted turbulence as follows. If the three-dimensional spectrum of the velocity fluctuations of the undistorted small-scale turbulence, $\Phi_{ij}^{(H)}$, is defined as

$$\overline{\hat{u}_i^{(H)*}(\mathbf{k}_0)\hat{u}_j^{(H)}(\mathbf{k}_0')} = \Phi_{ij}^{(H)}(\mathbf{k}_0)\delta(\mathbf{k}_0-\mathbf{k}_0'), \tag{3.28}$$

(where the asterisk denotes complex conjugation), then (3.19) and (3.26) may be used, in conjunction with (3.12) and (3.25), to obtain expressions for all the terms in (3.27) as functions of $\Phi_{ij}^{(H)}$, M_{ij} and Q_i. For example, the Reynolds stresses are given by

$$\overline{u_i^2} = \iiint M_{ik}^* M_{il}\Phi_{kl}^{(H)}\,\mathrm{d}k_1\mathrm{d}k_2\mathrm{d}k_3 \tag{3.29}$$

while the pressure-strain terms are

$$\begin{aligned}\overline{p\frac{\partial u_i}{\partial x_i}} &= \mathrm{Re}\left\{\iiint \mathrm{i}k_i Q_k^* M_{il}\Phi_{kl}^{(H)}\,\mathrm{d}k_1\mathrm{d}k_2\mathrm{d}k_3\right\}, \quad i=1,2,\\ \overline{p\frac{\partial u_3}{\partial x_3}} &= \mathrm{Re}\left\{\iiint Q_k^*\frac{\partial M_{3l}}{\partial x_3}\Phi_{kl}^{(H)}\,\mathrm{d}k_1\mathrm{d}k_2\mathrm{d}k_3\right\}.\end{aligned} \tag{3.30}$$

The pressure-velocity correlation (necessary for determining the pressure-flux term) is

$$\overline{pu_i} = \mathrm{Re}\left\{\iiint Q_k^* M_{il} \Phi_{kl}^{(H)} \mathrm{d}k_1 \mathrm{d}k_2 \mathrm{d}k_3\right\}. \tag{3.31}$$

Since the initial undistorted small-scale turbulence is assumed to be homogeneous and isotropic, its three-dimensional velocity spectrum can be related to the energy spectrum $E(k_0)$ through

$$\Phi_{ij}^{(H)}(\mathbf{k}_0) = \left(\delta_{ij} - \frac{k_{0i}k_{0j}}{k_0^2}\right)\frac{E(k_0)}{4\pi k_0^2}, \tag{3.32}$$

where $k_0 = (k_{01}^2 + k_{02}^2 + k_{03}^2)^{\frac{1}{2}}$ is the initial wavenumber magnitude. The energy spectrum of the undistorted small-scale turbulence is assumed to take the form attributed to von Kármán (also used, for example, in Hunt & Graham, 1978)

$$E(k_0) = u^2 l \frac{g_2 (k_0 l)^4}{(g_1 + (k_0 l)^2)^{\frac{17}{6}}} \tag{3.33}$$

where $g_1 = 0.558$ and $g_2 = 1.196$ are dimensionless constants. At high wavenumbers, this spectrum reproduces the well-known $k_0^{-5/3}$ power law behaviour corresponding to an inertial subrange.

3.3 Results

3.3.1 Axisymmetric straining flow

In the results that will be presented next, it is assumed that the large-scale flow (3.1) is an axisymmetric straining flow, since this seems to be the most natural form taken by an upwelling or downwelling zone in shear-free turbulence (Perot & Moin, 1995*a*). It must be recalled that (3.1) then becomes

$$U_1 = \alpha x_1, \quad U_2 = \alpha x_2, \quad U_3 = -2\alpha x_3. \tag{3.34}$$

Since α is the single parameter specifying the strain rate for this kind of flow, there is also a single parameter specifying the total strain suffered by the small-scale turbulence. This will be called c, following Batchelor & Proudman (1954), and its definition is

$$c = e_3 = \frac{1}{e_1 e_2} = \mathrm{e}^{-2\alpha t}. \tag{3.35}$$

The statistics of vector quantities tangential to the boundary will only be presented for the com-

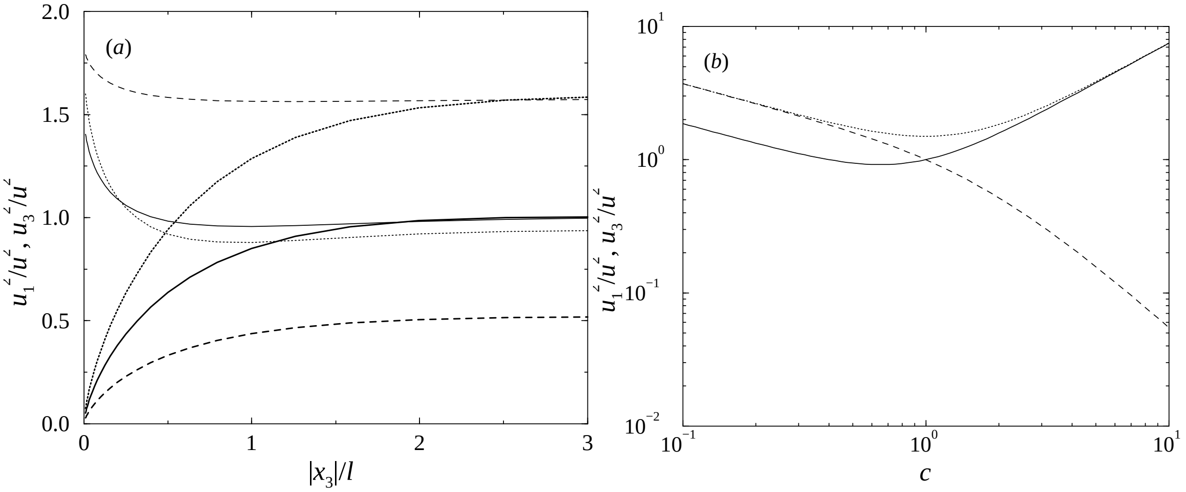

Figure 3.1 (*a*) Profiles of the Reynolds stresses. Thin lines: $\overline{u_1^2}$, thick lines: $\overline{u_3^2}$. Solid lines: $c = 1$ (undistorted), dotted lines: $c = 0.5$ (upwelling zone), dashed lines: $c = 2$ (downwelling zone). (*b*) Reynolds stresses as a function of c. Solid line: tangential Reynolds stress far from boundary, dotted line: tangential Reynolds stress at $x_3 = 0$, dashed line: normal Reynolds stress far from boundary.

ponent along the x_1 direction since, due to the initial isotropy of the small-scale turbulence and the symmetry of the flow (3.34), these statistics are equal for the components along any other tangential direction.

3.3.2 The Reynolds stresses

In the present model, the Reynolds stresses depend only on the distance from the boundary and on time (of which an appropriate dimensionless measure is the total strain c), so only these two parameters will be varied in the results that follow.

Figure 3.1(*a*) shows profiles of the tangential and normal components of the Reynolds stress for different values of c, as a function of distance from the boundary normalised by the integral length scale of the small-scale turbulence l. When $c = 1$, the turbulence is not distorted by the large-scale flow, and behaves in a way similar to that predicted by Hunt & Graham (1978). The Reynolds stresses tend to a normalised value of 1 far from the boundary. The tangential stress rises to 1.5 at the boundary and the normal stress tends to zero at the boundary, due to blocking. When $c = 0.5$ (upwelling zone), the tangential Reynolds stress decreases slightly far from the boundary and increases slightly at the boundary. The normal stress increases everywhere. When $c = 2$ (downwelling zone), the tangential Reynolds stress increases everywhere, but more so far from the boundary, and the normal Reynolds stress decreases everywhere.

The behaviour of the Reynolds stresses (and, for that matter, other statistics) far from the boundary and exactly at the boundary does not depend on the form of the energy spectrum adopted. It is only in the intermediate region, where the statistics change from their far-field value to their boundary value, that such spectral form is relevant. Figure 3.1(*b*) shows plots of the tangential Reynolds stresses far from the boundary and at the boundary and of the normal Reynolds stress far from the boundary, as functions of c. The values far from the boundary reproduce the classical results of Batchelor & Proudman (1954). When there is no distortion ($c = 1$), the results of Hunt & Graham (1978) are recovered.

When $c < 1$ (upwelling zone), the tangential Reynolds stress far from the boundary first decreases with c, while the tangential Reynolds stress at the boundary increases slowly, consistent with figure 3.1(*a*). For smaller values of c, both tangential Reynolds stresses increase at a rate which approaches asymptotically $\propto c^{-1/2}$. The normal Reynolds stress also increases at the same rate. For $c \ll 1$, the tangential Reynolds stress far from the boundary becomes half of both the tangential Reynolds stress at the boundary and the normal Reynolds stress far from the boundary.

When $c > 1$ (downwelling zone), the tangential Reynolds stress both far from the boundary and at the boundary increases at a rate which becomes asymptotically $\propto c$ for large values of c and the normal Reynolds stress decreases at a rate which becomes asymptotically $\propto \log(c)/c^2$ (cf. Batchelor & Proudman, 1954). The normal Reynolds stress becomes much smaller than the tangential Reynolds stress and the small-scale turbulence becomes approximately two-dimensional. Furthermore, the tangential Reynolds stresses far from the boundary and at the boundary become equal, which is a consequence of the normal velocity fluctuations approaching zero: if there are virtually no normal velocity fluctuations, the blocking effect is unable to transfer energy from the normal to the tangential motions.

3.3.3 Physical interpretation

The behaviour of the Reynolds stresses in figures 3.1(*a*, *b*) can be understood with the aid of the schematic diagrams of figures 3.2(*a*, *b*). Figure 3.2(*a*) shows that, in an upwelling zone, the horizontal vorticity is stretched and the vertical vorticity is compressed. This implies that the horizontal vorticity is amplified, whereas the vertical vorticity is attenuated. Since the horizontal vorticity receives contributions from the horizontal and vertical velocities, its amplification contributes to an increase of both the tangential and the normal Reynolds stresses. The vertical vorticity receives contributions only from the horizontal velocity, so its weakening contributes to a decrease of the tangential Reynolds stress. Apparently, this decrease is initially sufficient, far from the boundary, to counteract the increase induced by the stretching of horizontal vorticity, but the latter effect soon becomes dominant, leading to the observed increase of all the components of the Reynolds stress for moderate or large distortions. The downwelling zone can be understood by reversing the orientation of the arrows in the schematic of figure 3.2(*a*). As the flow evolves, the horizontal vorticity is compressed, and therefore

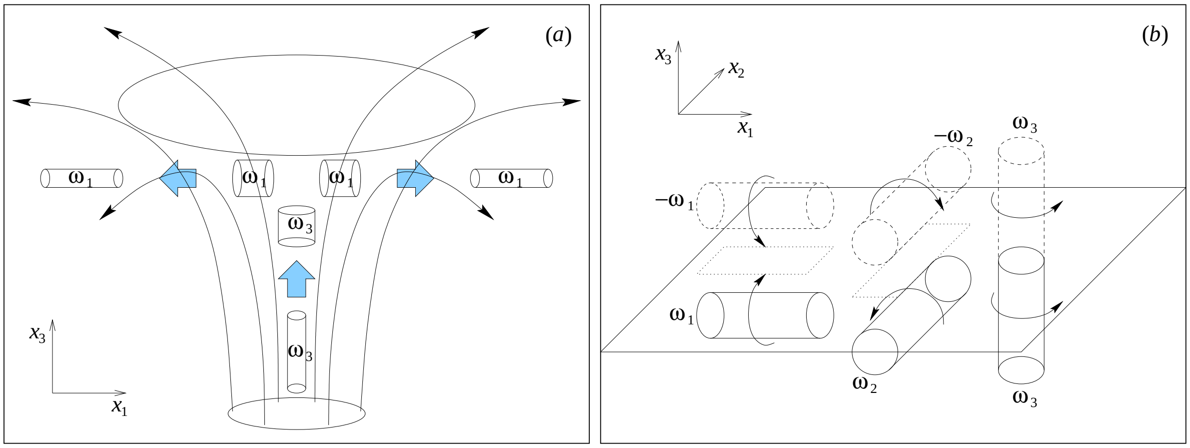

Figure 3.2 (*a*) Schematic diagram showing the vorticity distortion in an upwelling zone. (*b*) Schematic diagram showing the vortex tubes in isotropic turbulence and their images so that the blocking boundary condition is satisfied.

decreases in magnitude, and the vertical vorticity is stretched, and therefore increases in magnitude. The weakening of the horizontal vorticity leads to a decrease of the normal Reynolds stress and a negative contribution to the tangential Reynolds stress, but this tendency is counteracted by the faster increase of the tangential Reynolds stress, both at the boundary and far from the boundary, which is induced by the amplification of the vertical vorticity.

The relative magnitude of the components of the Reynolds stress far from the boundary and at the boundary can be understood with the aid of figure 3.2(*b*). In that figure, isotropic turbulence below the boundary is represented by 3 vortex tubes of similar intensity, oriented along the 3 coordinate directions. The blocking effect of the boundary is represented by the 3 image vortex tubes placed symmetrically above the boundary. The sign of the vorticity in the image vortex tubes is such that the vertical vorticity is extended symmetrically across the boundary and the horizontal vorticity is extended anti-symmetrically, so that the no-flux boundary condition is satisfied (Durbin & Hunt, 1980).

The blocking effect of the boundary when there is no additional distortion by the large-scale flow ($c = 1$) can be understood in the following way. Each vortex tube gives an equal contribution to the turbulent velocity, and hence to the Reynolds stress along the directions perpendicular to its axis. Suppose that the value of that contribution (which is here defined arbitrarily and is only important in relative terms) is 1/2. Then the vortex tube along x_1 gives a 1/2 contribution to the Reynolds stresses along x_2 and x_3, the vortex tube along x_2 gives a 1/2 contribution to the Reynolds stresses along x_1 and x_3 and the vortex tube along x_3 gives a 1/2 contribution to the Reynolds stresses along x_2 and x_3. All these contributions add up to Reynolds stresses of 1 along the 3 principal directions, corresponding to isotropic turbulence. Consider now the effect of the image vortex tubes at the boundary. The image vortex tube along x_1 gives a contribution $-1/2$ to the Reynolds stress along x_3 (in order to enforce the boundary condition), but a contribution $1/2$ to the Reynolds stress along x_2. Analogously, the image vortex tube along x_2 gives a contribution $-1/2$ to the Reynolds stress along x_3, but a contribution $1/2$

to the Reynolds stress along x_1. Finally, the image vortex tube along x_3 is the same vortex tube that would exist if the boundary was not there, and it adds a zero contribution to the Reynolds stresses along x_1 and x_2. Adding up all the contributions, it is concluded that the Reynolds stresses at the boundary along x_1 and x_2 have a value of 1.5 in the arbitrary units defined before, and the normal Reynolds stress is of course zero. This explains the well-known result of Hunt & Graham (1978), that the tangential stresses at the boundary in shear-free turbulence amplify by a factor of 1.5.

When $c \ll 1$ in an upwelling zone, the vertical vorticity becomes virtually zero and ceases to contribute to the Reynolds stresses. Then, it is only the vortex tubes along x_1 and x_2 that contribute to the Reynolds stresses. Far from the boundary, the effect of the image vortex tubes is not felt, and the vortex tube along x_1 contributes 1/2 to the Reynolds stress along x_2 and 1/2 to the Reynolds stress along x_3 (keeping the same units as before, for simplicity). On the other hand, the vortex tube along x_2 contributes 1/2 to the Reynolds stress along x_1 and 1/2 to the Reynolds stress along x_3. Adding all the contributions, the Reynolds stresses along x_1, x_2 and x_3 have relative magnitudes of 1/2, 1/2 and 1, respectively. This explains why the tangential Reynolds stress becomes half of the normal Reynolds stress for low values of c (see figure 3.1(*b*)). When the boundary is approached, the horizontal image vortex tubes are necessary to satisfy the boundary condition. The image vortex tube along x_1 gives a 1/2 contribution to the Reynolds stress along x_2 and a -1/2 contribution to the Reynolds stress along x_3, and the image vortex tube along x_2 gives a 1/2 contribution to the Reynolds stress along x_1 and a -1/2 contribution to the Reynolds stress along x_3. Adding all the contributions, it is concluded that the magnitude of the tangential Reynolds stresses at $x_3 = 0$ is 1, equal to that of the normal Reynolds stress far from the boundary, and twice the tangential Reynolds stress far from the boundary. This is in agreement with the ratios observed in figure 3.1(*b*) for low c.

When $c \gg 1$ in a downwelling zone, the horizontal vorticity is virtually zero and all the contributions to the Reynolds stresses come from the vertical vorticity. Since the vertical velocity fluctuations are associated with the horizontal vorticity, this means that the normal Reynolds stress is very small, which is indeed confirmed by figure 3.1(*b*). On the other hand, near the boundary, the image vortex tube along x_3 is simply an extension of the vertical vortex tube across the boundary, exactly as if the boundary did not exist. So the contribution of the vertical vorticity to the Reynolds stresses does not change as the boundary is approached. In other words, the tangential Reynolds stress maintains a constant magnitude throughout the turbulent fluid. This is consistent with figure 3.1(*b*), which shows that the tangential Reynolds stresses at the boundary and far from the boundary tend to the same value, when c is high.

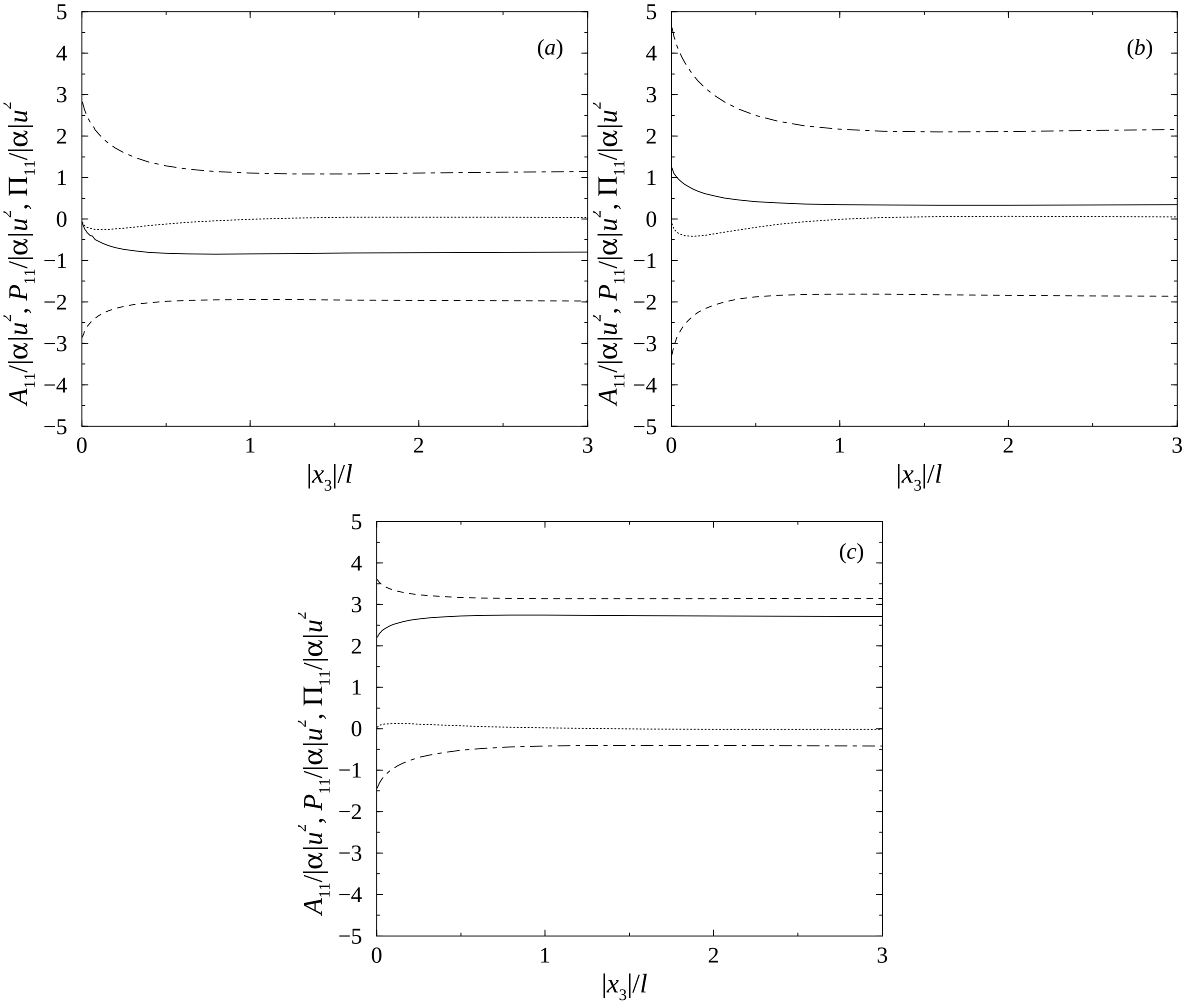

Figure 3.3 Profiles of the terms in the tangential Reynolds stress equation. Dotted line: advection, dashed line: production, dash-dotted line: pressure-strain, solid line: tendency (sum of previous terms). (*a*) $c = 1$, $\alpha > 0$ (upwelling flow, before distortion). (*b*) $c = 0.5$, $\alpha > 0$ (upwelling flow, after distortion). (*c*) $c = 2$, $\alpha < 0$ (downwelling flow, after distortion).

3.3.4 Analysis of the TKE budget

In order to investigate what physical processes are responsible for the observed time evolution of the Reynolds stresses, the various terms in the Reynolds stress equation (3.27) will be evaluated. The sum of all components of the Reynolds stress equation (for $i = 1, 2$ and 3) yields an equation for the evolution of the turbulent kinetic energy, $TKE = (1/2)(\overline{u_1^2} + \overline{u_2^2} + \overline{u_3^2})$.

Figure 3.3(*a*) shows profiles of the advection, production and pressure-strain terms, respectively defined as

$$A_{ii} = 2\alpha x_3 \frac{\partial}{\partial x_3}\left(\overline{u_i^2}\right), \quad P_{11} = -2\alpha\overline{u_1^2}, \quad \Pi_{ii} = \frac{2}{\rho}\overline{p\frac{\partial u_i}{\partial x_i}}, \tag{3.36}$$

in the tangential Reynolds stress equation, for an upwelling zone, at $c = 1$ (undistorted flow). The tendency of the Reynolds stress, which results from the sum of these 3 terms is also shown. The advection term is zero far from the boundary, because the Reynolds stress is homogeneous there, and at the boundary, because the normal component of the large-scale upwelling flow vanishes there. Overall, the advection term is small and slightly negative at $0 < |x_3| < l$ due to the fact that the impinging flow brings fluid with a smaller Reynolds stress towards the boundary. The production term is much larger in magnitude and negative everywhere (consistent with the vorticity arguments presented above), but more so at the boundary due to reinforcing by the image vortex tubes. Finally, the pressure-strain term is positive everywhere, with smaller magnitude than the production term far from the boundary and the same magnitude at the boundary. The tendency of the tangential Reynolds stress is negative far from the boundary and zero at $x_3 = 0$.

At a later stage in the development of the distortion, for a total strain $c = 0.5$ (figure 3.3(*b*)), the advection term has increased slightly in magnitude, but remains relatively small and negative, tending to zero far from and at the boundary. The production term remains negative and has increased slightly in magnitude at the boundary, while decreasing far from the boundary, and the pressure-strain term has increased and become more positive everywhere. Crucially, the balance between the terms is now different, because the pressure-strain term has become considerably larger than the production term, and the tendency of the tangential Reynolds stress is now positive everywhere, but especially so at the boundary, consistent with figures 3.1(*a*, *b*). Since the tangential Reynolds stress is now smaller than the normal Reynolds stress far from the boundary, but the normal Reynolds stress is always zero at the boundary, the pressure-strain term, which is positive, is promoting a return to isotropy of the small-scale turbulence far from the boundary, but contributing to a greater anisotropy at the boundary.

In the case of a downwelling zone, when $c = 1$, the various terms in the tangential Reynolds stress equation have the same magnitude as those presented in figure 3.3(*a*), but the opposite sign. Therefore, the advection term is small and positive, vanishing far from the boundary and at the boundary, the production term is positive, with a maximum at the boundary, and the pressure-strain term is negative and of larger magnitude than the production term, except at the boundary, where they balance each other. Accordingly, the time variation of the tangential Reynolds stress is positive everywhere except at the boundary, where it is zero.

At a later stage in the development of the downwelling flow, for a total strain $c = 2$ (figure 3.3(*c*)), this symmetry of behaviour has been lost. The advection term has decreased to become insignificant, the production term has increased in magnitude, especially far from the boundary, and the pressure strain-term has remained negative, while decreasing in magnitude. Since in this case the tangential Reynolds stress is everywhere larger than the normal Reynolds stress, the pressure-strain term contributes to a return to isotropy of the turbulence everywhere, particularly at the boundary. The energy budget is dominated by the production term, which imposes a steady increase of the tangential

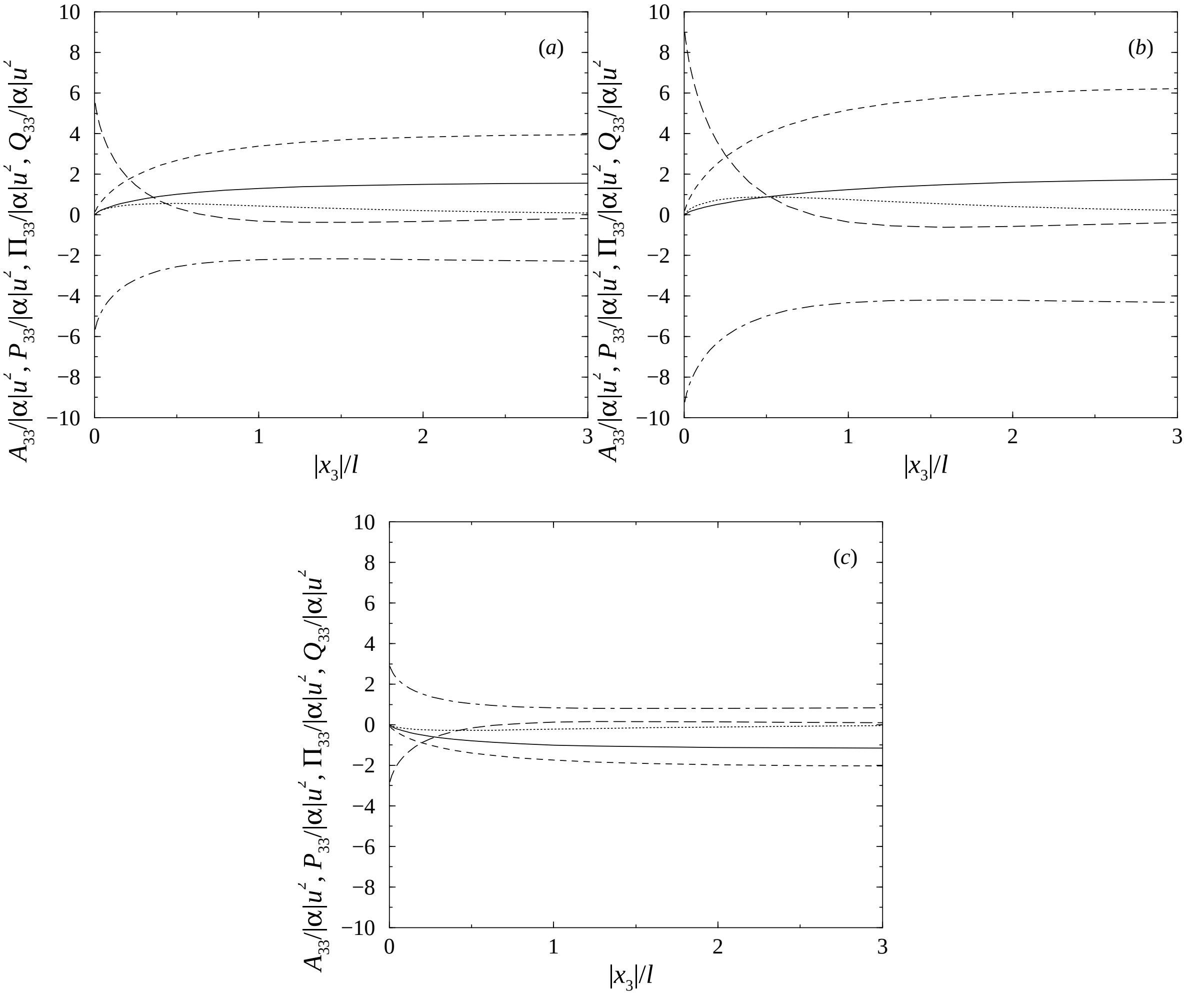

Figure 3.4 Profiles of the terms in the normal Reynolds stress equation. Dotted line: advection, dashed line: production, dash-dotted line: pressure-strain, long-dashed line: pressure flux, solid line: tendency (sum of previous terms). (*a*) $c = 1$, $\alpha > 0$ (upwelling flow, before distortion). (*b*) $c = 0.5$, $\alpha > 0$ (upwelling flow, after distortion). (*c*) $c = 2$, $\alpha < 0$ (downwelling flow, after distortion).

Reynolds stress.

Figure 3.4(*a*) presents profiles of the various terms in the normal Reynolds stress equation, for an upwelling zone, at $c = 1$. The symbols not already defined in (3.36) are

$$P_{33} = 4\alpha\overline{u_3^2}, \quad Q_{33} = -\frac{2}{\rho}\frac{\partial}{\partial x_3}\left(\overline{pu_3}\right), \tag{3.37}$$

and represent the production and the pressure-flux terms, respectively. The advection term is small and positive because the upwelling zone brings fluid to the boundary which originally had a larger normal Reynolds stress. For the same reasons as before, this term vanishes both far from the boundary and at the boundary. The production term is positive everywhere, due to horizontal vorticity stretching,

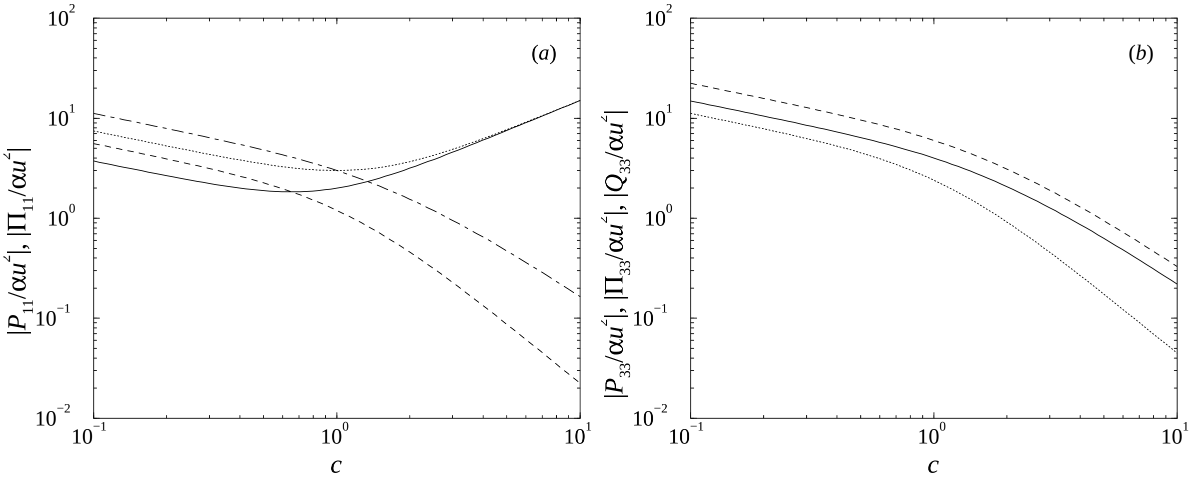

Figure 3.5 Absolute value of terms in the Reynolds stress equations as a function of c. (a) Tangential component. Solid line: production far from boundary, dotted line: production at $x_3 = 0$, dashed line: pressure-strain far from boundary, dash-dotted line: pressure-strain at $x_3 = 0$. (b) Normal component. Solid line: production far from boundary, dotted line: pressure-strain far from boundary, dashed line: pressure-strain and pressure flux at $x_3 = 0$.

except at the boundary, where it is zero, because the normal velocity is also zero there. The pressure-strain term is negative, with a maximum in magnitude at the boundary, and the pressure flux term has a positive maximum at the boundary, equal in magnitude to the minimum of the pressure-strain, but becomes slightly negative in an intermediate region and decays to zero far from the boundary. The pressure-strain term equals minus twice the pressure-strain term in the tangential Reynolds stress equation, due to continuity and the axial symmetry of the large-scale flow. At the boundary, the pressure-flux term exactly balances the pressure-strain term, since all other terms are zero. The tendency of the normal Reynolds stress is positive everywhere, except obviously at the boundary, where it is zero. This picture is not substantially changed when the upwelling flow evolves until $c = 0.5$ (figure 3.4(b)). The advection, production, pressure-strain and pressure-flux terms all increase somewhat in magnitude, but their qualitative behaviour remains the same.

In the case of a downwelling zone, at $c = 1$, the terms in the normal Reynolds stress equation are equal to those presented in figure 3.4(a) with the sign reversed. Hence, the advection term is small and negative, the production term is negative, except at the boundary, where it is zero, the pressure-strain term is positive, with a maximum at the boundary, and the pressure-flux term is negative, with the same magnitude as the pressure-strain term at the boundary, and decaying to zero far from the boundary. After the flow has evolved until the distortion is $c = 2$ (figure 3.4(c)), all these 4 terms have become smaller in magnitude, but their qualitative behaviour has not changed appreciably.

Figure 3.5(a) shows the absolute value of some of the terms in the tangential Reynolds stress equation, far from the boundary and at $x_3 = 0$, as a function of c. The production term is proportional to the Reynolds stress itself (as implied by (3.36)), increasing asymptotically as $c^{-1/2}$ when c decreases much below 1 and increasing asymptotically $\propto c$ when $c \gg 1$. The pressure-strain term, both at the boundary and far from the boundary, is of the same order of magnitude, and behaves asymptotically in the same way as the production term ($\propto c^{-1/2}$) when $c < 1$, but when $c > 1$ decays asymptotically like c^{-2} far from the boundary and like $\log(c)/c^2$ at $x_3 = 0$. Therefore, as the turbulence becomes progressively two dimensional in a downwelling zone, the relative importance of the pressure-strain term in the evolution of the Reynolds stresses decreases.

Figure 3.5(*b*) shows the same as figure 3.5(*a*), but for the terms in the normal Reynolds stress equation. The production term far from the boundary is again proportional to the Reynolds stress, consistently with (3.37), and the pressure-strain term and pressure-flux terms are of the same order of magnitude and have the same asymptotic behaviour ($\propto c^{-1/2}$) as the production term when $c < 1$. When $c \gg 1$, the pressure-strain term far from the boundary decays as c^{-2} (faster than the production term) but the pressure-strain and pressure-flux terms at $x_3 = 0$ show the same order of magnitude and asymptotic behaviour as the production term ($\propto \log(c)/c^2$). However, the absolute values of all these terms become insignificant at high c.

3.3.5 Discussion

In general, the ‘driving force’ behind the time evolution of the Reynolds stresses is the production term in the Reynolds stress equation. This term is responsible for moving the small-scale turbulence away from isotropy initially. The pressure-strain term always tends to oppose the production term. Far from the boundary (in the region where the Batchelor & Proudman (1954) theory can be applied), this always corresponds to a tendency towards isotropy. However, near the boundary, the pressure-strain term only contributes to make the small-scale turbulence isotropic in the case of a downwelling zone, whereas it tends to move the small-scale turbulence away from isotropy in an upwelling zone. This result ought to be taken into account in near-wall closures of the pressure-strain term for use in numerical models. Until now, in the studies where RDT is used to guide the development of such closures, the effect of boundaries is often not accounted for (Maxey, 1982; Johansson & Hallbäck, 1994). As the present results show, that may lead to the neglect of important physical processes. In the numerical simulations of Perot & Moin (1993) and Walker *et al.* (1996) (where there are both upwelling and downwelling zones near the boundary) the pressure-strain term in the TKE equation is identified as always contributing to the anisotropy of the turbulence near the boundary. The present results suggest that this happens because the magnitude of the pressure-strain term is considerably larger in an upwelling zone than in a downwelling zone, hence the contributions from the upwelling zones to this term tend to dominate. Although the pressure-strain terms always promote a return to isotropy of the small-scale turbulence in a downwelling zone, they become very inefficient in doing so at high values of c and have in fact vanishing importance in the TKE budget in the limit of two-dimensional turbulence.

An interesting question regarding the Reynolds stress budget is whether the sign of the tendency of the Reynolds stresses is determined primarily by the production term or by any other term in the corresponding equations. In the case of a downwelling zone or in the case of the normal Reynolds stress in an upwelling zone, the pressure strain term is of smaller magnitude than the production term, and the tendency of the Reynolds stress has the same sign as the production term. In the case of the tangential Reynolds stress in an upwelling zone, however, the tendency has the opposite sign to the production term and the same sign as the pressure-strain term (except for values of c near 1, far from the boundary). The tangential Reynolds stress evolution is thus driven by the energy imparted from the normal Reynolds stress through the pressure-strain correlations. That is why, in an upwelling zone, both the tangential and the normal Reynolds stresses increase in time.

3.3.6 The structure of the strain field

It is clear from figure 3.1(*b*) that the TKE increases with increasing distortion both in an upwelling zone ($c < 1$) and in a downwelling zone ($c > 1$). This is consistent with the enhanced turbulence intensity which is observed in experiments or numerical simulations of shear-free turbulence near boundaries at late times (Thomas & Hancock, 1977; Biringen & Reynolds, 1981). Although Hunt (1984*a*) argued that upwelling zones are more important in promoting this enhancement than downwelling zones, figure 3.1(*b*) shows that the TKE increases faster for a downwelling zone ($\propto c$) than for an upwelling zone ($\propto c^{-1/2}$). Hence both types of flow are important.

Most experiments or numerical simulations of shear-free turbulence consider stationary (Brumley & Jirka, 1987) or decaying turbulence (Perot & Moin, 1995*a*). The enhanced turbulence intensity near the boundary is detected either by the ratio between the TKE at the boundary and far from the boundary rising above 1, or equivalently by the ratio between the tangential Reynolds stress at the boundary and far from the boundary becoming larger than the value of 1.5 predicted by the theory of Hunt & Graham (1978). The second result follows from the first if the turbulence is isotropic away from the boundary, which is generally the case (Aronson *et al.*, 1997). Although the present model predicts that the ratio between the tangential Reynolds stress at $x_3 = 0$ and far from the boundary exceeds 1.5 in an upwelling zone, that behaviour is not linked with any relative increase of the TKE at the boundary, but is simply a manifestation that the turbulence has become anisotropic far from the boundary.

In fact, for the upwelling and the downwelling flows under consideration, the result of Hunt & Graham (1978)

$$\left(\overline{u_1^2} + \overline{u_2^2}\right)(x_3 = 0) = \left(\overline{u_1^2} + \overline{u_2^2} + \overline{u_3^2}\right)(x_3 \to -\infty) \tag{3.38}$$

remains valid, as can be confirmed in figures 3.1(*a*, *b*), since the solutions for the small-scale turbulence are obtained by directly applying Hunt & Graham's blocking correction to the small-scale turbulence already distorted by the straining flow. The reason why (3.38) holds in the model is because a uniform strain rate is assumed throughout the flow, and that strain is irrotational, allowing a decoupling of the effects of the large-scale flow and of blocking. It will be shown next that, when the non-uniformity of the large-scales in the turbulence is taken into account, the relative increase in TKE near the boundary results from the effect of blocking on the large-scale strain field.

Consider the structure of shear-free turbulence. On the scale of a small eddy, the large eddies in the turbulence can be viewed as deterministic and locally uniform flow structures, as considered in the present model. However, over scales much larger than their own, the large eddies behave in much the same way as the small eddies (Townsend, 1976) and tend to be statistically isotropic and homogeneous far from the boundary. Hence a possible way of modelling the structure of the large-scale strain field is by studying the strain field associated with the small eddies, and then extrapolating the results to the large eddies. In what follows, the present model for $c = 1$ (which is equivalent to Hunt & Graham's (1978) model), will be used to do just that. $c = 1$ is assumed, because the large eddies themselves are not subjected to any appreciable organised strain in shear-free turbulence.

According to (3.12) and (3.19), the strain rates of the turbulent velocity are defined as

$$\begin{aligned} \alpha_{ij} &= \frac{\partial u_i}{\partial x_j} = \iiint \mathrm{i}k_j M_{ik} \hat{u}_k^{(H)} \mathrm{e}^{\mathrm{i}(k_1x_1+k_2x_2)} \mathrm{d}k_1 \mathrm{d}k_2 \mathrm{d}k_3, \quad j = 1, 2, \\ \alpha_{i3} &= \frac{\partial u_i}{\partial x_3} = \iiint \frac{\partial M_{ik}}{\partial x_3} \hat{u}_k^{(H)} \mathrm{e}^{\mathrm{i}(k_1x_1+k_2x_2)} \mathrm{d}k_1 \mathrm{d}k_2 \mathrm{d}k_3. \end{aligned} \tag{3.39}$$

By analogy with (3.29), and using (3.28), the variances of these strain rates, which give an estimate of their magnitude, take the form

$$\begin{aligned} \overline{\alpha_{ij}^2} &= \iiint k_j^2 M_{ik}^* M_{il} \Phi_{kl}^{(H)} \mathrm{d}k_1 \mathrm{d}k_2 \mathrm{d}k_3, \quad j = 1, 2, \\ \overline{\alpha_{i3}^2} &= \iiint \frac{\partial M_{ik}^*}{\partial x_3} \frac{\partial M_{il}}{\partial x_3} \Phi_{kl}^{(H)} \mathrm{d}k_1 \mathrm{d}k_2 \mathrm{d}k_3. \end{aligned} \tag{3.40}$$

At arbitrary distances from the boundary, the expressions of these variances are rather complex. But they are much simpler far from the boundary and at the boundary, where they are independent of the form of the energy spectrum $E(k_0)$. In those regions, the $\overline{\alpha_{ij}^2}$ only depend on the initial value of the dissipation rate far from the boundary, ε, which is defined as

$$\varepsilon = 2\nu \int_0^\infty k_0^2 E(k_0) \mathrm{d}k_0. \tag{3.41}$$

For $c = 1$, the expressions of the components of the $\overline{\alpha_{ij}^2}$ matrix at $x_3 = 0$ and as $x_3 \to -\infty$ are found to be

$$\begin{aligned}
&\overline{\alpha_{ii}^2} = \frac{1}{15}\frac{\varepsilon}{\nu}, \quad \overline{\alpha_{ij}^2} = \frac{2}{15}\frac{\varepsilon}{\nu}, \quad i = 1, 2, 3, \quad i \neq j, \quad \text{as} \quad x_3 \to -\infty, \\
&\overline{\alpha_{11}^2} = \overline{\alpha_{12}^2} = \overline{\alpha_{21}^2} = \overline{\alpha_{22}^2} = \frac{1}{6}\frac{\varepsilon}{\nu}, \quad \overline{\alpha_{i3}^2} = \frac{1}{3}\frac{\varepsilon}{\nu}, \quad \overline{\alpha_{31}^2} = \overline{\alpha_{32}^2} = 0, \quad \text{at} \quad x_3 = 0. \qquad (3.42)
\end{aligned}$$

From (3.42), it is clear that, far from the boundary, the strain rates are statistically isotropic, like the velocity field itself, but near the boundary, the strain rates are modified by the blocking effect in two ways: (i) they increase in magnitude and (ii) they become anisotropic, adopting orientations compatible with the blocking boundary condition. Since strains with an isotropic distribution are more prone to cancellation than strains subject to a directional constraint, the second effect reinforces the first. Both these effects, which exist in real turbulence, lead to the small-scale turbulence being subjected to a substantially larger net straining rate at the boundary. Since the straining of the turbulence leads to an increase of its TKE, as seen before, this explains why the TKE at $x_3 = 0$ is larger than the TKE far from the boundary.

The axisymmetric straining flow used in the present model to represent the large scales in the turbulence represents the anisotropy of those scales due to the boundary in way that is approximated but qualitatively correct, simply by being aligned with the boundary. But by being uniform, this straining flow obviously fails to account for the weakening of the strain field and for its transition from anisotropic to isotropic as one moves away from the boundary (which is implied by (3.42)).

A modification to the present model which incorporates these effects in a heuristic manner is presented next.

3.4 Modifications to the model and comparison with data

3.4.1 A spatially limited upwelling/downwelling zone

The inhomogeneity of the strain field which was seen to exist in shear free turbulence can be incorporated in the present model by redefining the large-scale flow as

$$U_1 = \alpha x_1 \mathrm{e}^{m x_3}, \quad U_2 = \alpha x_2 \mathrm{e}^{m x_3}, \quad U_3 = -\frac{2\alpha}{m}\left(\mathrm{e}^{m x_3} - 1\right), \qquad (3.43)$$

where $1/m$ is a positive distance. This flow approximates the previously used straining flow (3.34) at the boundary, but decays exponentially to zero far from the boundary, as $x_3 \to -\infty$. The treatment in §3.3.6 showed that the strain rate far from the boundary is not zero, but simply smaller and isotropic, whereas the strain rate near the boundary is larger and anisotropic. Obviously, that situation is much more complex than that modelled here, but a connection may be established in the following way. In real turbulence, an equilibrium is reached between the distortion of the small scales by the large scales, which leads to an increase of the TKE, and the dissipation of the small scales, which leads to a decrease of the TKE. The equilibrium strain of the turbulence in a region with a larger strain rate is higher than the equilibrium strain in a region with a smaller strain rate (this effect is included, for example, in Maxey's (1982) equation (3.3)). Hence, to compare the results of the present model with data, it is more useful to think in terms of total strains than in terms of strain rates. Use of the large-scale flow (3.43) allows the equilibrium state of the small-scale turbulence far from the boundary to be arbitrarily defined as undistorted, and the more distorted equilibrium state existing at the boundary (due to the larger strain rate there) to be matched through the parameter c.

In the model used by Hunt (1984*a*) to estimate the nonlinear effects in shear-free turbulence, the flow in an upwelling zone is approximated as potential flow around a sphere. This flow has the advantage of possessing a strain that naturally tends to zero far from the boundary. However, since the flow is assumed to be stationary, and the turbulence is assumed to be homogeneous far from the sphere, the value of the total strain at the boundary is infinite. This leads to an infinite Reynolds stress at the boundary (cf. equation (2.20*b*) of Hunt, 1984*a*), which is not realistic. Since upwelling and downwelling zones are not steady but transient flow structures, the present time-dependent model is deemed more appropriate to treat them.

The new large-scale flow (3.43) satisfies mass conservation exactly, but not irrotationality, and has an associated vorticity of $O(mU)$. This flow can still be considered approximately irrotational if its vorticity is much smaller than its strain rate. Since the strain rate is of $O(U/L)$, approximate irrotationality holds if $mL \ll 1$. On the other hand, since $l \ll L$, the condition $mL \ll 1$ implies that $ml \ll 1$, and this means that the small-scale turbulence can still be considered locally homogeneous over the distance $1/m$. Hence the theoretical framework developed for a flow with a constant strain rate continues to be valid (as in Hunt (1973), for sufficiently small-scale turbulence), and the large-scale flow (3.43) can just be substituted in the original model, with m appearing as a parameter. Subject to these conditions, when (3.43) is used, the statistics of the small-scale turbulence will behave near the boundary exactly as for a constant strain rate, with the TKE becoming larger as c becomes larger or smaller than one. Over a distance l from the boundary, the statistics will change from their values modified by blocking to their values influenced only by the straining flow. Finally, over a larger distance from the boundary of $O(1/m)$, the statistics will decay towards their totally undistorted values.

Since the exponential factor in (3.43) aims to account for the effect of the boundary on the strain rate, and this effect is felt over a distance from the boundary of the order of the length scale of the large eddies, L, m should in fact be of $O(1/L)$. Furthermore, there is not, in real turbulence, a clear separation between the length scale L of a large-scale flow and that of the small-scale turbulence distorted by that flow, l. Although this choice disrespects both the condition for the irrotationality of the large-scale flow and the condition for local homogeneity of the turbulence, it will be assumed in the following calculations that $1/m = L = l$, because the agreement with data is optimised in that way.

3.4.2 The Reynolds stress profiles

Before comparing results from the modified model of the previous subsection with data, an additional aspect needs to be noted. In real shear-free turbulence, there are both upwelling and downwelling zones near the boundary. The statistics of this turbulence averaged over a whole plane parallel to the boundary should therefore be a mixture of the statistics in the upwelling zones and in the downwelling zones. Neglecting effects associated with the finite size of these zones, their only relevant parameter is their mass flux. Due to mass conservation, the total mass flux towards the boundary associated with the upwelling zones has to be the same as the total mass flux away from the boundary associated with the downwelling zones. In the present model, the mass flux towards the boundary is proportional to the strain rate of the large-scale flow. Hence, the global effect of all the upwelling zones and all the downwelling zones can taken into account by considering only one 'global' upwelling zone and one 'global' downwelling zone, with strain rates α, and $-\alpha$ respectively, representative of the total mass flux towards the boundary and the total mass flux away from the boundary. If, at a given time, the 'global' upwelling zone has a total strain c, the corresponding 'global' downwelling zone must have a total strain $1/c$, by continuity.

Figure 3.6(a) shows model results for the Reynolds stresses, for 'global' downwelling and upwelling zones with $c = 2.3$ and $c = 1/2.3 = 0.435$, respectively, compared with data from Thomas & Hancock (1977) for a shorter distance and a longer distance from the upstream end of the wind tunnel. The data at the upstream location are in quite good agreement with the theory of Hunt & Graham (1978) (present model with $c = 1$), because nonlinear effects are unimportant. Further downstream, however, the tangential Reynolds stress is larger and falls in between the theoretical lines calculated for the upwelling and the downwelling zones.

This suggests that the Reynolds stresses averaged over a plane parallel to the boundary can be determined simply by taking the average of the Reynolds stresses $\overline{u_i^{(U)2}}$, associated with the 'global' upwelling zone and the Reynolds stresses $\overline{u_i^{(D)2}}$, associated with the 'global' downwelling zone, namely

$$\overline{u_i^2} = \frac{1}{2}\left(\overline{u_i^{(U)2}} + \overline{u_i^{(D)2}}\right). \tag{3.44}$$

This approach is adopted in the theoretical results presented in figure 3.6(b), where some numerical model data from Biringen & Reynolds (1981), for an earlier and a later time, are also shown. The

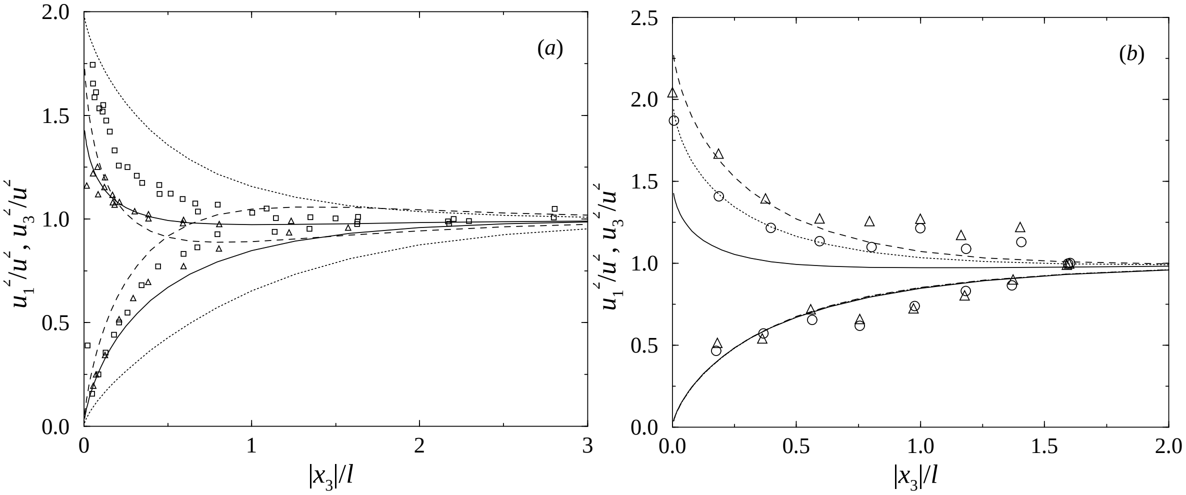

Figure 3.6 (*a*) Reynolds stress profiles for the large-scale flow (3.43). Solid lines: $c = 1$ (undistorted), dotted lines: $c = 2.3$ (downwelling zone), dashed lines: $c = 0.435$ (upwelling zone), triangles: data of Thomas & Hancock (1977) at upstream position, squares: data of Thomas & Hancock further downstream. (*b*) Average of the Reynolds stress profiles for upwelling and downwelling zones with the same intensity. Solid lines: $c = 1$; dotted lines: average of $c = 2.5$ and $c = 0.4$; dashed lines: average of $c = 3.2$ and $c = 0.3125$; circles: data of Biringen & Reynolds (1981) at earlier time; triangles: data of Biringen & Reynolds at later time.

values of c have been chosen so as to fit the data in the best possible way. Given the considerable scatter of the data, which is due to the relatively small ensemble used in the averaging process, the model does a very reasonable job in fitting the data.

3.4.3 The turbulent pressure field

A variable which is intrinsically related to the nonlinear interactions in the turbulence is the so-called 'slow' pressure. Kim (1989) presented results from numerical simulations of channel-flow on variances, correlations and spectra of both the fast pressure, which results from the interaction between the turbulence and the mean flow, and the slow pressure, which results from the interaction of the turbulence with itself. Perhaps the most striking aspect in Kim's plots of the pressure spectra (his figure 9) is that the slope of the spectra at high wavenumbers is steeper than predicted by theory, particularly near the channel wall, and does not differ appreciably between the fast and the slow pressures. Theoretical predictions indicate that the slope of the fast pressure should be $-11/3$ (Durbin, 1978) and the slope of the slow pressure should be $-7/3$ at high wavenumbers (Fung *et al.*, 1992).

Here, an attempt to explain these results is presented, based on the idea that the slow pressure results from the interaction of the small eddies in the turbulence with the large eddies, and that these large eddies can be represented by a uniform straining flow. This is equivalent to assuming that the slow pressure is in fact a fast pressure where the turbulence is replaced by the small-scale turbulence and the mean flow is replaced by the large-scale turbulence.

In the present linear model, the pressure field is produced by the interaction between the small-scale turbulence and the large-scale velocity gradients. That interaction happens everywhere, but if the large-scale flow used in the previous subsection is adopted, the model will produce no pressure fluctuations far from the boundary (since the large-scale flow tends to zero there). Hence, the straining flow used originally (3.34) will be adopted instead. It will be shown that the observed differences between the magnitude of pressure at the boundary and in the bulk of the flow can be explained simply in terms of the blocking effect of the boundary, and that the variation of the strain rate does not seem to be important in this case.

Making use of (3.25) and (3.26), the pressure variance is found to be

$$\overline{p^2} = \iiint Q_k^* Q_l \Phi_{kl}^{(H)} \mathrm{d}k_1 \mathrm{d}k_2 \mathrm{d}k_3, \tag{3.45}$$

and the one-dimensional pressure spectrum, whose definition is

$$\Pi_1(k_1, x_3, t) = \frac{1}{2\pi} \int \overline{p(x_1, x_2, x_3, t) p(x_1 + r_1, x_2, x_3, t)} \mathrm{e}^{-\mathrm{i}k_1 r_1} \mathrm{d}r_1, \tag{3.46}$$

can also be expressed as

$$\Pi_1 = \iint Q_k^* Q_l \Phi_{kl}^{(H)} \mathrm{d}k_2 \mathrm{d}k_3. \tag{3.47}$$

Figure 3.7(*a*) shows profiles of the pressure variance for undistorted turbulence and for an upwelling and a downwelling zone after some distortion has taken place. The first interesting feature is that the pressure variance increases towards the boundary, where it attains a maximum. This is caused by the contributions to the pressure associated with the image velocity field that is necessary to satisfy the blocking boundary condition. Regarding this feature, figure 3.7(*a*) resembles figures 2 and 3 of Kim (1989), where profiles of the root-mean-square pressure are presented. In these figures, the slow pressure also increases towards the boundary, but decreases slightly very near the boundary. The latter effect is probably due to the viscous boundary layer, and cannot be captured in the present inviscid model. The other interesting feature of figure 3.7(*a*) is that the pressure fluctuations associated with an upwelling zone are more intense than those associated with a downwelling zone (this is consistent with the trends of the pressure-strain terms verified in figure 3.5). Hence upwelling zones in shear-free turbulence beneath a free surface should be more important for surface wave generation than downwelling zones.

Figure 3.7(*b*) presents plots of the pressure spectrum predicted by the model, calculated for $c = 1$,

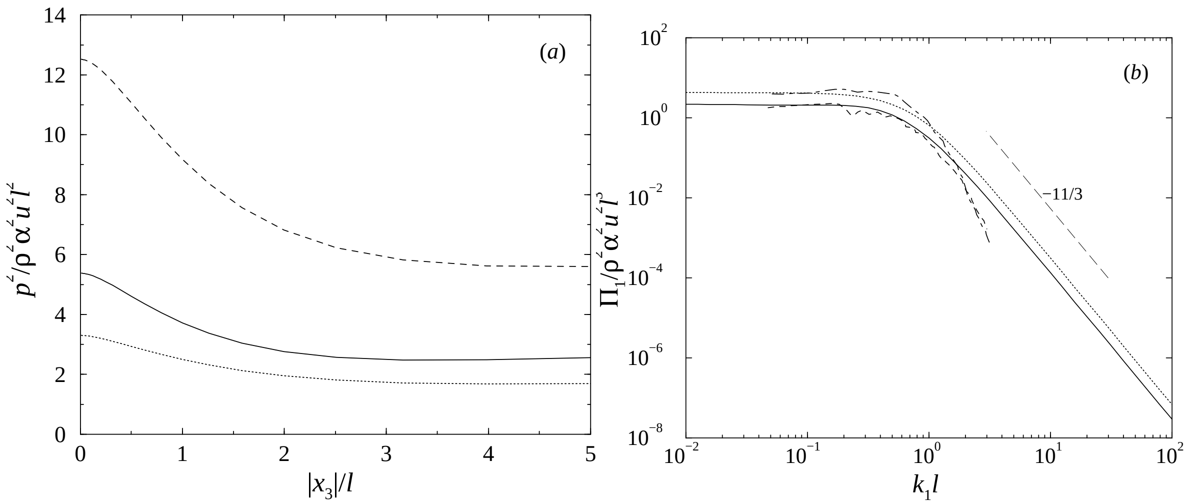

Figure 3.7 (*a*) Profiles of the pressure variance. Solid line: $c = 1$ (undistorted), dotted line: $c = 2$ (downwelling zone), dashed line: $c = 0.5$ (upwelling zone). (*b*) One-dimensional spectrum of the turbulent pressure fluctuations. Solid line: model, far from the boundary, dotted line: model, at $x_3 = 0$, dashed line: data of Kim (1989), far from the boundary, dash-dotted line: data of Kim, at $x_3 = 0$.

at the boundary and far from the boundary, compared with the numerical simulation data of Kim (1989). These data have been renormalised so as to be fitted by the theoretical curves in an optimal way, since it was impossible to find a relation between the normalisation used by Kim and that used in this chapter (the vertical scales of the graphs presented in figure 9 of Kim's paper have no label). Both the theoretical spectra and the data have larger magnitude at the boundary than far from the boundary. All the curves have a plateau and then a breakpoint and a sloping portion with negative slope at higher wavenumbers. The theoretical curves both have a slope of $-11/3$ at high wavenumbers, which is also the slope predicted by RDT for the fast pressure. The curves of the numerical data have a steeper slope at high wavenumbers, especially at the boundary. While this slope is higher than that predicted by the model, it is closer to that predicted by the model than to $-7/3$. On the other hand, this slope is approximately equal to the slope of the spectra of the fast pressure (not shown). This aspect is consistent with the model. At dimensionless wavenumbers $k_1 l$ not much greater than 1, the model results fit the data quite reasonably. One of the possible reasons for the observed discrepancies is that the slow pressure of Kim (1989) may be affected indirectly by the shear in the channel flow, which is not taken into account in the model.

3.5 Conclusions

An inviscid rapid-distortion model has been developed for studying the interaction between the large and small scales in shear-free turbulence beneath a flat boundary. The large-scale turbulence is treated as a steady, axisymmetric straining flow, while the small-scale turbulence is assumed to be homogeneous and initially isotropic far from the boundary. Subject to the condition that the small-scale turbulence has a velocity scale and a strain rate which are much smaller than those imposed by the large-scale flow, the model is linearised and solved in the spectral domain for the small-scale turbulence. Turbulence statistics, such as the Reynolds stresses and various inviscid source terms in the TKE budget are calculated, assuming that the undistorted small-scale turbulence is characterised by a prescribed energy spectrum.

The distortion of the small-scale turbulence by upwelling and downwelling zones existing in the turbulence is addressed by considering straining flows that transport fluid towards the boundary and away from the boundary, respectively. It is found that these two types of flow affect the small-scale turbulence in quite different ways. While the upwelling zone induces an increase of both the tangential and the normal Reynolds stresses of the small-scale turbulence, the downwelling zone induces an increase of the tangential Reynolds stress but a decrease of the normal Reynolds stress, rendering the turbulence almost two-dimensional for sufficiently large distortions. The ratio of the tangential Reynolds stress at the boundary and far from the boundary rises above 1.5 in the upwelling zone, approaching asymptotically 2 for large distortions, while it decreases below 1.5 in the downwelling zone, approaching asymptotically 1 for large distortions.

The TKE budget is analysed in detail. It is found that the evolution of the Reynolds stresses in time is determined primarily by the production term in the Reynolds stress equations in the case of a downwelling zone and for the normal component of the Reynolds stress in the case of an upwelling zone, but the evolution of the tangential component of the Reynolds stress in an upwelling zone is determined by the pressure-strain term. The pressure-strain terms act to move the turbulence towards isotropy everywhere in a downwelling zone, and in the bulk of the flow in an upwelling zone, but away from isotropy near the boundary, in an upwelling zone. The TKE of the small-scale turbulence rises with increasing distortion both in an upwelling zone and in a downwelling zone, and this rise occurs at the same rate at the boundary and far from the boundary, for a flow with a uniform strain, so that the value of the TKE remains equal in those two regions. However, observations show that the TKE tends to be larger near the boundary.

Such behaviour is due to the fact that the strain rate of upwelling and downwelling zones in fact varies with distance from the boundary. The characteristics of the strain field associated with the small-scale turbulence are investigated, and these characteristics are extrapolated to the large-scale flow, assuming scale invariance. It is found that the strain rates are stronger and more anisotropic near the boundary while they remain smaller and isotropic far from the boundary. This causes a larger net effective strain at the boundary and explains the larger TKE levels that are observed there. An approximate model is developed to address this aspect, where the strain rate decays exponentially to zero away from the boundary. The model is only formally valid when the distance over which the strain rate decays is much larger than the integral length scale of the small-scale turbulence, but in practice the Reynolds stress predictions are best when the two scales are equal. This reflects the lack of a scale separation in the turbulence with which the model output is compared.

The pressure field associated with the distortion of the small-scale turbulence by an upwelling or downwelling zone with a uniform strain rate has been calculated. It is found that the pressure variance intensifies at the boundary, due to the image velocity necessary to satisfy the boundary condition, and that the wavenumber spectra of the slow pressure, at the boundary and far from the boundary, exhibit a -11/3 power law behaviour at high wavenumbers, which is the same that RDT would predict for the fast pressure. Both the relative pressure magnitude and the power law behaviour of the spectra showed some qualitative agreement with direct numerical simulation data of the slow pressure by Kim (1989). This suggests that the increase in pressure magnitude at the boundary can be explained simply by the blocking effect, and that the high wavenumber behaviour of the pressure spectra in shear-free turbulence are determined primarily by the interaction between the large scales and the small scales in the turbulence.

3.6 Appendix. Expressions of Q_i

The components of the Q_i vector, introduced in (3.26), are defined as follows:

$$\begin{aligned}
Q_1 = {} & 2\rho\frac{1}{k^2}\left\{\left(\mathrm{e}^{\mathrm{i}k_3x_3} - \mathrm{i}\frac{k_3}{k_{12}}\mathrm{e}^{k_{12}x_3}\right)\left[\left(\frac{k_2k_{02}}{k^2}e_3 + \frac{k_3k_{03}}{k^2}e_2\right)\alpha_1\mathrm{i}k_1 - \frac{k_1k_{02}}{k^2}e_3\alpha_2\mathrm{i}k_2\right.\right. \\
& \left.\left. - \frac{k_1k_{03}}{k^2}e_2\alpha_3\mathrm{i}k_3\right] + k_1k_{03}e_2\frac{1}{2k_{12}}\left(x_3 - \frac{1}{k_{12}}\right)\mathrm{e}^{k_{12}x_3}\left(\alpha_1\frac{k_1^2}{k_{12}} + \alpha_2\frac{k_2^2}{k_{12}} - \alpha_3k_{12}\right)\right\} \\
Q_2 = {} & 2\rho\frac{1}{k^2}\left\{\left(\mathrm{e}^{\mathrm{i}k_3x_3} - \mathrm{i}\frac{k_3}{k_{12}}\mathrm{e}^{k_{12}x_3}\right)\left[\left(\frac{k_3k_{03}}{k^2}e_1 + \frac{k_1k_{01}}{k^2}e_3\right)\alpha_2\mathrm{i}k_2 - \frac{k_2k_{01}}{k^2}e_3\alpha_1\mathrm{i}k_1\right.\right. \\
& \left.\left. - \frac{k_2k_{03}}{k^2}e_1\alpha_3\mathrm{i}k_3\right] + k_2k_{03}e_1\frac{1}{2k_{12}}\left(x_3 - \frac{1}{k_{12}}\right)\mathrm{e}^{k_{12}x_3}\left(\alpha_1\frac{k_1^2}{k_{12}} + \alpha_2\frac{k_2^2}{k_{12}} - \alpha_3k_{12}\right)\right\} \\
Q_3 = {} & 2\rho\frac{1}{k^2}\left\{\left(\mathrm{e}^{\mathrm{i}k_3x_3} - \mathrm{i}\frac{k_3}{k_{12}}\mathrm{e}^{k_{12}x_3}\right)\left[\left(\frac{k_1k_{01}}{k^2}e_2 + \frac{k_2k_{02}}{k^2}e_1\right)\alpha_3\mathrm{i}k_3. - \frac{k_3k_{01}}{k^2}e_2\alpha_1\mathrm{i}k_1\right.\right. \\
& \left. - \frac{k_3k_{02}}{k^2}e_1\alpha_2\mathrm{i}k_2\right] - (k_1k_{01}e_2 + k_2k_{02}e_1)\frac{1}{2k_{12}}\left(x_3 - \frac{1}{k_{12}}\right)\mathrm{e}^{k_{12}x_3} \\
& \left.\left(\alpha_1\frac{k_1^2}{k_{12}} + \alpha_2\frac{k_2^2}{k_{12}} - \alpha_3k_{12}\right)\right\}. \qquad (3.48)
\end{aligned}$$

CHAPTER 4

The initial generation of surface waves by turbulent shear flow

4.1 Introduction

The question of how wind blowing over a water mass generates surface waves has received considerable attention since the classical review of Ursell (1956). Miles (1957) and Phillips (1957) presented the first two systematic treatments of this problem, suggesting two complementary wave generation mechanisms, which are presently widely accepted. Phillips' theory deals with the initiation of the wave field by a resonance of the pressure fluctuations contained in the turbulent air flow with the air-water interface, leading to a linear growth of the waves. Miles' theory addresses the subsequent amplification of the waves by a feedback, shear instability mechanism, and leads to exponential growth. More recently, the sheltering wave growth mechanism first proposed by Jeffreys (1925) was also shown to be important, and quantified in detail by van Duin & Janssen (1992) and Belcher & Hunt (1993). Both the shear instability and the sheltering mechanisms belong to the category of feedback instability mechanisms, leading to exponential growth, and corresponding to source terms in the wave energy budget roughly with the same form. The resonance mechanism and the feedback instability mechanisms have been included in various wave prediction numerical models (Hasselmann, 1988).

Ultimately, all wave growth is caused by travelling stress fluctuations applied at the air-water interface. When waves exist already, part of this stress is associated with the perturbation of the air or water flows by the wave field. This part of the stress is dominant for waves of sufficient amplitude, and has been the subject of the studies of Townsend (1972), Jacobs (1987), van Duin & Janssen (1992) and Belcher & Hunt (1993). At the initial stage of wave growth, the stress fluctuations associated only with the turbulence, which would exist even if the air-water interface was perfectly flat, determine the wave growth. These stresses, in particular their inviscid part (the pressure), are central to the theory developed by Phillips (1957)

Phillips (1957) found that the air-water interface responds to the turbulent pressure fluctuations in the airflow as a forced harmonic oscillator. Among all turbulent pressure fluctuations, the most efficient in generating waves are those advected by the wind at a velocity that matches the phase speed of waves having a similar length scale. These pressure fluctuations can interact resonantly with the air-water interface and make the waves grow fastest. Phillips derived an expression for the wave spectrum resulting from this resonant process as a function of the spectrum of the pressure fluctuations present in the airflow. Subsequent theoretical investigations on this subject resulted in only minor additions to Phillips' theory. Krasitskiy (1980) considered the effect of the viscous stresses on the initiation of surface waves, while Kitaigorodskii & Lumley (1983) and Sazontov & Shagalov (1984) used dimensional analysis to obtain crude definitions for the spectrum of the turbulent pressure fluctuations.

Only a few numerical and experimental studies have focussed on the initiation of surface waves. Gelci *et al.* (1985) and Giovanangeli & Memponteil (1985) used discrete vortices in the airflow to initiate the waves, but did not evaluate the pressure field. Their results were consistent with the existence of resonant wave growth, but were unable to demonstrate the quantitative accuracy of Phillips' theory. Kahma & Donelan (1988) used a homogeneous boundary layer flow similar to that implied in Phillips' (1957) paper, but were forced to assume rather strong approximations about the spatio-temporal structure of the pressure fluctuations, and consequently were very cautious when commenting on the order-of-magnitude agreement achieved between the theory and their data. Recently, the studies of Mellville *et al.* (1998) and Caulliez *et al.* (1998) have led to renewed interest in this subject.

One key problem in validating Phillips' theory using experimental data is related to the difficulty of measuring the turbulent pressure spectrum at the air-water interface in the absence of waves. After a turbulent wind starts blowing over a water mass, the waves generated as a result very soon begin to contaminate the pressure measurements through their feedback on the mean flow (Kahma & Donelan, 1988). On the other hand, the measurement of very small waves, which are those likely to be dominated by Phillips' mechanism, is itself technically complicated and requires great accuracy. These problems might be avoided through the use of numerical modelling, but numerical simulations of flows with a mobile free surface have only become available recently (Borue *et al.*, 1995; Tsai, 1998) due to the complexity of the boundary condition at the interface, which is generally linearised.

For all these reasons, the analytical model of Phillips (1957) remains at present a very useful tool to understand the initial stage of surface wave generation. If an actual wave spectrum is to be calculated from this model, however, some assumption about the form of the turbulent pressure spectrum is required. Kitaigorodskii & Lumley (1983) and Sazontov & Shagalov (1984) assumed in their theoretical studies that the pressure spectrum has a functional form suggested by dimensional analysis and a simplified spatio-temporal structure. However, since the spatio-temporal structure of the turbulence is crucial for determining the growth rate of the waves (Phillips, 1957), it would be preferable to model the pressure spectrum in a way that accounts for the detailed dynamics of the turbulence. That will be done in this chapter by using rapid distortion theory (RDT).

Being a linearised theory of turbulence, RDT is applicable to situations where the distortion of the turbulence by itself is negligible compared with the distortion of the turbulence by external forcings (Batchelor & Proudman, 1954). In the case of shear flows, this condition is satisfied where the shear rate is large compared with the typical frequency of the turbulent eddies, a situation that occurs in boundary layers (Lee *et al.*, 1990). RDT was first applied successfully to boundary layer flow by Townsend (1970), who was able to predict with good accuracy the spatial correlation functions of the turbulent velocity. Subsequently, the theory was generalised by Durbin (1978), Lee & Hunt (1989) and Mann (1994) to shear flows near a flat wall. While the studies of Lee & Hunt and Mann focussed on the turbulent velocity statistics, Durbin's study included calculations of the turbulent pressure fluctuations. Through the linear approximation, RDT enables the turbulent pressure field to be straightforwardly related to the turbulent velocity field, of which more details are known and better measurements can be made. Durbin's (1978) results for the correlations and spectra of the pressure at the boundary showed qualitative agreement with data.

Now, according to Phillips (1957), the turbulent pressure fluctuations at a flat boundary are exactly those responsible for the initiation of surface waves. Therefore, in this chapter, Durbin's (1978) RDT model is coupled with the wave generation model of Phillips (1957) and the complete model thus obtained is used to predict the initial growth of surface waves at an air-water interface. Through RDT, the surface wave spectrum is obtained as a function of the spectrum of the initial turbulent velocity, and the spectrum of the turbulent pressure does not need to be parameterised. Phillips (1957) addressed explicitly only the case where the pressure fluctuations responsible for generating the surface waves originate in the airflow. But the dominance of these over the pressure fluctuations in the water flow is not at all obvious. As noted by Belcher *et al.* (1994), the wind induces a shear current in the water which is characterised by a friction velocity $u_{*w} \approx (\rho_a/\rho_w)^{\frac{1}{2}} u_{*a}$, where ρ_a and ρ_w are, respectively, the densities of air and water, and u_{*a} is the friction velocity in the air. If the turbulent pressure fluctuations in the air and in the water are estimated, respectively, as $\rho_a u_{*a}^2$ and $\rho_w u_{*w}^2$, their magnitude is similar, and both pressure fluctuations should have the same relevance for wave growth.

However, it will be found that the decorrelation time for the turbulent pressure fluctuations in the airflow is much shorter than that in the water flow, making the turbulence in the water, according to the model, more effective for generating waves than turbulence in the air. This is consistent with the recent measurements of Caulliez *et al.* (1998) and Melville *et al.* (1998), which show that the appearance of the first visible waves generally follows the establishment of a turbulent shear current in the water.

The remainder of this chapter is organised as follows. In §4.2, the theoretical model for the initiation of surface waves by a turbulent shear flow will be presented. In §4.3, some statistics of the waves generated will be shown and their behaviour will be discussed in detail. Finally, in §4.4, the main conclusions of this chapter will be reported.

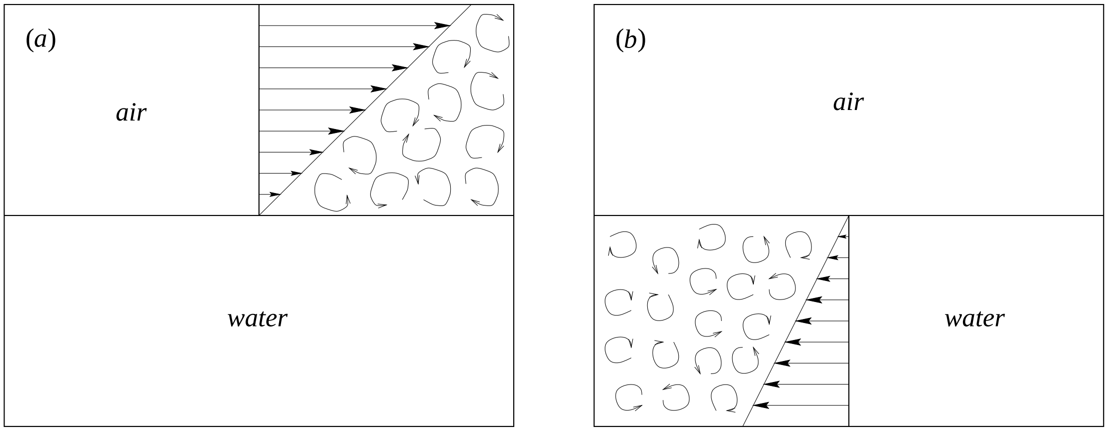

Figure 4.1 Schematic diagram showing the flow considered in (*a*) the uncoupled case and (*b*) the coupled case.

4.2 Theoretical model

Consider a situation where the air and the water are initially at rest and the interface that separates the two fluids coincides with the plane $x_3 = 0$. Assume now that, at $t = 0$, a horizontally homogeneous turbulent wind starts blowing over the water in the region $x_3 > 0$ (this will be called the *uncoupled case*) or that a horizontally homogeneous turbulent current starts flowing beneath the water surface in the region $x_3 < 0$ (this will be called the *coupled case*) (see figure 4.1) The turbulent wind or the turbulent current are associated with turbulent pressure fluctuations that will first initiate and then amplify surface waves at the air-water interface. The characteristics of such waves, when they have relatively low slope, and when the turbulence that generates them is relatively weak, constitute the main topic of this chapter. To tackle this problem, an inviscid RDT model of turbulent shear flow near a flat boundary similar to those used by Durbin (1978), Lee & Hunt (1989) and Mann (1994), is coupled with a wave generation model which essentially follows Phillips (1957).

The case of a mean flow with a linear shear profile of constant shear rate Γ and initially homogeneous and isotropic turbulence far from the boundary is considered for simplicity, since these approximations yielded satisfactory predictions of various turbulent velocity and pressure statistics in the RDT studies mentioned above. In this model, the presence of the boundary is taken into account by simply adding an initially irrotational correction to the velocity field, so that the boundary condition is satisfied (Durbin, 1978). Although this assumption would only be strictly valid if the boundary was suddenly introduced (Hunt & Graham, 1978), it is observed in measurements of shear-free turbulence (which is the type of turbulence that would exist before distortion by a wind or current) that the kinematic correction to the velocity due to the boundary is indeed approximately irrotational (Hunt, 1984*a*). This is inferred, for example, from the fact that the dissipation $\varepsilon \approx \nu\overline{|\omega|^2}$ remains approximately uniform near the boundary, hence the vorticity level $(\overline{|\omega|^2})^{\frac{1}{2}}$ is approximately constant throughout the fluid. However, unlike in the cases treated in chapters 2 and 3, the velocity correction due to the boundary becomes rotational due to the mean shear for $t > 0$.

The conditions necessary for the model to be valid are now quantified and discussed. The total velocity field $\mathcal{U}_i$ consists in this problem of 3 components: a mean component U_i, which corresponds to the mean wind or current, a turbulent component u_i, and a component associated with the orbital motions of the generated surface waves $u_i^{(W)}$. The pressure $\mathcal{P}$ can likewise be decomposed into a mean, a turbulent, and a wave-related part. Hence

$$\begin{aligned} &\mathcal{U}_i = U_i + u_i + u_i^{(W)}, \quad i = 1,2,3. \\ &\mathcal{P} = P + p + p^{(W)}. \end{aligned} \tag{4.1}$$

Consider the momentum equation,

$$\frac{\partial \mathcal{U}_i}{\partial t} + \mathcal{U}_j \frac{\partial \mathcal{U}_i}{\partial x_j} = -\frac{1}{\rho}\frac{\partial \mathcal{P}}{\partial x_i} + \nu \frac{\partial^2 \mathcal{U}_i}{\partial x_k^2}, \tag{4.2}$$

where ρ is the density and ν is the kinematic viscosity of the fluid under consideration. The decomposition (4.1) enables this equation to be expanded into a rather lengthy expression where each term can be separately scaled.

If L and U are the typical length and velocity scales of the mean flow and l and u are the typical length and velocity scales of the turbulence, the wavelength of the waves generated by the turbulence will also scale like l and the associated orbital velocities will be initially small, because they are proportional to the wave slope. Hence, as long as $u_i^{(W)} \leq u_i$, the scaling of the components u_i and $u_i^{(W)}$ may be lumped together. Provided that the Reynolds number $Re = UL/\nu$ is sufficiently large, the viscous terms in (4.2) can be neglected. On the other hand, assuming that $u \ll U$, $u/l \ll U/L$ and $u_i^{(W)} \leq u_i$, the leading order form of the momentum equation, involving only the mean variables, is

$$\frac{\partial U_i}{\partial t} + U_j \frac{\partial U_i}{\partial x_j} = -\frac{1}{\rho}\frac{\partial P}{\partial x_i}. \tag{4.3}$$

This equation may be subtracted from (4.2) and the nonlinear terms involving products of u_i or $u_i^{(W)}$ can be shown to be negligible compared with the remaining terms (Hunt, 1973). In that case, separate linear equations for the turbulent and wave motions can be obtained:

$$\begin{aligned} &\frac{\partial u_i}{\partial t} + U_j \frac{\partial u_i}{\partial x_j} + u_j \frac{\partial U_i}{\partial x_j} = -\frac{1}{\rho}\frac{\partial p}{\partial x_i}, \\ &\frac{\partial u_i^{(W)}}{\partial t} + U_j \frac{\partial u_i^{(W)}}{\partial x_j} + u_j^{(W)} \frac{\partial U_i}{\partial x_j} = -\frac{1}{\rho}\frac{\partial p^{(W)}}{\partial x_i}. \end{aligned} \tag{4.4}$$

Since the mean shear rate is Γ, then $U/L = \Gamma$, and the condition $U/L \gg u/l$ is equivalent to $\Gamma \gg u/l$.

Since the wave orbital velocity is $u_i^{(W)} = O(a_w k_w c_w)$, where c_w is the corresponding phase speed and $a_w k_w$ is the wave slope, the condition $u_i^{(W)} \leq u_i$ implies that $a_w k_w \leq u/c_w$. For a typical value of, for example, $u/c_w = 0.1$, this condition is satisfied for $a_w k_w \leq 0.1$, which is always true initially. When a random wave field is considered instead of a monochromatic surface wave, $a_w k_w$ may be replaced by the mean-square slope of the waves, MSS, and the phase speed c_w may be replaced by the phase speed of the dominant waves $\overline{c}_w$. An additional constraint on the model results from the fact that the shear tends to make the turbulence progressively more anisotropic, and when the degree of anisotropy reached is high enough, the nonlinear processes in the turbulence become more efficient in reducing the anisotropy than estimated above. This places a limit on the total distortion that the turbulence is allowed to undergo, Γt, which can be estimated from the study of Lee *et al.* (1990) to be around 10 (although in fact it depends on the shear rate).

Summarising, the conditions for the proposed model to be valid are

$$\frac{u}{U} \ll 1, \quad \frac{\Gamma l}{u} \gg 1, \quad Re \gg 1, \quad \mathrm{MSS}^{\frac{1}{2}} \frac{\overline{c}_w}{u} \leq 1, \quad \Gamma t \leq 10. \tag{4.5}$$

Of course, as the boundary at $x_3 = 0$ is approached, the scaling of the viscous terms changes and these terms become important at a distance from the boundary of the order of the viscous boundary layer thickness, $\delta \approx (\nu l/U)^{\frac{1}{2}}$ (Sternberg, 1962). For purposes of wave generation, viscosity is important not only for energy dissipation but also because it is associated with viscous stress fluctuations which contribute to wave growth alongside with the pressure fluctuations. The viscous stress fluctuations, which are appreciable only inside the viscous boundary layer can be estimated as

$$\tau_1 = \mu \frac{\partial u_1}{\partial x_3} = O(\rho \nu u/\delta) = O(\rho \nu^{\frac{1}{2}} u U^{\frac{1}{2}} l^{-\frac{1}{2}}). \tag{4.6}$$

while the pressure fluctuations are seen from the first equation of (4.4) and the previous scalings to be $p = O(\rho U u)$. The ratio of the viscous stress and pressure fluctuations is therefore

$$\frac{\tau_1}{p} = O\left(\frac{\rho \nu^{\frac{1}{2}} u U^{\frac{1}{2}} l^{-\frac{1}{2}}}{\rho U u}\right) = O(Re^{-\frac{1}{2}} (L/l)^{\frac{1}{2}}), \tag{4.7}$$

and it can be concluded that the viscous stresses are negligible provided that *Re* is sufficiently large.

The above scaling arguments justify the use of a generic linear and inviscid model for predicting the initial growth of surface waves by turbulence. The reasons why that model can be a combination of Phillips' (1957) wave growth model and Durbin's (1978) model of a turbulent shear flow bounded by a plane wall, are presented next.

According to Phillips' theory, the pressure fluctuations relevant for wave generation at the initial stage are those that exist at a flat air-water interface. Now, a flat free surface and a flat solid wall affect a turbulent flow primarily through blocking and viscous effects. The kinematic blocking effect is the same in the two types of boundary, but the viscous coupling with the adjacent fluid is different (see chapter 2), inducing different velocity profiles. Differences directly due to viscosity are confined to the region inside the viscous boundary layer. In this region, the source terms in the equation that gives the pressure are small (Kim, 1989), so the pressure is transmitted almost unchanged across the viscous boundary layer. Therefore, for the purpose of calculating the pressure field at the boundary, what is important is to model the flow outside the viscous boundary layer correctly (Durbin & Hunt, 1980). The pressure field at the boundary is relatively insensitive to the type of viscous coupling of the fluid with the boundary and can be modelled to a good approximation using the inviscid theory of Durbin (1978), developed for a wall.

As mentioned before, Durbin's model considers a mean flow with a constant shear rate. Because the pressure fluctuations responsible for generating the waves receive their greatest contributions from the flow very near the boundary, where the shear rate is particularly large, this assumption is probably accurate enough for this purpose (Durbin, 1978).

Throughout this chapter, the turbulent shear flow will be assumed to exist in the air but not in the water in the uncoupled case and in the water but not in the air in the coupled case. Since a wind necessarily induces a shear current in the water, real situations are a mixture between the coupled and the uncoupled cases, but for the purpose of comparing the relative importance of the flow in the air and in the water for generating surface waves, an analysis of these idealised cases seems justified.

4.2.1 Wave generation by turbulence

Because of the high density difference between air and water, the wave orbital motions in the air are not dynamically significant and the air-water interface can be treated approximately as a stress-free boundary, apart from the forcing induced by the turbulence (Phillips, 1957). In the uncoupled case, the distortion of the waves by the mean shear in the air is insignificant, and the waves are only affected by the pressure fluctuations induced at the boundary by the interaction of the turbulence with the shear flow. In the coupled case, the mean shear in the water not only interacts with the turbulence, generating the pressure fluctuations that drive the waves, but also distorts the waves, slightly altering their dispersion relation. Since the orbital motion of the waves generated initially does not penetrate to a depth greater than l, these waves are unlikely to be much affected by the variation of shear with depth. Thus, the approximation of a constant shear rate in the coupled case is probably also a good one for the wave distortion.

Both the turbulence and the surface waves are statistically horizontally homogeneous, but not stationary. The turbulence is inhomogeneous in the vertical direction, because of the blocking effect of the boundary. The turbulent velocity and pressure can thus be expressed as Fourier integrals along the horizontal directions, namely

$$\begin{aligned} u_i(\mathbf{x},t) &= \iint \hat{u}_i(k_1,k_2,x_3,t)\mathrm{e}^{\mathrm{i}(k_1x_1+k_2x_2)}\mathrm{d}k_1\mathrm{d}k_2, \\ p(\mathbf{x},t) &= \iint \hat{p}(k_1,k_2,x_3,t)\mathrm{e}^{\mathrm{i}(k_1x_1+k_2x_2)}\mathrm{d}k_1\mathrm{d}k_2, \end{aligned} \tag{4.8}$$

where $\hat{u}_i$ and $\hat{p}$ are time dependent Fourier amplitudes and (k_1,k_2) is the horizontal wavenumber vector. The surface elevation ζ associated with the wave field generated by the turbulence, and the corresponding orbital velocity and pressure can be expressed in a formally similar way,

$$\begin{aligned} \zeta(x_1,x_2,t) &= \iint \hat{\zeta}(k_1,k_2,t)\mathrm{e}^{\mathrm{i}(k_1x_2+k_2x_2)}\mathrm{d}k_1\mathrm{d}k_2, \\ u_i^{(W)}(\mathbf{x},t) &= \iint \hat{u}_i^{(W)}(k_1,k_2,x_3,t)\mathrm{e}^{\mathrm{i}(k_1x_1+k_2x_2)}\mathrm{d}k_1\mathrm{d}k_2, \\ p^{(W)}(\mathbf{x},t) &= \iint \hat{p}^{(W)}(k_1,k_2,x_3,t)\mathrm{e}^{\mathrm{i}(k_1x_1+k_2x_2)}\mathrm{d}k_1\mathrm{d}k_2, \end{aligned} \tag{4.9}$$

where $\hat{\zeta}$, $\hat{u}_i^{(W)}$ and $\hat{p}^{(W)}$ are time dependent Fourier amplitudes.

The linearised kinematic boundary condition at the air-water interface requires that the vertical velocity of the interface equals that of the adjacent fluid. In a frame of reference moving with the mean velocity at the air-water interface, this means

$$u_3(x_3=0) + u_3^{(W)}(x_3=0) = \frac{\partial\zeta}{\partial t}. \tag{4.10}$$

Since this equation is linear it can be satisfied if

$$\begin{aligned} u_3(x_3=0) &= 0, \\ u_3^{(W)}(x_3=0) &= \frac{\partial\zeta}{\partial t}, \end{aligned} \tag{4.11}$$

where the first equation is just the blocking condition for turbulence near a boundary without waves and the second is the well-known kinematic boundary condition for infinitesimal waves in the absence of turbulence. Using (4.9), the second equation of (4.11) can be expressed in terms of the Fourier amplitudes of the surface elevation and the orbital velocity as

$$\hat{u}_3^{(W)}(x_3=0) = \frac{\partial\hat{\zeta}}{\partial t}. \tag{4.12}$$

The dynamical boundary condition is obtained from the momentum equation for the orbital velocity, and is different in the coupled and in the uncoupled cases. The coupled case will be treated first, since it is more complicated, and the uncoupled case will be obtained next as a special case.

4.2.2 Coupled case

In the coupled case, the mean velocity field is given by

$$\begin{aligned} U_i &= \delta_{i1}\Gamma x_3 \quad \text{if} \quad x_3 < 0, \\ U_i &= 0 \quad \text{if} \quad x_3 > 0. \end{aligned} \tag{4.13}$$

The wave motion, which is primarily determined by what happens in the water, is appreciably affected by the shear so, for the mean flow given by (4.13), the second equation of (4.4) takes the form

$$\frac{\partial u_i^{(W)}}{\partial t} + U_1 \frac{\partial u_i^{(W)}}{\partial x_1} + u_3^{(W)} \delta_{i1} \frac{\mathrm{d}U_1}{\mathrm{d}x_3} = -\frac{1}{\rho_w} \frac{\partial p^{(W)}}{\partial x_i}, \tag{4.14}$$

where ρ_w is the density of the water. Taking the curl of this equation, a vorticity equation is obtained. If the vertical component of the vorticity equation is differentiated with respect to x_2 and subtracted from the derivative with respect to x_3 of the spanwise component of the vorticity equation, it follows that

$$\frac{\partial}{\partial t}\left(\frac{\partial^2 u_3^{(W)}}{\partial x_1^2} + \frac{\partial^2 u_3^{(W)}}{\partial x_2^2} + \frac{\partial^2 u_3^{(W)}}{\partial x_3^2}\right) + U_1(x_3)\frac{\partial}{\partial x_1}\left(\frac{\partial^2 u_3^{(W)}}{\partial x_1^2} + \frac{\partial^2 u_3^{(W)}}{\partial x_2^2} + \frac{\partial^2 u_3^{(W)}}{\partial x_3^2}\right) = 0. \tag{4.15}$$

This simplifies the problem considerably, since the only unknown wave quantity becomes the vertical orbital velocity $u_3^{(W)}$. Equation (4.15) has the general solution

$$\nabla^2 u_3^{(W)} = F(x_1 - U_1(x_3)t, x_2, x_3), \tag{4.16}$$

where F is an arbitrary function. If the wave motion is initially irrotational, then $F = 0$ at $t = 0$ and remains zero for all time, so

$$\nabla^2 u_3^{(W)} = 0. \tag{4.17}$$

The dynamical boundary condition is obtained by differentiating (4.14) for $i = 1$ with respect to x_1, adding it to the derivative of (4.14) for $i = 2$ with respect to x_2 and using continuity. This gives an equation for the horizontal divergence,

$$\frac{\partial}{\partial t}\left(\frac{\partial u_3^{(W)}}{\partial x_3}\right)+U_1\frac{\partial}{\partial x_1}\left(\frac{\partial u_3^{(W)}}{\partial x_3}\right)-\frac{\mathrm{d}U_1}{\mathrm{d}x_3}\frac{\partial u_3^{(W)}}{\partial x_1}=\frac{1}{\rho_w}\left(\frac{\partial^2 p^{(W)}}{\partial x_1^2}+\frac{\partial^2 p^{(W)}}{\partial x_2^2}\right), \tag{4.18}$$

which must be imposed at $x_3 = 0$. Since the waves are forced by the turbulence, the pressure at the interface is equal to the turbulent pressure p. In the linearised boundary condition (4.18), $p^{(W)}$ is evaluated at $x_3 = 0$ and results from 3 contributions: a turbulent part, a hydrostatic part, due to the weight of water associated with the surface elevation, and a part due to surface tension, which involves the curvature of the interface, namely

$$p^{(W)} = p+\rho_w\left[g\zeta-\gamma\left(\frac{\partial^2\zeta}{\partial x_1^2}+\frac{\partial^2\zeta}{\partial x_2^2}\right)\right], \tag{4.19}$$

where $g = 9.8\,\mathrm{m\,s^{-2}}$ is the acceleration of gravity and $\gamma = 72.6\times10^{-6}\mathrm{m^3\,s^{-2}}$ is the surface tension, and the curvature term has been linearised. Using this definition and (4.13), the dynamical boundary condition at $x_3 = 0$, (4.18), becomes

$$\frac{\partial}{\partial t}\left(\frac{\partial u_3^{(W)}}{\partial x_3}\right)-\Gamma\frac{\partial u_3^{(W)}}{\partial x_1}-g\left(\frac{\partial^2\zeta}{\partial x_1^2}+\frac{\partial^2\zeta}{\partial x_2^2}\right)+\gamma\left(\frac{\partial^2}{\partial x_1^2}+\frac{\partial^2}{\partial x_2^2}\right)^2\zeta=\frac{1}{\rho_w}\left(\frac{\partial^2 p}{\partial x_1^2}+\frac{\partial^2 p}{\partial x_2^2}\right). \tag{4.20}$$

To further simplify this equation, it is necessary to use (4.8) and (4.9), which will be done next.

Since the wave orbital motion has to decay to zero as the depth increases,

$$u_3^{(W)}(x_3\to-\infty)\to 0, \tag{4.21}$$

hence if $u_3^{(W)}$ satisfies (4.17) and is expressed as in (4.9), the corresponding Fourier amplitude takes the form

$$\hat{u}_3^{(W)} = \hat{u}_3^{(W)}(x_3=0)\mathrm{e}^{k_{12}x_3}, \tag{4.22}$$

where $k_{12} = (k_1^2+k_2^2)^{\frac{1}{2}}$. Inserting the definitions of $u_3^{(W)}$, ζ and p given by (4.8) and (4.9) into (4.20) and using also (4.22), it follows that, at $x_3 = 0$,

$$\frac{\partial\hat{u}_3^{(W)}}{\partial t}-\mathrm{i}\Gamma\frac{k_1}{k_{12}}\hat{u}_3^{(W)}+\left(gk_{12}+\gamma k_{12}^3\right)\hat{\zeta}=-\frac{k_{12}}{\rho_w}\hat{p}. \tag{4.23}$$

Finally, substituting $\hat{u}_3^{(W)}$ according to (4.12), an equation for the Fourier amplitude of the surface elevation results:

$$\frac{\partial^2 \hat{\zeta}}{\partial t^2} - \mathrm{i}\Gamma \frac{k_1}{k_{12}} \frac{\partial \hat{\zeta}}{\partial t} + \sigma_0^2 \hat{\zeta} = -\frac{k_{12}}{\rho_w} \hat{p}(x_3 = 0), \tag{4.24}$$

where

$$\sigma_0^2 = g k_{12} + \gamma k_{12}^3 \tag{4.25}$$

defines the natural angular frequency of surface waves in quiescent water. The solution of (4.24) subject to the boundary conditions $\hat{\zeta}(t=0) = \partial \hat{\zeta}/\partial t(t=0) = 0$ is

$$\hat{\zeta}(k_1, k_2, t) = -\frac{k_{12}}{\rho_w \sigma_1} \int_0^t \hat{p}(k_1, k_2, x_3 = 0, s) \mathrm{e}^{\mathrm{i}\frac{\Gamma k_1}{2k_{12}}(t-s)} \sin[\sigma_1(t-s)] \mathrm{d}s, \tag{4.26}$$

where σ_1 is defined as

$$\sigma_1^2 = \sigma_0^2 \left[1 + \left(\frac{\Gamma k_1}{2 k_{12} \sigma_0} \right)^2 \right]. \tag{4.27}$$

The solution (4.26) is expressed as a time integral involving the pressure fluctuations at the air-water interface. The surface elevation is therefore determined at each instant by the history of these pressure fluctuations since the inception of the turbulent current.

4.2.3 Waves in a laminar shear current

The role of the mean shear in distorting the waves can be understood more clearly by setting the turbulence to zero ($u_i = 0$), so that the turbulent pressure p vanishes. From (4.24), the equation governing the dynamics of the interface becomes

$$\frac{\partial^2 \hat{\zeta}}{\partial t^2} - \mathrm{i}\Gamma \frac{k_1}{k_{12}} \frac{\partial \hat{\zeta}}{\partial t} + \sigma_0^2 \hat{\zeta} = 0, \tag{4.28}$$

and, since this equation has no forcing, the behaviour of the wave variables becomes statistically stationary. The amplitude of the surface elevation $\hat{\zeta}$ can then be considered as the superposition of many components oscillating sinusoidally in time. Consider one of these components,

$$\hat{\zeta}(k_1, k_2, t) = \hat{\hat{\zeta}}(k_1, k_2, \sigma) \mathrm{e}^{-\mathrm{i}\sigma t}, \tag{4.29}$$

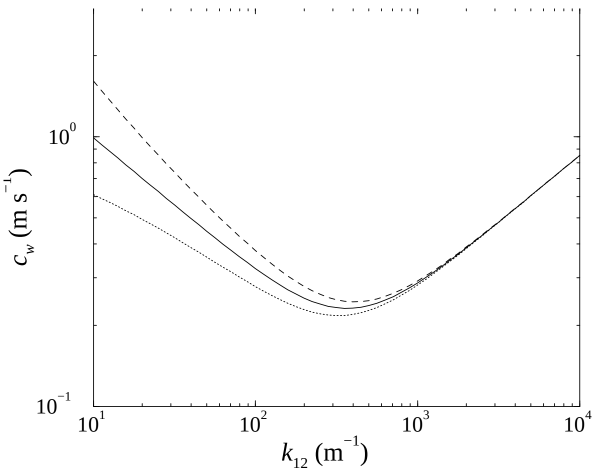

Figure 4.2 Phase speed of gravity-capillary waves in a linear shear current, along the direction of the current, for $\Gamma = 10\text{s}^{-1}$. Solid line: no shear, dotted line: with shear, waves propagating in the direction of the current; dashed line: with shear, waves propagating against the current.

where $\hat{\hat{\zeta}}$ is an amplitude not dependent on time. On substituting (4.29) in (4.28), the amplitude $\hat{\hat{\zeta}}$ cancels out and an equation that gives the dispersion relation of the waves is obtained:

$$\sigma^2 + \Gamma \frac{k_1}{k_{12}} \sigma - \sigma_0^2 = 0, \tag{4.30}$$

where σ is the angular frequency. The solution to (4.30) is

$$\sigma = -\Gamma \frac{k_1}{2k_{12}} \pm \left(\left(\Gamma \frac{k_1}{2k_{12}} \right)^2 + \sigma_0^2 \right)^{\frac{1}{2}} \tag{4.31}$$

and shows that the wave propagation is made anisotropic by the shear, with a maximum in anisotropy occurring along the streamwise (x_1) direction. In that direction, the phase velocity is $c_w = \sigma/k_{12}$ and given by

$$c_w = -\frac{\Gamma}{2k_{12}} \pm \left(\left(\frac{\Gamma}{2k_{12}} \right)^2 + c_0^2 \right)^{\frac{1}{2}}, \tag{4.32}$$

where $c_0 = \sigma_0/k_{12}$. This solution is well-known and was found, for example, as a leading order approximation in the treatment of waves on shear currents by Shrira (1993).

The effect of shear is to decrease the phase speed of waves propagating in the positive x_1 direction and to increase the phase speed of waves propagating in the negative direction. Equation (4.32) shows that this effect is especially important at low wavenumbers (see figure 4.2). Since the waves with the lowest wavenumbers (highest wavelengths) are those whose orbital motions penetrate more deeply, physically it is as if the fluid below the surface is 'carrying' the longer waves with its own motion (which is in the negative x_1 direction), while the shorter waves are only affected by the motion very near the surface, which is approximately zero. As (4.31) shows, this effect decreases like $\cos\theta = \frac{k_1}{k_{12}}$ as the direction of propagation θ changes from 0 (parallel to the current) to $\pi/2$ (perpendicular to the current). For waves perpendicular to the current, the mean shear does not affect the dispersion relation.

Since the existence of shear in the water changes the dispersion relation of freely propagating surface waves, it affects the resonance condition in the wave generation process by slightly modifying the velocity at which turbulent pressure fluctuations of a given scale have to be advected for resonant growth to occur.

4.2.4 Uncoupled case

For an interface forced by pressure fluctuations driven by a turbulent shear flow in the air and unsheared water flow, the mean velocity field takes the form

$$\begin{aligned} U_i &= \delta_{i1}\Gamma x_3 \quad \text{if} \quad x_3 > 0, \\ U_i &= 0 \quad \text{if} \quad x_3 < 0. \end{aligned} \tag{4.33}$$

In that case, the wave motion is not appreciably distorted by the mean shear (which has an effect $O(\rho_a/\rho_w)$ weaker than in the coupled case) and so, from the point of view of the waves, it is as if there was no shear at all. Then, the equation that the amplitude of the surface elevation must satisfy is obtained by simply setting $\Gamma = 0$ in (4.24), which gives

$$\frac{\partial^2\hat{\zeta}}{\partial t^2} + \sigma_0^2\hat{\zeta} = -\frac{k_{12}}{\rho_w}\hat{p}(x_3 = 0). \tag{4.34}$$

This is equivalent to Phillips' (1957) equation (2.12). The solution of (4.34) for an initially unperturbed interface, where $\hat{\zeta} = \partial\hat{\zeta}/\partial t = 0$ at $t = 0$, is

$$\hat{\zeta}(k_1, k_2, t) = -\frac{k_{12}}{\rho_w\sigma_0}\int_0^t \hat{p}(k_1, k_2, x_3 = 0, s)\sin[\sigma_0(t - s)]\mathrm{d}s. \tag{4.35}$$

In order to proceed further from (4.26) or (4.35), it is necessary to specify the turbulent pressure field. In the RDT approximation, the turbulent pressure fluctuations are linearly related to the turbulent velocity fluctuations. Since the pressure at a given point (and therefore also at the boundary) is determined by contributions of the velocity field coming from the whole domain (due to the elliptic nature of equation that gives the pressure), it is convenient to specify first the turbulent velocity field and only then calculate expressions for the pressure. This will be done in the next two subsections.

4.2.5 Turbulent shear flow near a boundary

The turbulent velocity field will now be determined in the RDT approximation, following Durbin (1978). A situation where the turbulence is below the boundary (coupled case), will be considered next as an example, but the treatment is analogous if the turbulence is above the boundary. Consider the first equation of (4.4) which, for a mean shear flow $U_i = \delta_{i1}\Gamma x_3$, can be written

$$\frac{\partial u_i}{\partial t} + U_1 \frac{\partial u_i}{\partial x_1} + u_3 \delta_{i1} \frac{dU_1}{dx_3} = -\frac{1}{\rho}\frac{\partial p}{\partial x_i}. \tag{4.36}$$

Taking the curl of this equation, a vorticity equation is obtained. If the vertical component of the vorticity equation is differentiated with respect to x_2 and subtracted from the derivative with respect to x_3 of the spanwise component of the vorticity equation, as was done in §4.2.2 for the wave orbital velocity, then an equation for u_3 formally analogous to (4.15) is obtained:

$$\frac{\partial}{\partial t}\left(\frac{\partial^2 u_3}{\partial x_1^2} + \frac{\partial^2 u_3}{\partial x_2^2} + \frac{\partial^2 u_3}{\partial x_3^2}\right) + U_1(x_3)\frac{\partial}{\partial x_1}\left(\frac{\partial^2 u_3}{\partial x_1^2} + \frac{\partial^2 u_3}{\partial x_2^2} + \frac{\partial^2 u_3}{\partial x_3^2}\right) = 0. \tag{4.37}$$

That equation has the solution

$$\nabla^2 u_3 = G(x_1 - U_1(x_3)t, x_2, x_3), \tag{4.38}$$

where G is an arbitrary function. But the similarities between the wave and turbulent motions end at this point. While the wave velocity is initially irrotational, the turbulent velocity is by definition rotational, so the function G is not zero and is defined instead by the initial condition (cf. Durbin, 1978)

$$G(x_1, x_2, x_3) = \nabla^2 u_3(x_1, x_2, x_3, t = 0). \tag{4.39}$$

The boundary and initial conditions of the problem become much simplified if it is recalled now that the turbulence far from the boundary is assumed to be homogeneous (Durbin, 1978). Since the shear rate Γ is constant, the turbulence remains homogeneous at all times. Thus, the turbulent velocity far from the boundary can be expressed as a three-dimensional Fourier integral,

$$u_i^{(H)}(\mathbf{x}, t) = \iiint \hat{u}_i^{(H)}(\mathbf{k}, t) \mathrm{e}^{\mathrm{i}\mathbf{k}\cdot\mathbf{x}} \mathrm{d}k_1 \mathrm{d}k_2 \mathrm{d}k_3, \tag{4.40}$$

where $\hat{u}_i^{(H)}$ is the Fourier amplitude, and the wavenumber vector $\mathbf{k} = (k_1, k_2, k_3)$ is time dependent due to the shear, which makes the turbulence anisotropic over time. Towards the boundary, the turbulence is made inhomogeneous in the x_3 direction by the blocking effect. This effect can be taken into account by adding to $u_i^{(H)}$ a correction which enables the flow to satisfy the boundary condition at the interface (first equation of (4.11)). The other boundary condition states that this correction decays to zero far from the boundary, as $x_3 \to -\infty$. Following Durbin (1978), the initial condition states that the correction is initially irrotational. The solution to the problem at $t = 0$ is then identical to that corresponding to shear-free turbulence near a wall (Hunt & Graham, 1978). In particular, the vertical velocity component takes the form

$$u_3(\mathbf{x}, t = 0) = \iiint \hat{u}_3^{(H)}(\mathbf{k}_0, t = 0) \left(\mathrm{e}^{\mathrm{i}k_{03}x_3} - \mathrm{e}^{k_{012}x_3} \right) \mathrm{e}^{\mathrm{i}(k_{01}x + k_{02}y)} \mathrm{d}k_{01}\mathrm{d}k_{02}\mathrm{d}k_{03}, \tag{4.41}$$

where $\mathbf{k}_0 = (k_{01}, k_{02}, k_{03}) = \mathbf{k}(t = 0)$ is the initial wavenumber vector and $k_{012} = (k_{01}^2 + k_{02})^{\frac{1}{2}}$. This expression can be introduced in (4.39) to obtain the form of the function $G(x_1, x_2, x_3)$. Replacing the argument x_1 of that function by $x_1 - U_1(x_3)t$ and substituting the resulting expression in (4.38) yields an equation for u_3 in the general, time-dependent case. This equation is again subject to the same boundary conditions as at $t = 0$.

It is found that the horizontal components of the wavenumber vector are not affected by the mean shear, and therefore $k_1(t) = k_{01}$, $k_2(t) = k_{02}$ and $k_{12} = k_{012}$, but the vertical component has a linear dependence on time (Townsend, 1976): $k_3(t) = k_{03} - k_{01}\Gamma t$. For simplicity, the shorter notation k_1, k_2 and k_{12} will be adopted henceforth instead of k_{01}, k_{02} and k_{012}. Accordingly, the time-dependent solution for the vertical velocity component is (Durbin, 1978)

$$u_3(\mathbf{x}, t) = \iiint \frac{k_0^2}{k^2} \hat{u}_3^{(H)}(\mathbf{k}_0, t = 0) \left(\mathrm{e}^{\mathrm{i}k_3x_3} - \mathrm{e}^{k_{12}x_3} \right) \mathrm{e}^{\mathrm{i}(k_1x_1 + k_2x_2)} \mathrm{d}k_1\mathrm{d}k_2\mathrm{d}k_3, \tag{4.42}$$

where $k_0 = (k_1^2 + k_2^2 + k_{03}^2)^{\frac{1}{2}}$ and $k = (k_1^2 + k_2^2 + k_3^2(t))^{\frac{1}{2}}$. The form of the horizontal velocity components u_1 and u_2 is rather more involved and has been obtained, for example, by Lee & Hunt (1989) and Mann (1994). However, for the problem of surface wave generation, only the pressure statistics are of interest, and in the RDT approximation these only depend on the vertical component of the turbulent velocity, as will be seen next.

4.2.6 Pressure in the RDT approximation

In §4.2.2 and §4.2.4, the wave amplitude was determined as a function of the amplitude of the turbulent pressure fluctuations at the air-water interface. The turbulent pressure field will now be related to the turbulent velocity field calculated in §4.2.5 making use of the simplifying assumptions of RDT. Again, the coupled case will be considered as an example, but the treatment for the uncoupled case is entirely analogous.

Taking the divergence of (4.36), it follows that

$$\nabla^2 p = -2\rho \frac{\mathrm{d}U_1}{\mathrm{d}x_3}\frac{\partial u_3}{\partial x_1}. \tag{4.43}$$

To obtain the turbulent pressure field everywhere, this equation has to be solved, subject to the boundary conditions

$$p(x_3 \to -\infty) = p^{(H)} \quad \text{and} \quad \frac{\partial p}{\partial x_3}(x_3 = 0) = 0, \tag{4.44}$$

where $p^{(H)}(\mathbf{x},t)$ is the pressure field associated with the turbulence far from the boundary, and where the boundary condition at $x_3 = 0$ was obtained from the vertical component of the momentum equation (4.36), taking into account the first equation of (4.11) (blocking condition). $p^{(H)}$ is defined as the solution of

$$\nabla^2 p^{(H)} = -2\rho \frac{\mathrm{d}U_1}{\mathrm{d}x_3}\frac{\partial u_3^{(H)}}{\partial x_1}. \tag{4.45}$$

Using (4.8), the Poisson equation (4.43) may be simplified, becoming an ordinary differential equation for the Fourier amplitudes of the pressure and velocity:

$$\frac{\partial^2 \hat{p}}{\partial x_3^2} - k_{12}^2 \hat{p} = -2\rho\Gamma \mathrm{i} k_1 \hat{u}_3. \tag{4.46}$$

The solution for the turbulent velocity (4.42), together with (4.8), may then be used, and the boundary conditions (4.44) applied.

After some algebra, the solution for the Fourier amplitude of the pressure is found to be

$$\hat{p} = 2\mathrm{i}\rho\Gamma \int k_1 \frac{k_0^2}{k^2}\hat{u}_3^{(H)} \left[\frac{1}{k^2}\mathrm{e}^{\mathrm{i}k_3x_3} + \left(\frac{x_3}{2k_{12}} - \frac{1}{2k_{12}^2} - \frac{\mathrm{i}k_3}{k_{12}k^2}\right)\mathrm{e}^{k_{12}x_3}\right]\mathrm{d}k_3, \tag{4.47}$$

which at the boundary takes the simplified form

$$\hat{p}(k_1,k_2,x_3=0,t) = \mathrm{i}\rho\Gamma\frac{k_1}{k_{12}^2}\int \frac{k_0^2}{(\mathrm{i}k_3+k_{12})^2}\hat{u}_3^{(H)}(\mathbf{k}_0, t=0)\mathrm{d}k_3, \tag{4.48}$$

as obtained by Durbin (1978). This form is independent of whether the turbulent fluid is above or below the boundary, and so gives the pressure fluctuations induced by the turbulence in the coupled or in the uncoupled case, if the density in (4.48) is replaced by the density of water or by the density of air, respectively.

Since the turbulent pressure that drives the waves is now known, it remains to substitute the pressure amplitude (4.48) in (4.26) and (4.35) to obtain the resulting wave field as a function of the turbulent velocity field. It is then possible to calculate statistics of the waves.

4.2.7 Statistics of the flow

Like turbulence itself, the waves generated by a turbulent shear flow must be characterised by a range of statistics, namely covariances, spectra and variances. Previous RDT studies have concentrated on the statistics of the turbulent velocity and pressure fields. This chapter focusses primarily on the statistics of the wave field induced by the turbulence.

First of all, it should be noted that, since the model is linear, the turbulent velocity and pressure, and the surface elevation at any point in space and at any time can always be related to the 'unperturbed' or 'undistorted' turbulence which is assumed to exist far from the boundary at the initial time. Hence,

$$\begin{aligned} u_i(\mathbf{x},t) &= \iiint M_{ij}(\mathbf{k},x_3,t)\hat{u}_j^{(H)}(\mathbf{k}_0,t=0)\mathrm{e}^{\mathrm{i}(k_1x_1+k_2x_2)}\mathrm{d}k_1\mathrm{d}k_2\mathrm{d}k_3, \\ p(\mathbf{x},t) &= \iiint Q_j(\mathbf{k},x_3,t)\hat{u}_j^{(H)}(\mathbf{k}_0,t=0)\mathrm{e}^{\mathrm{i}(k_1x_1+k_2x_2)}\mathrm{d}k_1\mathrm{d}k_2\mathrm{d}k_3, \\ \zeta(x_1,x_2,t) &= \iiint S_j(\mathbf{k},x_3,t)\hat{u}_j^{(H)}(\mathbf{k}_0,t=0)\mathrm{e}^{\mathrm{i}(k_1x_1+k_2x_2)}\mathrm{d}k_1\mathrm{d}k_2\mathrm{d}k_3, \end{aligned} \tag{4.49}$$

where the matrix M_{ij} and the vectors Q_j and S_j are given in appendix 1 (§4.5) for the flow under consideration. The matrix M_{ij} may be extracted from the expressions contained in the study of Mann (1994), where, however, there is a minor mistake which has been corrected in appendix 1. The vector Q_j may be obtained from the expressions in Durbin's (1978) study or (4.47) of this chapter. Finally, S_j can be determined after substituting (4.48) into (4.26) or (4.35).

Since the boundary at $x_3 = 0$ makes the turbulence inhomogeneous in the x_3 direction, it only makes sense to calculate spatial covariances and spectra along the x_1 and x_2 directions. The two-dimensional spectra corresponding to the variables in (4.49) are defined as

$$\begin{aligned} \Theta_{ij}(k_1,k_2,x_3,t) &= \frac{1}{(2\pi)^2}\iint \overline{u_i(\mathbf{x},t)u_j(x_1+r_1,x_2+r_2,x_3,t)}\mathrm{e}^{-\mathrm{i}(k_1r_1+k_2r_2)}\mathrm{d}r_1\mathrm{d}r_2, \\ \Pi(k_1,k_2,x_3,t) &= \frac{1}{(2\pi)^2}\iint \overline{p(\mathbf{x},t)p(x_1+r_1,x_2+r_2,x_3,t)}\mathrm{e}^{-\mathrm{i}(k_1r_1+k_2r_2)}\mathrm{d}r_1\mathrm{d}r_2, \\ \Psi(k_1,k_2,t) &= \frac{1}{(2\pi)^2}\iint \overline{\zeta(x_1,x_2,t)\zeta(x_1+r_1,x_2+r_2,t)}\mathrm{e}^{-\mathrm{i}(k_1r_1+k_2r_2)}\mathrm{d}r_1\mathrm{d}r_2, \end{aligned} \tag{4.50}$$

where the overbar denotes ensemble averaging, and where Θ_{ij} is the velocity spectrum, Π is the pressure spectrum and Ψ is the surface elevation spectrum. Taking into account (4.49), these spectra can be expressed as functions of the corresponding undistorted Fourier amplitudes in the following simplified way (cf. Hunt, 1973),

$$\begin{aligned}\Theta_{ij}(k_1,k_2,x_3,t) &= \int M_{ik}M_{jm}\Phi_{km}^{(H)}(\mathbf{k}_0)\mathrm{d}k_3,\\ \Pi(k_1,k_2,x_3,t) &= \int Q_k Q_m \Phi_{km}^{(H)}(\mathbf{k}_0)\mathrm{d}k_3,\\ \Psi(k_1,k_2,t) &= \int S_k S_m \Phi_{km}^{(H)}(\mathbf{k}_0)\mathrm{d}k_3,\end{aligned} \tag{4.51}$$

where the three-dimensional wavenumber spectrum of the undistorted turbulent velocity $\Phi_{km}^{(H)}$ can be related to the corresponding Fourier amplitude using

$$\overline{\hat{u}_i^{(H)}(\mathbf{k}_0)\hat{u}_j^{(H)}(\mathbf{k}_0')} = \Phi_{ij}^{(H)}(\mathbf{k}_0)\delta(\mathbf{k}_0-\mathbf{k}_0'). \tag{4.52}$$

If the undistorted turbulence is isotropic, this spectrum takes the form

$$\Phi_{ij}^{(H)}(\mathbf{k}_0) = \left(\delta_{ij} - \frac{k_{0i}k_{0j}}{k_0^2}\right)\frac{E(k_0)}{4\pi k_0^2}, \tag{4.53}$$

where $E(k_0)$ is the energy spectrum of the undistorted turbulence. Following Hunt & Graham (1978) and Durbin (1978), the well known von Kármán form of the energy spectrum, which has proved to be appropriate for inviscid calculations, is adopted here,

$$E(k_0) = u^2 l \frac{g_2(k_0 l)^4}{(g_1+(k_0 l)^2)^{\frac{17}{6}}}, \tag{4.54}$$

where $g_1 = 0.558$ and $g_2 = 1.196$ are dimensionless constants. u and l, the velocity and length scales of the turbulence used in (4.54), are defined, respectively, as the initial root-mean-square (RMS) turbulent velocity and integral length scale far from the boundary.

The two-dimensional spectra of (4.51) are functions of the horizontal wavenumbers k_1 and k_2. To obtain one-dimensional spectra, the expressions of these spectra have to be integrated over k_1 or k_2. To obtain covariances or variances of the velocity, pressure, or surface elevation, the expressions must be integrated simultaneously over k_1 and k_2.

Of particular interest in this chapter are the surface elevation statistics, which have a relatively simple explicit form, due to the fact that they only depend on the vertical component of the turbulent velocity. From (4.51) and appendix 1, the surface wave spectrum in the uncoupled case may be written

$$\Psi(k_1,k_2,t) = \frac{1}{4\pi}\frac{\rho_a^2}{\rho_w^2}\Gamma^2\frac{k_1^2}{\sigma_0^2}\int E(k_0)\left|\int_0^t \frac{\sin(\sigma_0(t-s))}{(-\mathrm{i}k_3(s)+k_{12})^2}\mathrm{d}s\right|^2 dk_{03}, \tag{4.55}$$

while in the coupled case, it has the form

$$\Psi(k_1,k_2,t) = \frac{1}{4\pi}\Gamma^2\frac{k_1^2}{\sigma_1^2}\int E(k_0)\left|\int_0^t \frac{\mathrm{e}^{\mathrm{i}\frac{\Gamma k_1}{2k_{12}}s}}{(-\mathrm{i}k_3(s)+k_{12})^2}\sin(\sigma_1(t-s))\mathrm{d}s\right|^2 dk_{03}. \tag{4.56}$$

The expressions between brackets in (4.55) and (4.56) can be expanded into an oscillating part and a growing part (see appendix 2, §4.6). The oscillating part, although formally accurate, corresponds to the addition of an oscillatory function of time and wavenumber to the spectra, which introduces undesired noise in the calculated statistics. For that reason, in the following numerical calculations, only the growing part of the solution will be considered. This is approximately equivalent to time averaging the spectra over an interval sufficiently long to filter the oscillations, but shorter than the time scale relevant for wave growth. It is also found that the time integrals in the expressions between brackets can be written explicitly in terms of exponential integral functions of a complex argument. The final form taken by these expressions is rather lengthy, so it has been left for appendix 3 (§4.7).

It can be seen from (4.55) and (4.56) that the integrals between brackets are somewhat akin to a Fourier transformation in the time domain. Over a sufficiently long interval, the factors $\sin(\sigma_0(t-s))$ and $\exp\left[(\mathrm{i}\Gamma k_1/2k_{12})s\right]\sin(\sigma_1(t-s))$ select frequencies of the forcing which are close to the resonance frequency, thus making the surface wave spectrum grow preferentially for the combination of frequency and wavenumber that corresponds to freely-propagating waves. The time-dependent expression in the denominator, however, increases in time and limits this growth.

4.2.8 Dimensionless parameters

In order to avoid redundancy when testing the model, it is convenient to reduce the number of input variables of the model to a minimum. This can be done by making the expressions of the surface wave spectrum dimensionless. $\Psi(k_1,k_2,t)$ has dimensions of $length^4$, hence (4.55) and (4.56) should be divided by l^4 to become dimensionless. The result is

$$\Psi'(k'_1,k'_2,t') = \frac{1}{4\pi}\frac{\rho_a^2}{\rho_w^2}\frac{k_1'^2}{\sigma_0'^2}\int E'(k'_0)\left|\int_0^{t'} \frac{\sin(\sigma'_0/\Gamma'(t'-s))}{(k'_{12}-\mathrm{i}k'_3(s))^2}\mathrm{d}s\right|^2 \mathrm{d}k'_{03} \tag{4.57}$$

in the uncoupled case and

$$\Psi'(k'_1,k'_2,t') = \frac{1}{4\pi}\frac{k_1'^2}{\sigma_1'^2}\int E'(k'_0)\left|\int_0^{t'} \frac{\mathrm{e}^{\mathrm{i}\frac{k'_1}{2k'_{12}}s}}{(k'_{12}-\mathrm{i}k'_3(s))^2}\sin(\sigma'_1/\Gamma'(t'-s))\mathrm{d}s\right|^2 \mathrm{d}k'_{03} \tag{4.58}$$

in the coupled case, where the primed variables which appear in both equations have been made dimensionless using l and u (e.g. $\Gamma' = \Gamma l/u$), except for the dimensionless time, which is defined as $t' = \Gamma t$. It can be seen from (4.57) and (4.58) that, apart from k_1' and k_2', the dimensionless surface wave spectrum depends on σ_1', t' and Γ' in the coupled case and σ_0', t', Γ' and ρ_a/ρ_w in the uncoupled case. The density ratio considered will always be that of the air to the water, so ρ_a/ρ_w can be taken as a constant. On the other hand, using the definition of σ_1 (4.27), it follows that

$$\sigma_1'^2 = \sigma_0'^2 \left[1 + \left(\frac{\Gamma' k_1'}{2k_{12}'\sigma_0'} \right)^2 \right], \tag{4.59}$$

hence σ_1' is a function of σ_0' and Γ' (apart from k_1' and k_2'), and the parameters relevant for the coupled case are the same as those relevant for the uncoupled case.

Now, from (4.25) it can be deduced that

$$\sigma_0'^2 = Fr^{-2} k_{12}' + We^{-1} k_{12}'^3, \tag{4.60}$$

where

$$Fr = \frac{u}{(gl)^{\frac{1}{2}}}, \quad We = \frac{lu^2}{\gamma} \tag{4.61}$$

are the Froude number and the Weber number, respectively. So the dimensionless natural frequency σ_0' depends on Fr, We and k_{12}'. From all these results, it can be concluded that the dimensionless parameters controlling Ψ' are Fr, We, t' and Γ'. As (4.60) shows, Fr and We only enter in the equation for Ψ' indirectly, through σ_0'. The Froude and the Weber numbers estimate the relative importance of the forcing at the interface due to the turbulence and the restoring forces due to gravity and surface tension, respectively. The larger these two numbers are, the easier it becomes for the interface to be deformed by the turbulence (see chapter 1).

Since g and γ are fixed physical constants, definition (4.61) implies that Fr and We are uniquely related to l and u and either pair of variables may be used interchangeably. As in Brocchini & Peregrine (2000*a*), l and u will be adopted instead of Fr and We as direct input parameters to the present surface wave model, because physically plausible values are more readily found for these dimensional quantities.

4.3 Results

Results will now be presented for the coupled and uncoupled cases. In the uncoupled case, the values of the turbulence intensity and the shear rate for the flow in the air are higher than the corresponding values in the water for the coupled case. This is done in a way that guarantees a similar magnitude for the pressure fluctuations in both cases. The scaling of the pressure fluctuations presented in §4.1 in fact suggests that this approximation may be reasonably realistic in air-water coupled flows. The idea is to show how the temporal structure of the turbulent pressure (not only its intensity) is important in the evolution of the wave field. As mentioned above, the input parameters are l, u, t' and Γ'. The relation between these parameters that ensures a similar pressure intensity in the coupled and in the uncoupled cases will be defined next.

The pressure variance at the interface induced by a turbulent shear flow existing in the air or in the water can be obtained by integrating the two-dimensional pressure spectrum Π in (4.51) over k_1 and k_2, making use of the expressions for Q_i available in appendix 1 (§4.5) and also (4.53). After some algebra, and using the dimensionless variables introduced in (4.57) and (4.58), the dimensionless pressure, which is defined as

$$p' = \frac{p}{\rho \Gamma u l}, \tag{4.62}$$

is found to have the variance

$$\overline{p'^2}(x_3' = 0, t') = \frac{1}{4\pi} \iiint \frac{k_1'^2}{k_{12}'^2} \frac{1}{k'^4(t')} E'(k_0') \mathrm{d}k_1' \mathrm{d}k_2' \mathrm{d}k_3'. \tag{4.63}$$

By inspection of (4.63), it is clear that the dimensionless pressure variance at the interface is only a function of t'. Hence, for a given t', the dimensional pressure variance is proportional to $(\rho \Gamma u l)^2$. This reasoning is valid both for turbulence in the water (coupled case) and for turbulence in the air (uncoupled case). So, in order to have pressure fluctuations of a similar magnitude in the coupled and uncoupled cases, the product $\Gamma u l$ has to be greater in the air than in the water by a factor ρ_w/ρ_a. In the following treatment, $\rho_w/\rho_a = 10^3$ is taken and, to satisfy the above constraint in a very simple way, Γ, u and l are each assumed to be greater in the air than in the water by a factor of 10. Although rough, this estimate is in clear qualitative agreement with experiment: it is well known that shear is more intense and turbulence more vigorous and characterised by larger eddies in the atmosphere than in the ocean (Donelan, 1990).

4.3.1 Mean square slope of the waves

The mean square slope (MSS) of the surface waves generated at the air-water interface will be determined first, because it gives a gross measure of the size of the waves. It should be emphasised that, since both gravity and surface tension were taken into account in the treatment of §4.2, the surface waves under consideration are gravity-capillary waves. The MSS can be found by integrating the surface elevation spectrum multiplied by k_{12}^2 over all wavenumbers:

$$\text{MSS} = \overline{\left(\frac{\partial \zeta}{\partial x_1}\right)^2} + \overline{\left(\frac{\partial \zeta}{\partial x_2}\right)^2} = \iint k_{12}^2 \Psi(k_1, k_2, t) \mathrm{d}k_1 \mathrm{d}k_2. \tag{4.64}$$

Figure 4.3 shows the evolution of the MSS of the surface waves predicted by the model for the coupled case as a function of dimensionless time t'. In figure 4.3(*a*), the sensitivity of the MSS to Γ', keeping l and u constant, is tested. It can be seen that the wave growth is faster and more sustained for higher values of Γ'. This was to be expected since, as shown in the previous subsection, the pressure fluctuations that generate the waves are proportional to Γ.

In figure 4.3(*b*), the MSS is plotted for different values of u, keeping Γ' and l constant. It is observed that the waves grow faster and for a longer time when u is higher. This is not surprising either, since the pressure fluctuations that drive the waves are proportional to u. There is an indirect effect which further promotes wave growth: when Γ' is kept constant and u is increased, Γ also increases proportionally. Because of this, the MSS is very sensitive to u.

Finally, figure 4.3(*c*) displays the variation of the MSS growth with l, keeping Γ' and u constant. It can be seen that the waves grow faster for lower values of l. While the pressure fluctuations that generate the waves are proportional to l, Γ decreases as l increases when Γ' is kept constant and the two effects cancel. However, since the dominant wavelength of the waves is approximately equal to the length scale of the turbulence l, waves of a given amplitude tend to be steeper for smaller l. Other qualitative aspects of these curves will be discussed in §4.3.2.

Quantitatively, for example when $l = 5\text{cm}$, $u = 5\text{cm}\,\text{s}^{-1}$ and $\Gamma' = 10$ (i.e. $\Gamma = 10\text{s}^{-1}$), the MSS takes a value of 0.002 at $t' = 3$. This means that the root-mean-square (RMS) slope takes a value of ≈ 0.05 at 0.3 s. Having in mind the value of l, this corresponds to waves of ≈ 2.5mm amplitude, which are necessarily visible. The chief criterion used in choosing the values of Γ', u and l used in figure 4.3 has been the ability of the model to produce waves with a RMS slope of $O(0.1)$ in the time interval considered. The values adopted for u, l and Γ' are also found to be of the same order of magnitude as those which can be inferred by inspection from the laboratory data of Melville *et al.* (1998), or Magnaudet & Thais (1995) (slightly higher than observed in the case of u). The value of t', on the other hand, is within the range of total distortions used by Townsend (1976) or Lee *et al.*

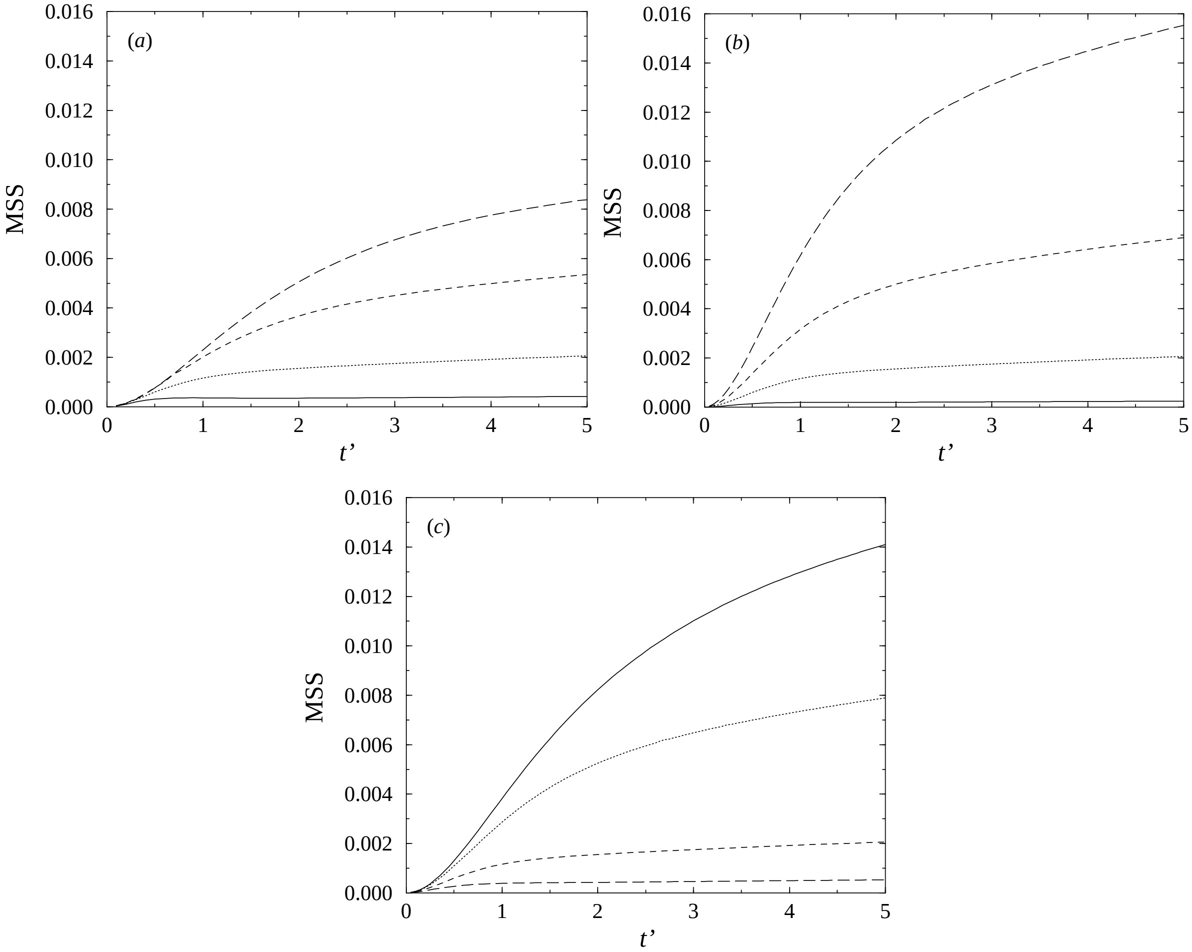

Figure 4.3 Time evolution of mean square slope of the waves in the coupled case. (*a*) $l = 5$cm, $u = 5\text{cm}\,\text{s}^{-1}$. Solid line: $\Gamma' = 5$, dotted line: $\Gamma' = 10$, dashed line: $\Gamma' = 20$, long-dashed line: $\Gamma' = 50$. (*b*) $l = 5$cm, $\Gamma' = 10$. Solid line: $u = 3\text{cm}\,\text{s}^{-1}$, dotted line: $u = 5\text{cm}\,\text{s}^{-1}$, dashed line: $u = 7\text{cm}\,\text{s}^{-1}$, long-dashed line: $u = 9\text{cm}\,\text{s}^{-1}$. (*c*) $u = 5\text{cm}\,\text{s}^{-1}$, $\Gamma' = 10$. Solid line: $l = 1$cm, dotted line: $l = 2$cm, dashed line: $l = 5$cm, long-dashed line: $l = 10$cm.

(1990). Hence, these are reasonably realistic values.

Figure 4.4 shows plots of the MSS as a function of t' in the uncoupled case for values of Γ', u and l ten times larger than those used in figure 4.3, so as to produce pressure fluctuations of the same magnitude. Two differences immediately stand out between figures 4.3 and 4.4. Firstly, in the uncoupled case the MSS values attained are much lower than in the coupled case, despite the turbulent pressure fluctuations being of the same magnitude. In all the three plots in figures 4.4(*a*–*c*), the MSS barely reaches 1×10^{-6}, which corresponds to a RMS slope of 1×10^{-3}. In a real situation, waves with such a slope would be invisible to the naked eye. Secondly, although the trends in the behaviour of wave growth with the parameters Γ', u and l are in the same sense as in the coupled case, the sensitivity to the shear rate Γ' is much reduced (see figure 4.4(*a*)). Both these aspects are linked with the decorrelation process of the turbulent pressure fluctuations over time, and will be explained in the

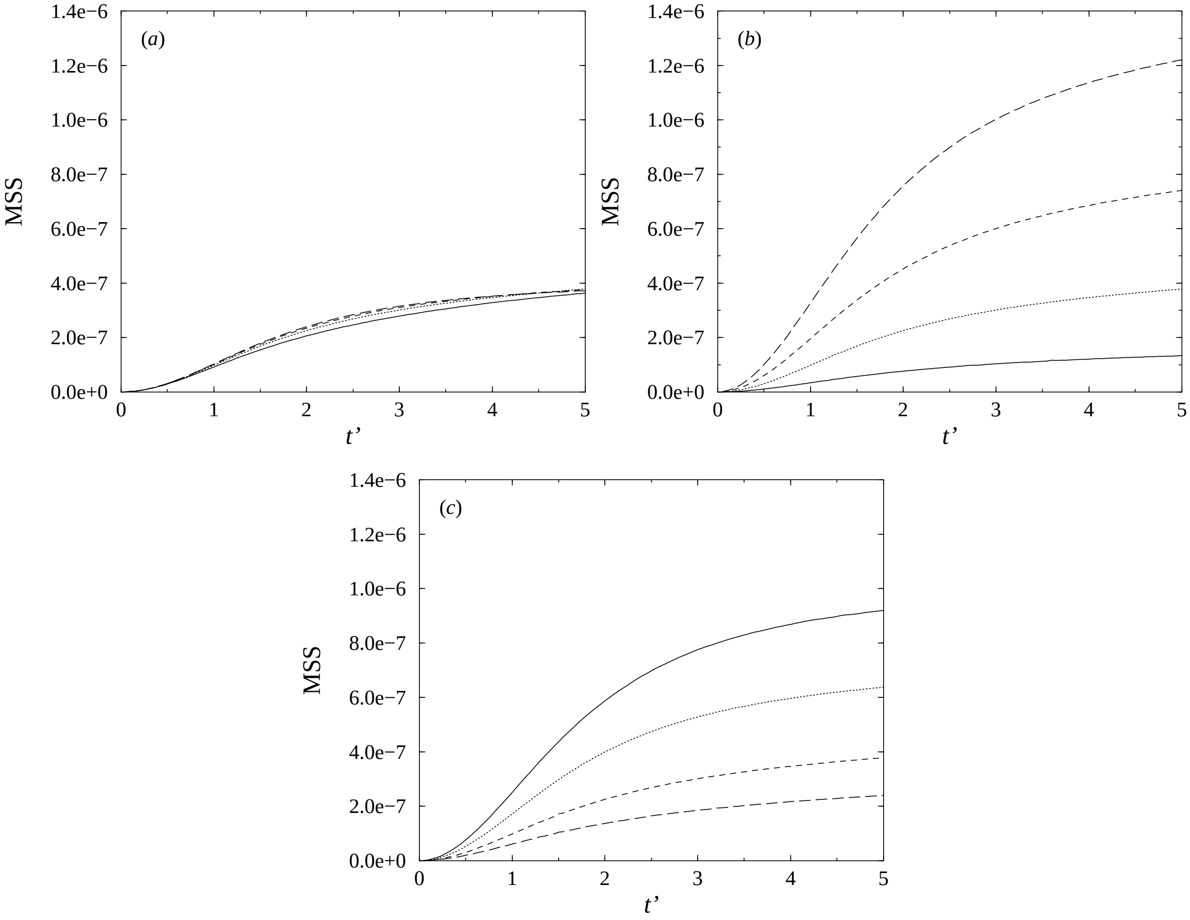

Figure 4.4 Time evolution of mean square slope of the waves in the uncoupled case. (*a*) $l = 0.5$m, $u = 0.5$m s^{-1}. Solid line: $\Gamma' = 50$, dotted line: $\Gamma' = 100$, dashed line: $\Gamma' = 200$, long-dashed line: $\Gamma' = 500$. (*b*) $l = 0.5$m, $\Gamma' = 100$. Solid line: $u = 0.3$m s^{-1}, dotted line: $u = 0.5$m s^{-1}, dashed line: $u = 0.7$m s^{-1}, long-dashed line: $u = 0.9$m s^{-1}. (*c*) $u = 0.5$m s^{-1}, $\Gamma' = 100$. Solid line: $l = 0.1$m, dotted line: $l = 0.2$m, dashed line: $l = 0.5$m, long-dashed line: $l = 1$m.

next subsection.

There is a considerable resemblance between the MSS curves presented in figure 4.3 of this chapter and those presented in figure 3 of Cox (1958). Qualitatively, in both cases the MSS initially increases at a fast rate, but later increases progressively slower, reaching an approximate plateau. This feature is also related to the time evolution of the pressure fluctuations, which will be addressed in the next subsection. Quantitatively, the time interval over which the waves grow rapidly (which can be evaluated visually from Cox's figure 3) is ≈ 0.5s, not very different from the value extracted previously from figure 4.3 of this chapter (0.3 s). The MSS values of figure 4.3 are smaller than those of Cox by less than an order of magnitude, while the values of figure 4.4 are insignificantly small by comparison. It thus seems that the coupled case explains Cox's results better than the uncoupled case, which leads to the conclusion that the initial wave growth observed in Cox's experiments may be driven by turbulence in the water rather than by turbulence in the air.

In Cox's figure 3, the fetch at which waves are initiated is progressively translated upstream as the windspeed increases, but is always greater than approximately 1m, for the range of windspeeds he considered. This also supports the idea that it is the turbulence in the water that generates the waves, because it is only after the wind has blown for some distance over the water that a shear current appears in the water and becomes turbulent (Caulliez *et al.*, 1998).

4.3.2 Decorrelation of the pressure fluctuations

To understand why the waves generated in the uncoupled case are much smaller than those generated in the coupled case despite the fact that the magnitude of the forcing pressure fluctuations is the same, recall that the spatio-temporal structure of these pressure fluctuations is also crucial for wave growth. Phillips (1957) pointed out that resonant wave growth occurs when pressure fluctuations advected over the air-water interface match both the wavenumber and the frequency or phase speed of free surface waves. The resonance process would be maximised if the pressure fluctuations with the appropriate 'dispersion relation' were rigidly advected, following the waves with which they are able to resonate. But such perfect resonance never happens in turbulent flows. Due to the interaction between the mean flow and the turbulence or the turbulence with itself, pressure patterns with given initial length and time scales lose coherence as they are transported by the velocity field, and are only capable of interacting resonantly with a wave for a finite time. That time is the decorrelation time of pressure, which Phillips calls θ in his theory. Corcos (1964) has suggested that, in a boundary layer flow, 'the dispersion of the sources of pressure by the mean stream may well be the dominant mechanism responsible for the convective lack of coherence of pressure'. In other words: the mean shearing of the turbulence may be the primary cause for the decorrelation of the pressure fluctuations. In the present RDT model, the mean shear is not the dominant mechanism for the decorrelation of the pressure fluctuations, but the only mechanism, since the turbulence does not interact with itself.

A function which contains useful information about the decorrelation time of pressure is the temporal covariance function of the turbulent pressure fluctuations. That function can be determined at the air-water interface by multiplying (4.48) at time t by the same expression at time $t + \Delta t$ (where Δt is a time lag), then using (4.8) and ensemble averaging. The resulting expression can then be made dimensionless, yielding

$$\overline{p'(t')p'(t'+\Delta t')} = \frac{1}{4\pi} \iiint \frac{k_1'^2}{k_{12}'^2} \frac{E'(k_0')}{(k_{12}' - \mathrm{i}k_3'(t'))^2 (k_{12}' + \mathrm{i}k_3'(t'+\Delta t'))^2} \mathrm{d}k_1' \mathrm{d}k_2' \mathrm{d}k_3', \qquad (4.65)$$

where $\Delta t' = \Gamma \Delta t$ is the dimensionless time lag. The dimensionless pressure covariance only depends on t' and $\Delta t'$. If this covariance is divided by the dimensionless pressure variance (4.63), the pressure correlation function is obtained. The pressure correlation has been plotted in figure 4.5 for $t' = 0$,

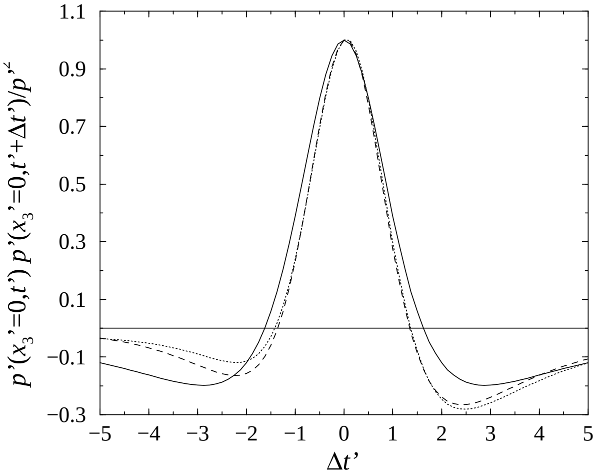

Figure 4.5 Temporal correlation of the pressure. Solid line: $t' = 0$, dotted line: $t' = 3$, dashed line: $t' = 5$.

3 and 5, as a function of $\Delta t'$. The dependence of this function on t' is relatively weak. Concerning the dependence on $\Delta t'$, the pressure correlation has a maximum at the origin, then becomes slightly negative, and for large values of $\Delta t'$ decays to zero. The point where this function intercepts the horizontal axis remains approximately the same for every t'. Now, the location of this intercept can be understood as giving one of the possible definitions of decorrelation time for pressure. In figure 4.5, the intercept corresponds to a value of $\Delta t' \approx 1.5$. So, it can be concluded that the dimensional decorrelation time for pressure is $\Delta t \approx 1.5/\Gamma$. Hence the turbulent pressure fluctuations remain coherent for a shorter time as the shear rate increases.

Since the shear rate is higher in the air than in the water, the decorrelation time for the turbulent pressure fluctuations is shorter in the air than in the water. This effect counteracts the proportionality of the pressure to the shear rate which was seen to exist at the beginning of §4.3. So, even if the pressure fluctuations in the air have the same magnitude as those in the water, they are considerably less coherent, and that is the reason for the reduced wave growth in the uncoupled case. The dimensionless number which best describes this effect is

$$\frac{\sigma_0'}{\Gamma'} = \frac{\sigma_0}{\Gamma}, \tag{4.66}$$

which appears in the argument of the sine function in the nondimensional solution for the wave spectrum (4.57), and also, more indirectly, in (4.58). When (4.66) is larger than 1, the turbulent pressure fluctuations decorrelate over a time longer than one period of the free surface waves and considerable resonant or near-resonant growth may be expected. Conversely, when (4.66) is smaller than 1, the pressure fluctuations decorrelate over a time shorter than one period of the free surface waves, and sustained growth is highly inhibited.

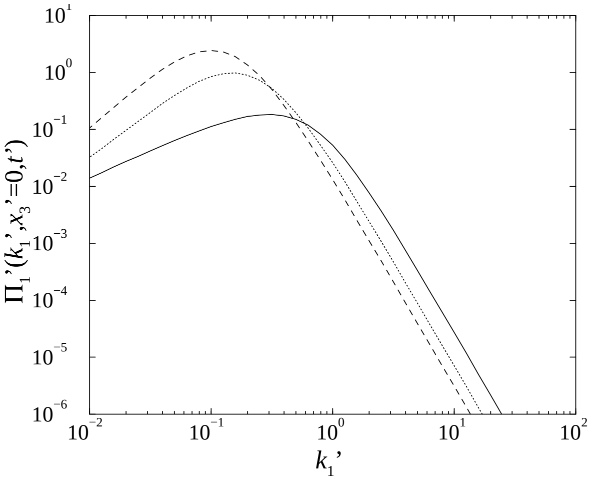

Figure 4.6 Dimensionless wavenumber spectrum of the pressure along the direction of the current. Solid line: $t' = 0$, dotted line: $t' = 3$, dashed line: $t' = 5$.

σ_0 depends on k_{12} and so is a function of the length of the surface waves. Since for turbulence with an integral length scale l, the dominant waves generated have a wavenumber $k_{12} \approx 2\pi/l$, the 'dominant' angular frequency $\overline{\sigma}_0 = \sigma_0(k_{12} = 2\pi/l)$ is more useful than σ_0 for evaluating the overall effect of the pressure decorrelation of the wave field. The dimensionless quantity which controls wave growth then becomes (4.66) with σ_0 replaced by $\overline{\sigma}_0$. The ratio $\overline{\sigma}_0/\Gamma$ is typically ≈ 4 in the coupled case and ≈ 0.1 in the uncoupled case so, according to the above remarks, wave growth is favoured in the first case and highly inhibited in the second. This is in agreement with the actual numerical results. Interestingly, an increase in either Γ or l contributes to a decrease in $\overline{\sigma}_0/\Gamma$. In the case of Γ, this happens for obvious reasons; in the case of l, through the decrease of the wavenumber at which the wave spectrum peaks, which results in a decrease of $\overline{\sigma}_0$.

The reason why the wave growth depends very weakly on Γ' in the uncoupled case (figure 4.4(*a*)) is that the effects of increasing Γ on the magnitude of the pressure fluctuations and on their decorrelation time almost offset each other for high values of Γ'.

A qualitative feature of figures 4.3 and 4.4 that was noted in §4.3.1 is the slowing down in the growth rate of the MSS as time progresses. That feature is related to the time evolution of the turbulent pressure fluctuations that force the waves as the turbulence is subjected to an increasingly large total distortion in the RDT model. It can be understood by plotting the time evolution of the one-dimensional pressure spectrum at the interface. That spectrum, which is seen from (4.51) to be

$$\Pi_1(k_1, x_3 = 0, t) = \iint Q_k Q_m \Phi_{km}^{(H)}(\mathbf{k}_0) \mathrm{d}k_2 \mathrm{d}k_3, \tag{4.67}$$

can be determined using the expressions for Q_k from appendix 1 (§4.5) and also (4.53), to yield, in dimensionless form,

$$\Pi'_1(k'_1, x'_3 = 0, t') = \frac{1}{4\pi} \iint \frac{k'^2_1}{k'^2_{12}} \frac{1}{k'^4(t')} E'(k'_0)\mathrm{d}k'_2\mathrm{d}k'_3, \tag{4.68}$$

where $\Pi'_1 = \Pi_1/(\rho^2\Gamma^2 u^2 l^3)$. The dimensionless pressure spectrum only depends on k'_1 and t' and is plotted in figure 4.6 for different values of t'. As time advances, the peak in the spectrum moves towards lower wavenumbers and the energy at high wavenumbers decreases. Therefore, the pressure forcing at the interface moves towards larger scales and these scales contribute less and less to the surface wave slope, making the slope grow progressively slower. This process corresponds to the elongation of the turbulent eddies in the streamwise direction, as observed, for example, in the numerical simulations of Lee *et al.* (1990). In this light, the initial, relatively fast, rise of the MSS curves in figure 3 of Cox (1958) may be interpreted as corresponding to the inception of turbulence in the water, and the levelling out of the curves as being due to the subsequent stretching of the turbulent eddies by shear in the boundary layer of the water flow.

4.3.3 Surface wave spectra

Despite its limitations, the model seems to indicate quite firmly that it is the turbulence in the water that initially drives the surface waves. Therefore, more detailed statistics of these waves will now be presented for the coupled case.

The curvature or saturation spectrum of the surface waves is defined as

$$B(k_1, k_2, t) = k^4_{12}\Psi(k_1, k_2, t). \tag{4.69}$$

This spectrum is dimensionless by definition, and will be plotted next in the functional form $B(k_{12}, \theta, t')$, where $\theta = \arctan(k_2/k_1)$ is the angle of the wavenumber vector with the direction of the current.

Figure 4.7 shows the sensitivity of the predicted curvature spectrum to the input variables Γ', l and u, for an angle $\theta = 0$ and a dimensionless time $t' = 5$. This time was chosen because, on the one hand, it is within the range of realistic total distortions (see last equation of (4.5)) and on the other corresponds to a stage where the MSS has almost stopped growing (see figure 4.3). The spectrum is plotted as a function of the dimensional wavenumber and not as a function of the dimensionless wavenumber, because the former variable is more frequently used in measurements of wave spectra and also because it bears out more clearly the important wavenumber $k_{min} = 367\text{m}^{-1}$. This wavenumber corresponds to the transition between the gravity and the capillary wave regimes, where the phase speed of surface waves is a minimum. The first aspect which stands out in figures 4.7(*a*–*c*) is that

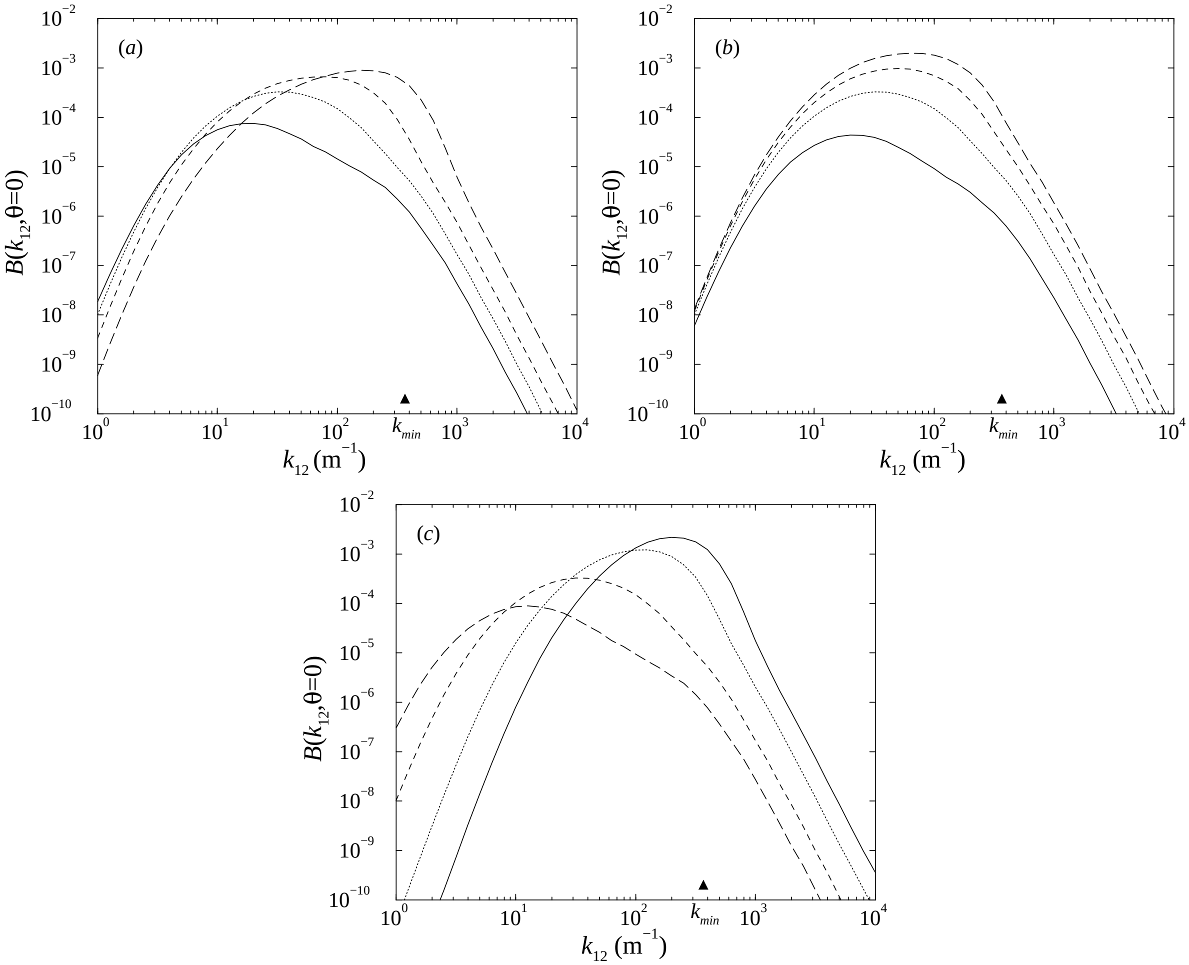

Figure 4.7 Curvature spectra of the waves along the direction of the current, in the coupled case, at dimensionless time $t' = 5$. (*a*) $l = 5$cm, $u = 5\text{cm}\,\text{s}^{-1}$. Solid line: $\Gamma' = 5$, dotted line: $\Gamma' = 10$, dashed line: $\Gamma' = 20$, long-dashed line: $\Gamma' = 50$. (*b*) $l = 5$cm, $\Gamma' = 10$. Solid line: $u = 3\text{cm}\,\text{s}^{-1}$, dotted line: $u = 5\text{cm}\,\text{s}^{-1}$, dashed line: $u = 7\text{cm}\,\text{s}^{-1}$, long-dashed line: $u = 9\text{cm}\,\text{s}^{-1}$. (*c*) $u = 5\text{cm}\,\text{s}^{-1}$, $\Gamma' = 10$. Solid line: $l = 1$cm, dotted line: $l = 2$cm, dashed line: $l = 5$cm, long-dashed line: $l = 10$cm.

the curvature spectra of the waves are sharply peaked. The peak occurs roughly at the wavenumber $k_{12} \approx 2\pi/l$, as predicted before. Some departure from this value towards lower wavenumbers can be attributed to the elongation that the turbulent eddies have suffered in the streamwise direction at $t' = 5$ (cf. figure 4.6).

In figure 4.7(*a*), it can be seen that, as Γ' increases, the level of $B(k_{12}, 0)$ generally increases, in agreement with figure 4.3. The peak of the spectrum moves to the right, towards k_{min}, and the zone to the left of the peak lowers slightly, while the zone to the right rises. This happens because, for a higher Γ, the ratio (4.66) is only larger than 1 (favouring wave growth) for a higher σ_0, and therefore for a higher k_{12}. The value of the spectrum at the peak varies between $\approx 8 \times 10^{-5}$ and $\approx 9 \times 10^{-4}$.

Figure 4.7(*b*) presents the dependence of the curvature spectrum on the turbulence RMS velocity u.

The spectral density increases with u everywhere, but more so at the peak and to the right of the peak. There is a drift of the peak towards higher wavenumbers as u increases, but much less pronounced than in figure 4.7(*a*). Maximum values of the spectrum vary between $\approx 5 \times 10^{-5}$ and $\approx 2 \times 10^{-3}$.

Finally, figure 4.7(*c*) shows the dependence of $B(k_{12}, 0)$ on the turbulence length scale l. There is a general decrease on the values of the spectrum as the length scale increases, in agreement with the MSS results. The spectral peak moves towards lower wavenumbers when l increases, as expected. In that process, the energy to the left of the peak increases, while that to the right decreases. Maximum values range from $\approx 9 \times 10^{-5}$ to $\approx 2 \times 10^{-3}$.

Some of the features just described can also be found in the laboratory data of Jähne & Riemer (1990) and Hwang *et al.* (1993) despite the fact that their wave spectra were measured at fetches of 90m and 16m, respectively, where certainly many effects not considered in the present model, such as nonlinear wave interactions, growth by feedback instability and wave breaking must have come into play. In figure 6(*a*) of Hwang *et al.* (1993), it is particularly significant that the curvature spectrum of the waves is sharply peaked, and that the peak tends to become centred around k_{min} as the wind-friction velocity increases (see also Jähne & Riemer (1990)). In figure 9 of Jähne & Riemer, the high-wavenumber part of the spectrum tends to rise relative to the low-wavenumber part of the spectrum as the windspeed increases, and that is also observed in the present model when either Γ' or u increases.

Since the wave field is always initiated by turbulent pressure fluctuations, and the feedback instability mechanisms that later become dominant, as well as the nonlinear wave interactions, can only modify the wave spectrum, it is perhaps to be expected that some of the features of the spectrum at the inception of the waves will be preserved. This may account for the similarities encountered between the model results and the data.

4.3.4 Angular energy distribution

The curvature spectrum contains information about the angular distribution of the wave energy, which will be analysed next.

Figure 8 of Jähne and Riemer (1990) shows that the energy distribution in $B(k_{12}, \theta)$ for the measured waves is relatively narrow for the whole range of wavenumbers considered at relatively low windspeeds, but broadens, especially at low wavenumbers when the windspeed increases. For windspeeds greater than $\approx 5.4\,\mathrm{m\,s^{-1}}$, the spectrum has a bimodal distribution at low wavenumbers, with peaks centred at some particular angle symmetrical about $\theta = 0$. The theoretical wave model of Kudryavtsev *et al.* (1999) also incorporates a broadening of the spectrum with decreasing wavenumber and increasing windspeed (see their figure 6).

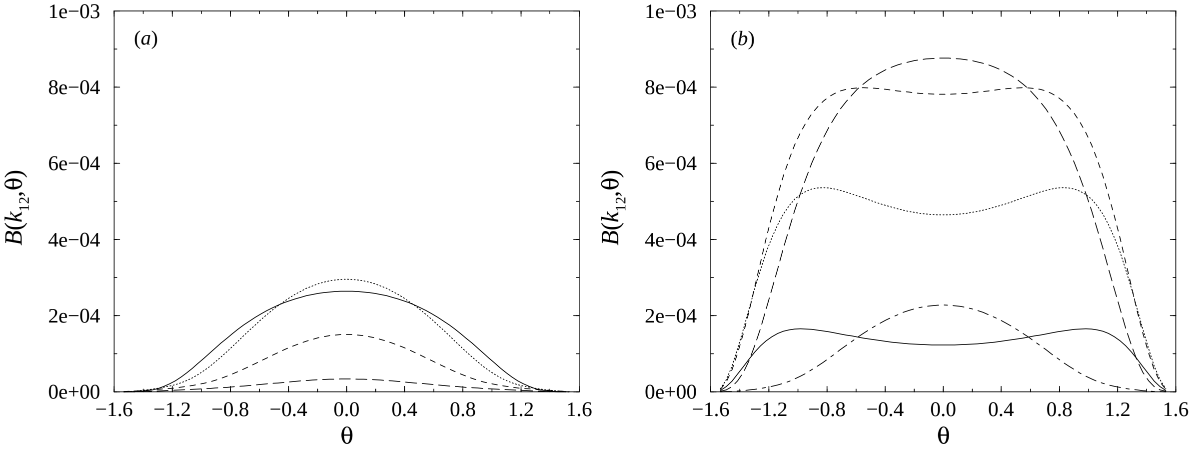

Figure 4.8 Variation of the curvature spectrum with direction, in the coupled case, for $l = 5$cm, $u = 5$cm s^{-1} and $t' = 5$. Solid line: $k_{12} = 20$m^{-1}, dotted line: $k_{12} = 50$m^{-1}, dashed line: $k_{12} = 100$m^{-1}, long-dashed line: $k_{12} = 200$m^{-1}, dash-dotted line: $k_{12} = 500$m^{-1}. (*a*) lower shear rate, $\Gamma' = 10$. (*b*) higher shear rate, $\Gamma' = 50$.

Figure 4.8 displays plots of $B(k_{12}, \theta)$, for various values of k_{12}, as a function of θ, at a dimensionless time $t' = 5$. In figure 4.8(*a*), the spectral density distribution varies with the angle approximately as $\cos^2 \theta$, because of the factor k_1^2 present in the expression of the wave spectrum (4.56). Only at the lowest wavenumber considered can a slight broadening be noticed. In figure 4.8(*b*), however, where the shear rate has been increased, a different behaviour can be observed. While at the highest wavenumber, the spectral density distribution is still peaked at $\theta = 0$, at lower wavenumbers the distribution becomes flattened and then bimodal, emulating qualitatively the experimental data. The wavenumbers for which this bimodal behaviour occurs ($k_{12} \leq 100$m^{-1}) roughly agree with those in figure 8(*d*) of Jähne & Riemer (1990), which corresponds to a windspeed of 7.3m s^{-1}.

Physically, the broadening of the spectrum occurs in the model because the pressure fluctuations at the interface move at different speeds according to their scale. Large-scale pressure fluctuations are induced by large turbulent eddies (Durbin, 1978) existing at a wide range of distances from the interface, and advected at a wide range of velocities. Hence, these pressure fluctuations are also advected at a wide range of velocities. The small-scale pressure fluctuations, on the other hand, are induced by small turbulent eddies at short distances from the interface, which all have a low advection velocity. Hence, these pressure fluctuations also move slowly. Since resonance requires that the pressure fluctuations follow the surface waves, short waves, which are generated by small-scale pressure fluctuations, choose preferentially the direction that minimises the difference between their phase speed and the small advection velocity of the pressure fluctuations that generate them. That direction corresponds to the angle $\theta = 0$. Longer waves, on the other hand, are generated by large-scale pressure fluctuations, which move faster, so the waves can satisfy resonance or near-resonance for various values of θ. That is why the curvature spectrum broadens as k_{12} decreases. The spectrum also broadens as Γ' increases, because a higher shear rate promotes a wider range of eddy advection velocities in the vicinity of the interface, thereby widening the range of θ at which resonance can occur.

In qualitative terms, the bimodal distribution of the wave spectrum could have been predicted from Phillips' (1957) theory on the basis of resonance arguments. However, the fact that the wave spectrum broadens as the wavenumber decreases is a result of the relation derived here between the turbulent pressure field and the turbulent velocity field. That relation has enabled the calculation of a precise form for the spectrum of the surface waves, which was beyond the possibilities of Phillips' theory. In figure 3 of Phillips (1957), the angular energy distribution of the wave spectrum always peaks at a certain 'critical' angle that depends on the wind velocity, and is zero for larger angles to the wind. By contrast, the present model is able to produce angular energy distributions that peak in the direction of the current, and also bimodal distributions that decay smoothly to zero after the peaks, clearly in better agreement with data.

4.3.5 Discussion

The present model probably underestimates wave growth for three reasons, all of them related to the linear approximation of RDT. Firstly, the model does not take into account the nonlinear part of the pressure, associated with the interaction of the turbulence with itself. The numerical simulations of Kim (1989) have shown that, in a turbulent channel flow, the linear and nonlinear parts of the pressure can have about the same magnitude, even at the channel wall. Secondly, the decorrelation time of the turbulent pressure fluctuations seems to be underestimated by RDT (see figure 15 of Corcos (1964), where the temporal pressure correlation is plotted for the total and linear parts of the pressure). This again inhibits wave growth, for the reasons pointed out in §4.3.2. Thirdly, the rendering of the turbulence anisotropic by shear is overestimated by RDT, since the neglected nonlinear processes tend to oppose this anisotropy. Because the increase in anisotropy is associated with the migration of the peak in the pressure spectrum to lower wavenumbers (see §4.3.2), the slowing down of the MSS growth rate observed in figure 4.3 is probably overestimated.

However, there is one aspect of the model which may lead to an overestimation of the pressure. That is the assumption of a constant shear rate throughout the domain. Since the pressure field is proportional in a nonlocal way to the shear rate, this approximation should overestimate the contributions to the surface pressure originating from some distance from the boundary, where the shear rate is in reality much lower than assumed. Nevertheless, the pressure has a much stronger dependence on the velocity field in the vicinity of the boundary (Kim, 1989), so this overestimation is probably moderate.

An important issue in the present model is how to determine the value of the shear rate Γ to use as an input variable. For all the runs carried out in this chapter, this was done in a rough way by direct inspection of the figure 4.7 of Melville *et al.* (1998). The shear rate in the top 1 or 2cm of the water flow was estimated as of $O(10\text{s}^{-1})$, and this order of magnitude was confirmed in the studies of shear currents of McLeish & Putland (1975) and of Tsai (1998). While the value of the shear rate immediately outside the viscous boundary layer is probably the most important for determining the pressure fluctuations, it is clear that some sort of average must be carried out over a certain distance from the boundary, because of the nonlocality of the contributions to the pressure. How that averaging may be done in an objective way is a problem that remains open.

4.4 Conclusions

A theoretical model has been developed for the initial stage of surface wave generation at an air-water interface by a turbulent shear flow. The problem of the onset of a turbulent wind and the problem of the onset of a turbulent shear current have been addressed separately by assuming that the turbulent shear flow exists in the air or in the water, respectively. Although the existence of winds in the atmosphere and currents in the ocean is closely linked because of the viscous coupling between the air and the water, the two processes are separated in this model, in order to assess the importance of each one of them. The case of a turbulent current is called the coupled case and the case of a turbulent wind is called the uncoupled case.

The model can be viewed as a combination between the wave generation model of Phillips (1957) and the turbulence rapid-distortion model of Durbin (1978). The air-water interface is assumed to be initially flat and at rest. Surface waves subsequently grow as a response to the pressure fluctuations induced at the interface by the turbulent shear flow. The pressure field at the interface is linearly related to the turbulent velocity field. This pressure results from the interaction taking place in the turbulent fluid between the mean shear and the turbulence. The turbulence is assumed to be statistically homogeneous in the horizontal directions, and isotropic far from the boundary at the initial time. The mean velocity is assumed to vary linearly with height or depth. Both the turbulent and wave velocity components are assumed to be weak, in the sense of being unable to self-interact or interact with one another, being affected only by the mean flow.

The mean-square-slope of the surface waves is calculated as a function of time in the coupled and in the uncoupled cases. It is found that the MSS increases faster for higher values of the dimensionless shear rate Γ', initial RMS turbulent velocity u and lower values of the initial integral length scale of the turbulence l. This is explained by the proportionality of the pressure applied at the interface to Γ and u, and by the inverse proportionality of the wave slope to l.

For pressure fluctuations of similar magnitude, the waves generated in the uncoupled case are much smaller than the waves generated in the coupled case. This behaviour is attributed primarily to differences in the ratio $\overline{\sigma}_0/\Gamma$ between the decorrelation time scale for pressure (which is $\propto 1/\Gamma$) and the period of the dominant waves ($\propto 1/\overline{\sigma}_0$). In the coupled case, Γ is smaller and $\overline{\sigma}_0$ larger (because the length scale of the dominant waves l is smaller), leading to a value of the ratio $\overline{\sigma}_0/\Gamma$ larger than 1. This allows the turbulence and the waves to interact for more than one wave period before the turbulent pressure fluctuations lose their coherence. In the uncoupled case, by contrast, Γ is larger and $\overline{\sigma}_0$ smaller (because the length scale of the dominant waves l is larger), resulting in a value of the ratio $\overline{\sigma}_0/\Gamma$ lower than 1. This means that the turbulent pressure fluctuations can not interact appreciably with the surface waves before decorrelating, and wave growth is strongly inhibited.

In the coupled case, plots illustrating the MSS time evolution are found to have a shape and magnitude consistent with plots of the same quantity derived from measurements by Cox (1958). The MSS initially increases in time relatively fast, but after a certain time slows down and reaches an approximate plateau. This phenomenon is attributed to the progressive elongation of the turbulent eddies in the streamwise direction by the shear, which causes the turbulent pressure fluctuations to force the air-water interface at progressively lower wavenumbers.

Wave curvature spectra are calculated in the coupled case, and plotted as a function of the wavenumber. These spectra are found to have a maximum roughly at the wavenumber $k_{12} \approx 2\pi/l$, and to satisfy power laws at higher and lower wavenumbers that result directly from the corresponding power laws of the turbulence spectrum. The wave curvature spectra are also plotted for discrete wavenumbers, as a function of the angle of propagation with the direction of the current, θ. The spectra are found to peak like $\cos^2\theta$ at $\theta = 0$ for all wavenumbers at low shear rates, but to peak at $\theta = 0$ for higher shear rates only at high wavenumbers, having a broader distribution at lower wavenumbers and a bimodal distribution at even lower wavenumbers. This scale dependent behaviour, which is consistent with spectra measured by Jähne & Riemer (1990), is found to be linked with the spatio-temporal structure of the pressure fluctuations, as modelled by RDT. Longer waves are excited by pressure fluctuations associated with larger and faster-moving turbulent eddies being advected at some distance from the boundary, while shorter waves grow due to the pressure fluctuations associated with smaller and slower-moving eddies, which exist closer to the boundary.

4.5 Appendix 1. Expressions of M_{ij}, Q_j and S_j

In the coupled case, the M_{ij} matrix can be written

$$\begin{aligned}
M_{11} &= \mathrm{e}^{\mathrm{i}k_3x_3}, \\
M_{12} &= 0, \\
M_{13} &= \mathrm{e}^{\mathrm{i}k_3x_3} \Bigg\{ \left(\frac{k_1k_{30}}{k_{12}^2} - \frac{k_1k_3}{k_{12}^2}\frac{k_0^2}{k^2} \right) - \frac{k_2^2k_0^2}{k_1k_{12}^3} \Bigg\{ \arctan\left(\frac{k_{30}}{k_{12}}\right) - \arctan\left(\frac{k_3}{k_{12}}\right)
\end{aligned}$$

$$\begin{aligned}
&+\frac{1}{2\mathrm{i}}\Big[\mathrm{e}^{2k_{12}x_3}\left[E_1((k_{12}+\mathrm{i}k_{30})x_3)-E_1((k_{12}+\mathrm{i}k_3)x_3)+\pi\mathrm{i}\left(\mathrm{sign}(k_3)-\mathrm{sign}(k_{30})\right)\right]\\
&-\left[E_1((-k_{12}+\mathrm{i}k_{30})x_3)-E_1((-k_{12}+\mathrm{i}k_3)x_3)\right]]\}\}-\mathrm{i}\mathrm{e}^{k_{12}x_3}\frac{k_1k_0^2}{k_{12}k^2},\\
&M_{21}=0,\\
&M_{22}=\mathrm{e}^{\mathrm{i}k_3x_3},\\
&M_{23}=\mathrm{e}^{\mathrm{i}k_3x_3}\Bigg\{\left(\frac{k_2k_{30}}{k_{12}^2}-\frac{k_2k_3}{k_{12}^2}\frac{k_0^2}{k^2}\right)+\frac{k_2k_0^2}{k_{12}^3}\Bigg\{\arctan\left(\frac{k_{30}}{k_{12}}\right)-\arctan\left(\frac{k_3}{k_{12}}\right)\\
&+\frac{1}{2\mathrm{i}}\Big[\mathrm{e}^{2k_{12}x_3}\left[E_1((k_{12}+\mathrm{i}k_{30})x_3)-E_1((k_{12}+\mathrm{i}k_3)x_3)+\pi\mathrm{i}\left(\mathrm{sign}(k_3)-\mathrm{sign}(k_{30})\right)\right]\\
&-\left[E_1((-k_{12}+\mathrm{i}k_{30})x_3)-E_1((-k_{12}+\mathrm{i}k_3)x_3)\right]]\}\}-\mathrm{i}\mathrm{e}^{k_{12}x_3}\frac{k_2k_0^2}{k_{12}k^2},\\
&M_{31}=M_{32}=0,\\
&M_{33}=\frac{k_0^2}{k^2}\left(\mathrm{e}^{\mathrm{i}k_3x_3}-\mathrm{e}^{k_{12}x_3}\right),
\end{aligned}\tag{4.70}$$

where ‘sign’ denotes the sign function and E_1 denotes the exponential integral function of order one. The Q_j vector is given by

$$\begin{aligned}
&Q_1=Q_2=0,\\
&Q_3=2\mathrm{i}\rho\Gamma k_1\frac{k_0^2}{k^2}\left[\frac{1}{k^2}\mathrm{e}^{\mathrm{i}k_3x_3}+\left(\frac{x_3}{2k_{12}}-\frac{1}{2k_{12}^2}-\frac{\mathrm{i}k_3}{k_{12}k^2}\right)\mathrm{e}^{k_{12}x_3}\right].
\end{aligned}\tag{4.71}$$

The corresponding expressions for the uncoupled case can be obtained by simply reflecting these expressions about the plane $x_3=0$, by replacing k_3 with $-k_3$, k_{03} with $-k_{03}$ and x_3 with $-x_3$.

The S_j vector is defined as

$$\begin{aligned}
&S_1=S_2=0,\\
&S_3=-2\mathrm{i}\frac{\rho_a}{\rho_w}\frac{\Gamma}{\sigma_0}\frac{k_1}{2k_{12}}k_0^2\int_0^t\frac{1}{(k_{12}+\mathrm{i}k_3)^2}\sin\left(\sigma_0(t-s)\right)\mathrm{d}s
\end{aligned}\tag{4.72}$$

in the uncoupled case and

$$\begin{aligned}
&S_1=S_2=0,\\
&S_3=-2\mathrm{i}\frac{\Gamma}{\sigma_1}\frac{k_1}{2k_{12}}k_0^2\int_0^t\frac{\mathrm{e}^{\mathrm{i}\frac{\Gamma k_1}{2k_{12}}(t-s)}}{(k_{12}+\mathrm{i}k_3)^2}\sin\left(\sigma_1(t-s)\right)\mathrm{d}s
\end{aligned}\tag{4.73}$$

in the coupled case.

4.6 Appendix 2. Growing and oscillating parts of Ψ

In (4.55) and (4.56), the terms between brackets can be expanded into a growing and an oscillating part. Expressions for these parts will be presented next in the coupled case. The expressions for the uncoupled case may then be found as a particular case.

After expressing the sine function in (4.56) in complex form, moving the factors explicitly dependent on time outside the integrals and rearranging, the term between brackets in (4.56) can be written

$$\left|\int_0^t \frac{\mathrm{e}^{\mathrm{i}\frac{\Gamma k_1}{2k_{12}}s}\sin\left(\sigma_1(t-s)\right)}{(k_{12}-\mathrm{i}k_3(s))^2}\mathrm{d}s\right|^2 = \frac{1}{4}\left|\int_0^t \frac{\mathrm{e}^{\mathrm{i}(\frac{\Gamma k_1}{2k_{12}}-\sigma_1)s}}{(k_{12}-\mathrm{i}k_3(s))^2}\mathrm{d}s\right|^2 + \frac{1}{4}\left|\int_0^t \frac{\mathrm{e}^{\mathrm{i}(\frac{\Gamma k_1}{2k_{12}}+\sigma_1)s}}{(k_{12}-\mathrm{i}k_3(s))^2}\mathrm{d}s\right|^2$$
$$-\mathrm{Re}\left\{\frac{1}{4}\mathrm{e}^{2\mathrm{i}\sigma_1 t}\int_0^t \frac{\mathrm{e}^{\mathrm{i}(\frac{\Gamma k_1}{2k_{12}}-\sigma_1)s}}{(k_{12}-\mathrm{i}k_3(s))^2}\mathrm{d}s\int_0^t \frac{\mathrm{e}^{\mathrm{i}(\frac{\Gamma k_1}{2k_{12}}+\sigma_1)s}}{(k_{12}+\mathrm{i}k_3(s))^2}\mathrm{d}s\right\}. \tag{4.74}$$

The third term on the right oscillates in time and was neglected in the numerical calculations, for reasons explained in §4.2.7. By making $\sigma_1 = \sigma_0$ and $\Gamma = 0$ in (4.74) only in the numerator of the fractions (i.e., not in k_3), the expression applicable to the uncoupled case, (4.55), is found:

$$\left|\int_0^t \frac{\sin\left(\sigma_0(t-s)\right)}{(k_{12}-\mathrm{i}k_3(s))^2}\mathrm{d}s\right|^2 = \frac{1}{4}\left|\int_0^t \frac{\mathrm{e}^{-\mathrm{i}\sigma_0 s}}{(k_{12}-\mathrm{i}k_3(s))^2}\mathrm{d}s\right|^2 + \frac{1}{4}\left|\int_0^t \frac{\mathrm{e}^{\mathrm{i}\sigma_0 s}}{(k_{12}-\mathrm{i}k_3(s))^2}\mathrm{d}s\right|^2$$
$$-\mathrm{Re}\left\{\frac{1}{4}\mathrm{e}^{2\mathrm{i}\sigma_0 t}\int_0^t \frac{\mathrm{e}^{-\mathrm{i}\sigma_0 s}}{(k_{12}-\mathrm{i}k_3(s))^2}\mathrm{d}s\int_0^t \frac{\mathrm{e}^{\mathrm{i}\sigma_0 s}}{(k_{12}+\mathrm{i}k_3(s))^2}\mathrm{d}s\right\}. \tag{4.75}$$

4.7 Appendix 3. Solution in terms of exponential integrals

The product of complex conjugate time integrals in (4.55) and (4.56) was seen in appendix 2 to be approximately equal to the first two terms on the right of (4.74) and (4.75), due to the fact that the third terms are oscillatory. Thus, the approximate solution for the wave growth only requires a calculation of the time integrals in the non-oscillatory terms. In the coupled case, these are

$$\int_0^t \frac{\mathrm{e}^{\mathrm{i}(\frac{\Gamma k_1}{2k_1 2}\pm\sigma_1)s}}{(k_{12}-\mathrm{i}k_3(s))^2}\mathrm{d}s = -\frac{1}{k_1\Gamma}\left(\frac{\mathrm{e}^{\mathrm{i}(\frac{\Gamma k_1}{2k_1 2}\pm\sigma_1)t}}{k_3(t)+\mathrm{i}k_{12}} - \frac{1}{k_{03}+\mathrm{i}k_{12}}\right)$$
$$+\mathrm{i}\frac{\frac{\Gamma k_1}{2k_{12}}\pm\sigma_1}{k_1^2\Gamma^2}\mathrm{e}^{-\frac{\frac{\Gamma k_1}{2k_{12}}\pm\sigma_1}{k_1\Gamma}(k_{12}-\mathrm{i}k_{03})}\left\{E_1\left(-\frac{\frac{\Gamma k_1}{2k_{12}}\pm\sigma_1}{k_1\Gamma}(k_{12}-\mathrm{i}k_3)\right)\right.$$
$$-E_1\left(-\frac{\frac{\Gamma k_1}{2k_{12}}\pm\sigma_1}{k_1\Gamma}(k_{12}-\mathrm{i}k_{03})\right) + \pi\mathrm{i}H\left(\frac{\frac{\Gamma k_1}{2k_{12}}\pm\sigma_1}{k_1\Gamma}k_{12}\right)\left[\mathrm{sign}\left(\frac{\frac{\Gamma k_1}{2k_{12}}\pm\sigma_1}{k_1\Gamma}k_3\right)\right.$$

$$\left.\left. -\mathrm{sign}\left(\frac{\frac{\Gamma k_1}{2k_{12}} \pm \sigma_1}{k_1\Gamma} k_{03}\right)\right]\right\}, \tag{4.76}$$

and in the uncoupled case

$$\begin{aligned}
&\int_0^t \frac{\mathrm{e}^{\pm \mathrm{i}\sigma_0 s}}{(k_{12} - \mathrm{i}k_3(s))^2}\mathrm{d}s = -\frac{1}{k_1\Gamma}\left(\frac{\mathrm{e}^{\pm \mathrm{i}\sigma_0 t}}{k_3(t) + \mathrm{i}k_{12}} - \frac{1}{k_{03} + \mathrm{i}k_{12}}\right) \\
&\pm \mathrm{i}\frac{\sigma_0}{k_1^2\Gamma^2}\mathrm{e}^{\mp \frac{\sigma_0}{k_1\Gamma}(k_{12} - \mathrm{i}k_{03})}\left\{E_1\left(\mp\frac{\sigma_0}{k_1\Gamma}(k_{12} - \mathrm{i}k_3)\right) - E_1\left(\mp\frac{\sigma_0}{k_1\Gamma}(k_{12} - \mathrm{i}k_{03})\right)\right. \\
&\left. + \pi \mathrm{i} H\left(\frac{\pm\sigma_0}{k_1\Gamma}k_{12}\right)\left[\mathrm{sign}\left(\pm\frac{\sigma_0}{k_1\Gamma}k_3\right) - \mathrm{sign}\left(\pm\frac{\sigma_0}{k_1\Gamma}k_{03}\right)\right]\right\},
\end{aligned} \tag{4.77}$$

where H is the Heaviside function.

CHAPTER 5

The distortion of turbulence by a progressive surface wave

5.1 Introduction

Turbulence and surface waves in the ocean can interact in a variety of ways. As mentioned in the previous chapter, turbulent pressure fluctuations and turbulent shear stresses are responsible for both the initiation of surface waves (Phillips, 1957) and their amplification by a sheltering mechanism (Belcher & Hunt, 1993). Surface waves can also be scattered (Phillips, 1959), distorted (Longuet-Higgins, 1996) and dissipated by turbulence existing in the water (Kitaigorodskii & Lumley, 1983).

Conversely, breaking waves (Melville, 1996), shear currents induced by the wind and thermal convection generate turbulence in the ocean surface layer, which is subsequently distorted by the wave orbital motions (Thais & Magnaudet, 1996). This distortion is of two types: on the one hand, there is the direct effect of the orbital motions, of first order in the wave slope, which has a straining rate of $O(a_w k_w \sigma_w)$, where a_w, k_w and σ_w are, respectively, the amplitude, wavenumber and angular frequency of the waves. This effect is relatively weak, because the wave motions are periodic and the total strain never exceeds $O(a_w k_w)$, which is small. On the other hand, there is the effect of the Stokes drift, of second order in the wave slope, whose straining rate can be estimated as $O(a_w^2 k_w^2 \sigma_w)$. Although this straining rate is even smaller, its effect is cumulative, and the total strain is of $O(a_w^2 k_w^2 \sigma_w t)$, where t is time. So, this second order effect is bound to affect turbulence appreciably after a sufficient number of wave cycles.

The distorting effect of the Stokes drift is at the basis of the explanation commonly accepted at present for the existence of Langmuir circulations in the ocean (Leibovich, 1983). Langmuir circulations are intense, elongated vortices, with their axes of rotation aligned with the wind and with the dominant surface waves. In the instability mechanism proposed by Craik & Leibovich (1976), these circulations result from the tilting and amplification, by the Stokes drift of the waves, of the vertical vorticity associated with an infinitesimal perturbation to the wind-induced shear current. Although the treatment of Craik and Leibovich addresses this interaction in a deterministic framework, considering the flow as laminar, the flow in the ocean surface layer is almost invariably turbulent. Field observations (Faller & Auer, 1988) and numerical simulations (McWilliams *et al.*, 1997) of the ocean surface layer in fact show that the streamwise vortices identified as Langmuir circulations have themselves a wide range of scales, and can therefore be seen as turbulence. They have been called *Langmuir* *turbulence* by McWilliams *et al.* (1997). Hence it is likely that turbulence plays an important role in the development of Langmuir circulations.

When turbulence coexists with waves and a shear current in the ocean surface layer, the interactions between these 3 flow components are necessarily complex, and probably best understood in isolation. Both the turbulence and the shear current are rotational, and their vorticity can be tilted and amplified by the Stokes drift of the wave. Only the shear current and the waves have been taken into account in the early theoretical studies of Langmuir circulations (Leibovich, 1983). The interaction between the turbulence and the shear current, which is akin to the mean flow–turbulence interaction occurring in numerous boundary layer flows (Lee *et al.*, 1990), has received some attention in the context of Langmuir circulations in McWilliams *et al.* (1997).

The interaction between the waves and the turbulence has been investigated experimentally by Green *et al.* (1972), Ölmez & Milgram (1992), Nepf & Monismith (1995) and Thais & Magnaudet (1996), but a systematic theoretical treatment of this situation has been lacking. The primary aim of this chapter is to examine the interaction between shear-free turbulence and a surface wave when the turbulence can be considered weak and slow compared with the wave. This is done by treating the wave as prescribed and deterministic, and the turbulence as a random velocity field, of which statistics can be calculated. Attention is focussed on the time evolution of the statistics of the velocity fluctuations, and also on their spatial structure. Turbulence distortion by a wave is briefly compared with turbulence distortion by a shear current using the model of chapter 4 for a turbulent flow with a constant shear rate. The energetics of the turbulence are analysed by scaling the turbulent kinetic energy (TKE) equation, and the consequences of the wave-turbulence interaction for the wave are investigated by scaling an equation for the wave energy.

The remainder of this chapter is organised as follows: in §5.2, the theoretical model of wave-turbulence interaction is presented. In §5.3, the results obtained from the model are analysed in detail. These concentrate on the time evolution of the Reynolds stresses and the integral length scales, over one wave cycle and over several wave cycles. These results are compared with those obtained for turbulence distorted by a shear current. The consequences of the energy transfer taking place between the turbulence and the wave are then analysed. The chapter ends with the main conclusions, in §5.4.

5.2 Theoretical model

Consider an infinite water mass bounded above by a free surface on which a progressive, monochromatic, surface wave is propagating. The wave is irrotational and has relatively low slope. It will be analysed here how turbulence beneath the free surface is distorted by the orbital motions associated with the wave. To tackle this idealised problem, the rapid distortion theory (RDT) of Hunt (1973) will be used.

The total velocity field $\mathcal{U}_i$ is split into a mean part, U_i, and a turbulent part, u_i, namely

$$\mathcal{U}_i = U_i(\mathbf{x}) + u_i(\mathbf{x}, t), \quad i = 1, 2, 3, \tag{5.1}$$

The mean velocity corresponds to the wave orbital motion expressed in a coordinate system travelling with the wave crests. Hence U_i is stationary. The wave is taken to propagate in the positive x_1 direction and, since the wave is also monochromatic, U_i is slab-symmetric and does not depend on x_2. The turbulence is assumed to be statistically stationary, homogeneous and isotropic far from the surface. At the initial time, the turbulence is assumed to be homogeneous and isotropic throughout the depth of the water column at a particular point of the wave phase. The turbulence is also assumed to be of a much smaller scale than the wave, so that the initial integral length scale of the turbulence l satisfies $l \ll \lambda_w$, where λ_w is the wavelength of the wave. The idea is then to analyse the evolution of the turbulence statistics following a water parcel as the wave propagates over the turbulence.

This idealised model approximates two physical situations: the first is a laboratory arrangement where mechanically generated surface waves propagate over a turbulent region created by an oscillating grid, as in the experiments of Ölmez and Milgram (1992) and Milgram (1998). The second situation is where turbulence is injected into the water by breaking surface waves at a particular time and location, being then distorted by subsequent waves. Of course, in the second case, the initial turbulence is not homogeneous and isotropic, but it is usually reasonably isotropic (Rapp & Melville, 1990) and its integral length scale is generally considerably smaller than the wavelength, since wave breaking is a highly localised process. Hence the condition $l \ll \lambda_w$ is approximately satisfied.

In the formulation adopted by Hunt (1973), RDT is based on the linearised inviscid equations of motion. For example, the linearised vorticity equation can be written

$$\frac{\partial \omega_i}{\partial t} + U_j \frac{\partial \omega_i}{\partial x_j} + u_j \frac{\partial \Omega_i}{\partial x_j} = \Omega_j \frac{\partial u_i}{\partial x_j} + \omega_j \frac{\partial U_i}{\partial x_j}, \tag{5.2}$$

where $\mathbf{\Omega} = \nabla \times \mathbf{U}$ is the vorticity of the mean flow and $\omega = \nabla \times \mathbf{u}$ is the vorticity of the turbulence. In the present case, U_i is the velocity associated with an irrotational surface wave, so $\Omega_i = 0$. If u is defined as the initial root-mean-square (RMS) velocity of the turbulence, U as the typical velocity scale of the mean flow and L as the typical length scale over which the mean flow varies, the conditions for the validity of (5.2) are that the turbulent velocity is sufficiently weak compared with the mean velocity, $u \ll U$, and that the strain rate of the mean flow is higher than that associated with the interaction of the turbulence with itself, $u/l \ll U/L$. The first condition is immediately satisfied if, additionally to the second, $l \ll L$ is also satisfied. It will be seen later that this last condition on the length scales is convenient if the equations of motion are to be simplified by being expressed in a curvilinear coordinate system aligned with the mean flow (Durbin & Hunt, 1980), because in that case the curvature terms in the equations are of $O(l/L)$ and can be neglected, i.e. the equations take at leading order the same form as in a cartesian coordinate system.

In the particular flow under consideration, the length scale of the mean flow is the wavelength of the wave λ_w and the strain rate associated with the wave is of $O(a_w k_w \sigma_w)$, so the conditions for which the linear RDT model is valid are

$$l \ll \lambda_w, \quad a_w k_w \gg \frac{u}{l\sigma_w}. \tag{5.3}$$

Hence, the turbulence has to be of relatively small scale and the steepness of the wave cannot be too small.

Turbulence generated by a grid (Brumley and Jirka, 1989) or associated with a wind-induced shear current (Melville *et al.*, 1998) generally has an integral length scale of $O(1\text{cm})$ or larger and turbulence generated by breaking waves is certainly not likely to be smaller than this (see table V of Kitaigorodskii *et al.*, 1983). Since the transition between the gravity and capillary regimes of surface waves occurs at a wavelength $\approx$ 1.7cm, the first condition of (5.3) is only satisfied if the wave that distorts the turbulence is a gravity wave. Then, if it is noted that, in the gravity regime, $\sigma_w = (2\pi g/\lambda_w)^{\frac{1}{2}}$, the second equation of (5.3) may also be expressed as a condition on the wavelength, and (5.3) takes the more compact form

$$l \ll \lambda_w \ll 2\pi g \left(\frac{l}{u} a_w k_w \right)^2 . \tag{5.4}$$

Taking the reasonable values $l = 5\text{cm}$, $u = 1\text{cm}\,\text{s}^{-1}$, $a_w k_w = 0.1$, and $g = 9.8\text{m}\,\text{s}^{-1}$, the following estimate for the range of applicability of the model is obtained:

$$5\text{cm} \ll \lambda_w \ll 15.4\text{m}. \tag{5.5}$$

This condition is easily satisfied for laboratory waves, and for an important fraction of the gravity waves existing in the ocean.

5.2.1 Mathematical formulation

For applying RDT to mean flows as complex as that associated with a progressive surface wave, it is convenient to express the vorticity equation (5.2) in the intrinsically lagrangian form due to Cauchy

(Batchelor & Proudman, 1954),

$$\omega_i(\mathbf{x},t) = \frac{\partial x_i}{\partial a_j}\omega_j(\mathbf{a},0), \tag{5.6}$$

where

$$x_i(\mathbf{a},t) = a_i + \int_0^t U_i(\mathbf{x},t')\mathrm{d}t' \tag{5.7}$$

is the position at time t of a fluid parcel with initial position a_i. $\partial x_i/\partial a_j$ is the strain tensor, which gives the ratio of the separations, along the 3 coordinate directions, of two infinitesimally distant material particles at a given time, following the fluid motion, and at the initial time. It should be noted that (5.6) is already a linearisation, like (5.2), and that $\Omega_i = 0$ has been assumed. If the mean flow was not irrotational, (5.6) would have to include Ω_i as well, and the strain tensor would include the distortion of the mean vorticity by the turbulent velocity, as pointed out recently by Nazarenko *et al.* (1999). This would make the calculations much more complicated.

Given the initial turbulent velocity field $u_i(\mathbf{a},0)$, the initial turbulent vorticity $\omega = \nabla \times \mathbf{u}$ is easily obtained by taking the curl and, once the strain tensor is known, the final velocity field may be recovered from the final vorticity obtained from (5.6) by solving the equation

$$\nabla^2\mathbf{u} = -\nabla \times \omega, \tag{5.8}$$

which results from taking the curl of the definition of turbulent vorticity. The remaining problem, therefore, is determining $\partial x_i/\partial a_j$ as a function of the mean velocity field.

Durbin (1978) noted that the form taken by the strain tensor was considerably simplified if the RDT problem was formulated in a streamline coordinate system. In fact, such formulation is not only advantageous for simplifying the form taken by the equations of motion but also for simplifying the boundary conditions, which would otherwise be awkward to impose. Therefore, in the present model, a curvilinear coordinate system is adopted, where x_1 (the direction along which the wave propagates) is replaced by ϕ, the velocity potential of the wave motion, x_2 remains as the cross-stream horizontal coordinate and x_3 (the vertical coordinate) is replaced by ψ, the streamfunction. The new curvilinear coordinates are defined by the relations

$$U_1 = \frac{\partial\phi}{\partial x_1} = \frac{\partial\psi}{\partial x_3}, \quad U_3 = \frac{\partial\phi}{\partial x_3} = -\frac{\partial\psi}{\partial x_1}. \tag{5.9}$$

The spatial coordinates and components of vectors in the new curvilinear system retain the subscripts 1, 2 and 3, respectively, for the direction along the streamlines, horizontally across the stream-

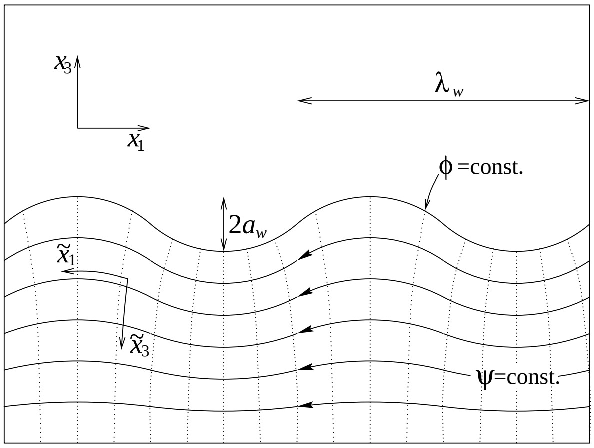

Figure 5.1 Schematic diagram of the model problem in a frame of reference moving with the wave, showing the streamlines (solid) and lines of constant potential (dotted), and the cartesian and curvilinear coordinate systems.

lines and along lines of constant potential, but are distinguished from their cartesian counterparts by a tilde. The infinitesimal length element in the direction along the streamlines is $\tilde{U}_1^{-1}\mathrm{d}\phi$, where $\tilde{U}_1 = (U_1^2 + U_3^2)^{\frac{1}{2}}$ and the length element along the lines of constant potential is $\tilde{U}_1^{-1}\mathrm{d}\psi$. The spatial derivatives along the 3 coordinate directions are defined as

$$\frac{\partial}{\partial \tilde{x}_1} = \tilde{U}_1 \frac{\partial}{\partial \phi}, \quad \frac{\partial}{\partial \tilde{x}_2} = \frac{\partial}{\partial x_2}, \quad \frac{\partial}{\partial \tilde{x}_3} = \tilde{U}_1 \frac{\partial}{\partial \psi}. \tag{5.10}$$

The flow configuration and coordinate systems for a surface wave propagating in the positive x_1 direction is presented schematically in figure 5.1. Note that the orientation of the curvilinear coordinates is approximately opposite to that of the cartesian coordinates (except for $\tilde{x}_2$), with $\tilde{x}_1$ pointing to the left and $\tilde{x}_3$ pointing downwards.

In the curvilinear coordinate system, Cauchy's equation takes an exact form analogous to (5.6), but the strain tensor is considerably simpler than when expressed in a cartesian coordinate system, namely

$$\frac{\partial \tilde{\mathbf{x}}}{\partial \tilde{\mathbf{a}}} = \begin{pmatrix} \frac{\tilde{U}_1}{\tilde{U}_{10}} & 0 & \tilde{U}_1 \frac{\partial \tau_0}{\partial \tilde{a}_3} - \tilde{U}_{10} \frac{\partial \tau}{\partial \tilde{x}_3} \\ 0 & 1 & 0 \\ 0 & 0 & \frac{\tilde{U}_{10}}{\tilde{U}_1} \end{pmatrix}, \tag{5.11}$$

where the subscript 0 denotes variables evaluated at the initial time, before any turbulence distortion has taken place, and τ is the *travel time* of a fluid parcel, defined as

$$\tau = \int^{\phi} \frac{\mathrm{d}\phi'}{\tilde{U}_1^2}. \tag{5.12}$$

For turbulence flowing around a bluff body (Hunt, 1973; Durbin, 1981), the 'initial position' used in the model, where the turbulence is undistorted, is infinitely upstream of the body, so U_{10} is the free-stream velocity, which is assumed constant. As a consequence $\partial\tau_0/\partial\tilde{a}_3 = 0$ and (5.11) simplifies further. If the mean flow is a periodic wave, however, there is no obvious choice for the initial position, which has to be imposed rather arbitrarily. $\tilde{U}_{10}$ and $\partial\tau_0/\partial\tilde{a}_3$ then depend on the location of the initial position relative to the phase of the wave and must be retained in (5.11). This dependence of the model on the initial position will be explored in §5.3. In the case of turbulence generated by a breaking wave, it is perhaps to be expected that the turbulence is injected at the forward slope of the wave (Rapp & Melville, 1990), and as a result, most of the calculations presented in §5.3 use this as the initial position.

5.2.2 The mean velocity field

The mean velocity field considered in the present model is that associated with a relatively small-amplitude, monochromatic surface wave, expressed in a frame of reference travelling with the phase velocity of the wave $c_w = \sigma_w/k_w$. Following Longuet-Higgins (1984), the wave motion is expressed here as a function of the curvilinear coordinates ϕ and ψ, but only the first term in the corresponding series expansion (his equation (4.4)) is considered. This is a good approximation for low wave slopes. The horizontal and vertical velocity components are

$$\begin{aligned} U_1 &= c_w \left(a_w k_w \mathrm{e}^{-k_w\psi/c_w} \cos(k_w\phi/c_w) - 1 \right) \\ U_3 &= -c_w a_w k_w \mathrm{e}^{-k_w\psi/c_w} \sin(k_w\phi/c_w), \end{aligned} \tag{5.13}$$

which satisfy continuity and irrotationality, and lead to

$$\tilde{U}_1 = c_w \left(1 + a_w^2 k_w^2 \mathrm{e}^{-2k_w\psi/c_w} - 2a_w k_w \mathrm{e}^{-k_w\psi/c_w} \cos(k_w\phi/c_w) \right)^{\frac{1}{2}} . \tag{5.14}$$

The advantage of this peculiar formulation of the wave motion is that it enables an easy analytical evaluation of the travel time function τ. On performing the integration over ϕ' in (5.12), the result is

$$\begin{aligned} \tau(\phi,\psi) = {} & \frac{2}{c_w k_w} \frac{1}{1 - a_w^2 k_w^2 \mathrm{e}^{-2k_w\psi/c_w}} \left[\arctan\left(\frac{1 + a_w k_w \mathrm{e}^{-k_w\psi/c_w}}{1 - a_w k_w \mathrm{e}^{-k_w\psi/c_w}} \tan\left(\frac{k_w\phi}{2c_w}\right) \right) \right. \\ & \left. + \pi \mathrm{Int}\left(\frac{k_w\phi/c_w + \pi}{2\pi} \right) \right] + f(\psi), \end{aligned} \tag{5.15}$$

where f is an arbitrary function and Int denotes 'integer part'. The second term between square brackets has to be introduced in order for τ to be a monotonically increasing function of the velocity potential, because the arctan function is limited to take values in the interval $(-\pi/2, \pi/2)$.

From (5.11), (5.14) and (5.15), it follows that the strain tensor is specified completely as a function of ϕ and ψ, ϕ_0 and ψ_0. Therefore, to obtain the evolution of the turbulence along the wave profile, values for ϕ_0 and ψ_0 must be chosen to specify the initial position, and then the relevant turbulent quantities may be calculated along a streamline ($\psi = \psi_0$), for different values of ϕ. However, it would be convenient to express the results as a function of more physically significant variables like time or space. A rigorous relation between the cartesian and the curvilinear coordinates requires the numerical resolution of complicated equations, but a very simple approximation, valid for low wave slopes, is readily available. Equations (5.9) and (5.13) show that, to zeroth order in the wave slope, $\phi \approx -c_w x_1$ and $\phi_0 \approx -c_w a_1$. Now, to the same order of approximation, it follows from (5.7) that $x_1 \approx a_1 - c_w t$. Then, subtracting the initial from the final potential, $\phi - \phi_0 = -c_w(x_1 - a_1) = c_w^2 t$, so that finally

$$t \approx (\phi - \phi_0)/c_w^2. \tag{5.16}$$

This shows that the time can be approximately related to the potential function. When the turbulence statistics are plotted as a function of time, in §5.3, t will always be defined according to (5.16), so it must be recalled, when interpreting the results, that (5.16) is only an approximate equality.

5.2.3 Fourier analysis of the turbulence

Far from the free surface, the turbulence is not affected by the wave nor directly by the boundary, and remains homogeneous, isotropic and stationary. Since the scale over which the motion associated with the wave varies is much larger than the initial integral length scale of the turbulence (see the first equation of (5.3)), at distances from the free surface in the range $l < \tilde{x}_3 < \lambda_w$, the turbulence is distorted by the wave motion (which penetrates to a depth of $O(\lambda_w)$), but not directly by the boundary. In this region, the turbulence is still locally homogeneous, in the sense that it varies over a length scale much larger than its own. So, for depths greater than l, it is justified to represent the turbulent velocity as a three-dimensional Fourier integral, with space and time dependent wavenumbers, in order to account for the slight inhomogeneity of the mean flow. This is the *slow-variation approximation*, also used by Durbin (1981). In the curvilinear coordinate system, the turbulent velocity is thus

$$\tilde{u}_i^{(H)}(\tilde{\mathbf{x}}, t) = \iiint \hat{\tilde{u}}_i^{(H)}(\tilde{\mathbf{k}}, \tilde{\mathbf{x}}, t) e^{i\tilde{\mathbf{k}}\cdot\tilde{\mathbf{x}}} d\tilde{k}_1 d\tilde{k}_2 d\tilde{k}_3, \tag{5.17}$$

where $\tilde{\mathbf{k}}(\tilde{\mathbf{x}}, t) = (\tilde{k}_1, \tilde{k}_2, \tilde{k}_3)$ is the wavenumber vector, and the spatial coordinates in the plane of the wave motion can be approximated locally as $\tilde{x}_1 = \phi/\tilde{U}_1$, $\tilde{x}_3 = \psi/\tilde{U}_1$. The vorticity of the turbulence may be expressed in a formally similar way:

$$\tilde{\omega}_i^{(H)}(\tilde{\mathbf{x}}, t) = \iiint \hat{\tilde{\omega}}_i^{(H)}(\tilde{\mathbf{k}}, \tilde{\mathbf{x}}, t) e^{i\tilde{\mathbf{k}}\cdot\tilde{\mathbf{x}}} d\tilde{k}_1 d\tilde{k}_2 d\tilde{k}_3. \tag{5.18}$$

Invoking the slow-variation approximation, it is now possible to relate the Fourier amplitudes of the turbulent velocity and of the turbulent vorticity through an algebraic relation, in exactly the same way as in a cartesian coordinate system, namely

$$\hat{\tilde{\omega}}_i^{(H)} = \varepsilon_{ijk}\mathrm{i}\tilde{k}_j\hat{\tilde{u}}_k^{(H)}, \tag{5.19}$$

where terms of higher order in the parameter (l/λ_w) have been ignored. Taking the external product of the wavenumber vector with this expression, an equation equivalent to (5.8) in the spectral domain is obtained,

$$\hat{\tilde{u}}_i^{(H)} = \varepsilon_{ijk}\mathrm{i}\frac{\tilde{k}_j}{k^2}\hat{\tilde{\omega}}_k^{(H)}, \tag{5.20}$$

where $k = (\tilde{k}_1^2 + \tilde{k}_2^2 + \tilde{k}_3^2)^{\frac{1}{2}}$ is the wavenumber magnitude.

The Cauchy equation can be expressed in terms of Fourier amplitudes by using (5.6) (with tildes, in the curvilinear coordinate system) and (5.18), yielding

$$\begin{aligned}
\hat{\tilde{\omega}}_i^{(H)}(\tilde{\mathbf{k}}, \tilde{\mathbf{x}}, t) &= \frac{\partial \tilde{x}_i}{\partial \tilde{a}_j}\mathrm{e}^{\mathrm{i}(\tilde{\mathbf{k}}_0\cdot\tilde{\mathbf{a}} - \tilde{\mathbf{k}}\cdot\tilde{\mathbf{x}})}\hat{\tilde{\omega}}_j^{(H)}(\tilde{\mathbf{k}}_0, \tilde{\mathbf{a}}, 0), \\
\tilde{k}_i(\tilde{\mathbf{x}}, t) &= \frac{\partial \tilde{a}_j}{\partial \tilde{x}_i}\tilde{k}_{0j},
\end{aligned} \tag{5.21}$$

where $\tilde{\mathbf{k}}_0 = (\tilde{k}_{01}, \tilde{k}_{02}, \tilde{k}_{03}) = \tilde{\mathbf{k}}(\tilde{\mathbf{a}}, 0)$ is the wavenumber vector at the initial time. Applying (5.19) to obtain the initial vorticity amplitude in (5.21) as a function of the velocity amplitude and inserting the final vorticity amplitude given by (5.21) into (5.20) yields

$$\hat{\tilde{u}}_i^{(H)}(\tilde{\mathbf{k}}, \tilde{\mathbf{x}}, t) = -\varepsilon_{ijk}\varepsilon_{lmn}\frac{\tilde{k}_j\tilde{k}_{0m}}{k^2}\frac{\partial \tilde{x}_k}{\partial \tilde{a}_l}\mathrm{e}^{\mathrm{i}(\tilde{\mathbf{k}}_0\cdot\tilde{\mathbf{a}} - \tilde{\mathbf{k}}\cdot\tilde{\mathbf{x}})}\hat{\tilde{u}}_n^{(H)}(\tilde{\mathbf{k}}_0, \tilde{\mathbf{a}}, 0), \tag{5.22}$$

which, together with the second equation of (5.21) and (5.17), completely defines the final distorted turbulent velocity field as a function of the initial undistorted turbulent velocity field.

5.2.4 Blocking effect of the boundary

At distances from the free surface of $O(l)$ or shorter, the turbulence is no longer locally homogeneous, since it is forced to adjust to the boundary condition in the direction normal to the boundary. For turbulence with sufficiently low Froude and Weber numbers (see chapter 1), the effect of the boundary is primarily blocking. This effect can be included in the model in a very simple way by adding an irrotational correction to the velocity field such that the normal velocity component of the turbulence vanishes at the boundary (Hunt & Graham, 1978). Equation (5.2) ensures that, for an irrotational mean flow, if an irrotational correction to the turbulent velocity exists initially, that correction remains irrotational at all subsequent times. The total velocity field thus becomes

$$\tilde{u}_i = \tilde{u}_i^{(H)} + \frac{\partial \phi^{(S)}}{\partial \tilde{x}_i}, \quad i = 1, 2, 3, \tag{5.23}$$

where $\phi^{(S)}(\tilde{\mathbf{x}}, t)$ is a velocity potential satisfying

$$\nabla^2 \phi^{(S)} = 0, \tag{5.24}$$

subject to the boundary conditions

$$\frac{\partial \phi^{(S)}}{\partial \tilde{x}_3}(\tilde{x}_3 = 0) = -\tilde{u}_3^{(H)}(\tilde{x}_3 = 0) \quad \text{and} \quad \phi^{(S)}(\tilde{x}_3 \to \infty) = 0. \tag{5.25}$$

Since the velocity potential $\phi^{(S)}$ decays rapidly to zero for $\tilde{x}_3 > l$, but remains locally homogeneous along the other two coordinate directions, it can be expressed as a two-dimensional Fourier integral as follows:

$$\phi^{(S)}(\tilde{\mathbf{x}}, t) = \iint \hat{\phi}^{(S)}(\tilde{k}_1, \tilde{k}_2, \tilde{\mathbf{x}}, t) \mathrm{e}^{\mathrm{i}(\tilde{k}_1 \tilde{x}_1 + \tilde{k}_2 \tilde{x}_2)} \mathrm{d}\tilde{k}_1 \mathrm{d}\tilde{k}_2. \tag{5.26}$$

Invoking again the slow-variation approximation, the solution of (5.24) which can be expressed in the form (5.26) and satisfies the boundary conditions (5.25), is formally identical to that found by Hunt & Graham (1978) for turbulence near a flat wall, namely

$$\hat{\phi}^{(S)}(\tilde{k}_1, \tilde{k}_2, \tilde{\mathbf{x}}, t) = \int \frac{\hat{\tilde{u}}_3^{(H)}(\tilde{\mathbf{k}}, \tilde{\mathbf{x}}, t)}{\tilde{k}_{12}} \mathrm{e}^{-\tilde{k}_{12} \tilde{x}_3} \mathrm{d}\tilde{k}_3, \tag{5.27}$$

where $\tilde{k}_{12} = (\tilde{k}_1^2 + \tilde{k}_2^2)^{\frac{1}{2}}$. This expression only differs from that of Hunt & Graham in that the turbulence is not perfectly homogeneous along the $\tilde{x}_1$ and $\tilde{x}_2$ directions, due to the wave motion, so that both the wavenumber $\tilde{\mathbf{k}}$ and $\hat{\tilde{u}}_3^{(H)}$ vary slowly in space and time.

From (5.17), (5.23) and (5.26), it follows that the total turbulent velocity field must be given by a two-dimensional Fourier integral in the form

$$\tilde{u}_i(\tilde{\mathbf{x}}, t) = \iint \hat{\tilde{u}}_i(\tilde{k}_1, \tilde{k}_2, \tilde{\mathbf{x}}, t) \mathrm{e}^{\mathrm{i}(\tilde{k}_1 \tilde{x}_1 + \tilde{k}_2 \tilde{x}_2)} \mathrm{d}\tilde{k}_1 \mathrm{d}\tilde{k}_2, \tag{5.28}$$

where the Fourier amplitude is defined as

$$\begin{aligned}\hat{\hat{u}}_i &= \int \hat{\hat{u}}_i^{(H)} \mathrm{e}^{\mathrm{i}\tilde{k}_3\tilde{x}_3} \mathrm{d}\tilde{k}_3 + \mathrm{i}\tilde{k}_i \hat{\phi}^{(S)}, \quad i = 1, 2 \\ \hat{\hat{u}}_3 &= \int \hat{\hat{u}}_3^{(H)} \mathrm{e}^{\mathrm{i}\tilde{k}_3\tilde{x}_3} \mathrm{d}\tilde{k}_3 + \frac{\partial \hat{\phi}^{(S)}}{\partial \tilde{x}_3}.\end{aligned} \tag{5.29}$$

Taking into account (5.22), (5.27) and (5.29), the Fourier amplitude of the total distorted turbulent velocity (including the effects of distortion by the wave and by the boundary) may be related to the initial undistorted amplitude through

$$\hat{\hat{u}}_i(\tilde{k}_1, \tilde{k}_2, \tilde{\mathbf{x}}, t) = \int \tilde{M}_{ij}(\tilde{\mathbf{k}}, \tilde{\mathbf{x}}, t) \hat{\hat{u}}_j^{(H)}(\tilde{\mathbf{k}}_0, \tilde{\mathbf{a}}, 0) \mathrm{d}\tilde{k}_3, \tag{5.30}$$

where the elements of the matrix $\tilde{M}_{ij}$ can be seen as 'transfer functions'. Since, as was just seen, the effect of the boundary may be taken into account by simply applying the changes due to blocking to the turbulence already distorted by the wave, the functions $\tilde{M}_{ij}$ may be decomposed as

$$\tilde{M}_{ij}(\tilde{\mathbf{k}}, \tilde{\mathbf{x}}, t) = \tilde{B}_{ik}(\tilde{\mathbf{k}}, \tilde{\mathbf{x}}, t) \tilde{W}_{kj}(\tilde{\mathbf{k}}, \tilde{\mathbf{x}}, t), \tag{5.31}$$

where the matrix $\tilde{B}_{ik}$ accounts for blocking and the matrix $\tilde{W}_{ik}$ accounts for distortion by the wave (cf. chapter 3). The effect of the wave is deduced from (5.22), and leads to

$$\tilde{W}_{in} = -\varepsilon_{ijk}\varepsilon_{lmn} \frac{\tilde{k}_j \tilde{k}_{0m}}{k^2} \frac{\partial \tilde{x}_k}{\partial \tilde{a}_l} \mathrm{e}^{\mathrm{i}(\tilde{\mathbf{k}}_0 \cdot \tilde{\mathbf{a}} - \tilde{\mathbf{k}} \cdot \tilde{\mathbf{x}})}, \tag{5.32}$$

while the effect of blocking is deduced from (5.27) and (5.29), yielding

$$\begin{aligned}\tilde{B}_{ii} &= \mathrm{e}^{\mathrm{i}\tilde{k}_3\tilde{x}_3} \\ \tilde{B}_{i3} &= \mathrm{i}\frac{\tilde{k}_i}{\tilde{k}_{12}} \mathrm{e}^{-\tilde{k}_{12}\tilde{x}_3}, \quad i = 1, 2 \\ \tilde{B}_{33} &= \mathrm{e}^{\mathrm{i}\tilde{k}_3\tilde{x}_3} - \mathrm{e}^{-\tilde{k}_{12}\tilde{x}_3},\end{aligned} \tag{5.33}$$

with the remaining elements of $\tilde{B}_{ij}$ being equal to zero.

The turbulent velocity distorted by both the wave orbital motion and by the boundary is thus completely defined as a function of the undistorted turbulent velocity. It remains to prescribe the characteristics of the undistorted turbulence and to calculate statistics of the turbulence at various stages of distortion.

5.2.5 Statistics of the turbulent velocity field

In order to analyse the structure of the turbulence, statistics of the turbulent velocity field are required. The intensity and correlation of the velocity fluctuations is characterised by the Reynolds stresses. These may be calculated from the Fourier amplitudes of the turbulent velocity using

$$\overline{\tilde{u}_i\tilde{u}_j} = \iiiint \overline{\hat{\tilde{u}}_i^*(\tilde{k}_1,\tilde{k}_2)\hat{\tilde{u}}_j(\tilde{k}_1',\tilde{k}_2')}\,\mathrm{d}\tilde{k}_1\mathrm{d}\tilde{k}_2\mathrm{d}\tilde{k}_1'\mathrm{d}\tilde{k}_2', \tag{5.34}$$

where the asterisk denotes complex conjugation and the overbar denotes ensemble averaging. Equation (5.30) implies that

$$\overline{\hat{\tilde{u}}_i^*(\tilde{k}_1,\tilde{k}_2)\hat{\tilde{u}}_j(\tilde{k}_1',\tilde{k}_2')} = \iint \tilde{M}_{ik}^*(\tilde{\mathbf{k}})\tilde{M}_{jl}(\tilde{\mathbf{k}}')\overline{\hat{\tilde{u}}_k^{(H)*}(\tilde{\mathbf{k}}_0)\hat{\tilde{u}}_l^{(H)}(\tilde{\mathbf{k}}_0')}\,\mathrm{d}\tilde{k}_3\mathrm{d}\tilde{k}_3'. \tag{5.35}$$

Now, the three-dimensional spectrum of the initial undistorted turbulent velocity $\tilde{\Phi}_{ij}^{(H)}$ is defined as

$$\overline{\hat{\tilde{u}}_i^{(H)*}(\tilde{\mathbf{k}}_0)\hat{\tilde{u}}_j^{(H)}(\tilde{\mathbf{k}}_0')} = \tilde{\Phi}_{ij}^{(H)}(\tilde{\mathbf{k}}_0)\delta(\tilde{\mathbf{k}}_0-\tilde{\mathbf{k}}_0'), \tag{5.36}$$

hence (5.34) and (5.35) can be used to obtain a simplified expression for the Reynolds stresses:

$$\overline{\tilde{u}_i\tilde{u}_j} = \iiint \tilde{M}_{ik}\tilde{M}_{jl}\tilde{\Phi}_{kl}^{(H)}\,\mathrm{d}\tilde{k}_1\mathrm{d}\tilde{k}_2\mathrm{d}\tilde{k}_3. \tag{5.37}$$

The spatial structure of the velocity fluctuations in the turbulence is characterised by the integral length scales of the turbulence. For the velocity fluctuations $\tilde{u}_i$ and $\tilde{u}_j$ and along the direction $\tilde{x}_l$ these are defined by

$$\tilde{L}_{ij}^{(l)} = \pi\frac{\tilde{\Theta}_{ij}^{(l)}(\tilde{k}_l=0)}{\overline{\tilde{u}_i\tilde{u}_j}}, \tag{5.38}$$

where $\tilde{\Theta}_{ij}^{(l)}$ is the one-dimensional wavenumber spectrum, along the $\tilde{x}_l$ direction, of the velocity fluctuations $\tilde{u}_i$ and $\tilde{u}_j$. The one-dimensional spectrum along $\tilde{x}_1$ is defined in terms of $\tilde{\Phi}_{kl}^{(H)}$ as

$$\tilde{\Theta}_{ij}^{(1)}(\tilde{k}_1,\tilde{x}_3,t) = \iint \tilde{M}_{ik}\tilde{M}_{jl}\tilde{\Phi}_{kl}^{(H)}\,\mathrm{d}\tilde{k}_2\mathrm{d}\tilde{k}_3, \tag{5.39}$$

and an analogous definition is valid for the spectrum along $\tilde{x}_2$.

The undistorted turbulence is assumed to be isotropic, so its three-dimensional spectrum is related to the energy spectrum in the following way:

$$\tilde{\Phi}_{ij}^{(H)}(\tilde{\mathbf{k}}_0) = \left(\delta_{ij} - \frac{\tilde{k}_{0i}\tilde{k}_{0j}}{k_0^2}\right)\frac{E(k_0)}{4\pi k_0^2}, \tag{5.40}$$

where $E(k_0)$ is the energy spectrum and $k_0 = (\tilde{k}_{01}^2 + \tilde{k}_{02}^2 + \tilde{k}_{03}^2)^{\frac{1}{2}}$ is the initial wavenumber magnitude. Following Hunt & Graham (1978), the well-known von Kármán energy spectrum, which mimics an inertial subrange at high wavenumbers, is adopted here,

$$E(k_0) = u^2 l \frac{g_2 (k_0 l)^4}{(g_1 + (k_0 l)^2)^{\frac{17}{6}}}, \tag{5.41}$$

where $g_1 = 0.558$ and $g_2 = 1.196$ are dimensionless constants.

All the statistics derived in this subsection are expressed in the curvilinear coordinate system aligned with the streamlines. However, these can be readily compared with statistics measured in a cartesian coordinate system, because the two coordinate systems are approximately equivalent for waves of low slope, and in fact coincide exactly at the wave crests and at the wave troughs.

5.2.6 Important parameters

There are seven basic variables controlling the behaviour of the present model: three of them are determined by the mean flow, in this case a surface wave. They are the amplitude a_w, wavenumber k_w and phase velocity c_w of the wave. Two further variables characterise the turbulence: the initial RMS turbulent velocity u and the initial integral length scale l. The remaining two variables are introduced by the initial conditions and the duration of the interaction between the turbulence and the wave: they are, respectively, the initial position relative to the wave phase, $\tilde{a}_1$, which may be approximated as $\tilde{a}_1 \approx \phi_0/c_w$, and time t, which as was seen in §5.2.2 is $t \approx (\phi - \phi_0)/c_w^2$. From these variables, it is possible to construct five independent dimensionless parameters:

$$a_w k_w, \quad k_w \tilde{a}_1, \quad k_w c_w t = \sigma_w t, \quad u/c_w, \quad k_w l. \tag{5.42}$$

It turns out that the statistics of the velocity field do not depend on the parameter u/c_w. So, in the following section, the sensitivity of the model results to the 4 remaining parameters will be tested. Graphs of the normalised Reynolds stresses $\overline{\tilde{u}_i\tilde{u}_j}/u^2$ and integral length scales $\tilde{L}_{ij}^{(k)}/l$ will be plotted as functions of t/T, where $T = 2\pi/\sigma_w$ is the wave period, keeping $a_w k_w$, $k_w\tilde{a}_1$ and $k_w l$ constant. A few profiles of the Reynolds stresses as a function of $\tilde{x}_3/l$ will also be presented, keeping $a_w k_w$, $k_w\tilde{a}_1$, $k_w l$ and t/T constant.

5.3 Results

Results for the distortion of turbulence during a single wave cycle are shown in §5.3.1. In §5.3.2, the distortion of the turbulence by the Stokes drift of the wave is addressed, with the presentation of results for the Reynolds stresses, TKE and integral length scales of the turbulence. In both subsections, the blocking effect of the boundary is ignored. This would correspond in practice to taking measurements at a depth $\tilde{x}_3 \approx l$. In §5.3.3, some results for turbulence distorted by a uniform shear are reproduced, and compared with the preceding results obtained for turbulence distorted by a wave. In §5.3.4, the blocking effect of the boundary is briefly examined, and found to lead to fairly trivial changes to the results. Finally, in §5.3.5 and §5.3.6, scaling analyses of the energy equations are performed, in order to estimate the energy transfer taking place between the wave and the turbulence and its effect on each component of the flow.

5.3.1 Turbulence modulation in a wave cycle

For waves of low slope, the distortion of the turbulence during a single wave cycle is always weak.

Figures 5.2–5.5 show graphs of the diagonal components of the Reynolds stress tensor (velocity variances) as a function of time normalised by the wave period, for different initial positions and different wave slopes. In figure 5.2, the initial position is on the forward slope of the wave, in figure 5.3, it is on the wave crest. In figure 5.4, the initial position is on the backward slope of the wave and in figure 5.5 it is on the wave trough.

Figures 5.2–5.5 show that the modulation of the Reynolds stresses by the wave intensifies as the wave steepness increases, as would be expected. This modulation is approximately sinusoidal at the lowest slopes, but becomes more and more asymmetric as $a_w k_w$ increases. This is partly due to the curvilinear coordinate system used, because ϕ varies faster at the wave troughs than at the wave crests, and the definition of t is based on ϕ (see (5.16)). The value of the Reynolds stresses does not repeat itself after one complete cycle, for the highest slopes considered. This is a manifestation of the irreversible part of the distortion, which is caused by the Stokes drift, and will be treated in detail in the next subsection.

The Reynolds stress tangential to the free surface in the streamwise direction, $\overline{\tilde{u}_1^2}$, attains a maximum approximately at the wave crest and a minimum at the wave trough. The Reynolds stress normal to the free surface, $\overline{\tilde{u}_3^2}$, attains a maximum at the wave trough and a minimum at the wave crest. The tangential Reynolds stress in the cross-stream or spanwise direction, $\overline{\tilde{u}_2^2}$, always increases first and then decreases, attaining a maximum approximately in the middle of the wave cycle, independent of the initial position.

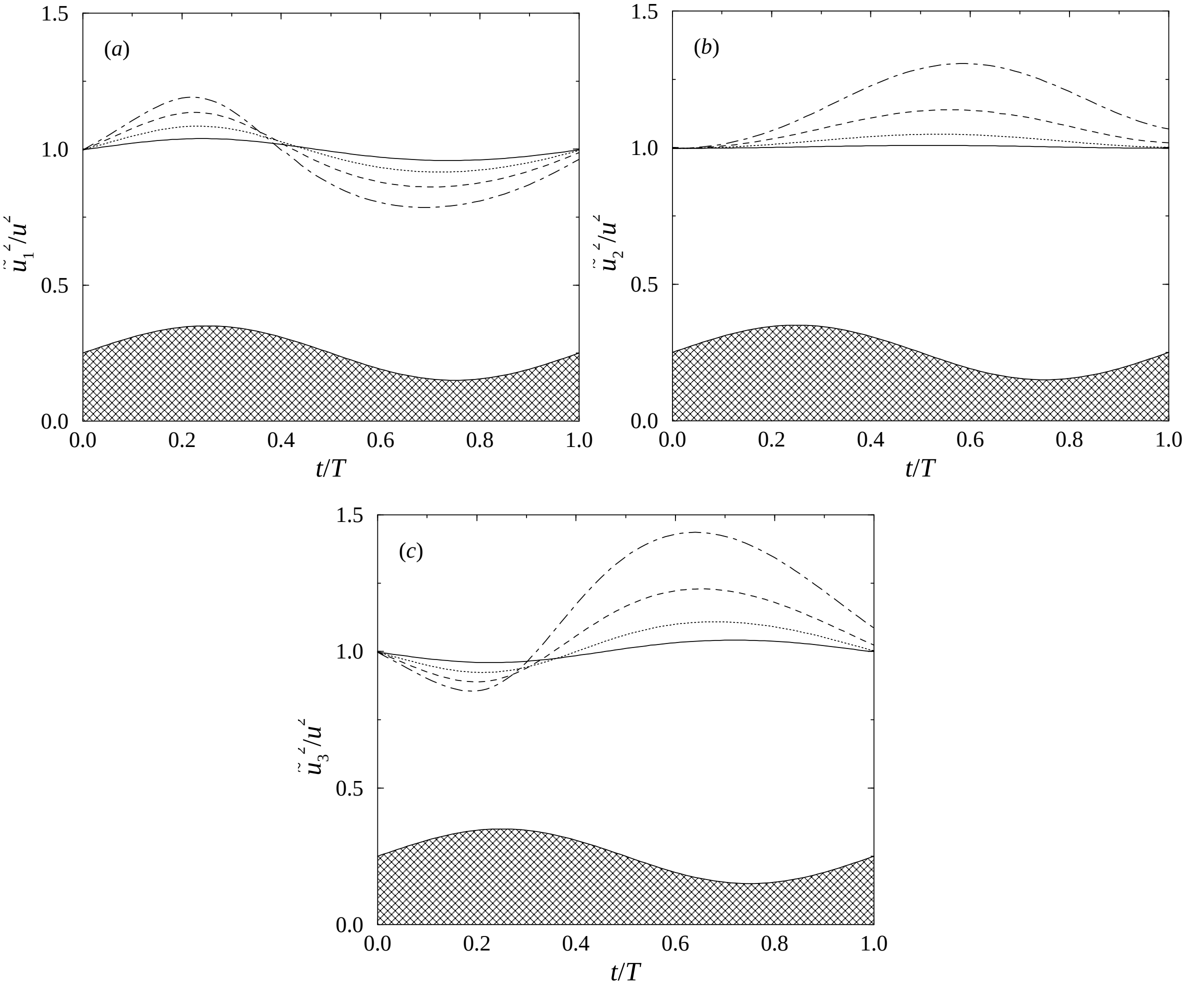

Figure 5.2 Modulation of the Reynolds stresses during a wave cycle, for $\tilde{x}_3 = 0$, $k_w l = 0.6$. Solid line: $a_w k_w = 0.05$, dotted line: $a_w k_w = 0.1$, dashed line: $a_w k_w = 0.15$, dash-dotted line: $a_w k_w = 0.2$, hatched profile: shape of the distorting wave (arbitrary scale). (*a*) streamwise component, (*b*) spanwise component, (*c*) normal component.

Experimental and theoretical support for an increase in the intensity of the vertical velocity fluctuations and a decrease in the intensity of the streamwise velocity fluctuations at a hill crest (here equivalent to a wave trough) is provided by the work of Britter *et al.* (1981) (their equation (3.3) and their figure 4(*b*)). Further experimental support for the predicted Reynolds stress modulation can be found in figure 10 of Thais & Magnaudet (1996), where the streamwise Reynolds stress is greater than the vertical stress at the wave crest, while the reverse happens at the wave trough.

The modulation of the streamwise and normal Reynolds stresses has a peak-to-peak amplitude of ≈ 0.2 for a wave slope of $a_w k_w = 0.1$ and ≈ 0.4 for $a_w k_w = 0.2$, whereas the modulation of the spanwise Reynolds stress has smaller amplitude, perhaps ≈ 0.1 for $a_w k_w = 0.1$ and ≈ 0.2 for $a_w k_w = 0.2$. Although the data of Thais & Magnaudet (1996) are affected by a stronger turbulence intensity at the wave trough, where the (fixed) probe almost touches the free-surface, it is possible

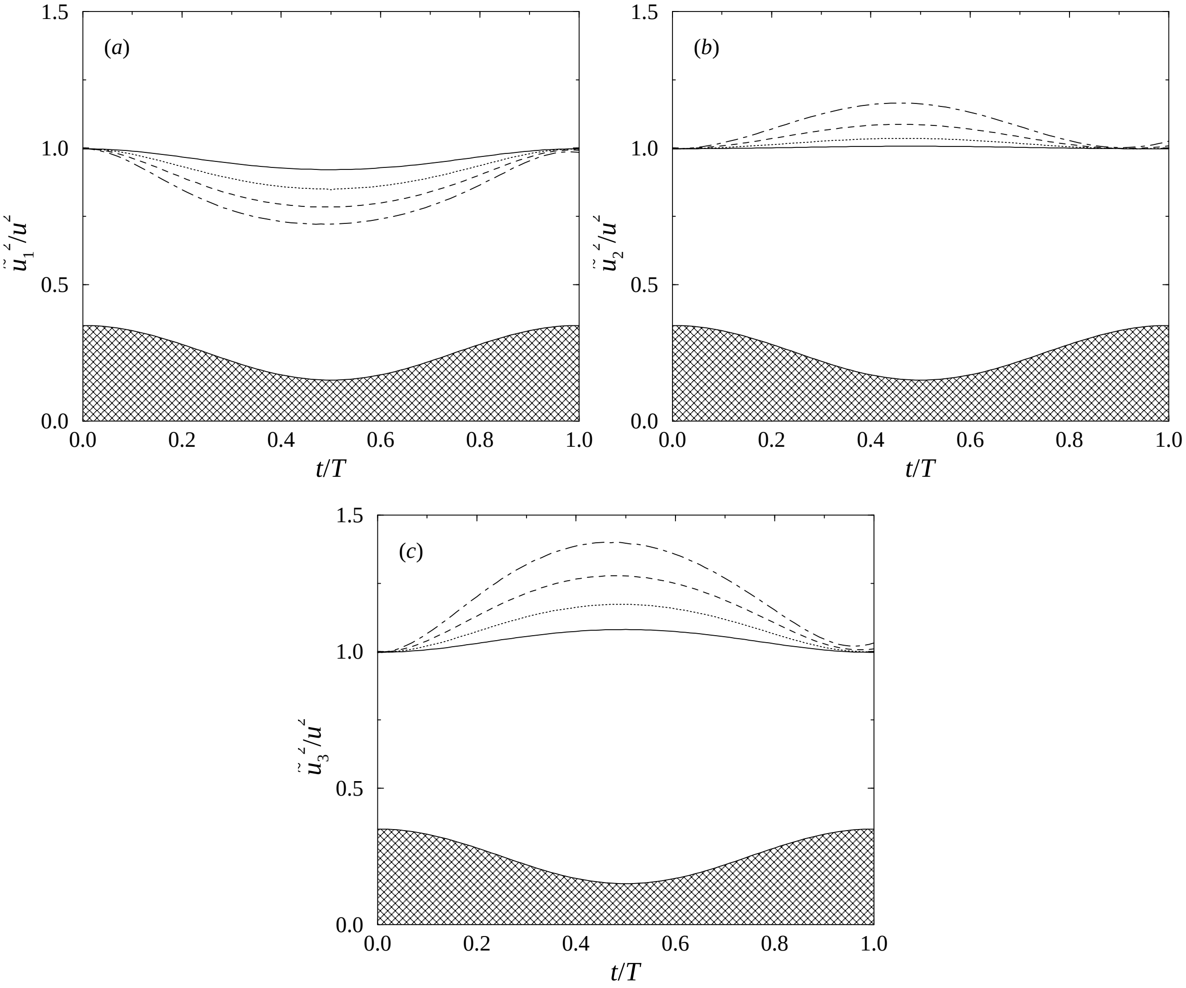

Figure 5.3 Modulation of the Reynolds stresses during a wave cycle, for $\tilde{x}_3 = 0$, $k_w l = 0.6$. Solid line: $a_w k_w = 0.05$, dotted line: $a_w k_w = 0.1$, dashed line: $a_w k_w = 0.15$, dash-dotted line: $a_w k_w = 0.2$, hatched profile: shape of the distorting wave (arbitrary scale). (*a*) streamwise component, (*b*) spanwise component, (*c*) normal component.

to estimate the peak to peak modulations of the streamwise and vertical Reynolds stresses from their figure 10 by determining the value by which the streamwise stress exceeds the vertical stress at the wave crest and the vertical stress exceeds the streamwise stress at the wave trough. From visual inspection, this is estimated as $\approx 0.2 - 0.3$, for a wave slope of ≈ 0.1, and is therefore consistent with the present results. The results will now be explained using a simplified model.

To first order in the wave slope, the distorting effect of a progressive surface wave on turbulence can be understood if the wave is described in a fixed cartesian coordinate system, where the orbital motion can be written

$$\begin{aligned} U_1(x_1, x_3) &= c_w a_w k_w \mathrm{e}^{k_w x_3} \cos(k_w x_1 - \sigma_w t) \\ U_3(x_1, x_3) &= c_w a_w k_w \mathrm{e}^{k_w x_3} \sin(k_w x_1 - \sigma_w t) \end{aligned} \tag{5.43}$$

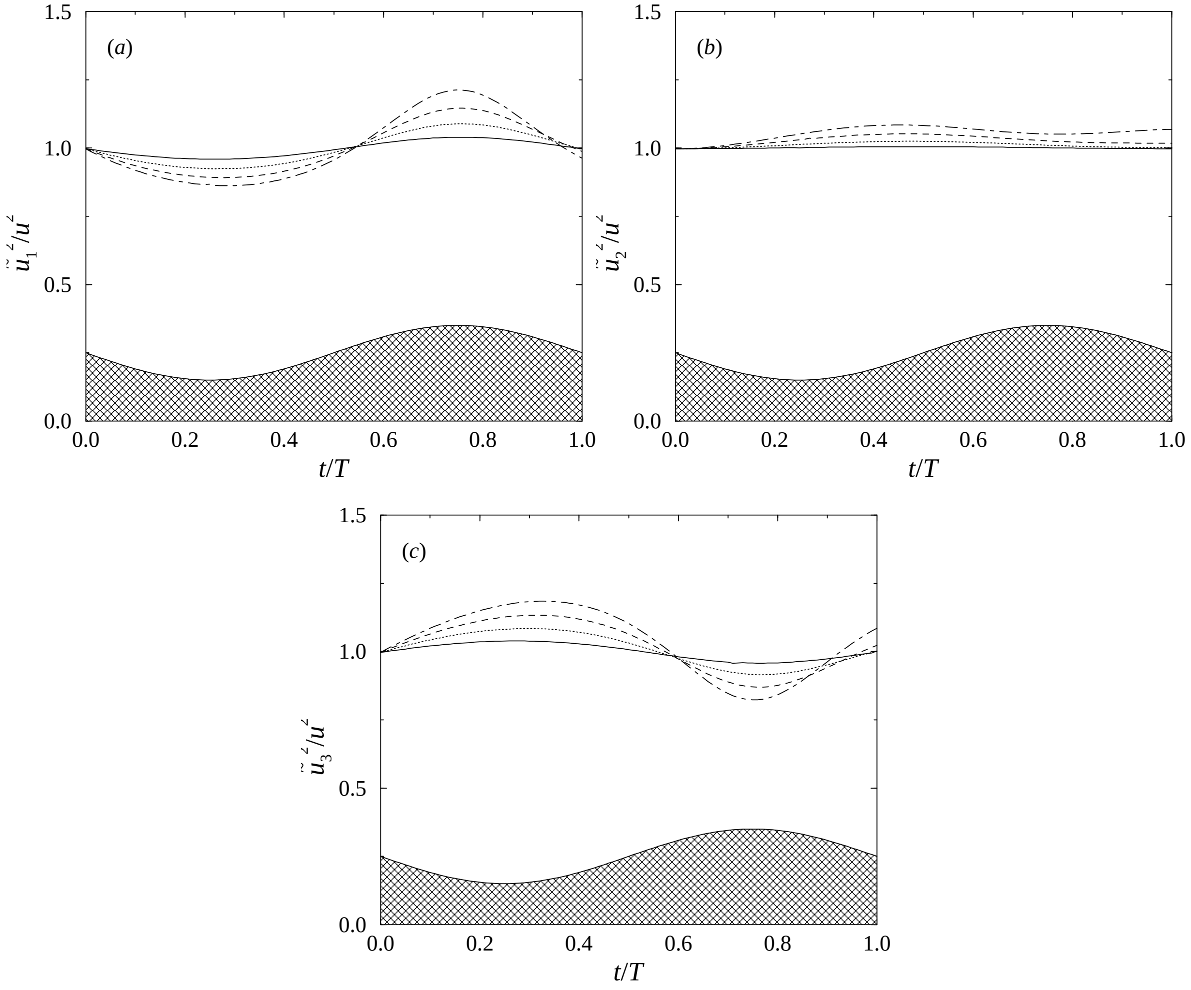

Figure 5.4 Modulation of the Reynolds stresses during a wave cycle, for $\tilde{x}_3 = 0$, $k_w l = 0.6$. Solid line: $a_w k_w = 0.05$, dotted line: $a_w k_w = 0.1$, dashed line: $a_w k_w = 0.15$, dash-dotted line: $a_w k_w = 0.2$, hatched profile: shape of the distorting wave (arbitrary scale). (*a*) streamwise component, (*b*) spanwise component, (*c*) normal component.

for a surface elevation

$$\zeta = a_w \cos(k_w x_1 - \sigma_w t). \tag{5.44}$$

If (5.7) is differentiated with respect to the initial position, it is found that

$$\frac{\partial x_i}{\partial a_j} = \delta_{ij} + \int_0^t \frac{\partial U_i}{\partial x_k}\frac{\partial x_k}{\partial a_j}\mathrm{d}t'. \tag{5.45}$$

When the wave slope is sufficiently low, the distortion is relatively weak and the strain tensor inside the integral may be approximated as $\partial x_k/\partial a_j \approx \delta_{kj}$. On the other hand, the integration in time may be changed from an integration following the fluid parcels to a time integration at a fixed point. Then,

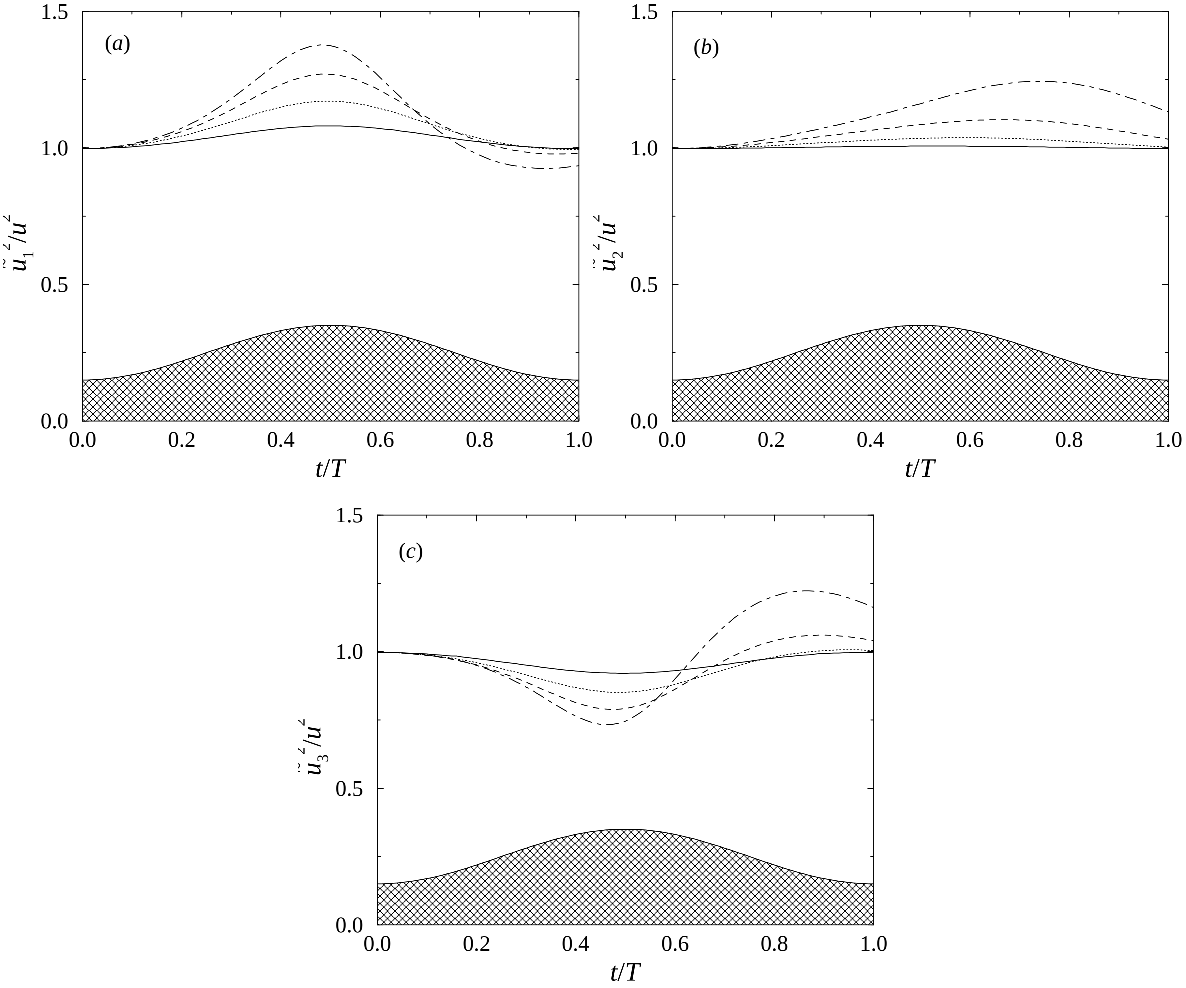

Figure 5.5 Modulation of the Reynolds stresses during a wave cycle, for $\tilde{x}_3 = 0$, $k_w l = 0.6$. Solid line: $a_w k_w = 0.05$, dotted line: $a_w k_w = 0.1$, dashed line: $a_w k_w = 0.15$, dash-dotted line: $a_w k_w = 0.2$, hatched profile: shape of the distorting wave (arbitrary scale). (*a*) streamwise component, (*b*) spanwise component, (*c*) normal component.

differentiating the expressions (5.43) and inserting them into the integrals of (5.45), it is found after integration that, for small $a_w k_w$, the following expressions are approximately valid:

$$\begin{aligned}
\frac{\partial x_1}{\partial a_1} &= 1 - a_w k_w \mathrm{e}^{k_w x_3} \left[\cos(k_w x_1 - \sigma_w t) - \cos(k_w x_1)\right], \\
\frac{\partial x_1}{\partial a_3} &= \frac{\partial x_3}{\partial a_1} = -a_w k_w \mathrm{e}^{k_w x_3} \left[\sin(k_w x_1 - \sigma_w t) - \sin(k_w x_1)\right] \\
\frac{\partial x_3}{\partial a_3} &= 1 + a_w k_w \mathrm{e}^{k_w x_3} \left[\cos(k_w x_1 - \sigma_w t) - \cos(k_w x_1)\right] \\
\frac{\partial x_1}{\partial a_2} &= \frac{\partial x_2}{\partial a_1} = \frac{\partial x_2}{\partial a_3} = \frac{\partial x_3}{\partial a_2} = 0, \quad \frac{\partial x_2}{\partial a_2} = 1.
\end{aligned} \tag{5.46}$$

These expressions show that $\partial x_1/\partial a_1$ is in phase opposition to the surface elevation and thus attains a maximum at the wave troughs and a minimum at the wave crests. This is best understood in the

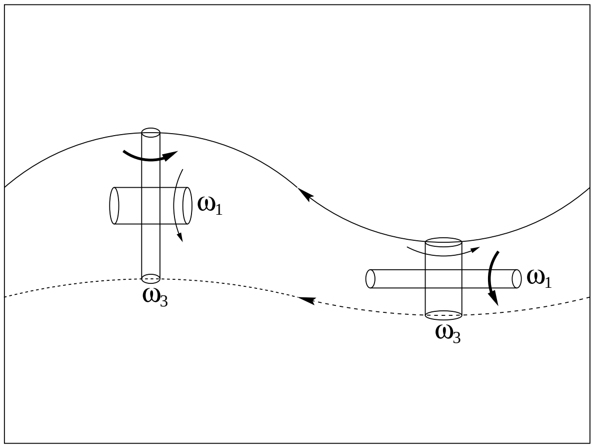

Figure 5.6 Schematic diagram showing the vorticity stretching and compression induced by the orbital motion at the crest and at the trough of a surface wave, in a frame of reference travelling with the wave.

coordinate system travelling with the wave as being the result of the acceleration that the fluid suffers as it moves from crest to trough. $\partial x_3/\partial a_3$, on the other hand, is in phase with the surface elevation and attains a maximum at the crests and a minimum at the troughs. This result follows from the previous one by continuity: a fluid parcel that is stretched in one direction, must contract in the other.

The effect of this distortion on the vorticity is shown schematically in figure 5.6. At the wave crests, the fluid elements are stretched vertically and compressed in the streamwise direction, leading to an intensification of the vertical vorticity and a weakening of the streamwise vorticity. Conversely, at the wave troughs the fluid elements are stretched in the streamwise direction and compressed in the vertical, leading to an amplification of the streamwise vorticity and a weakening of the vertical vorticity.

The streamwise vorticity has contributions from the spanwise and vertical velocity components and the vertical vorticity has contributions from the streamwise and spanwise velocity. Therefore, at the wave crests, the streamwise turbulence intensity should increase and the vertical turbulence intensity should decrease, while at the troughs, the streamwise turbulence intensity should decrease and the vertical turbulence intensity should increase. This reasoning seems to explain the qualitative behaviour of $\overline{\tilde{u}_1^2}$ and $\overline{\tilde{u}_3^2}$ over one wave cycle.

It can also be seen from (5.46) that $\partial x_1/\partial a_3$ and $\partial x_3/\partial a_1$ are both out of phase by $\pi/2$ relative to the surface elevation, attaining maxima on the backward slope of the wave and minima on the forward slope. These components of the strain tensor lead to additional irrotational tilting and stretching of vorticity, whose effects on the Reynolds stresses are not as obvious as those associated with the diagonal components.

The diagonal components of the strain tensor are the extensions suffered by the fluid in the 3 coordinate directions, defined as $e_i = \partial x_i / \partial a_i$. For a slab-symmetric straining flow in the $x_1 - x_3$ plane with the principal axes aligned with the cartesian coordinate system (Townsend, 1976), these extensions have to satisfy

$$e_1 = \beta, \quad e_2 = 1, \quad e_3 = \beta^{-1} \tag{5.47}$$

due to continuity. In the present case, it follows from (5.46) that

$$\beta \approx 1 - a_w k_w \mathrm{e}^{k_w x_3} \left[\cos(k_w x_1 - \sigma_w t) - \cos(k_w x_1) \right]. \tag{5.48}$$

It is then possible to use equation (3.11.9) of Townsend (1976) to estimate the magnitude of the Reynolds stress modulation attributable only to the extensions in the wave velocity field. Townsend's expressions state that, for β sufficiently close to 1,

$$\begin{aligned} \frac{\overline{u_1^2}}{u^2} &= 1 - \frac{4}{5}\frac{\beta - \beta^{-1}}{\beta + \beta^{-1}} \\ \frac{\overline{u_2^2}}{u^2} &= 1 + \frac{8}{35}(\beta - \beta^{-1})^2 \\ \frac{\overline{u_3^2}}{u^2} &= 1 + \frac{4}{5}\frac{\beta - \beta^{-1}}{\beta + \beta^{-1}}. \end{aligned} \tag{5.49}$$

Substituting β using (5.48) and truncating to the lowest order with respect to the perturbation (in this case the wave motion), (5.49) becomes

$$\begin{aligned} \frac{\overline{u_1^2}}{u^2} &= 1 + \frac{4}{5} a_w k_w \mathrm{e}^{k_w x_3} \left[\cos(k_w x_1 - \sigma_w t) - \cos(k_w x_1) \right] \\ \frac{\overline{u_2^2}}{u^2} &= 1 + \frac{32}{35} a_w^2 k_w^2 \mathrm{e}^{2 k_w x_3} \left[\cos(k_w x_1 - \sigma_w t) - \cos(k_w x_1) \right]^2 \\ \frac{\overline{u_3^2}}{u^2} &= 1 - \frac{4}{5} a_w k_w \mathrm{e}^{k_w x_3} \left[\cos(k_w x_1 - \sigma_w t) - \cos(k_w x_1) \right]. \end{aligned} \tag{5.50}$$

This confirms that the existence of a maximum in the streamwise Reynolds stress at the crest and a maximum in the normal Reynolds stress at the trough are due primarily to the extension and compression of the fluid parcels. Equation (5.50) also explains why the spanwise Reynolds stress always takes values above one independent of the initial position relative to the wave phase.

It is clear from (5.50) that both $\overline{u_1^2}/u^2$ and $\overline{u_3^2}/u^2$ are predicted to undergo oscillations of peak-to-peak amplitude $8/5(a_w k_w)$. For a wave slope of $a_w k_w = 0.2$, this corresponds to ≈ 0.32. On the other hand, $\overline{u_2^2}/u^2$ is predicted to undergo oscillations of peak-to-peak amplitude $32/35(a_w k_w)^2$ or

$128/35(a_w k_w)^2$ depending on the initial position relative to the wave phase. For a wave slope of 0.2, this corresponds to ≈ 0.04 and 0.15 respectively. These results are roughly consistent with what is observed in figures 5.2–5.5.

The differences between the predictions of this simplified model and those from the full model are due essentially to two factors: the neglect of the non-diagonal components of the strain tensor, for any wave slope, and the neglect of the Stokes drift, particularly at the highest slopes.

Equation (5.50) also helps to understand how the behaviour of the Reynolds stresses depends on the initial conditions. Due to the way in which the streamwise and normal Reynolds stresses are modulated, when the initial position is, for example, at a crest (figure 5.3(*a*)), the streamwise Reynolds stress departs from a maximum value, which can not be exceeded during its oscillation, whereas the normal Reynolds stress departs from a minimum (figure 5.3(*c*)). This corresponds to setting $k_w x_1 = 0$ in (5.50), which implies indeed that $\overline{u_1^2}/u^2$ is never larger than 1 and $\overline{u_3^2}/u^2$ is never smaller than 1. When the initial position is at a trough ($k_w x_1 = \pi$), exactly the reverse occurs, as can be confirmed in figures 5.5(*a*, *c*).

Given the constraint of initial isotropy of the RDT model, it would seem that the most ‘natural’ initial positions are those in between crests and troughs, because at those positions both the streamwise and normal Reynolds stresses are in the middle of their oscillations, and the flow appears as undistorted as possible. However, the same is still not true for the spanwise Reynolds stress, $\overline{u_2^2}$, since this stress always departs from a minimum. The problem, which is clear inspecting (5.46), is that there is no region in a monochromatic surface wave where the flow can be considered naturally undistorted. Any possible choice of initial position $k_w x_1$ in (5.46) leads to either the diagonal or the off-diagonal components of the strain tensor oscillating asymmetrically with respect to the undistorted state.

From a strictly mathematical viewpoint, this problem might only be avoided if the distorting wave was replaced by a finite wave packet, away from which it would perhaps be more justified to impose isotropy for the turbulence. However, that flow would no longer lead to an analytical travel time function $\tau(\phi, \psi)$, which is one of the main advantages of the present model. Furthermore, from a physical point of view, such situation would not be significantly more realistic than that considered here.

5.3.2 Effect of the Stokes drift

The distortion of the turbulence by the Stokes drift of the wave only becomes clear after a considerable number of wave cycles.

Figure 5.7 shows the evolution of the diagonal components of the Reynolds stress tensor during 10

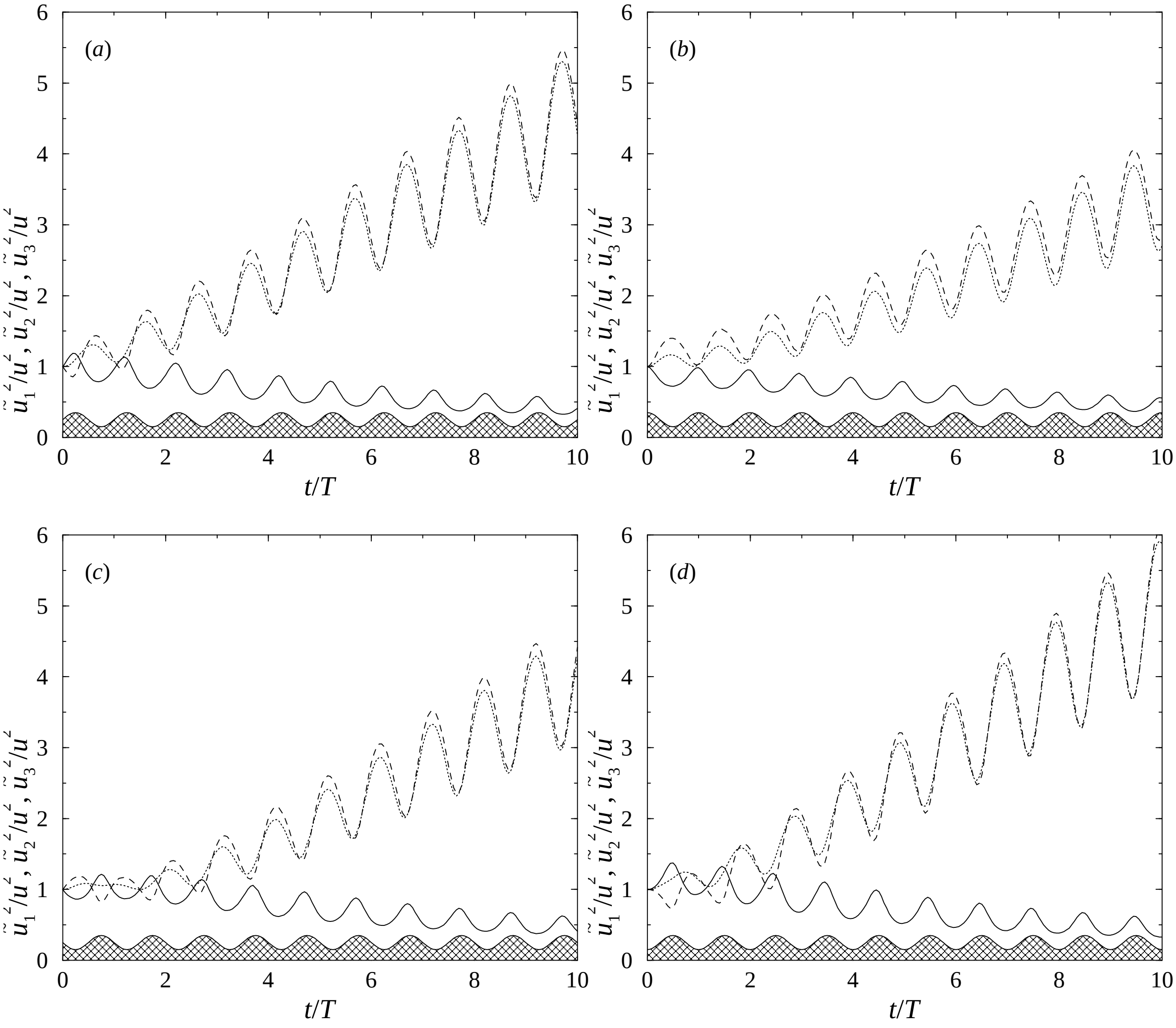

Figure 5.7 Evolution of the Reynolds stresses over 10 wave cycles, for $\tilde{x}_3 = 0$, $k_w l = 0.6$, $a_w k_w = 0.2$. Solid line: streamwise component, dotted line: spanwise component, dashed line: normal component, hatched profile: shape of the distorting wave (arbitrary scale). Turbulence initially at: (*a*) forward slope of wave, (*b*) wave crest, (*c*) backward slope of wave, (*d*) wave trough.

wave cycles, for a wave slope of 0.2 and different initial positions. It is observed that, like in figures 5.2–5.5, the streamwise Reynolds stress, $\overline{\tilde{u}_1^2}$, attains maxima at the crests of the wave and minima at the troughs, and the reverse happens with the normal Reynolds stress, $\overline{\tilde{u}_3^2}$. The spanwise Reynolds stress, $\overline{\tilde{u}_2^2}$, always increases initially irrespective of the phase relation to the wave, as observed in figures 5.2(*b*), 5.3(*b*), 5.4(*b*) and 5.5(*b*), but after a few periods becomes phase-locked to the normal stress, attaining maxima at the wave troughs and minima at the crests.

More importantly, the magnitude of the streamwise Reynolds stress progressively decreases, while the magnitudes of both the spanwise and the normal Reynolds stress progressively increase at a common rate. For the slope considered ($a_w k_w = 0.2$), $\overline{\tilde{u}_1^2}$ becomes approximately half of its initial value after 10 wave cycles, while $\overline{\tilde{u}_2^2}$ and $\overline{\tilde{u}_3^2}$ increase by a factor of about 4. This means that the turbulence

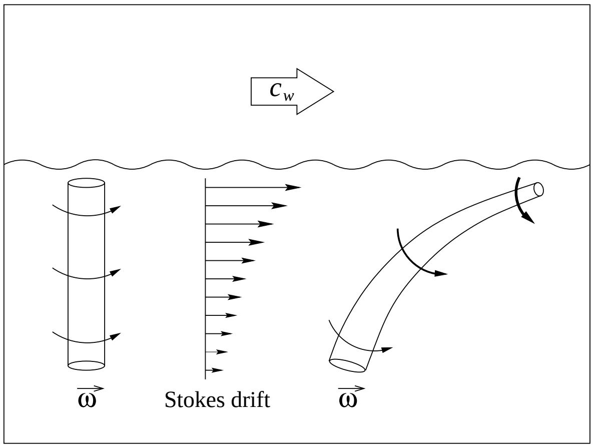

Figure 5.8 Schematic diagram showing the tilting and stretching of vorticity carried out by the Stokes drift of a surface wave over a number of wave cycles, in a fixed frame of reference.

becomes much more intense in the directions perpendicular to the direction of wave propagation. In other words: the turbulence becomes dominated by vortices with their axes of rotation aligned with the streamwise direction, as is the case in Langmuir circulations.

These results should be compared with those presented in figure 6 of McWilliams *et al.* (1997), from large-eddy simulations (LES) of turbulent flow in the ocean surface layer. That figure shows profiles of the Reynolds stresses for turbulence in a shear current (without the effect of a Stokes drift) and when both shear and a Stokes drift are present, with the Stokes drift presumably having the dominant role (Langmuir turbulence). In the case of Langmuir turbulence, the spanwise and normal components of the Reynolds stress are distinctly larger than the streamwise component. This is consistent with the results of figure 5.7.

The physical mechanism for the intensification of the streamwise vortices in the present model is the same as ‘mechanism 2’ of Craik & Leibovich (1976) for the generation of Langmuir circulations. It involves the tilting of vertical vorticity by the Stokes drift of the wave and its amplification as streamwise vorticity (figure 5.8). The difference is that ‘mechanism 2’ of Craik & Leibovich departs from an infinitesimal vertical vorticity perturbation, whereas in the present model, there is initially a finite and isotropic distribution of vorticity, associated with the turbulence, and the Stokes drift selectively amplifies the streamwise vorticity component.

Figure 5.9 shows the time evolution of the Reynolds shear stress, $\overline{\tilde{u}_1\tilde{u}_3}$, during 10 wave cycles, for the same conditions as figure 5.7. Since the turbulence is initially isotropic, the shear stress is initially zero. However, as the turbulence evolves, the shear stress grows to a negative value, stabilising at ≈ -0.7. Like the velocity variances, the shear stress also oscillates during a wave cycle. At initial stages in the turbulence evolution, shear stress maxima (in absolute value) coincide with the backward slopes of the waves, and shear stress minima with the forward slopes. After 10 wave cycles, as the

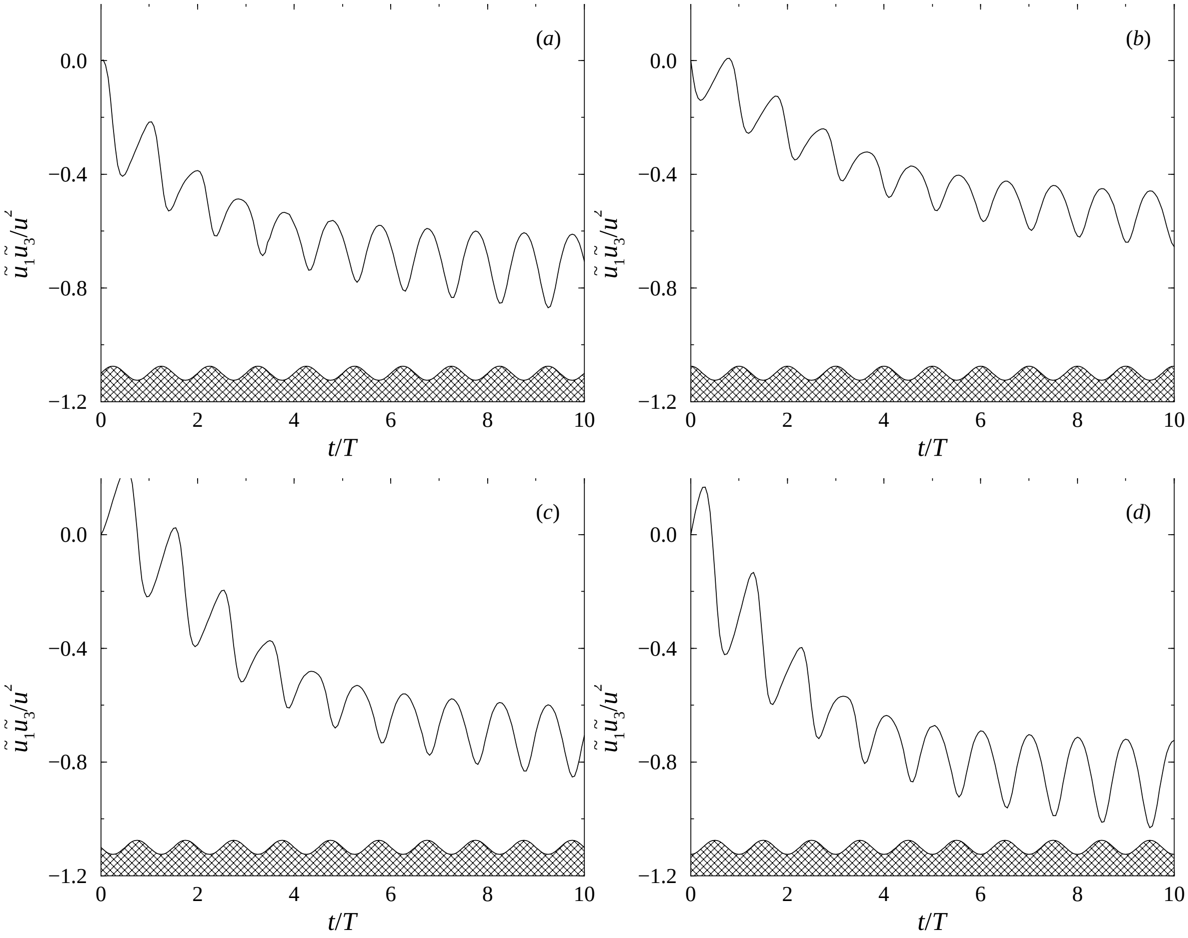

Figure 5.9 Evolution of the Reynolds stresses over 10 wave cycles, for $\tilde{x}_3 = 0$, $k_w l = 0.6$, $a_w k_w = 0.2$. Solid line: shear stress, hatched profile: shape of the distorting wave (arbitrary scale). Turbulence initially at: (*a*) forward slope of wave, (*b*) wave crest, (*c*) backward slope of wave, (*d*) wave trough.

shear stress appears to attain a stable mean value, the maxima occur instead at the wave crests and the minima occur at the wave troughs.

Physically, the existence of a non-zero shear stress in the turbulence is due to the skewing of the velocity fluctuations carried out by the Stokes drift. As the vorticity is tilted from the vertical to an orientation sloping along the direction of wave propagation, and is at the same time amplified, positive streamwise velocity fluctuations tend to be associated with negative normal velocity fluctuations, thereby making $\overline{\tilde{u}_1\tilde{u}_3}$ negative (see figure 5.8). The existence of a non-zero shear stress has important consequences for the energy balance of the turbulence, as will be seen in §5.3.5.

Figure 5.10 shows the time evolution of the turbulent kinetic energy, defined as $TKE = 1/2(\overline{\tilde{u}_1^2} + \overline{\tilde{u}_2^2} + \overline{\tilde{u}_3^2})$, during 10 wave cycles, for the same conditions as figure 5.7. It can be seen that the TKE is also modulated by the waves, displaying an oscillatory behaviour, and tends to become dominated by the spanwise and normal Reynolds stresses as time advances. The TKE progressively increases and

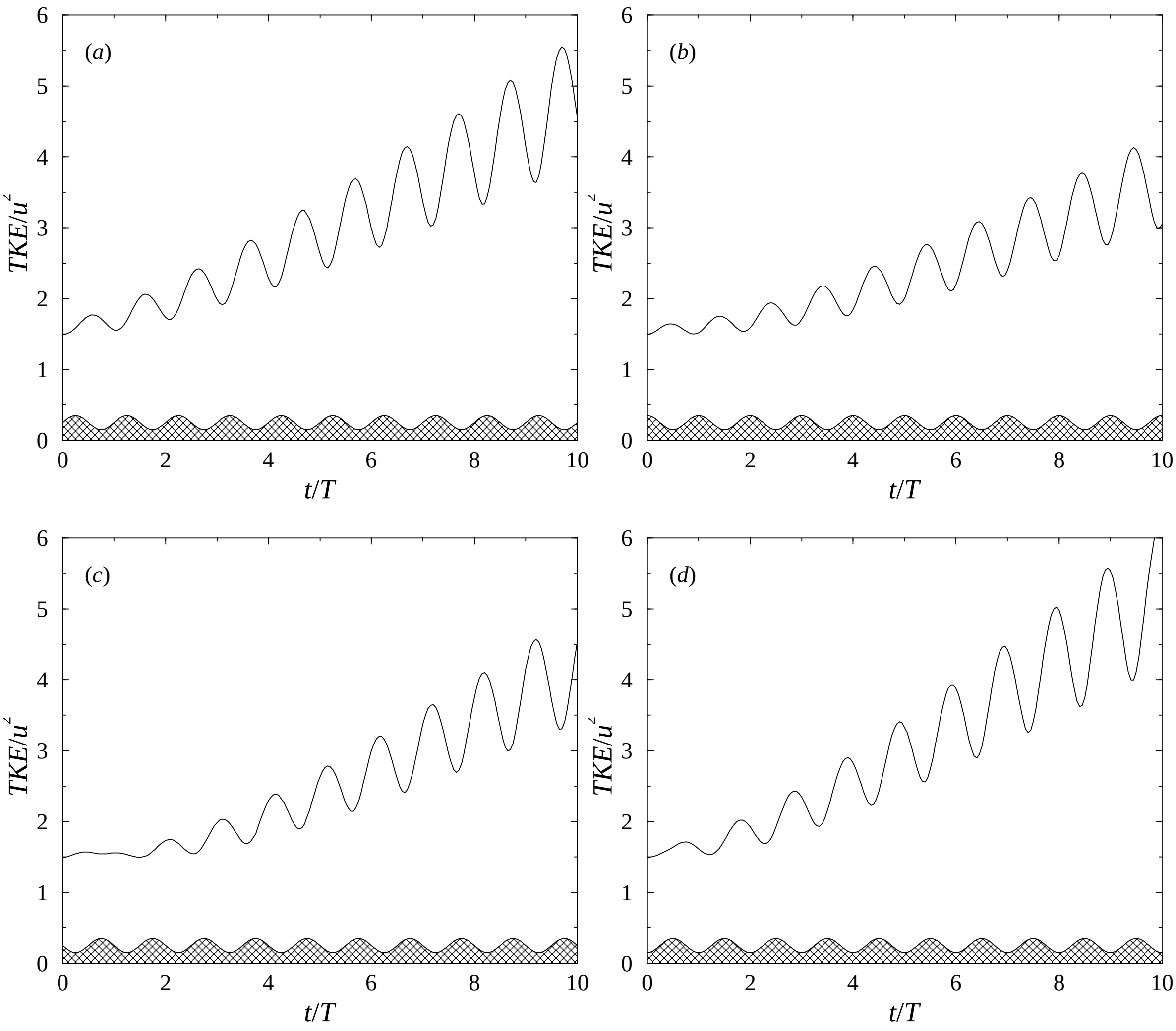

Figure 5.10 Evolution of the TKE over 10 wave cycles, for $\tilde{x}_3 = 0$, $k_w l = 0.6$, $a_w k_w = 0.2$. Solid line: turbulent kinetic energy, hatched profile: shape of the distorting wave (arbitrary scale). Turbulence initially at: (*a*) forward slope of wave, (*b*) wave crest, (*c*) backward slope of wave, (*d*) wave trough.

attains a value approximately 3 times higher than initially after 10 wave cycles.

Figures 5.2–5.5 have shown that the modulation of the turbulence in a wave cycle is sensitive to the initial conditions. Figures 5.7, 5.9 and 5.10 now show that not only the oscillatory behaviour but also the overall growth rate of the Reynolds stresses due to the Stokes drift depends on the initial conditions. For example, it is clear in figure 5.9 that the shear stress is largest when the initial position is at the wave trough (figure 5.9(*d*)) and smallest when it is at the wave crest (figure 5.9(*b*)). Correspondingly, the TKE growth rate is fastest when the initial position is at the wave trough (figure 5.10(*d*)) and slowest when it is at the wave crest (figure 5.10(*b*)). The remaining plots of figures 5.9 and 5.10 show the same trend, suggesting a link between TKE growth and the shear stress. This link will be confirmed and further explored in §5.3.5.

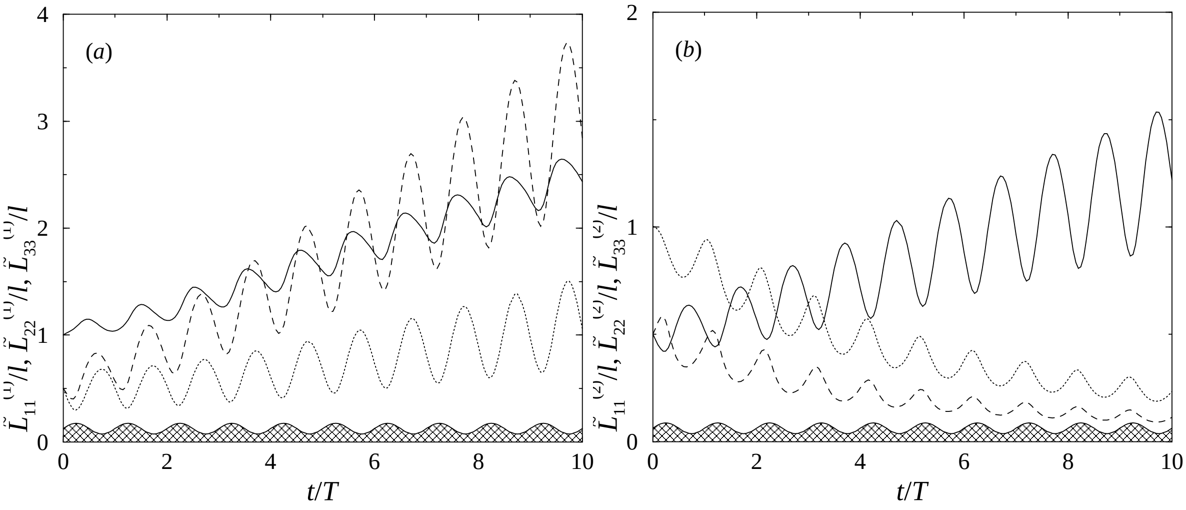

Figure 5.11 Evolution of the integral length scales over 10 wave cycles, for $\tilde{x}_3 = 0$, $k_w l = 0.6$, $a_w k_w = 0.2$. Hatched profile: shape of the distorting wave (arbitrary scale). (*a*) streamwise length scales. Solid line: $\tilde{L}_{11}^{(1)}$, dotted line: $\tilde{L}_{22}^{(1)}$, dashed line: $\tilde{L}_{33}^{(1)}$. (*b*) spanwise length scales. Solid line: $\tilde{L}_{11}^{(2)}$, dotted line: $\tilde{L}_{22}^{(2)}$, dashed line: $\tilde{L}_{33}^{(2)}$.

The behaviour of the Reynolds stresses over several wave cycles is different for different initial conditions because the average values of the Reynolds stresses, over the first wave cycle, are also different. On a time scale longer than a wave cycle, varying the initial position of the turbulence relative to the wave phase is thus approximately equivalent to varying the initial turbulence intensity slightly. However, the importance of the initial conditions is limited, because, as was seen in §5.3.1, the fractional variation of the Reynolds stresses due to varying the initial position is, at most, of $O(a_w k_w)$, which is small. That explains why the four graphs of figures 5.7, 5.9 and 5.10 resemble each other very much. For simplicity, all future results will consider an initial position on the forward slope of the wave.

The intensity of the turbulent velocity fluctuations has been characterised in detail for turbulence distorted by a surface wave. The spatial structure of the turbulent velocity fluctuations can now be characterised by the integral length scales of the turbulence. These length scales are modulated over a wave cycle, like the Reynolds stresses, but their evolution over several wave cycles is of greater interest.

Figure 5.11 presents the time evolution of the streamwise and spanwise integral length scales during 10 wave cycles, for a wave slope $a_w k_w = 0.2$. In figure 5.11(*a*), it can be seen that all the streamwise length scales increase in time. The streamwise length scale of the $\tilde{u}_1$ velocity fluctuations, $\tilde{L}_{11}^{(1)}$ becomes ≈ 2.5 times larger than initially after 10 wave cycles, while the corresponding amplification factors for the integral length scales of $\tilde{u}_2$ and $\tilde{u}_3$, $\tilde{L}_{22}^{(1)}$ and $\tilde{L}_{33}^{(1)}$, are ≈ 6 and ≈ 2, respectively. Figure 5.11(*b*) shows the time evolution of the spanwise integral length scales. It can be seen that only the integral length scale for the $\tilde{u}_1$ velocity component, $\tilde{L}_{11}^{(2)}$, increases in time, while the length scales for both $\tilde{u}_2$ and $\tilde{u}_3$, $\tilde{L}_{22}^{(2)}$ and $\tilde{L}_{33}^{(2)}$, decrease in time. After 10 wave cycles, $\tilde{L}_{11}^{(2)}$, $\tilde{L}_{22}^{(2)}$ and $\tilde{L}_{33}^{(2)}$ become respectively ≈ 2.5, ≈ 0.25 and ≈ 0.25 times their initial values.

These results imply that the anisotropy of the streamwise velocity fluctuations remains small, whereas the spanwise and normal velocity fluctuations become elongated in the streamwise direction, with this elongation being especially pronounced for the normal velocity fluctuations. Hence, the streamwise vortices induced by the Stokes drift in the present model not only have their axes of rotation aligned with the streamwise direction (as shown by the Reynolds stresses), but they are also elongated in that direction, a feature which is commonly observed in Langmuir circulations (Faller & Auer, 1988).

Again, these results should be compared with figures 12(*b–d*) of McWilliams *et al.* (1997), where horizontal cross-sections of the instantaneous velocity field are displayed, near the surface. While, in these figures, the streamwise velocity fluctuations display no appreciable elongation in their structure, the spanwise and normal velocity components (shown in figures 12(*b*, *c*)) have contours that are clearly elongated in the streamwise direction, with this elongation being more pronounced for the normal velocity. This is consistent with the results of figure 5.11, and provides evidence that Langmuir turbulence in the simulations of McWilliams *et al.* (1997) resembles turbulence distorted by a surface wave in the present model.

5.3.3 Comparison with turbulence distortion by shear

The shear current induced by the wind in the ocean surface layer and the Stokes drift of a wave appear at first to be rather similar, since both flows are characterised by a lagrangian transport that has a maximum at the surface and decays with depth. However, their fundamental dynamics are very different, as the numerical simulations of McWilliam *et al.* (1997) have made clear.

The interaction between the shear current and the turbulence can be very easily understood by using previous results applicable to turbulent boundary layer flows. At distances from the the boundary greater than l, the shear-flow model developed in chapter 4 reduces to the original RDT model of Townsend (1970) which is known to describe well the turbulence structure in boundary layers. That model, which assumes initially isotropic turbulence and a constant shear rate, is used in this subsection to examine turbulence distortion by a shear current.

Figure 5.12 shows the time evolution of the diagonal components of the Reynolds stress tensor for turbulence distorted by a shear flow aligned with the x_1 direction, having a shear rate Γ. This figure should be compared with figure 5.7, which shows similar quantities (albeit in the curvilinear coordinate system) for turbulence distorted by a surface wave. The behaviour of the stresses differs markedly between the two cases. While in Figure 5.7, the streamwise stress decreases and the spanwise and

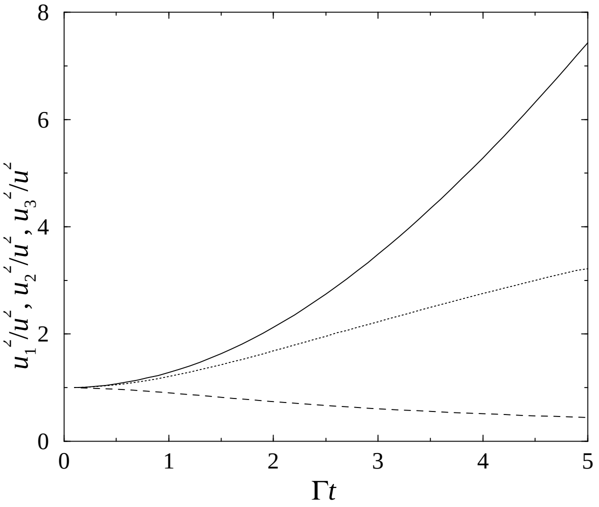

Figure 5.12 Evolution of the Reynolds stresses in a uniform shear flow, as a function of dimensionless time Γt. Solid line: streamwise component $\overline{u_1^2}$, dotted line: spanwise component $\overline{u_2^2}$, dashed line: normal component $\overline{u_3^2}$.

normal stresses increase over a number of wave periods, in figure 5.12, the streamwise and spanwise stresses, $\overline{u_1^2}$ and $\overline{u_2^2}$, increase and the normal stress, $\overline{u_3^2}$, decreases. And while in figure 5.7, the spanwise and normal stresses become much larger than the streamwise stress, in figure 5.12, $\overline{u_1^2}$ becomes larger than $\overline{u_2^2}$, which in turn becomes larger than $\overline{u_3^2}$. Physically, this behaviour is due to the existence of vorticity in the shear current, that does not exist in the Stokes drift. The tilting of vorticity of the mean flow by the turbulence, in the case of the current, counteracts, to a certain extent, the tilting of turbulent vorticity by the mean flow, so that $\overline{u_2^2}$ and $\overline{u_3^2}$ are prevented from becoming dominant (Lee & Hunt, 1989).

Figure 5.12 should be compared with figure 6 of McWilliams *et al.* (1997), where profiles of the Reynolds stresses in turbulence subject to a shear current (without the effect of a Stokes drift) are denoted by the solid curves. These curves show that the streamwise stress is larger than the spanwise stress, which in turn is larger than the normal stress. Hence, it can be concluded that the present constant-shear model is able to explain the anisotropy of the turbulent velocity fluctuations in a shear current.

Figures 5.13(*a*, *b*) display the time evolution of the integral length scales of the turbulence, for the same conditions as figure 5.12. Both the streamwise and the spanwise integral length scales of u_2, $L_{22}^{(1)}$ and $L_{22}^{(2)}$, decrease in time, and both the streamwise and the spanwise integral length scales of u_3, $L_{33}^{(1)}$ and $L_{33}^{(2)}$, increase in time. Hence the structure of these two velocity components remains approximately isotropic. However, the streamwise integral length scale of u_1, $L_{11}^{(1)}$, increases in time, while the spanwise length scale of the same velocity component, $L_{11}^{(2)}$, decreases in time. This means that the streamwise velocity fluctuations become elongated in the streamwise direction.

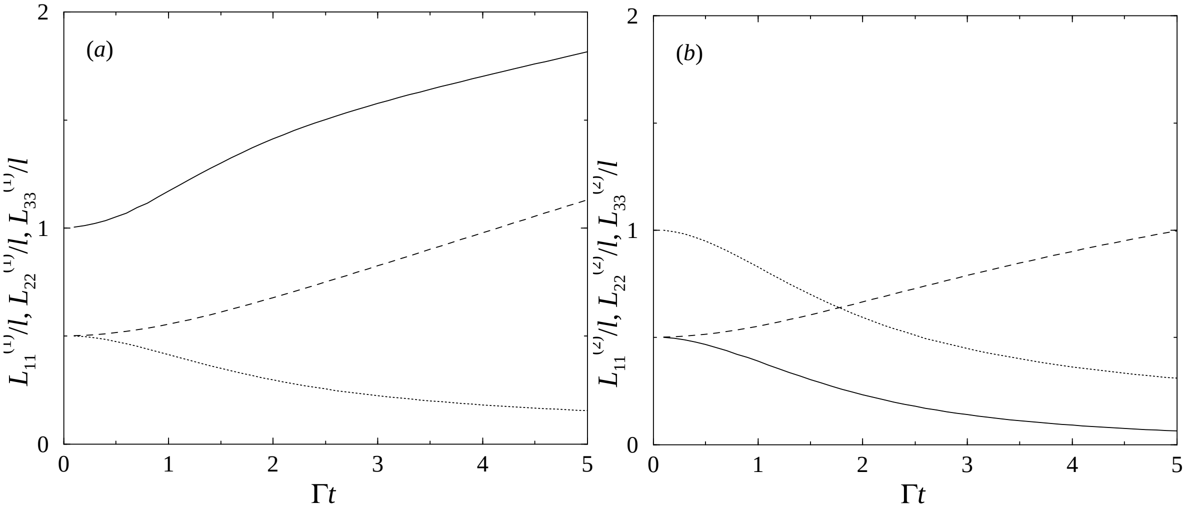

Figure 5.13 Evolution of the integral length scales in a uniform shear flow, as a function of dimensionless time Γt. (*a*) streamwise length scales. Solid line: $L_{11}^{(1)}$, dotted line: $L_{22}^{(1)}$, dashed line: $L_{33}^{(1)}$. (*b*) spanwise length scales: Solid line: $L_{11}^{(2)}$, dotted line: $L_{22}^{(2)}$, dashed line: $L_{33}^{(2)}$.

The contrast of these results with those presented for turbulence distorted by a surface wave are striking, as can be confirmed by comparing figure 5.13 with figure 5.11. While in figure 5.11, the structure of the $\tilde{u}_2$ and $\tilde{u}_3$ velocity fluctuations becomes elongated, in figure 5.13, the same happens but with the structure of u_1. Elongated structures in the streamwise turbulent velocity field are a well known feature of turbulent shear flows, where such structures are often called *streaky structures* (Kline *et al.*, 1967). Good examples of streaky structures produced in a turbulent boundary layer by DNS can be found, for example, in figures 5, 7 and 9 of Lee *et al.* (1990), where horizontal cross-sections of the streamwise turbulent velocity are shown.

The present comparison between the structure of turbulence distorted by a wave and turbulence distorted by a shear flow seems to be able to explain the 2 basic flow regimes observed in the LES of McWilliams *et al.* (1997): shear-flow turbulence and Langmuir turbulence. This indicates that the occurrence of one regime or the other is probably determined by the relative importance of the two physical processes modelled here in isolation. A rough way of quantifying the importance of each of these processes is by comparing the strain rate imposed by the Stokes drift $a_w^2 k_w^2 \sigma_w$ with the strain rate associated with the shear Γ, through the ratio

$$R = \frac{(a_w k_w)^2 \sigma_w}{\Gamma}. \tag{5.51}$$

If $R > 1$, the distortion by the Stokes drift should prevail, and streamwise vortices should be produced, while if $R < 1$, the distortion by shear should be more important, originating streaky structures. It was seen in chapter 4 that, in a turbulent shear current, $\Gamma = 10\text{s}^{-1}$ is a reasonable shear rate very near the surface. A reasonable value of σ_w for short waves is $\sigma_w = 10\text{s}^{-1}$. Since $a_w k_w$ is always much smaller than 1, (5.51) implies that $R \ll 1$, so the shear should dominate in this particular case. In fact, very low values of Γ, of $O(0.01\sigma_w)$, would be required for the Stokes drift to dominate, according to (5.51). Situations with weak shear could be favoured by vertical mixing in conditions of wave breaking.

But the explanation for this apparently excessive importance of the shear is that the above estimates are only valid at the surface. In real flows, the shear current weakens away from the surface over a distance of $O(l)$, hence Γ decays to zero over that distance. On the other hand, the Stokes drift decays to zero over a longer distance of $O(\lambda_w)$. Hence, as the depth increases, the effect of the Stokes drift could become greater than the effect of shear. Since by hypothesis $l \ll \lambda$, conditions favourable for the formation of streaky structures may only exist in a thin layer near the surface, where $\tilde{x}_3 \leq l$, while in the much larger region where $l < \tilde{x}_3 < \lambda_w$, streamwise vortices could develop. This is consistent with the observation by McWilliams *et al.* (1997) that Langmuir turbulence penetrates deeper than shear-flow turbulence.

On the other hand, situations where both shear and a Stokes drift are present are more complex than considered here, because the shear current also interacts with the wave motion, acting as an additional source of vorticity, which contributes to the vorticity of the streamwise vortices along with the turbulence (Leibovich, 1983). Hence the generation of such vortices is certainly more likely than suggested by (5.51).

The results presented until now have been calculated without taking into account the effect of blocking by the boundary on the turbulence. That effect will be considered briefly next.

5.3.4 Blocking effect of the boundary

As noted in §5.2.4, if at the initial time when the turbulence is undistorted by the wave, the blocking effect of the free surface is assumed to be described appropriately by the theory of Hunt & Graham (1978), this blocking effect remains purely kinematic at all subsequent times, and does not alter substantially the results obtained in the preceding sections (which are essentially linked with vorticity distortion).

Since Hunt & Graham's theory can be applied directly to the turbulence distorted by the wave, with the completely undistorted turbulence that formerly served as input being simply replaced by slowly varying turbulence, many of their conclusions remain valid, with slight alterations. For example, the result which states that the TKE at the boundary has the same value as the TKE far from the boundary is now reformulated as

$$(\overline{\tilde{u}_1^2} + \overline{\tilde{u}_2^2})(\tilde{x}_3 = 0) = (\overline{\tilde{u}_1^2} + \overline{\tilde{u}_2^2} + \overline{\tilde{u}_3^2})(\tilde{x}_3 \to \infty), \quad \text{when} \quad l \to 0, \lambda_w \to \infty. \tag{5.52}$$

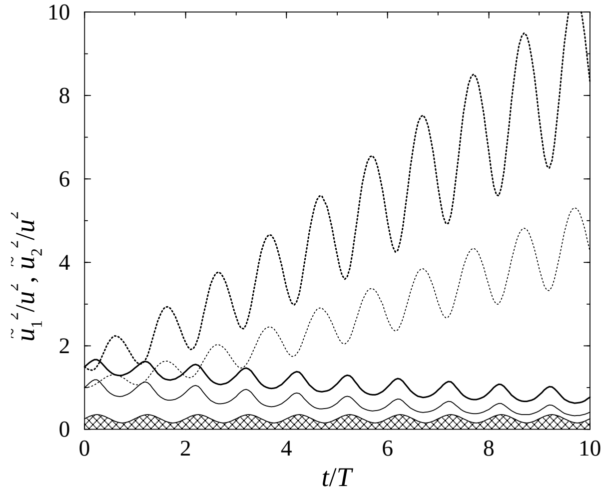

Figure 5.14 Evolution of the tangential Reynolds stresses over 10 wave cycles, with and without blocking, for $\tilde{x}_3 = 0$, $k_w l = 0.6$, $a_w k_w = 0.2$. Thick solid line: $\overline{\tilde{u}_1^2}$ with blocking, thin solid line: $\overline{\tilde{u}_1^2}$ without blocking, thick dotted line: $\overline{\tilde{u}_2^2}$ with blocking, thin dotted line: $\overline{\tilde{u}_2^2}$ without blocking, hatched profile: shape of the distorting wave (arbitrary scale).

This means that the TKE value at the boundary taking blocking into account is equal to the TKE value that would exist at the boundary if there was no blocking or, alternatively, approximately equal to the TKE immediately outside the layer directly influenced by blocking.

Figure 5.14 shows the time evolution of the streamwise and spanwise Reynolds stresses, $\overline{\tilde{u}_1^2}$ and $\overline{\tilde{u}_2^2}$, during 10 wave cycles, with and without blocking. The curves relative to the blocked and non-blocked cases only differ in magnitude, and there are no appreciable differences in shape. The factor by which the curves with blocking exceed those without blocking increases from 1.5 at the initial time (as predicted by Hunt & Graham, 1978) to a higher value later. This is due to the fact that, in the blocked case, both $\overline{\tilde{u}_2^2}(l \ll \tilde{x}_3 \ll \lambda_w)$ and $\overline{\tilde{u}_3^2}(l \ll \tilde{x}_3 \ll \lambda_w)$ increase due to the Stokes drift, but only $\overline{\tilde{u}_1^2}(\tilde{x}_3 = 0)$ and $\overline{\tilde{u}_2^2}(\tilde{x}_3 = 0)$ are not zero at the boundary (of which $\overline{\tilde{u}_1^2}(\tilde{x}_3 = 0)$ decreases in time).

Figure 5.15 presents profiles of the Reynolds stresses with and without blocking, at $t/T = 5$, for different values of the dimensionless wavenumber $k_w l$. It is found that $k_w l$ only influences the shape of the Reynolds stresses in between the surface and the region far from the surface, leading to a faster or slower decay of the profiles due to the distorting flow of the wave. Obviously, the longer the wavelength (i.e., the smaller $k_w l$), the deeper the distorting effect of the wave can penetrate. However, the value of the Reynolds stresses exactly at the boundary does not depend on $k_w l$, either when blocking is considered or when it is not. This justifies *a posteriori* why the parameter $k_w l$ has not been varied in previous tests.

Figures 5.15(*a*, *b*) show that, in the blocked case, $\overline{\tilde{u}_1^2}$ and $\overline{\tilde{u}_2^2}$ are amplified at the boundary by a factor greater than 1.5 relative to the unblocked case, consistent with figure 5.14. The distortion caused by the wave counteracts this amplification in figure 5.15(*a*), so that $\overline{\tilde{u}_1^2}$ at the boundary is only

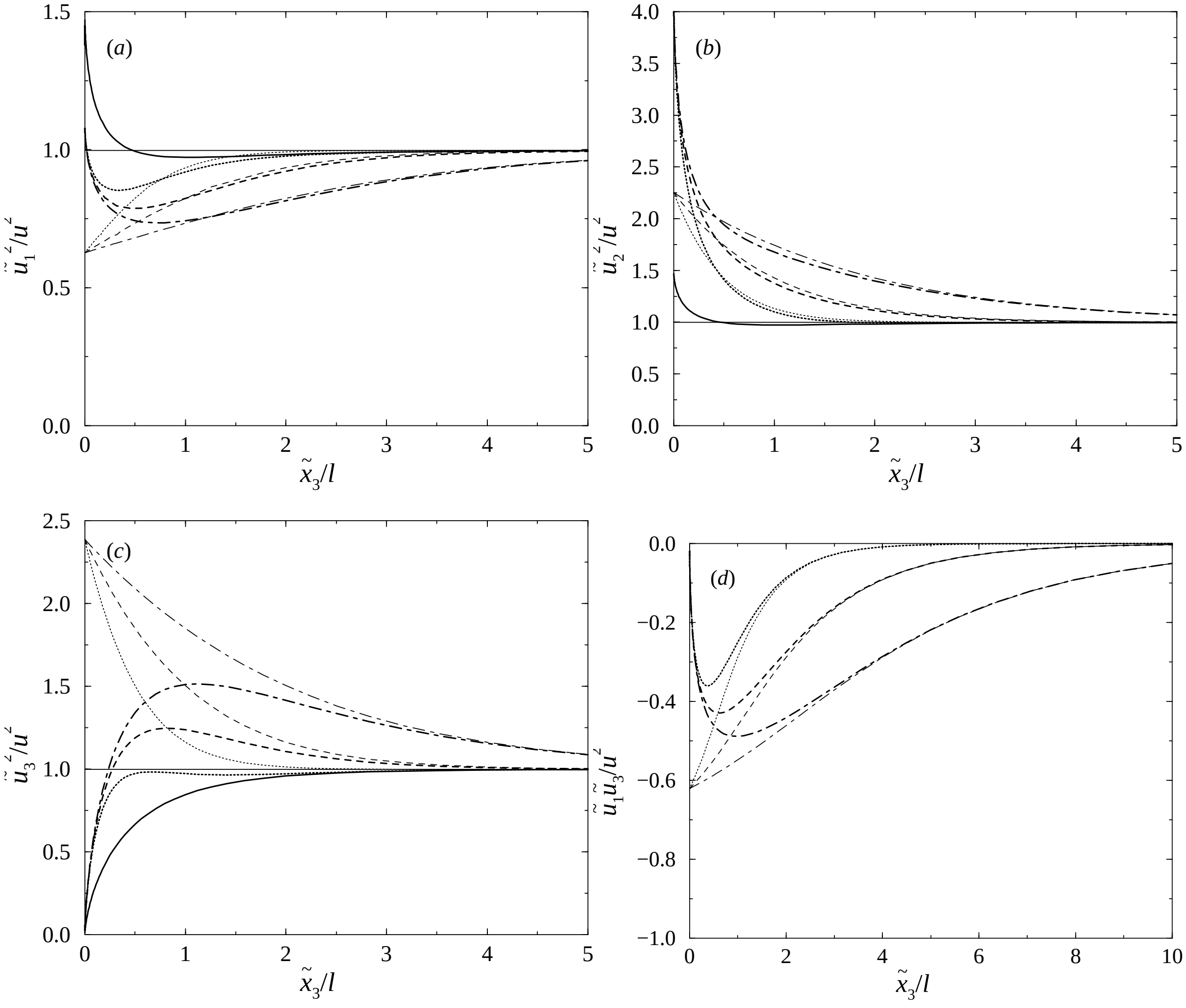

Figure 5.15 Profiles of the Reynolds stresses, with and without blocking, for $a_w k_w = 0.2$. Thick lines: with blocking, thin lines: without blocking. Solid lines: at $t/T = 0$, dotted lines: at $t/T = 5$, with $k_w l = 0.6$, dashed lines: at $t/T = 5$ with $k_w l = 0.3$, dash-dotted lines: at $t/T = 5$ with $k_w l = 0.15$. (*a*) streamwise component, (*b*) spanwise component, (*c*) normal component, (*d*) shear stress.

slightly larger than far from the boundary, whereas in figure 5.15(*b*), the distortion caused by the wave reinforces the amplification of $\overline{\tilde{u}_2^2}$ due to blocking. In figure 5.15(*c*), it can be seen that $\overline{\tilde{u}_3^2}$ is forced to decay to zero towards the boundary over a length scale l, as expected, retaining nevertheless a value greater than 1 in the region $l \ll \tilde{x}_3 \ll \lambda_w$. When blocking is considered, the shear stress, $\overline{\tilde{u}_1\tilde{u}_3}$ also has to decay to zero towards the boundary, for obvious reasons (figure 5.15(*d*)).

5.3.5 Estimation of the TKE growth

In §5.3.2, it was found that an increase in the TKE is predicted by the present model of turbulence distortion by a wave, which is related to the straining of the turbulence by the Stokes drift of the wave.

In order to estimate this increase, it is necessary to derive an equation for the TKE compatible with the assumptions of the model. The TKE equation is here derived in a cartesian coordinate system, for simplicity. But when the terms in that equation are estimated, the results of the preceding sections, which were found in the curvilinear coordinate system, will be used directly, since the behaviour of the statistics, in either coordinate system, is approximately equal.

The linearised momentum equation consistent with (5.2) is

$$\frac{\partial u_i}{\partial t} + U_j \frac{\partial u_i}{\partial x_j} + u_j \frac{\partial U_i}{\partial x_j} = -\frac{1}{\rho}\frac{\partial p}{\partial x_i}, \tag{5.53}$$

where ρ is the water density and p is the turbulent pressure. The required TKE equation may be obtained by multiplying (5.53) by u_i, adding all the expressions for $i = 1, 2, 3$ and ensemble averaging. This yields

$$\frac{\mathrm{d}}{\mathrm{d}t}\left(\frac{\overline{u_1^2}+\overline{u_2^2}+\overline{u_3^2}}{2}\right) = (\overline{u_3^2}-\overline{u_1^2})\frac{\partial U_1}{\partial x_1} - 2\overline{u_1 u_3}\frac{\partial U_1}{\partial x_3} - \frac{1}{\rho}\left[\frac{\partial}{\partial x_1}(\overline{p u_1}) + \frac{\partial}{\partial x_2}(\overline{p u_2}) + \frac{\partial}{\partial x_3}(\overline{p u_3})\right]. \tag{5.54}$$

The last 3 terms between square brackets in (5.54) appear in flux form and are associated with the redistribution of energy between different regions of the turbulence through pressure forces. The first two terms on the right-hand side are turbulence production terms by the mean flow, in the present case the surface wave. According to (5.43) and (5.44), $\partial U_1/\partial x_1$ attains maxima on the backward slopes of the wave. On the other hand, figure 5.7 shows that $\overline{u_1^2}$ attains maxima at the wave crests, while $\overline{u_3^2}$ attains maxima at the wave troughs. The product $(\overline{u_3^2} - \overline{u_1^2})\partial U_1/\partial x_1$ is thus in quadrature, and gives an insignificant net contribution to the TKE. By contrast, both $-\overline{u_1 u_3}$ (see figure 5.9) and $\partial U_1/\partial x_3$ are in phase with the wave crests. Therefore, when $\partial U_1/\partial x_3$ is positive, $-\overline{u_1 u_3}$ has a larger value than when $\partial U_1/\partial x_3$ is negative, so $-\overline{u_1 u_3}\partial U_1/\partial x_3$ tends to be more positive than negative. This leads, through (5.54), to a net positive contribution to the TKE, which is the primary reason why the TKE increases.

In order to test this reasoning, the growth rate of the TKE due only to the term $-2\overline{u_1 u_3}\partial U_1/\partial x_3$ will be estimated and compared with the growth rate predicted by the full model. The approximate model is given by:

$$\frac{\mathrm{d}}{\mathrm{d}t}\left(\frac{\overline{u_1^2}+\overline{u_2^2}+\overline{u_3^2}}{2}\right) \approx -2\overline{u_1 u_3}\frac{\partial U_1}{\partial x_3} \approx -2\overline{u_1 u_3} a_w^2 k_w^2 \sigma_w, \tag{5.55}$$

where, in the second approximate equality, $\partial U_1/\partial x_3$ has been substituted bearing in mind that the net contribution of the production term to the TKE is made only through the Stokes drift. The Stokes drift has been evaluated according to equation (3.3.5) of Phillips (1977). To compare this estimate more easily with the dimensionless growth rates available in figure 5.10, it should be noted that $\mathrm{d}/\mathrm{d}t =$

$(\sigma_w/2\pi)\mathrm{d}/\mathrm{d}(t/T)$, hence (5.55) becomes

$$\frac{\mathrm{d}}{\mathrm{d}(t/T)}\left(\frac{\overline{u_1^2}+\overline{u_2^2}+\overline{u_3^2}}{2u^2}\right) \approx -4\pi\frac{\overline{u_1u_3}}{u^2}a_w^2k_w^2. \tag{5.56}$$

Taking $a_wk_w = 0.2$ and $-\overline{u_1u_3}/u^2 \approx 0.7$, as suggested by the final portions of the graphs of figure 5.9, it follows that $\mathrm{d}/\mathrm{d}(t/T)(TKE/u^2) = 0.35$. This is in remarkable agreement with the value that can be extracted directly from the slopes of the final portions of the curves in figure 5.10. It thus appears that the estimates made above and the connection established between the TKE increase and the Reynolds shear stress are well founded.

To obtain an idea of the time-scales involved in the development of the streamwise vortices in the present model, a still rougher estimate may be carried out. Noting that $u_i = O(u)$ and $-\overline{u_1u_3} = O(u^2)$ (5.55) may be scaled as

$$\frac{u^2}{T_d} = u^2a_w^2k_w^2\sigma_w, \tag{5.57}$$

where T_d is the development time scale. With minor rearranging, (5.57) becomes

$$T_d = \frac{1}{a_w^2k_w^2\sigma_w}. \tag{5.58}$$

Taking reasonable values for the variables, like $a_wk_w = 0.1$ and $\sigma_w = 10\mathrm{s}^{-1}$, it is found that $T_d = 10\mathrm{s}$. Hence the streamwise vortices that contain most of the TKE grow relatively fast.

5.3.6 Estimation of turbulence-induced wave decay

The preceding results have established how the TKE of turbulence beneath a surface wave increases due to the distortion of the turbulence by the Stokes drift. Although in the RDT model used, the turbulent flow has no feedback whatsoever on the mean flow, which is taken as fixed, in real situations that is not the case. If a mean flow and a turbulent flow coexist in a fluid and the energy of the turbulent flow increases, that energy has to come from the mean flow, which correspondingly weakens. In the present case, the mean flow is associated with a surface wave, so the energy transfer taking place to the turbulence as the wave distorts the turbulence is necessarily linked with a decay of the wave. A mechanism of wave decay due to the straining of turbulence by the Stokes drift was first referred in the Introduction of Phillips (1959), who called it ‘eddy viscosity interaction’. Although Phillips (1959) did not establish a connection between the generation of streamwise vortices (which were in fact almost unstudied at the time) and wave decay, that connection is implicit in his qualitative arguments involving vorticity stretching. It will be shown in this subsection that the energy transfer from the waves to the turbulence through this eddy-viscosity interaction can indeed account for the turbulence-induced wave decay observed in the experimental study of Ölmez & Milgram (1992).

Consider the momentum equation for the mean flow in a cartesian coordinate system, now taking into account the Reynolds stresses:

$$\frac{\partial U_i}{\partial t} + U_j \frac{\partial U_i}{\partial x_j} = -\frac{1}{\rho}\frac{\partial P}{\partial x_i} - \frac{\partial}{\partial x_j}(\overline{u_i u_j}), \tag{5.59}$$

where P is the mean pressure. If this equation is multiplied by U_i and the resulting expressions for $i = 1$ and 3 are added (noting that the $i = 2$ component is zero for the monochromatic wave under consideration), an equation for the kinetic energy of the wave is obtained, namely

$$\begin{aligned} \frac{\mathrm{d}}{\mathrm{d}t}\left(\frac{U_1^2+U_3^2}{2}\right) &= (\overline{u_1^2} - \overline{u_3^2})\frac{\partial U_1}{\partial x_1} + 2\overline{u_1 u_3}\frac{\partial U_1}{\partial x_3} - \frac{\partial}{\partial x_1}(U_1\overline{u_1^2} + U_3\overline{u_1 u_3}) \\ &- \frac{\partial}{\partial x_3}(U_1\overline{u_1 u_3} + U_3\overline{u_3^2}) - \frac{1}{\rho}\left(\frac{\partial}{\partial x_1}(PU_1) + \frac{\partial}{\partial x_3}(PU_3)\right). \end{aligned} \tag{5.60}$$

The last 6 terms on the right-hand side appear in flux form, and so are related to transport processes, which do not change the total kinetic energy. The first two terms, however, are formally identical and with the opposite sign to those found on the right-hand side of the TKE budget (5.54). It is clear that these terms are associated with the energy transfer from the wave motion to the turbulent motion.

Since the growth rate of the TKE was estimated very accurately assuming it to be solely determined by the production terms mentioned above, by analogy with (5.55) it seems reasonable to estimate the decay of the kinetic energy of the wave due to the existence of turbulence from (5.60), as simply

$$\frac{\mathrm{d}}{\mathrm{d}t}\left(\frac{U_1^2+U_3^2}{2}\right) \approx 2\overline{u_1 u_3}\frac{\partial U_1}{\partial x_3}. \tag{5.61}$$

It remains to apply the same scaling ideas leading to (5.57) to the right-hand side of (5.61), and to note that the kinetic energy of the wave is $(U_1^2+U_3^2)/2 = O(a_w^2 k_w^2 c_w^2)$. Then, (5.61) may be scaled as

$$\frac{\mathrm{d}}{\mathrm{d}t}(a_w^2 k_w^2 c_w^2) \approx -u^2 a_w^2 k_w^2 \sigma_w \quad \Rightarrow \quad \frac{1}{a_w}\frac{\mathrm{d}a_w}{\mathrm{d}t} \approx -\frac{u^2}{c_w^2}\sigma_w, \tag{5.62}$$

which implies that the wave decays exponentially in time due to the turbulence, with an attenuation rate

$$\beta_t = a\frac{u^2}{c_w^2}\sigma_w, \tag{5.63}$$

where a is a dimensionless constant of $O(1)$.

The attenuation of surface waves due to turbulence has been investigated, for example, by Skoda (1972), Green *et al.* (1972), van Hoften & Karaki (1976) and Kitaigorodskii & Lumley (1983). In their theoretical study, Kitaigorodskii & Lumley identified a wave decay mechanism involving the transport of wave energy away from the surface by the turbulent velocity field, and parameterised that process in terms of the friction velocity of the turbulence. However, they emphasised that this process was only significant in a random wave field, and not for a periodic wave. Skoda (1972), Green *et al.* (1972) and van Hoften & Karaki (1976) performed experiments where they measured the decay of approximately monochromatic, mechanically generated waves, due to turbulence induced by rotating paddles, an oscillating grid and channel bottom friction, respectively. Ölmez and Milgram (1992) studied again the decay of periodic waves due to grid-generated turbulence, and re-analysed the data of Skoda (1972). Unlike most previous authors, they presented an extensive list of all the relevant parameters of the problem, including the intensity and length scale of the turbulence. They parameterised the wave attenuation in terms of the turbulence mixing rate, by resorting to dimensional analysis. In the present notation, their formula for the temporal attenuation rate is

$$\beta_t = 0.103 \frac{u}{l^{\frac{1}{3}} \lambda_w^{\frac{2}{3}}}, \tag{5.64}$$

where the constant 0.103 has been adjusted to their experimental data. In the graph that tests this relation (Ölmez & Milgram's figure 11), the scatter of the data points is considerable. Although relation (5.64) fits well Ölmez & Milgram's own data, the fit is not so good for the data of Skoda (1972), which they also present. The data of Skoda appear to be more sensitive to the parameter $u/(l^{\frac{1}{3}} \lambda_w^{\frac{2}{3}})$ and accordingly concentrate more above the theoretical line corresponding to (5.64). In particular, there are 2 points of Skoda's data which lie outside their graph, corresponding to a very high decay rate.

Figure 5.16 shows Ölmez & Milgram's (1992) and Skoda's (1972) experimental data for the attenuation rate of surface waves plotted as a function of $(u/c_w)^2 \sigma_w$ instead. The straight line corresponds to the formula (5.63) with $a = 0.6$. As in figure 11 of Ölmez & Milgram (1992), the scatter is quite considerable. This is to be expected, since the attenuation rate due to turbulence can only be calculated as a residue of the wave decay due to other processes (e.g. geometric spreading in Ölmez & Milgram's axisymmetric experiments, or channel wall friction in Skoda's experiments), and is thus subject to a large error. It was decided to include in figure 5.16 the data points of Skoda which lie outside figure 11 of Ölmez & Milgram (1992). They still depart very much from the present theoretical line.

In figure 5.16, the 2 data points with the highest value of $(u/c_w)^2 \sigma_w$ are fitted worse by the present theoretical line than in figure 11 of Ölmez & Milgram (1992), but there is no reason to believe that they deserve more confidence than the two outlying points of Skoda (1972). The great majority of the

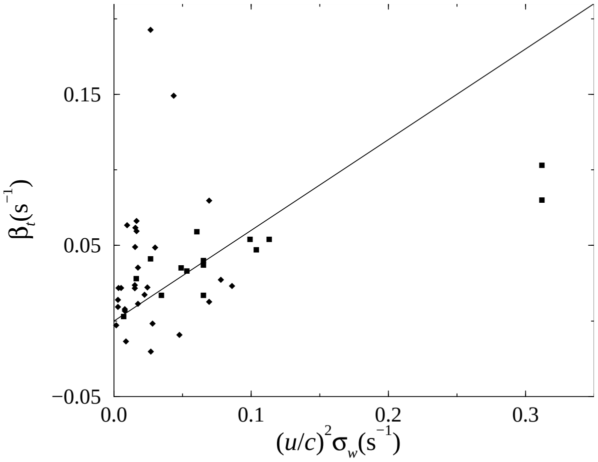

Figure 5.16 Comparison with experimental data of the temporal wave attenuation rate predicted by theory. Solid line: equation (5.63) with $a = 0.6$, squares: data from Ölmez & Milgram (1992), diamonds: data from Skoda (1972) (taken from Ölmez & Milgram, 1992).

data points, however (40 in total), concentrate approximately inside an ellipsoid with the longest axis roughly aligned with the theoretical line. The scatter can not be considered worse than in figure 11 of Ölmez & Milgram (1992). This provides convincing evidence that the scaling developed here for the wave attenuation due to turbulence is at least as acceptable, in order-of-magnitude terms, as (5.64). Indeed, the fact that the slope of the line fitted to the data using (5.63) is closer to one than that fitted using (5.64) might be considered an advantage of the present scaling.

It should be pointed out that both the data of Ölmez & Milgram (1992) and of Skoda (1972) marginally satisfy the assumptions of RDT, (5.3). In particular, in Ölmez & Milgram (1992)

$$4.36 < \frac{\lambda_w}{l} < 7.10, \quad 0.583 < a_w k_w \sigma_w \frac{l}{u} < 2.663 \tag{5.65}$$

except for one of the outlying points, which has $a_w k_w \sigma_w l/u = 0.399$. For that particular point, the departure from theory might be justified as resulting from gross violation of the condition $a_w k_w \sigma_w l/u \gg 1$. On the other hand, in Skoda's data,

$$1.57 < \frac{\lambda_w}{l} < 10.296 \tag{5.66}$$

and it was impossible to find information about the slope of the waves used by Skoda in Ölmez & Milgram's study.

The results of the present subsection consolidate the link established by Phillips (1959) between the stretching of vorticity by the Stokes drift in turbulence beneath a surface wave and the enhancement of wave energy dissipation by turbulence. The physical mechanism addressed here is inviscid, so it is not, in a strict sense, a mechanism of dissipation, but of energy transfer. The predicted decay of the wave energy is exponential and, according to (5.63), the attenuation rate depends on the frequency or wavenumber of the wave in the same way as in the shear instability wave generation mechanism of Miles (1957) or the non-separated sheltering mechanism of Belcher & Hunt (1993). Using the dispersion relation of gravity waves, which implies that $\sigma_w c_w = g$, it can be shown that (5.63) leads to a temporal attenuation rate that is $\propto \sigma_w^3$. The corresponding spatial attenuation rate, which is obtained by dividing the temporal attenuation rate by the group velocity of the wave $c_g \approx (1/2)c_w$ (Ölmez & Milgram, 1992), is then $\propto \sigma_w^4$. This kind of dependence is compatible with the experimental results shown in figure 4 of Green *et al.* (1972).

The attenuation is therefore expected to be most important at wavenumbers or frequencies which are high, but lower than those where viscous dissipation becomes dominant. Having in mind that the wave attenuation rate due to viscous dissipation is $4\nu k_w^2$ (Lamb, 1932), where ν is the kinematic viscosity of the water, the present mechanism is relevant when

$$\frac{u^2}{c_w^2}\sigma_w \gg 4\nu k_w^2 \quad \Rightarrow \quad u \gg (4\nu\sigma_w)^{\frac{1}{2}}. \tag{5.67}$$

Taking $\sigma_w = 1\mathrm{s}^{-1}$ and noting that $\nu = 1 \times 10^{-6}\mathrm{m}^2\,\mathrm{s}^{-1}$, it is concluded that u must be considerably larger than $2\mathrm{mm\,s}^{-1}$ (not a difficult condition to satisfy in the ocean). Alternatively, the criterion (5.67) can be expressed as

$$\sigma_w \ll \frac{u^2}{4\nu}, \tag{5.68}$$

which, if it is assumed $u = 2\mathrm{cm\,s}^{-1}$, gives $\sigma_w \ll 100\mathrm{s}^{-1}$, corresponding approximately to $\lambda_w \gg 1.5\mathrm{cm}$. Wavelengths outside this range would be excluded anyway because of the condition requiring the scale of the wave to be much larger than the scale of the turbulence (first equation of (5.3)). The mechanism addressed here is therefore primarily a gravity wave dissipation mechanism.

5.4 Conclusions

A rapid-distortion model has been used to study the interaction between initially homogeneous, shear-free turbulence and a progressive, irrotational surface wave. The model is applicable when the integral length scale of the turbulence is much smaller than the wavelength of the wave and the slope of the wave is high enough that the straining of the turbulence by the wave is stronger than the straining of the turbulence by itself.

As a result of distortion by the orbital motions of the wave, the turbulent Reynolds stresses undergo a modulation over a wave cycle, with the streamwise Reynolds stress attaining maxima at the wave crests and minima at the wave troughs and the reverse happening with the normal Reynolds stress. This behaviour is consistent with the experimental results of Thais & Magnaudet (1996).

Over several wave cycles, the turbulence becomes strongly anisotropic due to the tilting of the vertical vorticity by the Stokes drift and its subsequent amplification as streamwise vorticity. The streamwise Reynolds stress becomes progressively smaller, while the spanwise and normal Reynolds stresses both amplify over time. This corresponds, in a statistical sense, to the formation of intense streamwise vortices. The integral length scales of the turbulence indicate that these vortices are elongated in the streamwise direction, like Langmuir circulations. The structure of the turbulence predicted by the model is found to resemble that of ‘Langmuir turbulence’ in the LES of McWilliams *et al.* (1997).

The effect of turbulence distortion by a shear current is examined by using a rapid-distortion model of turbulence in a uniform shear flow. The differences relative to turbulence distorted by a wave are striking. In the case of the shear flow, the streamwise Reynolds stress becomes the largest of all Reynolds stresses and the structure of the streamwise velocity fluctuations becomes elongated in the streamwise direction, showing signs of the ‘streaky structures’ produced, for example, in the DNS of Lee *et al.* (1990).

The increase of the TKE associated with the formation of the intense streamwise vortices in the turbulence distorted by a surface wave is linked with the existence of a negative shear stress in the turbulence, and the tendency of the TKE is found to be proportional to $-\overline{u_1 u_3}$. The time scale for the amplification of the TKE is obtained by scaling the TKE equation, and found to be of $O(1/(a_w^2 k_w^2 \sigma_w))$.

Finally, the effect of the turbulence on the distorting surface wave is estimated by scaling the equation for the kinetic energy of the wave. It is found that the energy of the wave decreases due to the energy transfer taking place to the turbulence. The wave therefore decays through the attenuation mechanism identified by Phillips (1959) as ‘eddy-viscosity interaction’. The wave decay is found to be exponential, with an attenuation rate of $O((u/c_w)^2 \sigma_w)$, which is consistent with the laboratory data of Ölmez & Milgram (1992).

These results enable to establish a definite link between the generation of streamwise vortices in turbulence beneath a surface wave and the enhanced decay of that wave due to the turbulence. The results also provide an explanation for the existence of ‘Langmuir turbulence’, since the anisotropy of that kind of turbulence, both in terms of the intensity of the various velocity components and in terms of their length scales, is predicted correctly. Some caution is necessary regarding these results, since the model does not account for the simultaneous presence of a Stokes drift and a shear current. But the importance of that current as an additional source of vorticity is deemed to be limited, in many situations, to a thin layer near the surface, whereas the interaction between turbulence and the Stokes drift penetrates deeper.

CHAPTER 6

Conclusions

A number of simplified model problems relevant for understanding fundamental aspects of the interaction between turbulence and a free surface have been considered. The important findings achieved using these models will be recalled next.

In the viscous model of shear-free turbulence near flat boundaries, presented in chapter 2, the aim was to analyse the differences between the viscous coupling of the turbulence with a solid wall and with a free surface, and to explain existing direct numerical simulation (DNS) data of the turbulence dissipation rate. For that purpose, an energy spectrum with a viscous cutoff was adopted for the turbulence. This spectrum allowed a correct prediction of the dependence on the Reynolds number of the dimensionless dissipation rate, in agreement with the DNS data of Jimenez *et al.* (1993) and Wang *et al.* (1996). Profiles of the turbulence dissipation rate tangential and normal to the two types of boundary were then calculated, and found to agree extremely well with profiles obtained using DNS by Perot & Moin (1993). The tangential dissipation rate is higher near a solid wall than in the bulk of the flow because the no-slip boundary condition leads to large velocity gradients across the viscous boundary layer. In contrast, the weaker constraint of no stress at a free surface leads to the dissipation rate close to the free surface actually being smaller than in the bulk of the flow. This partly explains why tangential velocity fluctuations parallel to a free surface are so large (see, for example, Perot & Moin, 1995*a*). In addition, it was shown that it is the adjustment of the large energy-containing eddies across the viscous boundary layer that controls the dissipation rate profiles, which explains why rapid-distortion theory can give quantitatively accurate values for the dissipation rate at short times. It was also found that the dissipation rates obtained from the model evaluated at early times actually yield useful estimates of the dissipation obtained from the DNS at times when nonlinear processes are significant. It is concluded that the main role of the nonlinear processes is to arrest growth by linear processes of the viscous boundary layer after about one large-eddy turnover time.

In the inviscid model of shear-free turbulence near a flat boundary, presented in chapter 3, the aim was to understand how nonlinear interactions in the turbulence are affected by a wall or a flat free surface. This was done by considering the distortion of small-scale turbulence by axisymmetric straining flows representing the large-scale upwelling or downwelling zones in the turbulence. It was found that, in a downwelling zone, the tangential Reynolds stresses increase in time, while the normal Reynolds stress decreases in time, and the small-scale turbulence becomes approximately two-dimensional. In an upwelling zone, both the tangential and the normal Reynolds stresses increase in time, and the turbulence remains three-dimensional. In both cases, the turbulent kinetic energy (TKE) increases everywhere, but the ratio between its value at the boundary and far from the boundary remains 1, if the straining rate is constant. In shear-free turbulence, it is observed (Thomas & Hancock, 1977; Biringen & Reynolds, 1981) that the TKE near the boundary is larger than the TKE far from the boundary, even near solid walls, where it was seen in chapter 2 that there is no minimum in dissipation. This can be explained by the presence of upwelling and downwelling zones near the boundary, where the net strain is high and highly anisotropic, and a transition into an isotropic strain field as one moves away from the boundary, where there is a great deal of cancellation of the distortions and the net strain is weaker. When this effect is mimicked in the model by considering straining flows that decay exponentially away from the boundary, the calculated Reynolds stresses show good agreement with the data of Thomas & Hancock (1977) and Biringen & Reynolds (1981). The pressure-strain terms in the TKE equation are found to lead to a return to isotropy of the small-scale turbulence everywhere, except in the near-boundary region of upwelling zones. The turbulent pressure fluctuations are found to be more intense in an upwelling zone than in a downwelling zone, suggesting that the former flow may be more important for surface wave generation than the latter. Pressure spectra calculated at the boundary and far from the boundary in the case of a flow with a constant strain rate show reasonable agreement with spectra of the ‘slow’ pressure obtained from DNS data by Kim (1989), indicating that the high wavenumber tail of these spectra may be dominated by contributions due to the interactions between the large and the small scales of the turbulence.

In the model of surface wave initiation by a turbulent shear flow, presented in chapter 4, the aim was to extend the inviscid theory of Phillips (1957) by relating the pressure fluctuations that generate the waves to the velocity fluctuations in the turbulence, and to compare the relative importance of turbulence in the air and turbulence in the water for surface wave generation. It was found that, for flows producing turbulent pressure fluctuations of a similar magnitude, a turbulent shear flow in the water (coupled case) is much more efficient for generating surface waves of considerable slope than a turbulent shear flow in the air (uncoupled case). This is in agreement with the findings of Caulliez *et al.* (1998), who report that the first visible waves in their wave tank only appear when the water flow becomes turbulent. Wave generation is more efficient in the coupled case than in the uncoupled case because the decorrelation time of the turbulent pressure fluctuations is longer in the water than in the air – hence the turbulence in the water can interact with the free surface for a longer time – and also because the integral length scale of the turbulent eddies is shorter in the water than in the air – hence waves of a larger slope tend to be excited. In the coupled case, wave slopes of ≈ 0.1 are attained in realistic times (Cox, 1958), while in the uncoupled case the free surface remains almost perfectly flat. The predicted time evolution of the mean-square slope (MSS) of the waves resembles qualitatively graphs of the same quantity in the experimental study of Cox (1958), suggesting that the initial growth of the measured waves is due to the onset of turbulence in the water. Calculated curvature spectra of the waves are found to display a peak at the wavenumber corresponding to the integral length scale of the turbulence, satisfying at lower and higher wavenumbers power laws resulting directly from the assumed turbulence spectrum. These spectra qualitatively resemble the curvature spectra of waves measured in the laboratory by Hwang *et al.* (1993). The directional distribution of energy in the calculated spectra shows a peak in the direction of the flow for low shear rates of the turbulent flow (with a $\cos^2$ dependence on the propagation angle), but broadens and becomes bimodal at low wavenumbers for higher shear rates, in accordance with observations (Jähne & Riemer, 1990) and theoretical models (Kudryavtsev, 1999). This behaviour results from the emergence of truly resonant waves (as understood by Phillips, 1957) when the velocity of the flow at the level that forces the dominant waves rises above their minimum phase speed $c_{min} \approx 23 \mathrm{cm\,s}^{-1}$.

In the model of shear-free turbulence distorted by a surface wave, presented in chapter 5, the aim was to investigate in what ways the structure of initially homogeneous and isotropic turbulence is affected by the wave motion, and also, indirectly, how the wave is affected by the turbulence. It was found that, on the time scale of a wave period, the Reynolds stresses are modulated by the orbital motion of the wave, and undergo oscillations with the same period as the wave. The streamwise Reynolds stress attains maxima at the wave crests and minima at the wave troughs, while the Reynolds stress normal to the free surface attains maxima at the wave troughs and minima at the crests. This modulation is consistent with the laboratory measurements of Thais & Magnaudet (1996). On the time scale of several wave periods, the streamwise Reynolds stress progressively decreases in magnitude, while the spanwise and normal Reynolds stresses increase, rendering the turbulence approximately two dimensional and dominated by intense streamwise vortices. The streamwise integral length scales of the spanwise and normal velocity fluctuations increase, while the spanwise length scales of the same velocity fluctuations decrease. Hence the streamwise vortices become elongated in the streamwise direction. This structure is found to resemble the structure of 'Langmuir turbulence', produced in the large-eddy simulations of McWilliams *et al.* (1997). The formation of streamwise vortices can be explained by the tilting of vertical vorticity initially present in the turbulence by the Stokes drift of the wave, and its amplification as streamwise vorticity. This is the same physical mechanism as that proposed by Craik & Leibovich (Leibovich, 1983) for the formation of Langmuir circulations. However, in Craik & Leibovich's theory, the source of vorticity for the circulations is a wind-induced shear current, whereas in the present model the source of vorticity is the turbulence which is assumed to exist initially in the water, due to for example, wave breaking (Melville, 1996). The role of the shear current in the dynamics of the turbulence is studied by using a model of turbulence distorted by a uniform shear. It is found that, in turbulence subject to shear, the streamwise Reynolds stress becomes dominant, and the streamwise velocity fluctuations are elongated in the streamwise direction, forming 'streaky structures' (Lee *et al.*, 1990). Whether the turbulence behaves as shear-flow turbulence or Langmuir turbulence therefore seems to depend on whether the distorting effects of the Stokes drift or of the shear dominate. By scaling the TKE equation, the growth rate of the turbulent kinetic energy is found to be of $O((a_w k_w)^2 \sigma_w)$, where $a_w k_w$ is the wave slope and σ_w is the angular frequency of the wave. The energy transfer taking place to the turbulence as the streamwise vortices intensify is related to a weakening of the wave motion, corresponding to the wave decay mechanism termed by Phillips (1958) ‘eddy viscosity interaction’. This effect is estimated by scaling the equation for the kinetic energy of the wave. When the estimated attenuation rate is compared with recent laboratory data on wave decay due to turbulence (Ölmez & Milgram, 1992), order-of-magnitude agreement is achieved.

6.1 Applications and future work

The idealised model problems addressed in this thesis can be seen as building blocks that help to understand the dynamics of turbulence near free surfaces.

The findings of chapter 2 regarding the linear dynamics of the viscous boundary layer in shear-free turbulence may enable the improvement of closures for the dissipation terms near boundaries in numerical models, as in Perot & Moin (1993). The behaviour of the dissipation predicted by the model at a free surface may also help to understand gas transfer at air-water interfaces (Theofanous, 1984), since the normal dissipation at the boundary is related to the surface divergence of the flow.

The treatment of the nonlinear dynamics of shear-free turbulence near boundaries, presented in chapter 3, is useful in two ways. Firstly, it shows how the small-scale turbulence is affected by large-scale flow structures that are ever-present in turbulence near boundaries: upwelling and downwelling zones (Perot & Moin, 1995*a*). Secondly, it provides exact calculations of the inviscid source terms in the turbulent kinetic energy equation, including the pressure-strain terms. These results may help to parameterise those terms near boundaries in numerical models, as done in Johansson & Hallbäck (1994) for unbounded turbulence.

The results of chapter 4 on surface wave initiation by a turbulent shear flow are useful primarily for a more complete understanding of the wave energy balance in oceans or lakes. While the initial generation of surface waves has generally been attributed to turbulence in the air (Phillips, 1957; Kahma & Donelan, 1988), the results presented here show the importance of turbulence in the water, whose effect should be included in the wave balance equations. Due to the highly idealised nature of the flow employed in the rapid-distortion model, comparisons with data were mainly qualitative. It would be useful to perform direct numerical simulations of similar flows and compare their results with those obtained here. The rapid-distortion model could also be used to calculate the source terms in the turbulent kinetic energy equation, as was done in chapter 3 for shear-free turbulence. This would provide insights about the near-boundary dynamics of shear turbulence, which are more complicated than the dynamics of shear-free turbulence, or unbounded shear turbulence (Maxey, 1982), because the interaction of the mean vorticity and the turbulent vorticity is substantially modified by the blocking effect of the boundary (Lee & Hunt, 1989).

The distortion of turbulence by a progressive surface wave, treated in chapter 5, is perhaps the model problem considered in this thesis with the widest range of possible applications. The predictions of how the turbulence structure is affected by the Stokes drift, generating streamwise vortices, are relevant for developing parameterisations of these vortices in numerical models of ocean flows that do not resolve them. Furthermore, the structure of the turbulence, particularly when it is organised in streamwise vortices, is known to control pollutant dispersion in the ocean surface layer (Faller & Auer, 1988) and gas transfer across the air-water interface (Faller & Perini, 1984). It would be interesting to relate more extensively the turbulence distortion mechanism addressed in this chapter to the classical mechanism of Craik & Leibovich (1976) for the generation of Langmuir circulations. From the viewpoint of the waves, the turbulence-induced wave decay which was seen to be associated with the intensification of the streamwise vortices is obviously of great importance as a sink term in the wave energy balance, and should be included in the balance equations (Hasselmann, 1988). It would also be useful to compare the wave attenuation rate predicted by the model with further experimental or numerical simulation data, in order to test its validity and to better calibrate the adjustable constant.

All the model problems in this thesis have been solved using rapid-distortion theory. The analytical solutions obtained for the turbulent velocity field are thus in a form which is adequate to be implemented directly in kinematic simulations of turbulence (Perkins *et al.*, 1990). These numerical simulations retain only the dynamics that are contained in the rapid-distortion solutions, so they are much cheaper to run than models involving a full resolution of the Navier-Stokes equations. By adding a random phase to the Fourier components of the rapid-distortion solutions, kinematic simulations allow the calculation of actual flow fields, that can be compared with those produced by more realistic models, and the computation of flow trajectories (Fung *et al.*, 1992). While it would be interesting to perform kinematic simulations of all the flows considered in the thesis, it is intended in particular to study the trajectories of a tracer released at the free surface of a turbulent flow distorted by a surface wave (the problem of chapter 5). The aim is to see if the tracer tends to concentrate in rows aligned with the streamwise direction, as happens in Langmuir circulations (Melville *et al.*, 1998).

APPENDIX A

Surface wave generation by shear-free turbulence

A.1 Introduction

It was initially intended to address the problem of surface wave generation by shear-free turbulence at an air-water interface using a simple extension of Hunt & Graham's (1978) RDT model of shear-free turbulence near a wall.

A similar approach was first used by Carruthers & Hunt (1986) to address the generation of gravity waves in a stably stratified layer above a turbulent layer. During the course of the work leading to this thesis, another study was published by Fernando & Hunt (1997), who treated the case of turbulence near a sharp interface separating two fluids of different densities, and calculated statistics of the interfacial waves generated by the turbulence. Fernando & Hunt's model appeared to provide a framework that could be applied directly to the problem of wave generation at an air-water interface, requiring only the addition of the effect of surface tension, which was not considered in the original treatment. However, the way in which the turbulent pressure is treated in that model leads to serious concerns about its applicability.

It is well known that wave generation is an intrinsically dynamical process, which is essentially driven by pressure (Phillips, 1957). However, Hunt & Graham's (1978) inviscid model is purely kinematic, and produces no pressure fluctuations. To enable their models to produce the pressure fluctuations that are required to generate waves, both Carruthers & Hunt (1986) and Fernando & Hunt (1997), introduced a crucial assumption about the spatio-temporal structure of the turbulence, which will be shown to be formally inconsistent. This formal inconsistency is not serious for the generation of waves that are not resonant (the situation treated in detail by Carruthers & Hunt and Fernando & Hunt) because the order of magnitude of the pressure is predicted correctly, but reservations exist when the model is applied to resonant wave growth, because of the crucial way in which this process depends of the spatio-temporal structure of the turbulence (see chapter 4).

First of all, it will be shown that Hunt & Graham's linearised equations do not produce turbulent pressure fluctuations, and are thus unable to generate waves. Then, it will be shown how the assumption of Carruthers & Hunt (1986) and Fernando & Hunt (1997) about the spatio-temporal structure of turbulence is inconsistent with the equations of motion, but generates a pressure field of the right order of magnitude. Finally, this assumption will be adopted, despite its inconsistency, to calculate resonant wave growth, and a physical interpretation of the results will be presented.

A.2 Theoretical model

The linearised inviscid momentum equation applicable to turbulence in the absence of a mean flow is

$$\frac{\partial u_i}{\partial t} = -\frac{1}{\rho}\frac{\partial p}{\partial x_i}, \tag{A.1}$$

where u_i is the turbulent velocity, p is the turbulent pressure and ρ is the density of the fluid under consideration. The mass conservation equation is

$$\frac{\partial u_i}{\partial x_i} = 0. \tag{A.2}$$

Taking the curl of (A.1) yields the vorticity equation

$$\frac{\partial \omega_i}{\partial t} = 0, \tag{A.3}$$

where $\omega = \nabla \times \mathbf{u}$ is the turbulent vorticity.

Now, (A.3), implies that the rotational part of u_i does not depend on time. Since the flow consists of a rotational part plus an irrotational part, (A.2) implies that the irrotational part of u_i cannot depend on time either. Therefore, the velocity field must be frozen, and (A.1) reduces to

$$\frac{\partial u_i}{\partial t} = -\frac{1}{\rho}\frac{\partial p}{\partial x_i} = 0. \tag{A.4}$$

Hence it can be concluded that the turbulent pressure is a constant, and by definition of fluctuating quantity, equal to zero.

Carruthers & Hunt (1986) and Fernando & Hunt (1997) assume in their models that the turbulence far from the boundary is statistically homogeneous, isotropic and stationary. The turbulent velocity can then be expressed as a 4-dimensional Fourier integral as

$$u_i^{(H)}(\mathbf{x},t) = \iiiint \hat{u}_i^{(H)}(\mathbf{k},\sigma)\mathrm{e}^{\mathrm{i}(\mathbf{k}\cdot\mathbf{x}-\sigma t)}\mathrm{d}k_1\mathrm{d}k_2\mathrm{d}k_3\mathrm{d}\sigma. \tag{A.5}$$

where $\hat{u}_i^{(H)}$ is a Fourier amplitude, $\mathbf{k} = (k_1, k_2, k_3)$ is a wavenumber vector and σ is an angular frequency. Now, the only possible choice of σ consistent with (A.4) is $\sigma = 0$. But equation (2.5*b*) of

Carruthers & Hunt (1986) and equation $(2.1)^d$ of Fernando & Hunt are equivalent to setting

$$\sigma = uk, \tag{A.6}$$

where $k = (k_1^2 + k_2^2 + k_3^2)^{\frac{1}{2}}$ is the wavenumber value and u the root-mean-square (RMS) velocity of the turbulence. This assumption, which has also been used in the kinematic simulations of Turfus & Hunt (1987) and Perkins *et al.* (1990), makes the turbulence evolve in time and have approximately correct temporal statistics, without having to account for complicated dynamical processes. However, (A.6) is clearly inconsistent with the equations of motion.

Since the only velocity scale of the turbulence is u, if the the various terms in (A.1) are estimated, using (A.6), it is found that the turbulent pressure scales as ρu^2, which is correct for shear-free turbulence (Batchelor, 1950). Regarding this particular aspect then, (A.6) appears to mimic correctly the nonlinear effects that are neglected in the linearised fundamental equations. In the following calculations, (A.6) will be adopted to treat the problem of wave generation, in order to see how it affects the wave growth rates.

A.2.1 The wave generation problem

Like the turbulent velocity $u_i^{(H)}$ that is ultimately responsible for driving the waves, all the turbulent and wave variables are horizontally homogeneous. Hence both the interface elevation ζ and the turbulent pressure p can be expanded as two-dimensional Fourier integrals as

$$\begin{aligned} \zeta(x_1, x_2, t) &= \iint \hat{\zeta}(k_1, k_2, t) e^{i(k_1 x_1 + k_2 x_2)} dk_1 dk_2, \\ p(\mathbf{x}, t) &= \iint \hat{p}(k_1, k_2, x_3, t) e^{i(k_1 x_1 + k_2 x_2)} dk_1 dk_2. \end{aligned} \tag{A.7}$$

The wave orbital motion is equally horizontally homogeneous, and assumed to be irrotational. Using mass conservation and the kinematic and the dynamical boundary conditions at the interface (see chapter 4), the Fourier amplitude of the surface elevation is found to satisfy

$$\frac{\partial^2 \hat{\zeta}}{\partial t^2} + \sigma_0^2 \hat{\zeta} = -\frac{k_{12} \hat{p}(x_3 = 0)}{\rho}, \tag{A.8}$$

where $k_{12} = (k_1^2 + k_2^2)^{\frac{1}{2}}$ and

$$\sigma_0 = (g k_{12} + \gamma k_{12}^3)^{\frac{1}{2}} \tag{A.9}$$

is the natural frequency of surface waves, g is the acceleration of gravity and γ is the surface tension. This is equivalent to Phillips' (1957) equation (2.12), and shows that the Fourier amplitude of the surface elevation behaves like a forced harmonic oscillator driven by the turbulent pressure forcing at the air-water interface.

Following Carruthers & Hunt (1986) and Fernando & Hunt (1997), rapid distortion theory enables to relate the turbulent pressure p to the turbulent velocity field, and this considerably simplifies the wave generation problem. Taking the horizontal divergence of (A.1) and using (A.2) yields

$$\frac{\partial}{\partial t}\frac{\partial u_3}{\partial x_3} = \frac{1}{\rho}\left(\frac{\partial^2 p}{\partial x_1^2} + \frac{\partial^2 p}{\partial x_2^2}\right), \tag{A.10}$$

which may then be applied at the air-water interface. Since the turbulent pressure field responsible for the initial wave growth is that in the absence of any waves (Phillips, 1957), the turbulent velocity field on the left-hand side of (A.10) is also that in the absence of waves, being given by the solutions of Hunt & Graham (1978). In contrast with (A.5), Hunt & Graham did not represent $u_i^{(H)}$ explicitly as a Fourier integral in time. However, when the turbulence far from the boundary is assumed stationary, that approach may be followed (Fernando & Hunt, 1997), and the expression obtained for the vertical component of the turbulent velocity taking into account blocking by the boundary is

$$u_3(\mathbf{x},t) = \iiiint \hat{u}_3^{(H)}(\mathbf{k},\sigma)\left(\mathrm{e}^{\mathrm{i}k_3x_3} - \mathrm{e}^{k_{12}x_3}\right)\mathrm{e}^{-\mathrm{i}\sigma t}\mathrm{d}k_1\mathrm{d}k_2\mathrm{d}k_3\mathrm{d}\sigma. \tag{A.11}$$

This equation may then be inserted into (A.10), and if (A.7) is also used, an expression for the turbulent pressure amplitude is obtained. At the interface, that expression takes the form

$$\hat{p}(k_1,k_2,x_3=0,t) = -\frac{\rho}{k_{12}}\iint \hat{u}_3^{(H)}(\mathbf{k},\sigma)\sigma\left(\mathrm{i} - \frac{k_3}{k_{12}}\right)\mathrm{e}^{-\mathrm{i}\sigma t}\mathrm{d}k_3\mathrm{d}\sigma, \tag{A.12}$$

which may be substituted on the right-hand side of (A.8).

The solution of (A.8) for an initially unperturbed interface is well known from Phillips (1957) and chapter 4 of this thesis. The corresponding solution for the wave spectrum is

$$\Psi(k_1,k_2,t) = \frac{k_{12}^2}{\rho^2\sigma_0^2}\int_0^t\int_0^t \overline{\hat{p}^*(k_1,k_2,0,r)\hat{p}(k_1,k_2,0,s)}\sin[\sigma_0(t-r)]\sin[\sigma_0(t-s)]\mathrm{d}r\mathrm{d}s. \tag{A.13}$$

where the overbar denotes ensemble averaging and the asterisk denotes complex conjugation. Now, noting from (A.12) that the pressure field is statistically stationary (because the velocity field that generates it is also statistically stationary), a wavenumber-frequency pressure spectrum $\hat{\Pi}(k_1,k_2,\sigma)$

may be introduced, being defined as

$$\overline{\hat{\hat{p}}^*(k_1,k_2,\sigma)\hat{\hat{p}}(k_1',k_2',\sigma')} = \hat{\Pi}(k_1,k_2,\sigma)\delta(k_1-k_1')\delta(k_2-k_2')\delta(\sigma-\sigma'), \qquad \text{(A.14)}$$

where

$$\hat{p}(k_1,k_2,0,t) = \int \hat{\hat{p}}(k_1,k_2,\sigma)\mathrm{e}^{-\mathrm{i}\sigma t}\mathrm{d}\sigma. \qquad \text{(A.15)}$$

Equations (A.14) and (A.15) may then be substituted in (A.13), yielding an equation for the surface wave spectrum as a function of the wavenumber-frequency spectrum of the turbulent pressure.

A sufficiently long time after the turbulent forcing has begun, the only turbulent pressure fluctuations that give appreciable contributions to the integral on the right-hand side of (A.13) are those whose frequency satisfies $\sigma = \sigma_0(k_{12})$. The wave spectrum then becomes dominated by resonant contributions and the equation that gives the wave growth in the notation of Hasselmann (1968) can be obtained:

$$\frac{\partial \Psi}{\partial t} = \frac{\pi}{2}\frac{k_{12}^2}{\rho^2\sigma_0^2}\left(\hat{\Pi}(k_1,k_2,\sigma_0) + \hat{\Pi}(k_1,k_2,-\sigma_0)\right). \qquad \text{(A.16)}$$

Finally, using (A.12), (A.14) and (A.15), the wavenumber-frequency spectrum of the turbulent pressure may be related to the wavenumber-frequency spectrum of the turbulent velocity far from the boundary, $\chi_{ij}^{(H)}$, yielding

$$\hat{\Pi}(k_1,k_2,\sigma) = \rho^2\frac{\sigma^2}{k_{12}^2}\int\left(1+\frac{k_3^2}{k_{12}^2}\right)\chi_{33}^{(H)}(\mathbf{k},\sigma)\mathrm{d}k_3, \qquad \text{(A.17)}$$

where $\chi_{ij}^{(H)}$ is defined as

$$\overline{\hat{\hat{u}}_i^{(H)*}(\mathbf{k},\sigma)\hat{\hat{u}}_j^{(H)}(\mathbf{k}',\sigma')} = \chi_{ij}^{(H)}(\mathbf{k},\sigma)\delta(\mathbf{k}-\mathbf{k}')\delta(\sigma-\sigma'). \qquad \text{(A.18)}$$

The crucial assumption of Carruthers & Hunt (1986) and Fernando & Hunt (1997) states that the wavenumber-frequency spectrum of the turbulent velocity can be related to the corresponding wavenumber spectrum $\Phi_{ij}^{(H)}$ through (cf. (A.6))

$$\chi_{ij}^{(H)}(\mathbf{k},\sigma) = \Phi_{ij}^{(H)}(\mathbf{k})\delta(\sigma-uk). \qquad \text{(A.19)}$$

This means that the turbulent velocity field is treated like a superposition of waves with the ‘dispersion relation’ (A.6). The definition of the wavenumber spectrum $\Phi_{ij}^{(H)}$ adopted here is that appropriate for isotropic turbulence and can also be found in Hunt & Graham (1978), or in chapter 4 of this thesis (equation (4.53)).

A.3 Results and discussion

Equation (A.16) shows that the wave spectrum grows linearly in time, and proportionally to the pressure spectrum at the wavenumber k_{12} and frequency σ that satisfy the dispersion relation of free surface waves. Due to linearisation, that pressure spectrum is in turn proportional to the velocity spectrum at the same wavenumber and frequency (see (A.17)). It should be noted that (A.16) and (A.17) are physically consistent, since they were derived from the original linearised equations of motion. It is only when, as a result of (A.19), it is assumed that $\sigma \neq 0$ in (A.17) that the model becomes inconsistent, for the reasons explained before. But that inconsistency is necessary if any pressure forcing, and the resulting wave growth, are to be predicted.

Although the equations in §A.2 have been derived for turbulence in the water, this model can be applied to turbulence in the water or to turbulence in the air. The wave motions themselves are always dominated by the dynamics of the water-side of the domain, because of the large density difference existing between air and water, so the density in (A.16) must always be replaced by the density of water ρ_w. In the expression for the turbulent pressure forcing, (A.17), the density may be replaced by the density of water or by the density of air, ρ_a, depending on whether the interface is forced from below or from above. For a similar RMS velocity u and integral length scale of the turbulence l, the effect of the density is simply to make the spectral growth rates for turbulence in the air smaller by a factor $\approx 10^{-6}$ than for turbulence in the water. Of course, the fact that u and l are generally larger in the atmosphere than in the ocean tends to counter this effect, at least partly (see chapter 4).

For an isotropic wave field, such as that generated by horizontally isotropic turbulence, the omni-directional slope spectrum of the air-water interface is defined as

$$S(k_{12}) = 2\pi k_{12}^3 \Psi(k_{12}). \tag{A.20}$$

Figure A.1 shows the growth rate of the omni-directional slope spectrum, for plausible values of l and u, in the case of turbulence in the air. It can be seen that the growth rate increases as the RMS turbulent velocity u increases, as would be expected, but as u becomes larger than the minimum phase speed of surface waves $c_{min} \approx 23\mathrm{cm\,s}^{-1}$, which occurs at the wavenumber $k_{min} \approx 3.67\mathrm{cm}^{-1}$, a gap where there is no resonant growth appears, centred on k_{min}. The gap becomes wider as u increases. This can be understood with the aid of the schematic diagram of figure A.2(a). The resonance condition states that σ, the frequency of the turbulence, has to be equal to σ_0, the natural frequency of the surface waves.

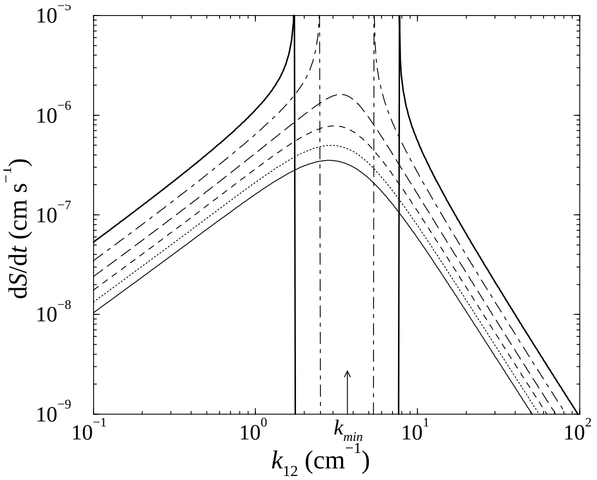

Figure A.1 Resonant wave growth for turbulence in the air, using assumption (A.19). Integral length scale of the turbulence $l = 30$cm. Thin solid line: $u = 19\text{cm s}^{-1}$, dotted line: $u = 20\text{cm s}^{-1}$, dashed line: $u = 21\text{cm s}^{-1}$, long-dashed line: $u = 22\text{cm s}^{-1}$, dash-dotted line: $u = 24\text{cm s}^{-1}$, thick solid line: $u = 26\text{cm s}^{-1}$.

Now, (A.6) and (A.9) show that

$$\sigma = \sigma_0 \quad \Rightarrow \quad uk = c_w k_{12}, \tag{A.21}$$

where c_w is the phase speed of the wave. Since k_{12} is by definition smaller than k, (A.21) means that resonance can only occur if $u < c_w$. The gap in the graph of figure A.1 includes the wavenumbers for which this condition is not met. The schematic diagram of figure A.2(*b*) explains in more detail the resonance mechanism. Resonance happens when a Fourier component of the turbulent pressure becomes phase locked with a surface wave having the same horizontal propagation velocity. For this to be possible, a Fourier component of the pressure of wavelength λ_t that excites a monochromatic wave of wavelength λ_w must travel at an angle θ_R to the horizontal such that $\cos\theta_R = u/c_w = \lambda_t/\lambda_w$. When $u > c_w$, or $\lambda_t > \lambda_w$, there can be no resonant wave growth. The gap in the graph of figure A.1 only appears because, in the present model, the turbulence advection is parameterised in a rather artificial way, as a superposition of wave-like components all travelling at the same 'phase speed' u, albeit in different directions (see (A.6)).

A slightly more realistic approach is to model the turbulence still as a superposition of independent Fourier modes, but with a 'phase speed' characterised by a gaussian distribution, as suggested in the study of Fung *et al.* (1992) on kinematic simulation of turbulence. In that case, assumption (A.19) is replaced by

$$\chi_{ij}^{(H)}(\mathbf{k},\sigma) = \Phi_{ij}^{(H)}(\mathbf{k}) \frac{1}{(2\pi)^{\frac{1}{2}}\Sigma(k)} \exp\left(-(\sigma - \overline{\sigma}(k))^2/2\Sigma^2(k)\right), \tag{A.22}$$

where $\overline{\sigma}$ is an average frequency and Σ is the corresponding standard deviation. Equation (A.22)

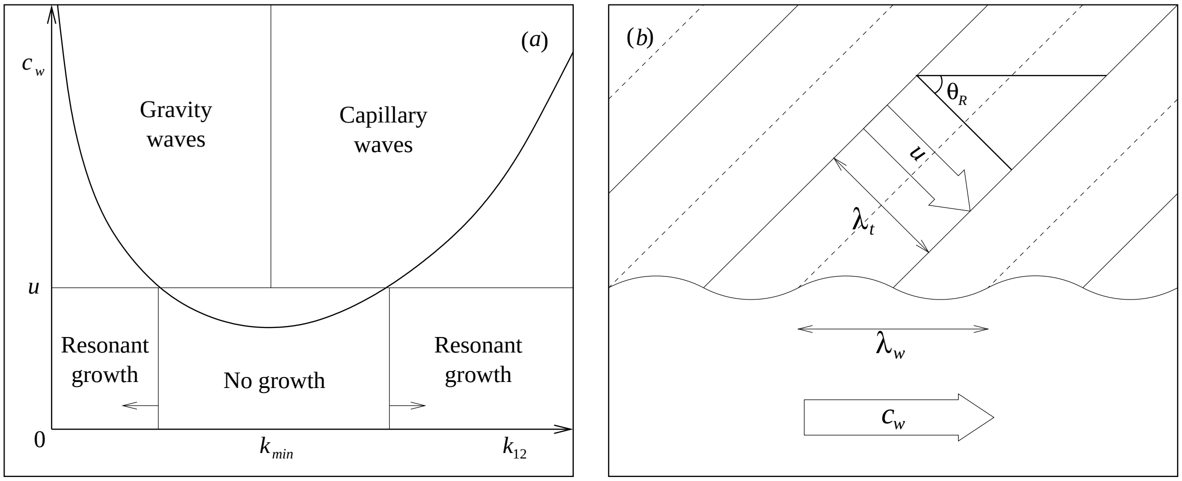

Figure A.2 (*a*) Schematic diagram showing the resonance conditions. The thick solid curve represents the phase speed of surface waves c_w. (*b*) Schematic diagram of the general mechanism for resonance.

implies that there is a gaussian distribution of frequencies for each Fourier component of the turbulence having a given wavenumber magnitude. The average frequency is chosen here as $\overline{\sigma} = uk$ and the standard deviation is defined as $\Sigma = 0.25\overline{\sigma}$, being proportional to $\overline{\sigma}$, in accordance with the ideas of Fung *et al.* (1992).

Figure A.3(*a*) shows the resonant growth rate of the omni-directional slope spectrum for the same conditions as figure A.1, but with the new assumption (A.22). The theoretical curves in figure A.3(*a*) are quite similar to those of figure A.1 except for the highest values of u, in the region where the gap existed. The gap has now been filled, and become simply a dip in the curves, centred on k_{min}. This can be understood by noting that the second equality of (A.21) is no longer valid, since there is now a distribution of 'advection velocities' of the turbulence, and not only one velocity, u. The curves giving the spectral growth rate in figure A.3(*a*) somewhat resemble the spectra shown in figure 1 of Zhang (1995). This would suggest that turbulence exclusively in the air might be responsible for the dip at the wavenumber k_{min} which is observed not only in Zhang's data but also in wave spectra measured by other authors (Cox, 1958; Jähne and Riemer, 1990). The plausibility of this idea can be tested by analysing the order of magnitude of the wave growth rate.

A global measure of the 'size' of the waves is mean-square-slope (MSS) of the interface, which is defined as

$$\overline{\left(\frac{\partial\zeta}{\partial x_1}\right)^2} + \overline{\left(\frac{\partial\zeta}{\partial x_2}\right)^2} = \int_0^\infty S(k_{12})\mathrm{d}k_{12}. \tag{A.23}$$

In figure 1 of Zhang (1995) and also in numerous other data, the MSS is generally of $O(0.01)$, corresponding to a root-mean-square (RMS) slope of $O(0.1)$ (wave slopes much higher than these values are prevented from occurring by nonlinear processes like wave breaking). The growth rates of the

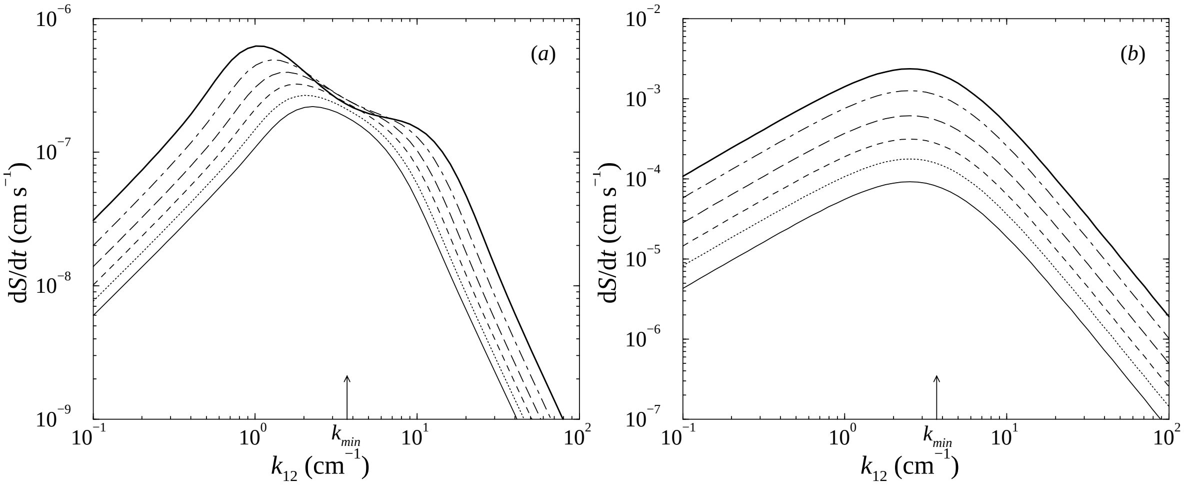

Figure A.3 (*a*) Resonant wave growth using assumption (A.22). (*a*) Turbulence in the air, same conditions as figure A.1. (*b*) Turbulence in the water. Integral length scale $l = 4$cm. Thin solid line: $u = 2$cm s^{-1}, dotted line: $u = 2.3$cm s^{-1}, dashed line: $u = 2.6$cm s^{-1}, long-dashed line: $u = 3$cm s^{-1}, dash-dotted line: $u = 3.5$cm s^{-1}, thick solid line: $u = 4$cm s^{-1}.

MSS calculated for the values of l and u used in figure A.3(*a*) are found to range between 1.0 and $3.4{\times}10^{-5}\text{s}^{-1}$. This means that a RMS slope of 0.1 would be attained in between 5 and 17 minutes. These time scales are manifestly much larger than the observed time scales for wave development. Hence, the model can not explain the initial growth of surface waves.

That initial wave growth might be explained by turbulence in the water. Figure A.3(*b*) shows the growth rate of the omni-directional slope spectra of waves generated by turbulence in the water, for plausible values of l and u. There is now unimpeded resonant growth for waves of any length (because $u < c_{min}$), hence there is not a dip in the curves of the spectral growth rate at the wavenumber k_{min}. Regarding this aspect, the curves of figure A.3(*b*) resemble less those of Zhang (1995) than in the case of turbulence in the air. However, the magnitude of the growth rate is somewhat greater than for turbulence in the air, ranging between $3.2 \times 10^{-4}\text{s}^{-1}$ and $8.2 \times 10^{-3}\text{s}^{-1}$ for the values of l and u used in figure A.3(*b*). For these growth rates, the time interval required to attain waves with a RMS slope of 0.1 would be between 1.2s and 31s, which is much closer to the observed time scales for wave development. Hence the initial growth of surface waves might be attributed to the onset of turbulence in the water induced, for example, by a wind blowing over the air-water interface, a result which is consistent with the findings of chapter 4.

These results are interesting, and suggest that the model is able to predict wave growth rates with a plausible order of magnitude. But it would be risky to attach too much significance to them, since, as was seen before, the pressure field which is ultimately responsible for generating the waves is obtained in a way that is formally inconsistent with the fundamental equations, and the physics of the model are thus incorrect. That was the reason why the presentation of this model has been relegated to an appendix.

REFERENCES

ARONSON, D., JOHANSSON, A. V. AND LÖFDAHL, L. 1997 Shear-free turbulence near a wall. *J. Fluid Mech.*, **338**, 363–385.

BATCHELOR, G. K. 1950 Pressure fluctuations in isotropic turbulence. *Proc. Camb. Phil. Soc.*, **47**, 359–374.

BATCHELOR, G. K. 1953 *The Theory of Homogeneous Turbulence*. Cambridge University Press.

BATCHELOR, G. K. AND PROUDMAN, I. 1954 The effect of rapid distortion of a fluid in turbulent motion. *Q. J. Mech. Appl. Math.*, **7**, 83–103.

BELCHER, S. E. AND HUNT, J. C. R. 1993 Turbulent shear flow over slowly moving waves. *J. Fluid Mech.*, **251**, 109–148.

BELCHER, S. E., HARRIS, J. A. AND STREET, R. L. 1994 Linear dynamics of wind waves in coupled turbulent air flow. Part 1. Theory. *J. Fluid Mech.*, **271**, 119–151.

BIRINGEN, S. AND REYNOLDS, W. C. 1981 Large-eddy simulation of the shear-free turbulent boundary layer. *J. Fluid Mech.*, **103**, 53–63.

BORUE, V., ORSZAG, S. A. AND STAROSELSKY, I. 1995 Interaction of surface waves with turbulence: direct numerical simulation of turbulent open-channel flow. *J. Fluid Mech.*, **286**, 1–23.

BRITTER, R. E., HUNT, J. C. R. AND RICHARDS, K. J. 1981 Air flow over a two-dimensional hill: studies of velocity speed-up, roughness effects and turbulence. *Q. J. Roy. Met. Soc.*, **107**, 91–110.

BROCCHINI, M. AND PEREGRINE, D. H. 2000*a* The dynamics of turbulence at free surfaces. Part 1. Description of strong turbulence at a free surface. *Submitted to J. Fluid Mech.*

BROCCHINI, M. AND PEREGRINE, D. H. 2000*b* The dynamics of turbulence at free surfaces. Part 2. Free-surface boundary conditions. *Submitted to J. Fluid Mech.*

BRUMLEY, B. H. AND JIRKA, G. H. 1987 Near-surface turbulence in a grid-stirred tank. *J. Fluid Mech.*, **183**, 235–263.

CARRUTHERS, D. J. AND HUNT, J. C. R. 1986 Velocity fluctuations near an interface between a turbulent region and a stably stratified layer. *J. Fluid Mech.*, **165**, 475–501.

CAULLIEZ, G., RICCI, N. AND DUPONT, R. 1998 The generation of the first visible wind waves. *Phys. Fluids*, **10**, 757–759.

CORCOS, G. M. 1964 The structure of the turbulent pressure field in boundary-layer flows. *J. Fluid Mech.*, **18**, 353–378.

COX, C. S. 1958 Measurements of slopes of high-frequency wind waves. *J. Mar. Res.*, **16**, 199–225.

CRAIK, D. D. AND LEIBOVICH, S. 1976 A rational model for Langmuir circulations. *J. Fluid Mech.*, **73**, 401–426.

DONELAN, M. A. 1990 Air-sea interaction. In *The sea: ocean engineering science.* Volume 9. John Wiley & Sons.

DUIN, C. A. VAN AND JANSSEN, P. A. E. M. 1992 An analytical model of the generation of surface gravity waves by turbulent air flow. *J. Fluid Mech.*, **236**, 197–215.

DURBIN, P. A. 1978 Rapid distortion theory of turbulent flows. PhD thesis, University of Cambridge.

DURBIN, P. A. 1981 Distorted turbulence in axisymmetric flow. *Q. J. Mech. Appl. Math.*, **34**, 489–500.

DURBIN, P. A. 1993 A Reynolds stress model for near-wall turbulence. *J. Fluid Mech.*, **249**, 465–498.

DURBIN, P. A. AND HUNT, J. C. R. 1980 On surface pressure fluctuations beneath turbulent flow round bluff bodies. *J. Fluid Mech.*, **100**, 161–184.

FALLER, A. J. AND AUER, S. J. 1988 The roles of Langmuir circulations in the dispersion of surface tracers. *J. Phys. Oceanogr.*, **18**, 1108–1123.

FALLER, A. J. AND PERINI, C. 1984 The roles of Langmuir circulations in gas transfer across natural water surfaces. In *Gas transfer at water interfaces*, edited by W. Brutsaert and G. H. Jirka, D. Reidel Publishing Company.

FERNANDO, H. J. S. AND HUNT, J. C. R. 1997 Turbulence, waves and mixing at shear-free density interfaces. Part 1. A theoretical model. *J. Fluid Mech.*, **347**, 197–234.

FUNG, J. C. H., HUNT, J. C. R., MALIK, N. A. AND PERKINS, R. J. 1992 Kinematic simulation of homogeneous turbulence by unsteady random Fourier modes. *J. Fluid Mech.*, **236**, 281–318.

GELCI, R., RAMAMONJIARISOA, A. AND HERVOUET, J. Y. 1985 Génération de vagues de gravité par des allées de tourbillons aériens mobiles. *J. Mécanique Théorique et Appliqué*, **4**, 463–483.

GIOVANANGELI, J. P. AND MEMPONTEIL, A. 1985 Resonant and non-resonant waves excited by periodic vortices in airflow over water. *J. Fluid Mech.*, **159**, 69–84.

GOLDSTEIN, M. E. 1978 Unsteady vortical and entropic distortions of potential flows round arbitrary obstacles. *J. Fluid Mech.*, **89**, 433–468.

GREEN, T., MEDWIN, H. AND PAQUIN, J. E. 1972 Measurements of surface wave decay due to underwater turbulence. *Nature Physical Science*, **237**, 115–117.

HASSELMANN, K. 1962 On the non-linear energy transfer in a gravity-wave spectrum. Part 1. General Theory. *J. Fluid Mech.*, **12**, 481–500.

HASSELMANN, K. 1968 Weak-interaction theory of ocean waves. In *Basic Developments in Fluid Dynamics*, vol. 2, ed. M. Holt, Academic Press.

HASSELMANN, K. 1988 The WAM model – a 3rd generation ocean wave prediction model. *J. Phys. Oceanogr.*, **18**, 1775–1810.

HOFTEN, J. D. A. VAN AND KARAKI, S. 1976 *The interaction of gravity waves and turbulent channel flow.* Technical Report, Department of Civil Engineering, Colorado State University.

HUNT, J. C. R. 1973 A theory of flow round two-dimensional bluff bodies. *J. Fluid Mech.*, **61**, 625–706.

HUNT, J. C. R. 1984*a* Turbulence structure in thermal convection and shear-free boundary layers. *J. Fluid Mech.*, **138**, 161–184.

HUNT, J. C. R. 1984*b* Turbulence structure and turbulent diffusion near gas-liquid interfaces. In *Gas transfer at water interfaces*, edited by W. Brutsaert and G. H. Jirka, D. Reidel Publishing Company.

HUNT, J. C. R. 1988 Studying turbulence using direct numerical simulation: 1987 Center for Turbulence Research NASA Ames/Stanford Summer Programme. *J. Fluid Mech.*, **190**, 375–392.

HUNT, J. C. R. AND CARRUTHERS, D. J. 1990 Rapid distortion theory and the 'problems' of turbulence. *J. Fluid Mech.*, **212**, 497–532.

HUNT, J. C. R. AND GRAHAM, J. M. R. 1978 Free stream turbulence near plane boundaries. *J. Fluid Mech.*, **84**, 209–235.

HWANG, P. A., TRIZNA, D. B. AND WU, J. 1993 Spatial measurements of short wind waves using a scanning slope sensor. *Dyn. Atmos. Oceans*, **20**, 1–23.

JACOBS, S. J. 1987 An asymptotic theory for the turbulent flow over a progressive wave. *J. Fluid Mech.*, **174**, 69–80.

JÄHNE, B. AND RIEMER, K. S. 1990 Two-dimensional wavenumber spectra of small-scale water surface waves. *J. Geophys. Res.*, **95**, 11531–11546.

JEFFREYS, H. 1925 On the formation of water waves by wind. *Proc. Roy. Soc. London (A)*, **107**, 189–206.

JIMÉNEZ, J., WRAY, A. A., SAFFMAN, P. G. AND ROGALLO, R. S. 1993 The structure of intense vorticity in isotropic turbulence. *J. Fluid Mech.*, **255**, 65–90.

JOHANSSON, A. V. AND HALLBÄCK, M. 1994 Modelling of rapid pressure-strain in Reynolds-stress closures. *J. Fluid Mech.*, **269**, 143–168.

KAHMA, K. K. AND DONELAN, M. A. 1988 A laboratory study of the minimum wind speed for wind wave generation. *J. Fluid Mech.*, **192**, 339–364.

KEVLAHAN, N. K.-R. AND HUNT, J. C. R. 1997 Nonlinear interactions in turbulence with strong irrotational straining. *J. Fluid Mech.*, **337**, 333–364.

KIDA, S. AND HUNT, J. C. R. 1989 Interaction between different scales of turbulence over short times. *J. Fluid Mech.*, **201**, 411–445.

KIM, J. 1989 On the structure of pressure fluctuations in simulated turbulent channel flow. *J. Fluid Mech.*, **205**, 421–451.

KITAIGORODSKII, S. A. 1997 Effect of Breaking of wind-generated waves on the local atmosphere-ocean interaction. *Izv. Atmos. Oceanic Phys.*, **33**, 828–836.

KITAIGORODSKII, S. A. AND DONELAN, M. A. 1984 Wind-wave effects on gas transfer. In *Gas transfer at water surfaces*, edited by W. Brutsaert and G. H. Jirka, D. Reidel Publishing Company.

KITAIGORODSKII, S. A. AND LUMLEY, J. L. 1983 Wave-turbulence interactions in the upper ocean. Part I: The energy balance on the interacting fields of surface wind waves and wind-induced three-dimensional turbulence. *J. Phys. Oceanogr.*, **13**, 1977–1987.

KITAIGORODSKII, S. A., DONELAN, M. A., LUMLEY, J. L. AND TERRAY, E. A. 1983 Wave-turbulence interactions in the upper ocean. Part II: Statistical characteristics of wave and turbulent components of the random velocity field in the marine surface layer. *J. Phys. Oceanogr.*, **13**, 1988–1999.

KLINE, S. J., REYNOLDS, W. C., SCHTRAUSS, F. A. AND RUNSTADLER, P. W. 1967 The structure of turbulent boundary layers. *J. Fluid Mech.*, **30**, 741–773.

KOMORI, S., MURAKAMI, Y. AND UEDA, H. 1989 The relationship between surface-renewal and bursting motions in an open-channel flow. *J. Fluid Mech.*, **203**, 103–123.

KOMORI, S., NAGAOSA, R., MURAKAMI, Y., CHIBA, S., ISHII, K. AND KUWAHARA, K. 1993 Direct numerical simulation of three-dimensional open-channel flow with zero-shear gas-liquid interface. *Phys. Fluids*, **5**, 115–125.

KRASITSKIY, V. P. 1980 Generation of wind waves in the initial stage. *Izv. Atmos. Oceanic Phys.*, **16**, 898–900.

KUDRYAVTSEV, V. N., MAKIN, V. K. AND CHAPRON, B. 1999 Coupled sea surface-atmosphere model - 2. Spectrum of short wind waves. *J. Geophys. Res.*, **104**, 7625–7639.

LAMB, H. 1932 *Hydrodynamics*. 6th edition. Cambridge University Press.

LEE, M. J. AND HUNT, J. C. R. 1989 The structure of sheared turbulence near a plane boundary. *7th Simp. on Turbulent Shear Flows, Stanford.*

LEE, M. J., KIM, J. AND MOIN, P. 1990 Structure of turbulence at high shear rate. *J. Fluid Mech.*, **216**, 561–583.

LEIBOVICH, S. 1983 The form and dynamics of Langmuir circulations. *Ann. Rev. Fluid Mech.*, **15**, 391–427.

LONGUET-HIGGINS, M. S. 1984 New integral relations for gravity waves of finite amplitude. *J. Fluid Mech.*, **149**, 205–215.

LONGUET-HIGGINS, M. S. 1996 Surface manifestations of turbulent flow. *J. Fluid Mech.*, **308**, 15–29.

MAGNAUDET, J. AND THAIS, L. 1995 Orbital rotational motion and turbulence below laboratory wind water waves. *J. Geophys. Res.*, **100**, 757–771.

MANN, J. 1994 The spatial structure of neutral atmospheric surface-layer turbulence. *J. Fluid Mech.*, **273**, 141–168.

MAXEY, M. R. 1982 Distortion of turbulence in flows with parallel streamlines. *J. Fluid Mech.*, **124**, 261–282.

MCLEISH, W. AND PUTLAND, G. E. 1975 Measurements of wind-driven flow profiles in the top millimeter of water. *J. Phys. Oceanogr.*, **5**, 516–518.

MCWILLIAMS, J. C., SULLIVAN, P. P. AND MOENG, C.-H. 1997 Langmuir turbulence in the ocean. *J. Fluid Mech.*, **334**, 1–30.

MELVILLE, W. K. 1996 The role of surface-wave breaking in air-sea interaction. *Ann. Rev. Fluid Mech.*, **28**, 279–321.

MELVILLE, W. K., SHEAR, R. AND VERON, F. 1998 Laboratory measurements of the generation and evolution of Langmuir circulations. *J. Fluid Mech.*, **364**, 31–58.

MILES, J. W. 1957 On the generation of surface waves by shear flow. *J. Fluid Mech.*, **3**, 185–204.

MILGRAM, J. H. 1998 Short wave damping in the simultaneous presence of a surface film and turbulence. *J. Geophys. Res.*, **103**, 15717–15727.

NAZARENKO, S., KEVLAHAN, N. K.-R. AND DUBRULLE, B. 1999 WKB theory for rapid distortion of inhomogenous turbulence. *J. Fluid Mech.*, **390**, 325–348.

NEPF, H. M. AND MONISMITH, S. G. 1995 Longitudinal vortices beneath breaking waves. *J. Geophys. Res.*, **100**, 16211–16221.

ÖLMEZ, H. S. AND MILGRAM, J. H. 1992 An experimental study of attenuation of short water waves by turbulence. *J. Fluid Mech.*, **239**, 133–156.

PAN, Y. AND BANERJEE, S. 1995 Numerical study of free-surface turbulence in channel flow. *Phys. Fluids*, **7**, 1649–1664.

PERKINS, R. J., CARRUTHERS, D. J., DRAYTON, M. J. AND HUNT, J. C. R. 1990 Turbulence and diffusion at density interfaces. In *Phase-Interface Phenomena in Multiphase Flow*, Hemisphere.

PEROT, B. AND MOIN, P. 1993 *Shear-free turbulent boundary layers: physics and modeling.* Report No. TF-60, Thermosciences Division, Department of Mechanical Engineering, Stanford University.

PEROT, B. AND MOIN, P. 1995*a* Shear-free turbulent boundary layers. Part 1. Physical insights into near-wall turbulence. *J. Fluid Mech.*, **295**, 199–227.

PEROT, B. AND MOIN, P. 1995*b* Shear-free turbulent boundary layers. Part 2. New concepts for Reynolds stress transport equation modelling of inhomogeneous flows. *J. Fluid Mech.*, **295**, 229–245.

PHILLIPS, O. M. 1957 On the generation of waves by turbulent wind. *J. Fluid Mech.*, **2**, 417–445.

PHILLIPS, O. M. 1959 The scattering of gravity waves by turbulence. *J. Fluid Mech.*, **5**, 177–192.

PHILLIPS, O. M. 1977 *The dynamics of the upper ocean*. Cambridge University Press.

RAPP, R. AND MELVILLE, W. 1990 Laboratory measurements of deep-water breaking waves. *Philos. Trans. Roy. Soc. London A*, **331**, 735–800.

SALVETTI, M. V., ZANG, Y., STREET, R. L. AND BANERJEE, S. 1997 Large-eddy simulation of free-surface decaying turbulence with dynamic subgrid-scale models. *Phys. Fluids*, **9**, 2405–2419.

SAZONTOV, A. G. AND SHAGALOV, S. V. 1984 A contribution to the theory of generation of hydrodynamic wave turbulence at an interface. *Izv. Atmos. Oceanic Phys.*, **20**, 511–517.

SHRIRA, V. I. 1993 Surface waves on shear currents: solution of the boundary-value problem. *J. Fluid Mech.*, **252**, 565–584.

SIMPSON, J. J. 1984 On the exchange of oxygen and carbon dioxide between ocean and atmosphere in an eastern boundary current. In *Gas transfer at water surfaces*, edited by W. Brutsaert and G. H. Jirka, D. Reidel Publishing Company.

SKODA, J. D. 1972 The interaction of waves and turbulence in water. Ph.D. thesis. University of California, Berkeley.

STERNBERG, J. 1962 A theory for the viscous sublayer of a turbulent flow. *J. Fluid. Mech.*, **13**, 241.

TAYLOR, G. I. 1935 Turbulence in a contracting stream. *Z. angew. Math. Mech.*, **15**, 91–96.

TENNEKES, H. AND LUMLEY, J. L. 1972 *A first course in turbulence*. The MIT Press.

THAIS, L. AND MAGNAUDET, J. 1996 Turbulent structure beneath surface gravity waves sheared by the wind. *J. Fluid Mech.*, **328**, 313–344.

THEOFANOUS, T. G. 1984 Conceptual models of gas exchange. In *Gas transfer at water surfaces*, edited by W. Brutsaert and G. H. Jirka, D. Reidel Publishing Company.

THOMAS, N. H. AND HANCOCK, P. E. 1977 Grid turbulence near a moving wall. *J. Fluid Mech.*, **82**, 481–496.

TOWNSEND, A. A. 1970 Entrainment and the structure of turbulent flow. *J. Fluid Mech.*, **41**, 13–46.

TOWNSEND, A. A. 1972 Flow in a deep turbulent boundary layer over a surface distorted by water waves. *J. Fluid Mech.*, **55**, 719–735.

TOWNSEND, A. A. 1976 *The structure of turbulent shear flow, 2nd edition*. Cambridge University Press.

TOWNSEND, A. A. 1980 The response of sheared turbulence to additional distortion. *J. Fluid Mech.*, **81**, 171–191.

TSAI, W.-T. 1998 A numerical study of the evolution and structure of a turbulent shear layer under a free surface. *J. Fluid Mech.*, **354**, 239–276.

TURFUS, C. AND HUNT, J. C. R. 1987 A stochastic analysis of the displacements of fluid elements in inhomogeneous turbulence using Kraichnan's method of random modes. In *Advances in Turbulence*, Springer.

URSELL, F. 1956 Wave generation by wind. In *Surveys in Mechanics*, edited by G. K. Batchelor and R. M. Davis, pp. 216–249. Cambridge University Press.

UZKAN, T. AND REYNOLDS, W. C. 1967 A shear-free turbulent boundary layer. *J. Fluid Mech.*, **28**, 803–821.

WALKER, D. T., LEIGHTON, R. I. AND GARZA-RIOS, L. O. 1996 Shear-free turbulence near a flat free surface. *J. Fluid Mech.*, **320**, 19–51.

WANG, L., CHEN, S., BRASSEUR, J. G. AND WYNGAARD, J. C. 1996 Examination of hypotheses in the Kolmogorov refined turbulence theory through high-resolution simulations. Part 1. Velocity field. *J. Fluid Mech.*, **309**, 113–156.

ZHANG, X. 1995 Capillary-gravity and capillary waves generated in a wind wave tank: observations and theories. *J. Fluid Mech.*, **289**, 51–82.